UNIVERSITY OF CALIFORNIA SAN DIEGO

Diagnosis, Prognosis, and Maintenance Decision Making for Civil Infrastructure

A dissertation submitted in partial satisfaction of the requirements for the degree

Doctor of Philosophy

in

Structural Engineering

By

Manuel A. Vega

Committee in charge:

Michael D. Todd, Chair
Gilberto Mosqueda, Co-Chair
Joel P. Conte
William S. Hodgkiss
Jose I. Restrepo
Matthew D. Smith

2020

The Dissertation of Manuel A. Vega is approved, and it is acceptable in quality and form for publication on microfilm and electronically:

_____

_____

_____

_____

_____

Co-chair

_____

Chair

University of California San Diego

2020

DEDICATION

This dissertation is dedicated to my wife, Eliza, for her support and patience while I worked towards to complete my PhD research. Also, I dedicate this to my amazing kids Sofia, Madison, Diego and Michael, who are with my wife my world and motivation in life. As well, to my aunt Belinda who always believed in me and helped me to obtain a higher education.

EPIGRAPH

All models are wrong, but some are useful. —George E. P. Box

TABLE OF CONTENTS

LIST OF FIGURES

LIST OF TABLES

ACKNOWLEDGEMENTS

The work presented in this dissertation could not have been possible without the support of many people. First and foremost, my advisor, Michael Todd, who has guided me and most important believed in me to success in my academic journey. I am grateful to him for always being available when I need his mentorship and guidance. I also want to thank Gilberto Mosqueda, who gave me the opportunity to come to UCSD and help me to complete part of this dissertation. I also want to thank the other members of my committee, Joel Conte, William Hodgkiss, Jose Restrepo and Matthew Smith, who have provided directly and indirectly suggestions to improve my research work. Additionally, I want to thank Zhen Hu, who I have the chance to work very closely in the last year of my PhD research and contributed significantly to my work.

Portions of this dissertation have been published or are currently being considered for publication. Chapter 2 is composed of a first authored publication:

Vega, Manuel A., and Michael D. Todd. 2020. "A Variational Bayesian Neural Network for Structural Health Monitoring and Cost-Informed Decision-Making in Miter Gates." Structural Health Monitoring, no. Special Issue. https://doi.org/10.1177/1475921720904543.

Chapter 3 is composed by two articles that have been submitted and currently under review for publication:

Vega, Manuel A., Zhen Hu, and Michael D. Todd. 2020. "Optimal Maintenance Decisions for Deteriorating Quoin Blocks in Miter Gates Subject to Uncertainty in the Condition Rating Protocol." Reliability Engineering & System Safety 204. https://doi.org/10.1016/j.ress.2020.107147.

Vega, Manuel A., Zhen Hu, Travis B. Fillmore, Matthew D. Smith, and Michael D. Todd. 2020. "Integration of Abstracted Inspection Data and Structural Health Monitoring for Damage Prognosis of Miter Gates (under review)." Reliability Engineering & System Safety.

Chapter 4 is currently in preparation for publication as an extension of:

Vega, Manuel A., Mukesh K. Ramancha, Joel P. Conte, and Michael D. Todd. 2021. "Efficient Bayesian Inference of Miter Gates Using High-Fidelity Models." In 38th International Modal Analysis Conference. Houston, Texas: Springer.

Chapter 5 is composed of a first authored publication:

Vega, Manuel A., Andreas H. Schellenberg, Humberto Caudana, and Gilberto Mosqueda. 2020. "Implementation of Real-Time Hybrid Shake Table Testing Using the UCSD Large High-Performance Outdoor Shake Table." International Journal of Lifecycle Performance Engineering Volume 4 (Special Issue on Hybrid Simulation for Multi-Hazard Engineering): 80–102. https://doi.org/10.1504/IJLCPE.2020.108939.

VITA

2014 Bachelor of Science, Brigham Young University, Provo

2015 Master of Science, University of Michigan, Ann Arbor

2018-2020 SMART Student Intern, U.S. Army Engineer Research and Development Center

2020 Doctor of Philosophy, University of California San Diego

PUBLICATIONS

Journal Papers:

Vega, Manuel A., Zhen Hu, Travis B. Fillmore, Matthew D. Smith, and Michael D. Todd. 2020. "Integration of Abstracted Inspection Data and Structural Health Monitoring for Damage Prognosis of Miter Gates." Reliability Engineering & System Safety (under review).

Vega, Manuel A., Zhen Hu, and Michael D. Todd. 2020. "Optimal Maintenance Decisions for Deteriorating Quoin Blocks in Miter Gates Subject to Uncertainty in the Condition Rating Protocol." Reliability Engineering & System Safety 204. https://doi.org/10.1016/j.ress.2020.107147.

Vega, Manuel A., and Michael D. Todd. 2020. "A Variational Bayesian Neural Network for Structural Health Monitoring and Cost-Informed Decision-Making in Miter Gates." Structural Health Monitoring, no. Special Issue. https://doi.org/10.1177/1475921720904543.

Vega, Manuel A., Andreas H. Schellenberg, Humberto Caudana, and Gilberto Mosqueda. 2020. "Implementation of Real-Time Hybrid Shake Table Testing Using the UCSD Large High-Performance Outdoor Shake Table." International Journal of Lifecycle Performance Engineering, no. Special Issue. https://doi.org/10.1504/IJLCPE.2020.10031046

Vega, Manuel A., Mukesh K. Ramancha, Joel P. Conte, and Michael D. Todd. 2021 "A comparison of physics based model updating frameworks for reliability of Miter Gates." (in progress)

Yang, Yichao, Mayank Chadha, Zhen Hu, **Manuel A. Vega**, Matthew D. Parno, and Michael D. Todd. 2021. "A Probabilistic Optimal Sensor Design Framework for Structural Health Monitoring using Risk Weighted *f*-Divergence." (draft completed)

Chadha, Mayank, Mukesh K. Ramancha, **Manuel A. Vega**, Joel P. Conte, and Michael D. Todd. 2021. "Risk Profile Dependent State-Determination of Structures." (in progress)

Conference Papers

Vega, Manuel A., Mukesh K. Ramancha, Joel P. Conte, and Michael D. Todd. 2021. "Efficient Bayesian Inference of Miter Gates Using High-Fidelity Models." In 38th International Modal Analysis Conference. Houston, Texas: Springer.

Vega, Manuel A., Ramin Madarshahian, Travis B. Fillmore, and Michael D. Todd. 2019. "Optimal Maintenance Decision for Deteriorating Components in Miter Gates Using Markov Chain Prediction Model." In Structural Health Monitoring 2019: Enabling Intelligent Life-Cycle Health Management for Industry Internet of Things (IIOT), 1471–78. Lancaster, PA: DEStech Publications, Inc. https://doi.org/10.12783/shm2019/32269.

Vega, Manuel, Ramin Madarshahian, and Michael D. Todd. 2019. "Classification of Damage in Miter Gates Using Hierarchical Clustering to Identify Optimal Sensing." In 9th International Conference on Structural Health Monitoring of Intelligent Infrastructure. ST. Louis, Missouri.

Vega, Manuel, Ramin Madarshahian, and Michael D. Todd. 2019. "A Neural Network Surrogate Model for Structural Health Monitoring of Miter Gates in Navigation Locks." In 37th International Modal Analysis Conference, 93–98. Orlando, Florida. https://doi.org/10.1007/978-3-030-12075-7_9.

Caudana, Humberto, **Manuel Vega**, and Gilberto Mosqueda. 2017. "Effects of Time Delays and Filtered Feedback in Hybrid Simulation with Shake Table." In 3rd Huixian International Forum on Earthquake Engineering for Young Researchers. Champaign, Illinois.

Alvarez-Sanchez, R., **M. Vega**, J. Restrepo, and F. Perez. 2017. "Virtual Hybrid Simulation Based on OpenSees/Abaqus of a Parking Structure Located in Mexicali BC." In XXI National Congress of Earthquake Engineering, Mexican Society of Earthquake Engineering. Guadalajara, Mexico.

ABSTRACT OF THE DISSERTATION

Diagnosis, Prognosis, and Maintenance Decision Making for Civil Infrastructure

by

Manuel A. Vega

Doctor of Philosophy in Structural Engineering

University of California San Diego, 2020

Michael D. Todd, Chair
Gilberto Mosqueda, Co-Chair

Due to the aging of civil infrastructure and the associated economic impact, there is an increasing need to continuously monitor their structural and non-structural components for system life-cycle management, including maintenance prioritization. Many times, this monitoring process involves different types of data sources collected at different time scales and resolutions, such as abstracted rating data from human inspections, historical failure record data, uncertain cost data, high-fidelity physics-based simulation data, and online high-resolution structural health monitoring (SHM) data. The heterogeneity of the data sources poses challenges to the diagnostic/prognostic implementation of decision-making for maintenance. Using components of

a miter gate as the exemplary case study, this dissertation presents a condition-based maintenance framework to demonstrate how to integrate various data sources using Bayesian and Machine Learning (ML) methods for effective SHM, and Prognostics and Health Management (PHM). In particular, this thesis focuses on the different pieces of the proposed framework, which are (1) surrogate based model updating for damage diagnosis; (2) integration of abstracted data and SHM for damage prognosis; (3) diagnostics of multiple forms of damage in miter gates; and (4) validation of physics-based diagnostic models using hybrid structural testing.

Chapter 1

INTRODUCTION

Maintenance planning has been extensively studied for various engineering systems. Current approaches can be roughly classified into two categories, namely time-based maintenance (TBM) and condition-based maintenance (CBM). CBM is closely related to condition monitoring (CM), which is a damage detection implementation based on a condition monitoring process applied to rotating machinery (Mitchell 2007). When applied to civil engineering and aerospace systems, CM is referred to as structural health monitoring (SHM) with the important distinction that SHM is done more or less continuously and uses a permanently-installed system. When the diagnosis results of either CM or SHM are used to trigger maintenance decision, a condition-based maintenance (CBM) decision policy arises.

1.1. Time-based maintenance (TBM)

TBM (also known as periodic-based maintenance) assumes that the estimated failure behavior is statistically or experientially known (Yam et al. 2001). Statistical modelling, such as Weibull analysis (Weibull 1951), is widely used in TBM to identify failure characteristics of a component or system. The goal of TBM models is to find the optimal policy that minimize a cost function. TBM approaches have been developed for both repairable or nonrepairable systems (Barlow and Hunter 1960). The complexity of a TBM model depends on the targeted system such as single-system, multi-systems, parallel and series structure. Applications for single components or multi-components systems are found in (Das and Acharya 2004; Castro and Sule Alfa 2004)

and (Nakagawa and Yasui 2005; Childress and Durango-Cohen 2005) respectively. A more extensive review of TBM applications can be found here (Ahmad and Kamaruddin 2012). Chapter 3 will show an example of a TBM approach applied to inspection rating data of a single components of a hydraulic civil structure.

1.2. Condition-based maintenance (CBM)

CBM is the most modern and popular maintenance technique among researchers and industry. CBM has gained increasing attention recently as a preferred approach to TBM. CBM is a maintenance approach that combines data-driven reliability models and information from a condition monitoring process (e.g. continuous monitoring, periodic inspection or non-periodic inspection). Based on the underlying degradation model, CBM models can be categorized into two subgroups: 1) models that assume discrete-state deterioration and 2) models that assume continuous state deterioration. A most extensive list of CBM application can be found in here (Y. Zhu et al. 2010; Tian et al. 2011; Tian and Liao 2011; Alaswad and Xiang 2017). Most of the CBM applications available in the literature are for mechanical systems, aerospace systems, or manufacturing systems. For large civil engineering infrastructure, most of the applications have been applied to bridge engineering (Petcherdchoo, Neves, and Frangopol 2008; Saydam and Frangopol 2015; Gong and Frangopol 2020). In CBM, maintenance schedules are predicted based on the results from diagnosis and prognosis. For diagnosis and prognosis, the approaches can be classified into physics-based approach (M. E. Orchard and Vachtsevanos 2007; Daigle and Goebel 2011; An et al. 2011), data-driven approach (Zio and Di Maio 2010; Mohanty et al. 2009; Galar et al. 2012; Ye and Xie 2015), and hybrid approach (J. Xu and Xu 2011; Liao and Kottig

2014). Hybrid approaches that combine the physics-based approach with data-driven approach to improve the CBM predictive capabilities is the focus of Chapter 3.

1.2.1 Structural Health Monitoring (SHM)

The term SHM generally refers to the implementation of a damage detection strategy for an engineering system. This implementation involves: i) periodically sampled response measurements, ii) extraction of damage-sensitive features from these measurements and ii) damage diagnosis using these features with either an inverse-problem approach or a data driven approach. Depending on the field of engineering, there are pros and cons for both approaches when applied to an engineering system.

For civil engineering systems, the inverse problem approach is usually carried out by using a physics-based model (e.g. finite element (FE) model) of the civil structure. An "inverse" problem refers to problems where the system parameters are estimated from measured response quantities. Generally, a physics-based model is a "forward" problem where the system responses (e.g. FE output response) are predicted as a function of the (known) system parameters (e.g. FE inputs). This approach is more desirable when only limited SHM data that relates the input and output of the system is available. More details of this approach will be discussed in section 1.2.2. When sufficient SHM monitoring data is available, a data driven approach can be taken. It can also be an alternative when physics-based models do not explain sufficiently the physics of the system. More details of this approach will be discussed in section 1.2.3.

As stated earlier, CBM can make use of the SHM diagnostic capabilities to have access to the current state (a.k.a. state estimation) or model parameters (a.k.a. parameter estimation) of the system of interest. However, SHM data may contain noise due to the sensor behavior and environmental and operational variability. Also, SHM data could be bias due to calibration error;

in other words, this bias reflects a deviation of the signals from the correct ones. In the next section, more discussion details of the SHM diagnostic capabilities using an inverse problem approach with a physical based model to is presented.

1.2.2 Damage Diagnosis using Physics based Model Updating

When measurement data from sensors is available, researchers rely on Finite Element (FE) model updating techniques to estimate the unknown parameters to infer the current state of the system. For hydraulic infrastructure systems (e.g. dams, miter gates), several researchers (M. A. Vega et al. 2021; Ramancha et al. 2019; Y. Yang, Madarshahian, and Todd 2019) have updated physics-based linear and nonlinear FE models using simulated measurement data. Also, FE models have been used to study crack propagation and fatigue of miter gates (Mahmoud, Chulahwat, and Riveros 2018). For other civil infrastructure systems, researchers have successfully performed model updating of mechanics-based linear FE models using real measurement data (Moaveni, Conte, and Hemez 2009; Jang, Li, and Spencer 2013). However, only recently are there efforts to perform model updating of mechanics-based nonlinear FE model of full-scale civil system using real measurement data (Ramancha et al. 2020). Other efforts have performed model updating of mechanics-based nonlinear FE model using simulated measurement data (Astroza et al. 2017; Jensen et al. 2017). Furthermore, researchers have used the predictions of updated mechanics-based FE models for reliability assessments (Okasha, Frangopol, and Orcesi 2012). Recently, researchers have made use of surrogate models to serve as fast emulators of computationally expensive FE models, whose predictions are also used for reliability assessments (Bichon, McFarland, and Mahadevan 2011; Jensen et al. 2017; M. Vega, Madarshahian, and Todd 2019; Z. Wang and Shafieezadeh 2020). Chapter 3 and 4 will make use of a Gaussian process regression (GPR) model as a fast emulators of computationally expensive FE models.

Besides the faster diagnosis capabilities, it is important to note that these surrogate models cannot overperform the FE accuracy, and therefore they can perform as well as the FE that originally represented the structural system. However, a FE model will always contain model discrepancy between the FE model and the true system. Reducing or accounting for this model discrepancy during the model updating process can significantly improve SHM diagnostic capabilities. To reduce the model discrepancy, especially in systems with highly nonlinear behavior, researchers rely on structural testing to validate and improve specific FE models when limited SHM data is available. In the next section, an alternative structural testing method suitable for calibration and validation of a high nonlinear structural component is briefly discussed.

1.2.2.1 Model Validation via Structural Testing

There are several well-established methods to conduct structural testing for evaluating the behavior of structural systems and/or components thereof. In structural systems that behave observationally as a linear elastic system, experimental modal analysis has been used to determine the dynamic characteristics of the system in terms of the modal parameters. This type of analysis can be accomplished using traditional forced vibration testing (e.g. using hammer or shaker). However, damage may introduce nonlinearities into the system, which violates some or all the basic assumptions for experimental modal analysis (Farrar and Worden 2012). These assumptions require that the structure i) obeys the linearity principles of superposition and homogeneity, ii) is time invariant, and iii) exhibits reciprocity.

Many times, for civil engineering infrastructure, SHM data in the damaged condition where nonlinearity is introduced is not readily available. This led researchers to rely on laboratory testing to evaluate nonlinear model of systems or components, whose FE model or model parameters generally are not as accurate as the FE models of systems that behave as a linear elastic system. In

civil engineering, there are several laboratories that allow structural systems to be exposed to dynamic loading conditions from seismic events, wind, blast, impact, waves, fire, and traffic. However, to make these tests as accurate as possible, large testing programs may be required, which may impose economic challenges and limitations depending on the laboratory load capacity. Hybrid simulation is currently a well-developed method to conduct laboratory testing that reduces partially the limitations mentioned earlier. In hybrid simulation, a conventional FE analysis is performed where physical models of some portions of the structure are embedded in the numerical model. These physical models are tested in the laboratory and coupled even in real time with the numerical model part of the analysis. Generally, the portion of the system of interest that is not well understood is to be physically modeled in the laboratory. The portion whose behavior is well captured by numerical models is maintained as a numerical model and coupled with the physical model.

Structures subjected to seismic loading has been a very attractive system for hybrid simulation testing which includes systems such as building and bridges. Also, FE element model updating has been used in hybrid simulation to update the parameters of the nonlinear material models as the test progresses (Hashemi, Masroor, and Mosqueda 2014; Xiaoyun Shao, Mueller, and Mohammed 2016). Chapter 5 will show an example of model validation of a highly nonlinear components using a structural hybrid test, which includes two implementations denoted as hard real time hybrid simulation and soft real time hybrid simulation. The term *hard* refers to the fact that the FE numerical part is run in a true real-time hardware/software environment such as Simulink Real-Time (SimulinkRT, formerly known as xPC target) (Mathworks 2015), which is directly connected to run at the same clock time as the shake table controller, in other words the equation of motion of the numerical FE model is solved in real time and synchronized with the

controller. While the term *soft* refers to the fact that an external FE models is intended to run faster than real time to send signals at each time step to the controller so real time execution can still be achieved in the full hybrid model.

1.2.3 Damage Diagnosis using Data Driven Models

The data driven approach uses a mathematical model to learn the mapping function that transforms input variables (e.g. output response or extracted feature of the system) into the output variable (e.g. healthy and damage states of interest for the structure or SHM damage diagnosis). Supervised learning algorithms can be used when data is available from these input and output variables. On the other hand, unsupervised learning algorithms can be used when only data from the input variable (e.g. output response or extracted feature of the system) is available. Note that the data driven approach in this case is learning directly the inverse function of the system, i.e., the mapping from the output response or extracted feature of the system to assign to the relevant diagnostic label. If this diagnostic label is defined as a class, the supervised learning algorithm used is known as classification. Conversely, if the diagnosis label is defined in a continuous fashion, the supervised learning algorithm used is known as regression analysis. This approach is more desirable when large amount of SHM data that relates the input and output of the system is available. Various SHM damage diagnosis algorithms for civil engineering infrastructure, such as bridges (Mikami, Tanaka, and Hiwatashi 1998; H. Xu and Humar 2006; Shu et al. 2013) and buildings (Masri et al. 1996; Kim, Yoon, and Kim 2000; N. Wang et al. 2018), have been implemented based using data driven models.. Chapter 2 will show an example of a CBM approach using Bayesian Neural Network (BNN) data driven model.

1.2.4 Prognostics and Health Management (PHM)

PHM is an engineering approach that in addition to diagnosis assessments of engineering system (from either CM or SHM), it includes predictions of the future state and reliability of the system based on degradation data. This degradation data encodes information about the degradation behavior of the system, and thus it may be used to build degradation models. As with diagnosis, prognosis may employ the use of physics-based approaches or data driven approaches to build a physical degradation model or a data driven degradation model. Additionally, PHM uses its prediction capabilities to inform life cycle management, which target to optimize a certain system performance criterion (e.g. cost, availability, reliability, etc.). In summary, PHM enables engineers to turn available data into information that enhance the current knowledge of the system and also provides a policy to maintain the system optimally.

In some engineering applications, researchers have tried to model the evolution/degradation of damage using physical degradation models such as applications in fatigue crack growth (An, Choi, and Kim 2012; Li et al. 2017; Leung et al. 2019) and corrosion growth (Guedes Soares, Garbatov, and Zayed 2011; C. Wang and Elsayed 2020). These physical degradation models are developed based on the understanding of physical behavior and (usually) validated by experiments. On the other hand, data driven degradation models are used when the evolution/degradation of damage is not well understood either due to limited understanding of the physical phenomenon or when the damage cannot be measured continuously or measured directly. As before, the measured data used to parametrize a degradation model (i.e. physical or data driven) can be defined in a discrete or continuous state as it will be shown in the next subsections.

1.2.4.1 Discrete Degradation

In some civil infrastructure, inspections are based on discrete rating systems such as bridges (Graybeal et al. 2002), offshore structures (Y. Zhang, Kim, and Tee 2017), pavements (Abaza 2017) and other structures (Mohseni et al. 2017).

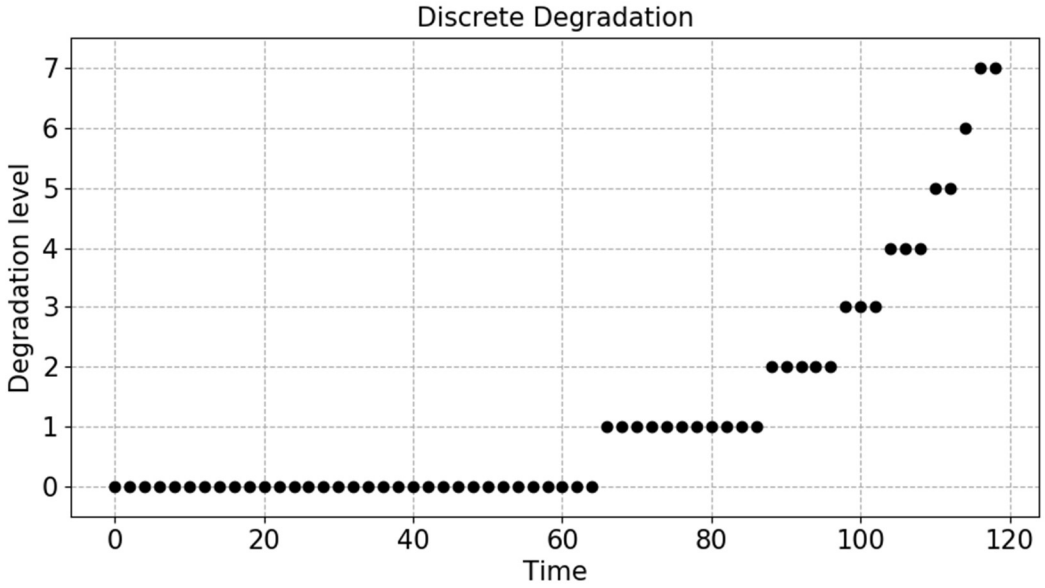

Figure 1.1: Idealized discrete degradation data (noise free)

Figure 1.1 shows an example of discrete degradation data, where the degradation level is categorized into discrete states/rating (e.g. 0-7). Data driven approaches (e.g. a Markov transition matrix) are generally used to explain discrete degradation models as shown in several studies of deteriorating systems. However, few studies have studied CBM policies using this type of degradation models. Section 3.5 will show a CBM framework that uses discrete degradation model.

1.2.4.2 Continuous Degradation

For many systems, a continuous degradation model can be built when SHM data is available or using a physics-based approach when data is limited but whose predictions of the damage are in a continuous domain as shown in Figure 1.2. Lately, CBM has been implemented for systems with continuous degradation models and available SHM data (Lu, Tu, and Lu 2007;

Arzaghi et al. 2017). Section 3.8 will show a CBM framework that uses continuous stochastic degradation model, which account for the uncertainty of the degradation model by assuming a family of continuous degradation models.

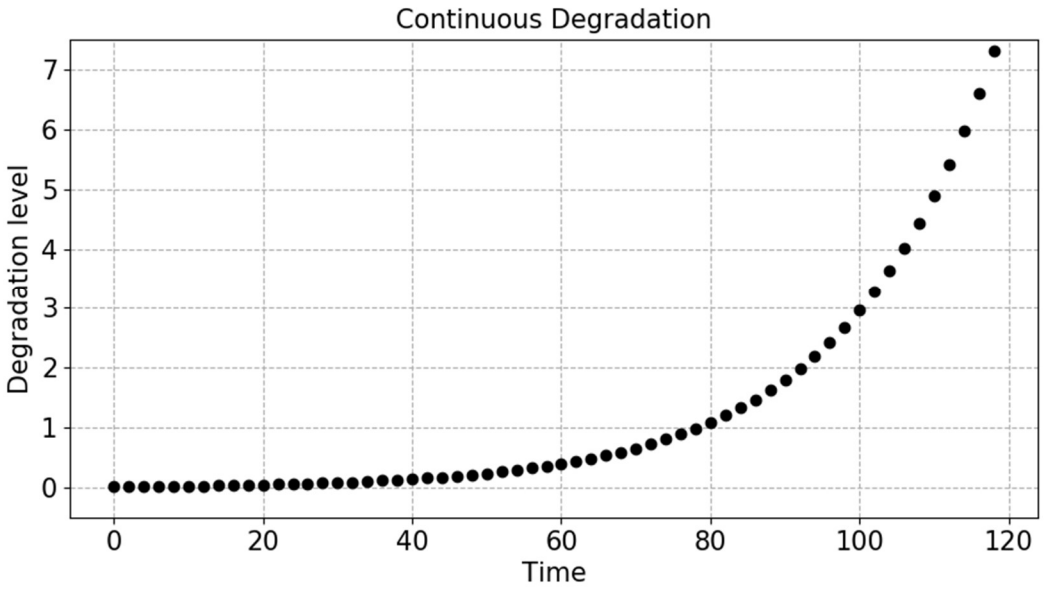

Figure 1.2: Idealized continuous degradation data (noise free)

1.2.4.3 Remaining Useful Life (RUL)

Once the degradation model is defined, this model can be used to predict the remaining useful life (RUL). The RUL is the remaining time until the degradation grows to a threshold. For a stochastic degradation model, the RUL is a distribution that can be calculated by estimating the corresponding end of life (EOL) distribution and subtracting the current time. The EOL expected value is the corresponding predicted time to when the degradation reaches the critical damage threshold, which would trigger a maintenance action. The threshold of degradation usually would be based on engineering experience and/or knowledge. However, this threshold may also be computed when enough failure data is given Figure 1.3 shows a schematic of how to use the predictions to calculate the EOL and RUL distributions.

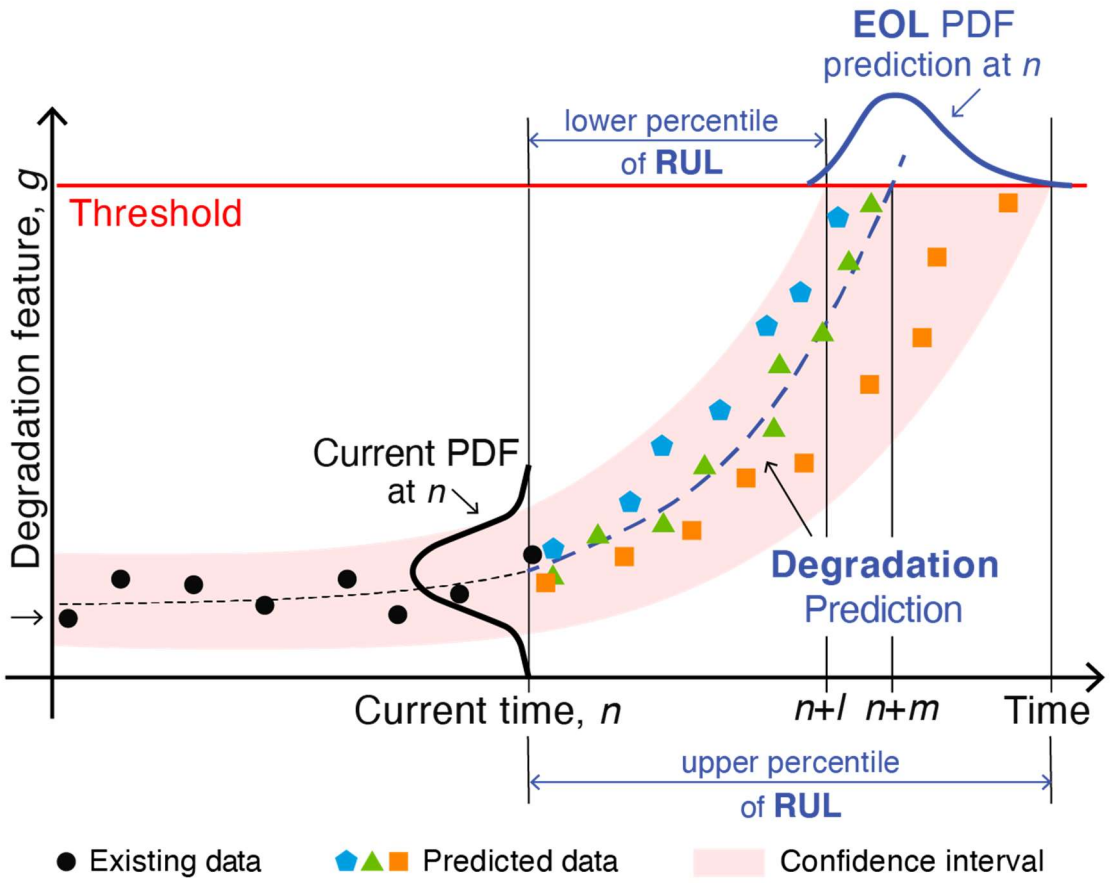

Figure 1.3: RUL calculation based on continuous degradation data

1.3. Optimal Maintenance using (long-term) Life Cycle Cost

For TBM and CBM application, several different cost functions can be used to optimize a specific criterion, e.g., cost minimization, availability maximization, or multi-objective functions including optimal threshold design. More details of different types of objective functions can be found in (Alaswad and Xiang 2017). In the work presented in this thesis, a cost minimization function will be presented and used for TBM and CBM purposes (see Chapter 3).

1.4. Research Objectives, Organization of Thesis and Contributions:

For large civil infrastructure, current approaches mainly use either data-driven methods (e.g. Markov transition matrix or other statistical method) or physics-based approach (e.g. FE

model updating). For the case of the miter gate and many other structures, a physics-based approach which employs high-fidelity FE model to predict the miter gate response is required by the decision maker, due to the lack of data required for data-driven approach. In order to use physics-based approaches for prognostics, a degradation state equation would be needed. The degradation of some critical components of the miter gate, however, is not fully well understood, which makes the physics-based prognostics challenging. Based on these challenges, the objectives of this work are the following:

1) Overcome the physics-based prognostics challenge by integrating physics-based SHM with a statistical-based state transition matrix.
2) Provide a CBM framework applicable to civil structures (demonstrated on horizontally-framed miter gates) that have online health monitoring systems and are subject to condition rating (e.g. OCA) data.
3) Extend and suggest recommendations to improve the current diagnosis capabilities of particular civil structures of interest.

To realize these objectives, this thesis contains four chapters that will explain in detail the aforementioned objectives and also will expand on the different topics reviewed earlier. **Chapter 2** will show a SHM diagnosis framework using the data driven approach to map SHM monitoring data to damage, and a discrete degradation model is introduced to suggest optimal maintenance based on the diagnosis results for a given damage threshold. **Chapter 3** will show a TBM framework based on historical condition ratings. It will also show a CBM framework based on online health monitoring systems and condition ratings. Additionally, this chapter will explain how to overcome the challenge of integrating physics-based SHM with a statistical-based state transition matrix. **Chapter 4** will show the diagnosis of multiple forms of damage of a

horizontally-framed miter gates and it will suggest further work steps to perform multi-component CBM. Finally, **Chapter 5** will show explain in detail an alternative structural testing approach to perform model validation of a high nonlinear components whose FE models may not fully capture its behavior and therefore introduce significant model error.

Figure 1.4 summarizes the different pieces that are needed to perform diagnosis, prognosis, and maintenance decisions under the work presented in this research work. The chapters of this thesis will cover the majority of these blocks shown in this Figure.

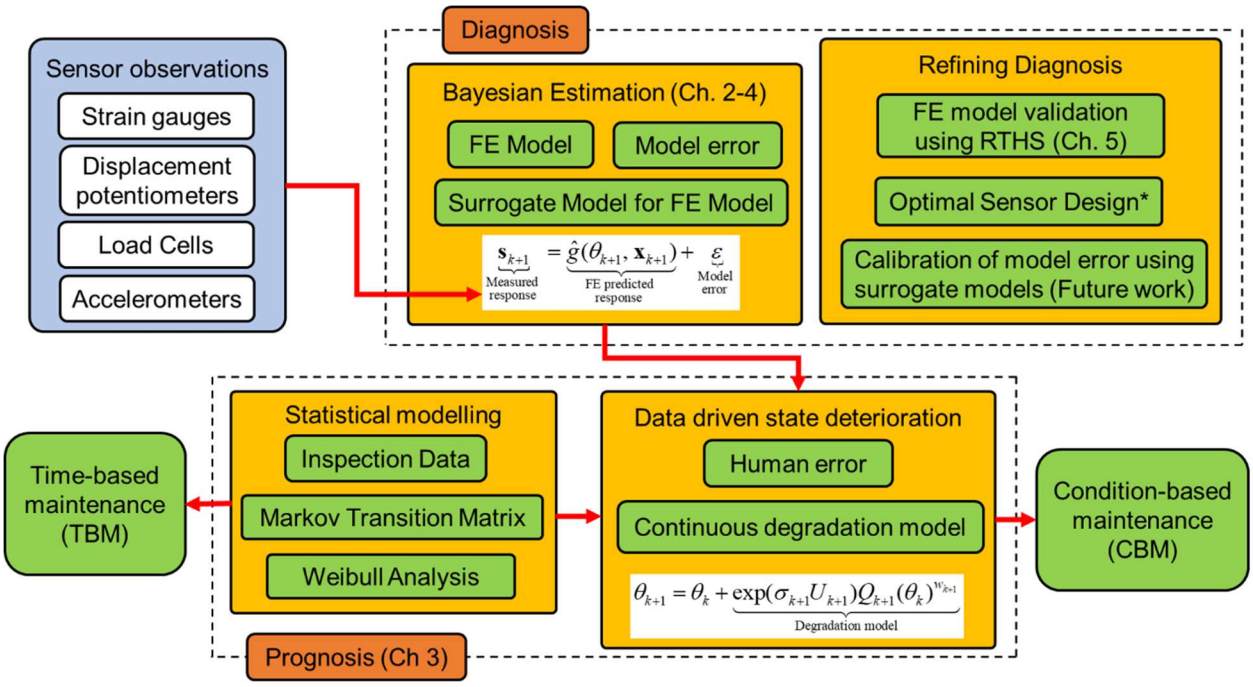

Figure 1.4: Proposed framework for diagnosis, prognosis, and maintenance decision making for civil infrastructure

The contributions presented on the different chapters of this dissertation can be summarized as:

1) Development of a CBM approach based on a surrogate modeling method assuming sufficient monitoring data is available.

2) Development of a new hybrid CBM approach that integrates high-fidelity FE model-based SHM with inspection data-based transition matrix for effective diagnosis, prognosis, and maintenance planning;
3) Quantification of effects of uncertainty in OCA ratings on maintenance planning;
4) Account for the effects of human errors in the OCA rating transition information in terms of diagnosis and prognosis;
5) Development of surrogate modeling method to overcome the computational challenge in FE model-based SHM; and
6) Diagnosis of different form of damage in miter gates is accomplished by performing Bayesian inference using a validated high-fidelity FE model.
7) Implementation of the hybrid simulation method on the UCSD large high performance outdoor shake table, which includes a test for verification and validation of a highly nonlinear mid-story isolation model.

Chapter 2

A VARIATIONAL BAYESIAN NEURAL NETWORK FOR STRUCTURAL HEALTH MONITORING AND COST-INFORMED DECISION-MAKING IN MITER GATES

2.1. Abstract

Many physics-based and surrogate models used in structural health monitoring (SHM) are affected by different sources of uncertainty such as model approximations and simplified assumptions. Optimal SHM and prognostics are only possible with uncertainty quantification that leads to an informed course of action. In this chapter, a Bayesian Neural Network (BNN) using variational inference is applied to learn a damage feature from a high-fidelity finite element model. BNNs can learn from small and noisy datasets and are more robust to overfitting than Artificial Neural Networks (ANNs), which make it very suitable for applications such as SHM. Also, uncertainty estimates obtained from a trained BNN model are used to build a cost-informed decision-making process. To demonstrate the applicability of BNNs, an example of this approach applied to miter gates is presented. In this example, a degradation model based on real inspection data is used to simulate the damage evolution.

2.2. Introduction

An ANN is a machine learning algorithm widely used in many areas in science and engineering. They are attractive alternatives to physics-based modeling, particularly for complex structures with unknown failure modes or highly variable operational and environmental inputs (Stoffel, Bamer, and Markert 2018). Most of the applications in civil engineering are in pattern

recognition problems. The first journal article on neural network application in civil/structural engineering was published by Adeli and Yeh (H. Adeli and Yeh 1989), which was an ANN algorithm trained to inform if a particular engineering design was acceptable or not. Hajela and Berke (Hajela and Berke 1991) applied ANN algorithms for structural optimization. Theocaris and Panagiotopoulos (Theocaris and Panagiotopoulos 1993) used ANN algorithms to learn the parameter identification problem in fracture mechanics. For SHM applications, Wu et al. (Wu, Ghaboussi, and Garrett 1992) and Feng and Bahng (Feng and Bahng 1999) trained an ANN algorithm to detect structural damage in the form of reduction in member stiffness on a multistory shear building and reinforced concrete bridge columns respectively. Other researchers used changes in modally-derived features such as mode shapes, eigenvectors and Ritz vectors, from numerical and experimental samples, to train an ANN to diagnose damage (Elkordy, Chang, and Lee 1994; Lam, Yuen, and Beck 2006).

Various other SHM algorithms for civil engineering infrastructure, such as bridges (Mikami, Tanaka, and Hiwatashi 1998; H. Xu and Humar 2006; Shu et al. 2013) and buildings (Masri et al. 1996; Kim, Yoon, and Kim 2000; N. Wang et al. 2018), have been implemented based on ANN architectures. Waszczyszyn and Ziemianski (Waszczyszyn and Ziemiański 2005) and Adeli (Hojjat Adeli 2001) reviewed several more application in civil engineering including the use of neural networks in analysis and design of structures, system identification, structural control, finite element (FE) mesh generation and other disciplines in civil engineering. Some researchers have used ANNs as surrogate models, using validated FE models to generate data to train the network (Rocchetta et al. 2018; Tan et al. 2017; Shu et al. 2013; H. Xu and Humar 2006). Many of these researchers have used ANNs as emulators of computationally expensive high-fidelity finite element model runs.

In general, ANN algorithms are trained using optimization techniques such as gradient descent (Ruder 2016). Therefore, ANN models are generally used to build point prediction models. Recently, Bayesian prediction models have started to be more attractive for damage assessment, especially in civil engineering because the limited amount of data available to build a reliable deterministic point prediction model. Many researchers use Gaussian Process (GP) regression to build Bayesian prediction models for civil engineering structures (Parno, O'Connor, and Smith 2018). However, GP models are computationally challenging for high-dimensional spaces or otherwise "large" data sets. Due to the scalability limitations in GP models (H. Liu et al. 2018; Shi, Khan, and Zhu 2019; Flam-shepherd, Requeima, and Duvenaud 2017), BNN (Yin and Zhu 2018; Chua and Goh 2005; Arangio and Bontempi 2015) models have started to be more practical model when dealing with high-dimensional space. In the case of SHM, this space depends on the number of spatially-distributed sensors and their collection (monitoring) frequency. BNNs are preferred over deterministic mathematical models such as neural networks because they account for uncertainty in their parameters (i.e., weights and biases) and propagate this into their predictions. Such uncertainty management is critical to support decision-making, which is the necessary outcome of an SHM process (Todd and Flynn 2011). BNNs are more robust against overfitting because a posterior distribution of the parameters is considered instead of using deterministic parameters that minimize the empirical risk during training. Also, BNN may be trained using limited and noisy data, while ANNs typically tend to require more and lower-noise training data for equivalent performance.

In this chapter, a BNN is trained with a FE model due to such highly-limited data availability. Therefore, this probabilistic prediction models also serve as a surrogate model of a validated high-fidelity FE model, which sometimes are unable to be used efficiently to make fast

predictions. Specifically, the BNN model is trained to assess the condition of quoin blocks in miter gates, which are essential civil structures for navigation system in rivers. In this work, a degradation model based on real inspection data of miter gates is used to simulate the damage evolution. Additionally, a cost function is introduced to improve prioritization of maintenance events of components of miter gates. The added value of using SHM in miter gates is evaluated in term of maintenance cost savings. The ultimate goal of the authors is to set up a SHM workflow that allows further optimization in term of cost savings, and this chapter presents one realization of this goal within a civil structural monitoring application.

2.3. Bayesian Neural Network

2.3.1 Artificial Neural Network

Two of the main problems in machine learning are classification (for discrete classes) and regression (for continuous processes). An ANN is a powerful supervised learning algorithm that can be used to solve classification and non-linear regression problems. In the context of an SHM problem, an ANN can be trained to learn the relationship between sensor values or features derived from sensor values and damage classes or parameters. Figure 2.1 shows the ANN architecture used in this chapter and the non-linear functions (i.e. sigmoid and softplus) that are used to learn the relationship between sensor information and structural damage targets.

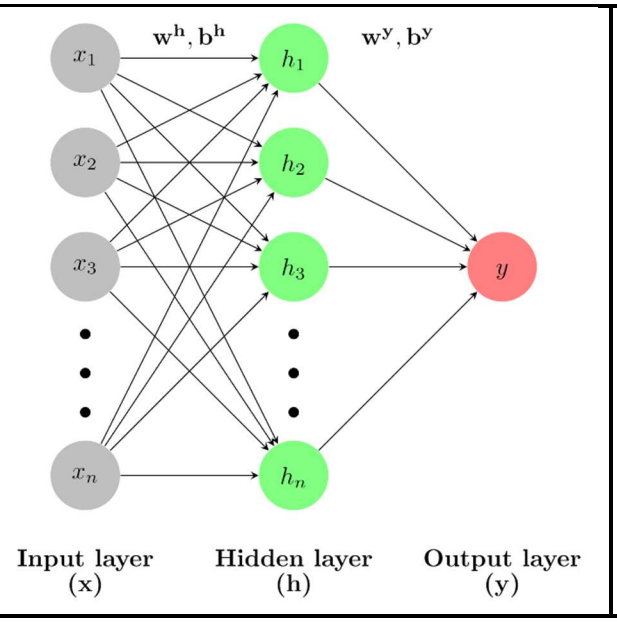

$\mathbf{h} = f(\mathbf{w}^h\mathbf{x} + \mathbf{b}^h)$, $\mathbf{y} = g(\mathbf{w}^y\mathbf{h} + \mathbf{b}^y)$,
$\mathbf{w}^h$, $\mathbf{w}^y$: weight matrix;
$\mathbf{b}^h$, $\mathbf{b}^y$: bias vector

where f and g are non-linear functions:

$f(z) = \dfrac{1}{1+e^{-z}}$, and

$g(z) = \log(1+e^{z})$.

Figure 2.1: ANN architecture and definitions

Generally, gradient descent algorithms are used to train neural networks. These algorithms objective is to find the ANN parameters (i.e. weights and biases) that minimize an error or loss function that depends on the ANN outputs (y) and the true (training) output values. The training error is known in the machine learning community as the empirical risk. Commonly, regularization is used to avoid overfitting, i.e., substantially degrading network performance when it is presented any data set other than the training set. Another way to train an ANN to be robust against overfitting is to use a Bayesian approach to find the parameters of the network. The uncertainty in these weights and biases can be propagated into network predictions, which is useful in the context SHM problems that involves (cost-informed) decisions.

2.3.2 Bayesian Neural Network

BNNs are essentially neural networks with a prior distribution on their network parameters (Neal 1996). The joint posterior distribution of the network parameters -including the covariance matrix, $\boldsymbol{\Sigma}$, of the assumed zero mean error- after observing a set of training data $\mathbf{D} = \{\mathbf{x}_i, \mathbf{y}_i\}_{i=1}^{N}$ may be expressed as:

$$p(\mathbf{w},\mathbf{b},\boldsymbol{\Sigma}\mid\mathbf{Y},\mathbf{X})=\frac{p(\mathbf{Y}\mid\mathbf{w},\mathbf{b},\boldsymbol{\Sigma},\mathbf{X})p(\mathbf{w},\mathbf{b},\boldsymbol{\Sigma}\mid\mathbf{X})}{p(\mathbf{Y}\mid\mathbf{X})}$$
$$=\frac{p(\mathbf{Y}\mid\mathbf{w},\mathbf{b},\boldsymbol{\Sigma},\mathbf{X})p(\mathbf{w},\mathbf{b},\boldsymbol{\Sigma})}{\iiint_{\mathbf{w},\mathbf{b},\boldsymbol{\Sigma}} p(\mathbf{Y}\mid\mathbf{w},\mathbf{b},\boldsymbol{\Sigma},\mathbf{X})p(\mathbf{w},\mathbf{b},\boldsymbol{\Sigma})\,d\mathbf{w}d\mathbf{b}d\boldsymbol{\Sigma}}, \tag{2.1}$$

where $\mathbf{w}$ and $\mathbf{b}$ represents the weights and biases of the BNN, respectively. Also, $\mathbf{X}$ and $\mathbf{Y}$ are defined as $\mathbf{X}=\left[\mathbf{x}_1^T,\mathbf{x}_2^T,...,\mathbf{x}_N^T\right]^T\in\mathbb{R}^{(N\times\dim(\mathbf{x}))\times 1}$ and $\mathbf{Y}=\left[\mathbf{y}_1^T,\mathbf{y}_2^T,...,\mathbf{y}_N^T\right]^T\in\mathbb{R}^{(N\times\dim(\mathbf{y}))\times 1}$ respectively.

The conditional distribution, $p(\mathbf{w},\mathbf{b},\boldsymbol{\Sigma}\mid\mathbf{X})$ is equivalent to $p(\mathbf{w},\mathbf{b},\boldsymbol{\Sigma})$ due to conditional independence. The marginal probability density function, $p(\mathbf{Y}\mid\mathbf{X})$, can be obtained by integrating $\iiint_{\mathbf{w},\mathbf{b},\boldsymbol{\Sigma}} p(\mathbf{Y}\mid\mathbf{w},\mathbf{b},\boldsymbol{\Sigma},\mathbf{X})p(\mathbf{w},\mathbf{b},\boldsymbol{\Sigma})\,d\mathbf{w}d\mathbf{b}d\boldsymbol{\Sigma}$, which it is generally mathematically intractable. Furthermore, the likelihood function $p(\mathbf{Y}\mid\mathbf{w},\mathbf{b},\boldsymbol{\Sigma},\mathbf{X})$ can be expressed as:

$$p(\mathbf{Y}\mid\mathbf{w},\mathbf{b},\boldsymbol{\Sigma},\mathbf{X})=\prod_{i=1}^{N}p(\mathbf{y}_i\mid\mathbf{w},\mathbf{b},\boldsymbol{\Sigma}_i,\mathbf{x}_i). \tag{2.2}$$

In this chapter, the following measurement model/equation is assumed:

$$\mathbf{y}_i=NN(\mathbf{x}_i;\mathbf{w};\mathbf{b})+\boldsymbol{\varepsilon}_i,\ \text{where}\ \boldsymbol{\varepsilon}_i\sim\mathcal{N}\left(\mathbf{0},\underbrace{\begin{bmatrix}\sigma_{11}^2 & \sigma_{12}^2 & \cdots & \sigma_{1k}^2\\ \sigma_{21}^2 & \sigma_{22}^2 & \cdots & \sigma_{2k}^2\\ \vdots & \vdots & \ddots & \vdots\\ \sigma_{k1}^2 & \sigma_{k2}^2 & \cdots & \sigma_{kk}^2\end{bmatrix}}_{\boldsymbol{\Sigma}_i}\right),\ k=\dim(\mathbf{y}_i) \tag{2.3}$$

which is equivalent to write the following:

$$p(\mathbf{y}_i\mid\mathbf{w},\mathbf{b},\boldsymbol{\Sigma}_i,\mathbf{x}_i)\sim\mathcal{N}(NN(\mathbf{x}_i;\mathbf{w};\mathbf{b}),\boldsymbol{\Sigma}_i)$$
$$=\frac{1}{(2\pi)^{k/2}}\left|\boldsymbol{\Sigma}_i\right|^{-1/2}\exp\left\{-\frac{1}{2}\left[\mathbf{y}_i-NN(\mathbf{x}_i;\mathbf{w};\mathbf{b})\right]\boldsymbol{\Sigma}_i^{-1}\left[\mathbf{y}_i-NN(\mathbf{x}_i;\mathbf{w};\mathbf{b})\right]^T\right\}, \tag{2.4}$$

where $\boldsymbol{\Sigma}_i$ is the covariance of the measurement error between observation $\mathbf{y}_i$ and model prediction $NN(\mathbf{x}_i;\mathbf{w};\mathbf{b})$ with weights $\mathbf{w}$, biases $\mathbf{b}$, and input $\mathbf{x}_i$. Also $\mathcal{N}(\ )$ represent a normal distribution parametrized by its mean and variance, and $k = \dim(\mathbf{y}_i)$.

For the prior $p(\mathbf{w},\mathbf{b},\boldsymbol{\sigma})$, it is assumed that $\mathbf{w}$, $\mathbf{b}$ and $\boldsymbol{\Sigma}$ are statistically independent. The joint prior can be expressed as follows:

$$p(\mathbf{w},\mathbf{b},\boldsymbol{\Sigma}) = p(\mathbf{w}) \times p(\mathbf{b}) \times \prod_{i=1}^{N} p(\boldsymbol{\Sigma}_i), \tag{2.5}$$

where $p(\mathbf{w}) \sim \mathcal{N}(\mathbf{0},\mathbf{I})$, $p(\mathbf{b}) \sim \mathcal{N}(\mathbf{0},\mathbf{I})$, and $p(\boldsymbol{\Sigma}_i) \sim \text{Lognormal}(2\mathbf{I},\mathbf{I})$ are the priors used in this chapter.

The posterior predictive distribution of $\mathbf{Y}_{\text{test}}$ for a set of observed points $\mathbf{X}_{\text{test}}$ is then

$$p(\mathbf{Y}_{\text{test}} \mid \mathbf{X}_{\text{test}}, \mathbf{Y}_{\text{train}}, \mathbf{X}_{\text{train}}) = \iiint_{\mathbf{w},\mathbf{b},\boldsymbol{\Sigma}} p(\mathbf{Y}_{\text{test}} \mid \mathbf{w},\mathbf{b},\boldsymbol{\Sigma},\mathbf{X}_{\text{test}}) p(\mathbf{w},\mathbf{b},\boldsymbol{\Sigma} \mid \mathbf{Y}_{\text{train}},\mathbf{X}_{\text{train}}) d\mathbf{w} d\mathbf{b} d\boldsymbol{\Sigma}, \tag{2.6}$$

where the joint posterior distribution, $p(\mathbf{w},\mathbf{b},\boldsymbol{\Sigma} \mid \mathbf{Y}_{\text{train}},\mathbf{X}_{\text{train}})$, is estimated after observing a set of training data $(\mathbf{X}_{\text{train}},\mathbf{Y}_{\text{train}})$. The covariance matrix ($\boldsymbol{\Sigma}$) of the assumed zero mean error is also treated as an unknown parameter during training, and its uncertainty is also accounted in the BNN predictions.

2.3.3 Variational Inference

In order to obtain a trained BNN for predictions, the key part is to calculate the posterior distribution of the parameters after observing the (training) data. The posterior distribution of the parameters is typically mathematically intractable due to the normalization term (see Eq. (2.1)), which is a high-dimensional integral. The two most popular approximation methods to obtain the posterior distribution are Markov chain Monte Carlo (MCMC) and variational inference (VI). For BNNs, there many parameters to be inferred making this a high-dimensional problem. MCMC is

proven to approximate very well to the true posterior. MCMC algorithms involve sampling-based methods, and it is very challenging to sample a high-dimensional posterior (Morzfeld, Tong, and Marzouk 2017). The Gibbs sampler is one MCMC algorithm that can work on high-dimensional space; however, it still can be computationally expensive (Geman and Geman 1984). Therefore, VI is a more practical approach in this case, which is becoming popular in BNN designs (Sun et al. 2019). In this chapter, VI is employed to infer the high-dimensional space of the parameters of the BNN that serves as a mathematical model of a nonlinear mapping between inputs and targets.

2.3.3.1 Variational Inference for a Bayesian Neural Network

The idea of VI is to postulate a family of distributions, Q, and to find the closest member, $q^*(\mathbf{w},\mathbf{b},\boldsymbol{\Sigma})$, from the family of distributions that approximates to the posterior distribution, $p(\mathbf{w},\mathbf{b},\boldsymbol{\Sigma}\,|\,\mathbf{Y},\mathbf{X})$, using Kullback–Leibler (KL) divergence to maximize the evidence lower bound (ELBO). For simplification purposes the parameter, $\boldsymbol{\theta}$, would represent the parameters $\mathbf{w}$, $\mathbf{b}$, and $\boldsymbol{\Sigma}$ as follow:

$$q^*(\boldsymbol{\theta}) = \arg\min_{q(\boldsymbol{\theta})\in Q} \mathrm{KL}(q(\boldsymbol{\theta}) \,||\, p(\boldsymbol{\theta}\,|\,\mathbf{Y},\mathbf{X})), \tag{2.7}$$

where the KL divergence between the variational distribution $q(\boldsymbol{\theta})$ and posterior distribution $p(\boldsymbol{\theta}\,|\,\mathbf{Y},\mathbf{X})$ can be defined as:

$$\begin{aligned}
&\mathrm{KL}(q(\boldsymbol{\theta}) \,||\, p(\boldsymbol{\theta}\,|\,\mathbf{Y},\mathbf{X})) \\
&\quad = \int_{-\infty}^{\infty} q(\boldsymbol{\theta}) \log \frac{q(\boldsymbol{\theta})}{p(\boldsymbol{\theta}\,|\,\mathbf{Y},\mathbf{X})} = \mathrm{E}_{q(\boldsymbol{\theta})}[\log \frac{q(\boldsymbol{\theta})}{p(\boldsymbol{\theta}\,|\,\mathbf{Y},\mathbf{X})}] \\
&\quad = \mathrm{E}_{q(\boldsymbol{\theta})}[\log q(\boldsymbol{\theta})] - \mathrm{E}_{q(\boldsymbol{\theta})}[\log p(\boldsymbol{\theta}\,|\,\mathbf{Y},\mathbf{X})] \\
&\quad = \mathrm{E}_{q(\boldsymbol{\theta})}[\log q(\boldsymbol{\theta})] - \mathrm{E}_{q(\boldsymbol{\theta})}[\log \frac{p(\mathbf{Y}\,|\,\boldsymbol{\theta},\mathbf{X})\,p(\boldsymbol{\theta})}{p(\mathbf{Y}\,|\,\mathbf{X})}] \\
&\quad = \mathrm{E}_{q(\boldsymbol{\theta})}[\log q(\boldsymbol{\theta})] - \mathrm{E}_{q(\boldsymbol{\theta})}[\log(p(\mathbf{Y}\,|\,\boldsymbol{\theta},\mathbf{X})\,p(\boldsymbol{\theta}))] + \mathrm{E}_{q(\boldsymbol{\theta})}[\log p(\mathbf{Y}\,|\,\mathbf{X})].
\end{aligned} \tag{2.8}$$

The $\mathrm{E}_{q(\boldsymbol{\theta})}[\log p(\mathbf{Y} \mid \mathbf{X})]$ term is constant because the normalization term, $p(\mathbf{Y} \mid \mathbf{X})$, is a constant. Next, the ELBO is defined as

$$\mathrm{ELBO}(q(\boldsymbol{\theta})) = \mathrm{E}_{q(\boldsymbol{\theta})}[\log(p(\mathbf{Y} \mid \boldsymbol{\theta}, \mathbf{X})p(\boldsymbol{\theta}))] - \mathrm{E}_{q(\boldsymbol{\theta})}[\log q(\boldsymbol{\theta})]. \tag{2.9}$$

Substituting Eq. (2.9) into Eq. (2.7) yields

$$\mathrm{KL}(q(\boldsymbol{\theta}) \,||\, p(\boldsymbol{\theta} \mid \mathbf{Y}, \mathbf{X})) = -\mathrm{ELBO}(q(\boldsymbol{\theta})) + \mathrm{E}[\log p(\mathbf{Y} \mid \mathbf{X})]. \tag{2.10}$$

Now, the closest member, $q^*(\boldsymbol{\theta})$, from the family of distributions that approximates to the posterior distribution can be found by maximizing the ELBO:

$$q^*(\boldsymbol{\theta}) = \arg\min_{q(\boldsymbol{\theta}) \in Q} \mathrm{KL}(q(\boldsymbol{\theta}) \,||\, p(\boldsymbol{\theta} \mid \mathbf{Y}, \mathbf{X})) = \arg\max_{q(\boldsymbol{\theta}) \in Q} \mathrm{ELBO}(q(\boldsymbol{\theta})). \tag{2.11}$$

So now, the inference of the posterior distribution can be seen as an optimization problem. For comparison purposes with loss functions used for training an ANN model, the following loss function, L, is defined:

$$\begin{aligned} L(q(\boldsymbol{\theta})) &= -\mathrm{ELBO}(q(\boldsymbol{\theta})) = -\mathrm{E}_{q(\boldsymbol{\theta})}[\log(p(\mathbf{Y} \mid \boldsymbol{\theta}, \mathbf{X})p(\boldsymbol{\theta}))] + \mathrm{E}_{q(\boldsymbol{\theta})}[\log q(\boldsymbol{\theta})] \\ &= -\mathrm{E}_{q(\boldsymbol{\theta})}[\log p(\mathbf{Y} \mid \boldsymbol{\theta}, \mathbf{X})] - \mathrm{E}_{q(\boldsymbol{\theta})}[\log p(\boldsymbol{\theta})] + \mathrm{E}_{q(\boldsymbol{\theta})}[\log q(\boldsymbol{\theta})] \\ &= -\mathrm{E}_{q(\boldsymbol{\theta})}[\log p(\mathbf{Y} \mid \boldsymbol{\theta}, \mathbf{X})] + \mathrm{E}_{q(\boldsymbol{\theta})}[\log \frac{q(\boldsymbol{\theta})}{p(\boldsymbol{\theta})}] \\ &= -\mathrm{E}_{q(\boldsymbol{\theta})}[\log p(\mathbf{Y} \mid \boldsymbol{\theta}, \mathbf{X})] + \mathrm{KL}(q(\boldsymbol{\theta}) \,||\, p(\boldsymbol{\theta})). \end{aligned} \tag{2.12}$$

Substituting Eq. (2.2) into Eq. (2.12), the following is equation is obtained:

$$\begin{aligned} &L(q(\mathbf{w}, \mathbf{b}, \boldsymbol{\Sigma})) \\ &= -\mathrm{E}_{q(\mathbf{w},\mathbf{b},\boldsymbol{\Sigma})}[\log\left(\textstyle\prod_{i=1}^{N} p(\mathbf{y}_i \mid \mathbf{w}, \mathbf{b}, \boldsymbol{\Sigma}_i, \mathbf{x}_i)\right)] + \mathrm{KL}(q(\mathbf{w}, \mathbf{b}, \boldsymbol{\Sigma}) \,||\, p(\mathbf{w}, \mathbf{b}, \boldsymbol{\Sigma})) \\ &= -\sum_{i=1}^{N} \mathrm{E}_{q(\mathbf{w},\mathbf{b},\boldsymbol{\Sigma})}[\log p(\mathbf{y}_i \mid \mathbf{w}, \mathbf{b}, \boldsymbol{\Sigma}_i, \mathbf{x}_i)] + \mathrm{KL}(q(\mathbf{w}, \mathbf{b}, \boldsymbol{\Sigma}) \,||\, p(\mathbf{w}, \mathbf{b}, \boldsymbol{\Sigma})). \end{aligned} \tag{2.13}$$

Now, the simplified equation is obtained after substituting Eq. (2.4) into Eq. (2.13):

$$
\begin{aligned}
L(q(\mathbf{w},\mathbf{b},\boldsymbol{\Sigma})) &= -\sum_{i=1}^{N} \mathrm{E}_{q(\mathbf{w},\mathbf{b},\boldsymbol{\Sigma})}[\log p(\mathbf{y}_i \mid \mathbf{w},\mathbf{b},\boldsymbol{\Sigma}_i,\mathbf{x}_i)] + \mathrm{KL}(q(\mathbf{w},\mathbf{b},\boldsymbol{\Sigma}) \,||\, p(\mathbf{w},\mathbf{b},\boldsymbol{\Sigma})) \\
&= -\sum_{i=1}^{N} \mathrm{E}_{q(\mathbf{w},\mathbf{b},\boldsymbol{\Sigma})}[\log(\frac{1}{(2\pi)^{k/2}}|\boldsymbol{\Sigma}_i|^{-1/2}) \\
&\quad + \left\{-\frac{1}{2}\left[\mathbf{y}_i - NN(\mathbf{x}_i;\mathbf{w};\mathbf{b})\right]\boldsymbol{\Sigma}_i^{-1}\left[\mathbf{y}_i - NN(\mathbf{x}_i;\mathbf{w};\mathbf{b})\right]^T\right\})] \\
&\quad + \mathrm{KL}(q(\mathbf{w},\mathbf{b},\boldsymbol{\Sigma}) \,||\, p(\mathbf{w},\mathbf{b},\boldsymbol{\Sigma}))
\end{aligned}
\tag{2.14}
$$

If the following covariance matrix is assumed:

$$
\boldsymbol{\Sigma}_i = \begin{bmatrix} \sigma^2 & \cdots & 0 \\ \vdots & \ddots & \vdots \\ 0 & \cdots & \sigma^2 \end{bmatrix} = \sigma^2\mathbf{I} = \lambda^{-1}\mathbf{I}, \tag{2.15}
$$

assuming also that $\boldsymbol{\Sigma}_i$'s are statistically independent between observation $\mathbf{y}_i$. Then the loss function can be expressed as:

$$
\begin{aligned}
L(q(\mathbf{w},\mathbf{b},\lambda)) &= -\sum_{i=1}^{N} \mathrm{E}_{q(\mathbf{w},\mathbf{b},\lambda)}[\frac{k}{2}(2\pi) + \frac{k}{2}\log\lambda^{-1} + \left\{-\frac{\lambda}{2}\left\|\mathbf{y}_i - NN(\mathbf{x}_i;\mathbf{w};\mathbf{b})\right\|^2\right\})] \\
&\quad + \mathrm{KL}(q(\mathbf{w},\mathbf{b},\lambda) \,||\, p(\mathbf{w},\mathbf{b},\lambda)).
\end{aligned}
\tag{2.16}
$$

The first term in Eq. (2.16) is known as the *average likelihood*, which can be minimized when the model prediction $NN(\mathbf{x}_i;\mathbf{w};\mathbf{b})$ explains the observed data $\mathbf{y}_i$. This term is also minimized when the variational distribution $q(\mathbf{w},\mathbf{b},\lambda)$ is optimally selected. The second term is the KL divergence between the variational distribution $q(\mathbf{w},\mathbf{b},\lambda)$ and the prior $p(\mathbf{w},\mathbf{b},\lambda)$, which minimizes the loss when the variational distribution is close to the prior. Therefore, this loss function balances the variational distribution $q(\mathbf{w},\mathbf{b},\lambda)$ with the likelihood $\prod_{i=1}^{N} p(\mathbf{y}_i \mid \mathbf{w},\mathbf{b},\lambda,\mathbf{x}_i)$ and the prior $p(\mathbf{w},\mathbf{b},\lambda)$. For further details on how to compute these terms given different types of variational distributions and how to derive their respective gradients of the loss function can be found here (Blei, Kucukelbir, and McAuliffe 2017; Ostwald 2019). There are several gradient

based methods to calculate the optimal $q(\mathbf{w},\mathbf{b},\lambda)$ that minimize this loss function (or maximize the ELBO). A stochastic gradient descent strategy has been used for this application using the Edward (Tran et al. 2017) probabilistic framework, which is based on Tensorflow (Abadi et al. 2016), a widely used programming language for deep learning neural networks. This gradient descent method consists in calculating a noisy gradient from Monte Carlo samples of the ELBO distribution.

2.4. Damage Detection using BNN Surrogate Model

In structural health monitoring (SHM), damage classification (or regression) is generally an inverse problem, e.g., damage (input) causes change in an observable (output). Therefore, a Bayesian approach using a finite element model (or a surrogate model) is generally used to infer the inverse problem. In this chapter, a BNN surrogate model is used to directly learn the inverse problem, where the output data (e.g., strain measurements) and input data (i.e. the damage, to be defined below) of a validated FE model become the input data and output data, respectively, for the BNN surrogate model. Figure 2.2 illustrates the data used to validate the FE model, the data generated to train the BNN model, and introduces the need of a degradation model (i.e. damage evolution) to allow cost-informed decisions, which is explain in section 2.5.

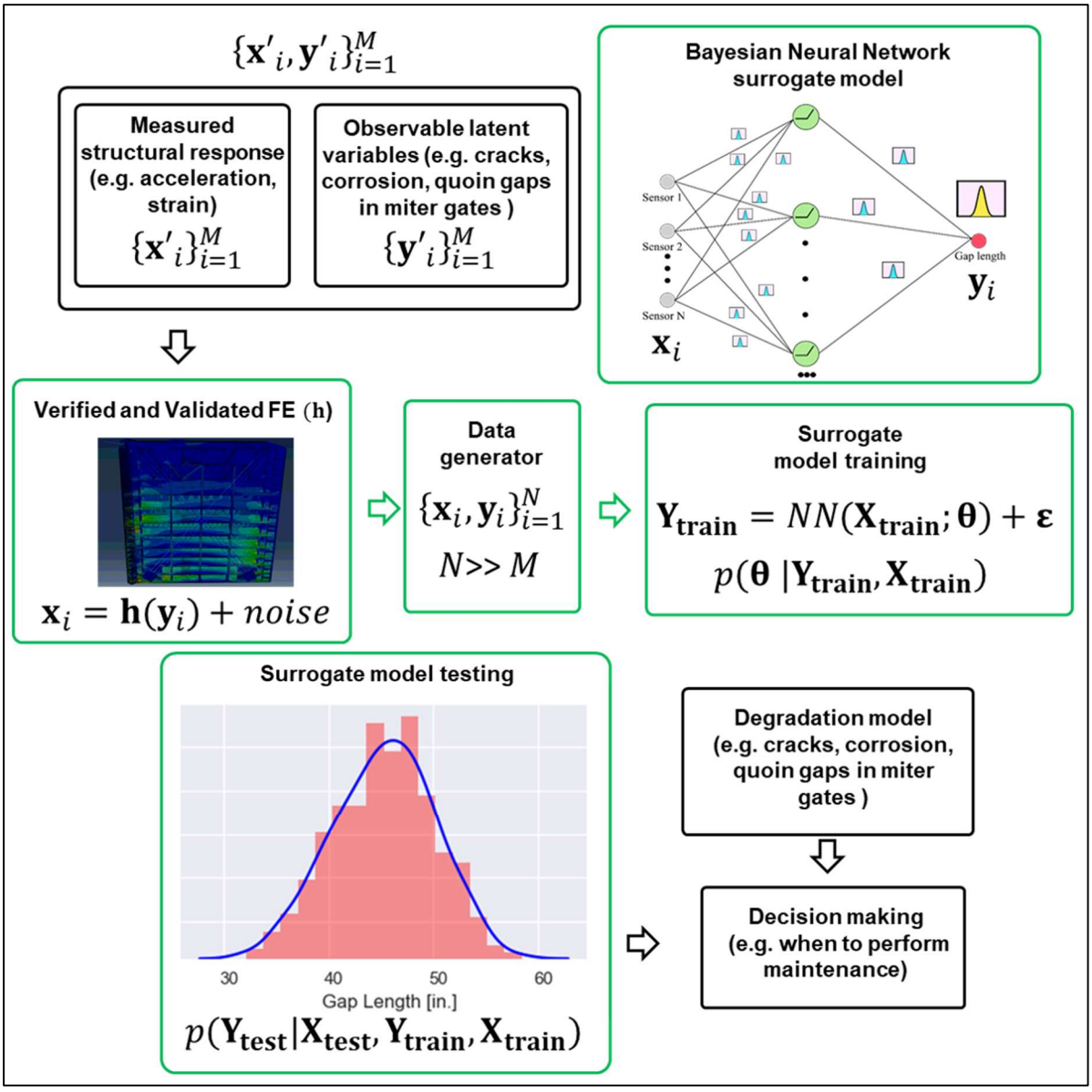

Figure 2.2: Decision flow based on BNN model for damage detection

2.4.1 High Fidelity Finite Element Model of Miter Gates

It is imperative in the cargo ship navigation to avoid unexpected closures, which can cause considerable economical loss to the marine cargo and associated industries. In the United States, the U.S. Army Corps of Engineers (USACE) owns and operates 236 locks at 191 sites (U.S. Army Corps of Engineers Headquarters 2018). According to a report published by USACE in 2017, more than half of these assets are older than their economic design life of 50 years and need a prudent

structural health monitoring solution to ensure their safe and reliable operation (Foltz 2017). SHM of miter gates of navigation locks, as shown in Figure 2.3, are a good case study on which to demonstrate feasibility of using BNNs as a damage detection solution for a real-world problem.

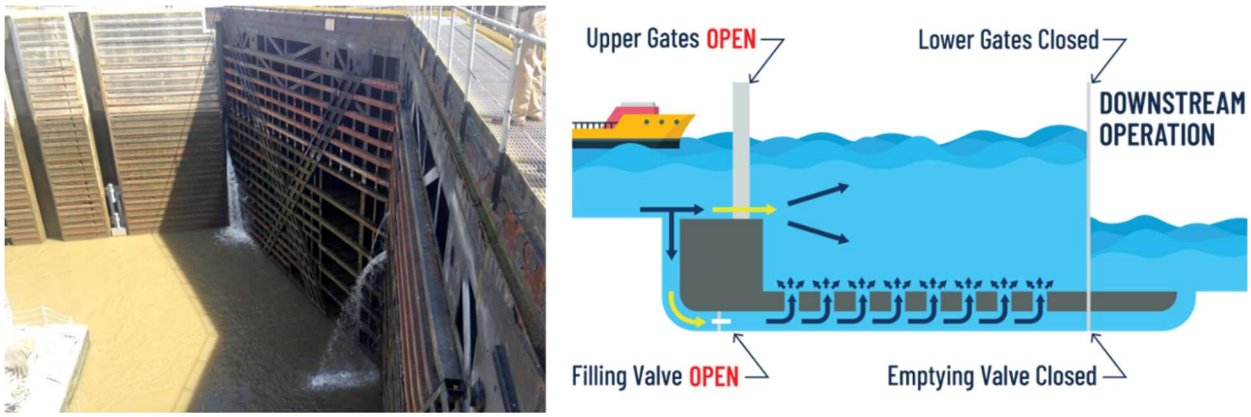

Figure 2.3: Navigation in Miter Gates

Some lock operators and experienced engineers from USACE (Foltz 2017) have stated that the condition of the quoin and gaps between the lock wall and the quoin block is one of the primary concerns within the inspection, maintenance, and repair cycle. A "gap" is somewhat generically referred to as the loss of bearing contact between the quoin attached to the gate and the lock wall. Such a gap in the quoin block changes the load path in the miter gate, leading often to higher stresses at some places in the lock gate (e.g., the pintle), which in turn can lead to operational and/or structural failure. Some miter gates owned by USACE are currently instrumented with strain gauges for in-situ data acquisition (U.S. Army Corps of Engineers Headquarters 2007). The fundamental inference is made that changes in the gap contact state will lead to observable changes in the measured gate strain field.

FE models could be used to map the strain gauges data to a specific gap condition (usually quantified by size) in an inverse analysis. However, these models are computationally expensive to run, and sometimes they are not feasible for real-time health monitoring or for monitoring fluctuating environmental effects. Consequently, a surrogate model with fast predictions of the

target damage (e.g., the gap) can be employed. Figure 2.4 shows the ABAQUS FE model for the Greenup miter gate located in the Ohio River in Kentucky, USA. The FE model has been previously validated (Eick et al. 2018) with the available strain gage readings from the Greenup miter gate. The Greenup gate is a brand-new gate where a negligible gap was assumed for validation purposes. All the element in the gate are 3D linear shells elements to reduce the computational cost of such a large model.

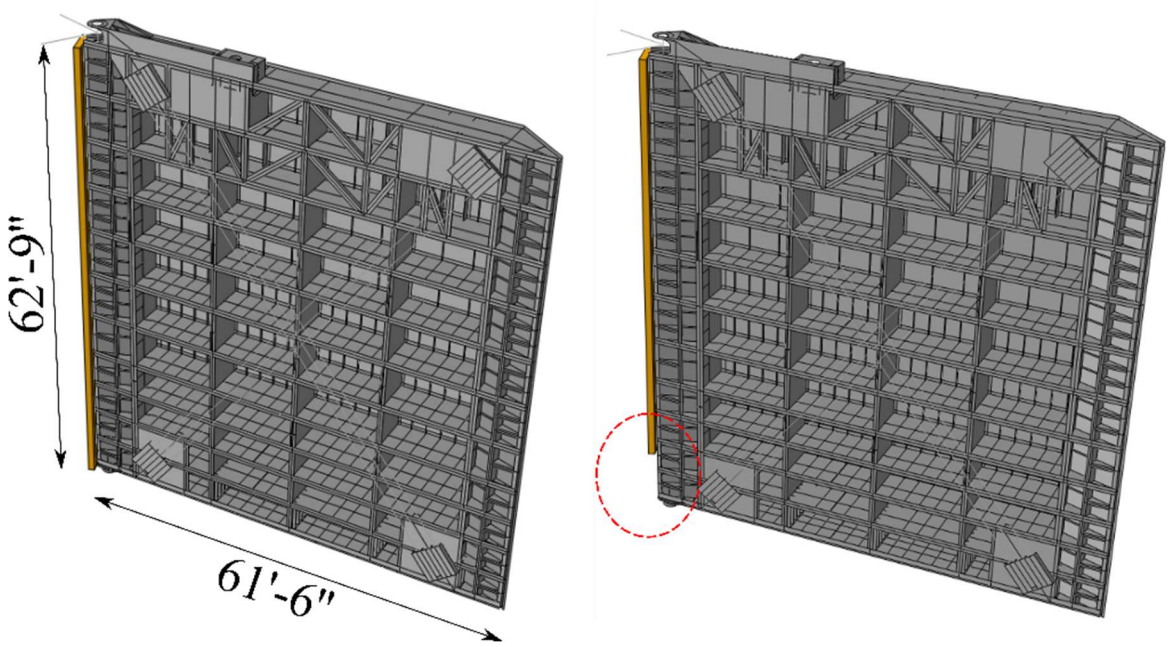

Figure 2.4: Gap modeling (Left: No gap, Right: Schematic gap)

A contact-type constraint is used between the lock wall (denoted in yellow) and the gate (denoted in gray), making this a nonlinear problem. To impose the contact constraint the Lagrange multiplier method was employed. The strain gauge locations are far from the contact area, mostly due to physical constraints in the miter gate, but this far-field location also mitigates errors due to the method employed to enforce the contact constraint. The opposite side of the lock wall uses fixed boundary conditions, and symmetry boundary conditions are used at the right end (i.e., miter) of the gate to simulate the right leaf.

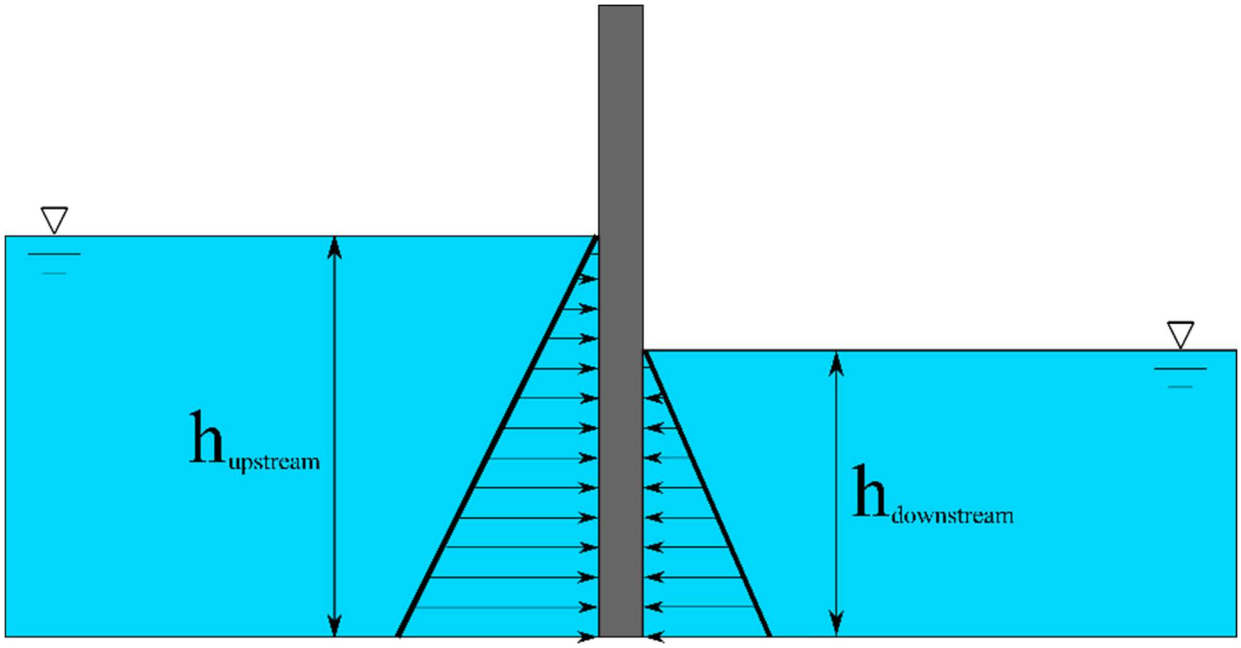

Figure 2.5: Hydrostatic loading on miter gates

Figure 2.5 shows the upstream and downstream hydrostatic loading that the miter gate experiences. Also, the environmental temperature, which will add thermal strain effects, is defined as the values recorded by thermometers located at the actual Greenup gate.

2.4.2 BNN Architecture and Results

The architecture used in this chapter contains 2 layers with 50 neurons in its hidden layer and biases at each hidden neuron. A parametric studied using a 2-layer network was carried using an ANN model with different numbers of neurons in its hidden layer. It was found that using 50 neurons yielded a higher testing accuracy than the other architectures used. Ten different (10, 20, …., 90 and 100 neurons) architectures were considered to arrive to this architecture, which each architecture took from 2 to 5 minutes for training and testing using a single CPU processor. Regularization was considered to penalize architectures with more parameters (i.e. neurons). A 2-layer architecture (i.e., 1 hidden layer) was selected because it can learn any continuous mathematical function (Csáji 2001). Further studies could be carried using a deeper neural network architecture, but the simplest universal approximator was considered most desirable.

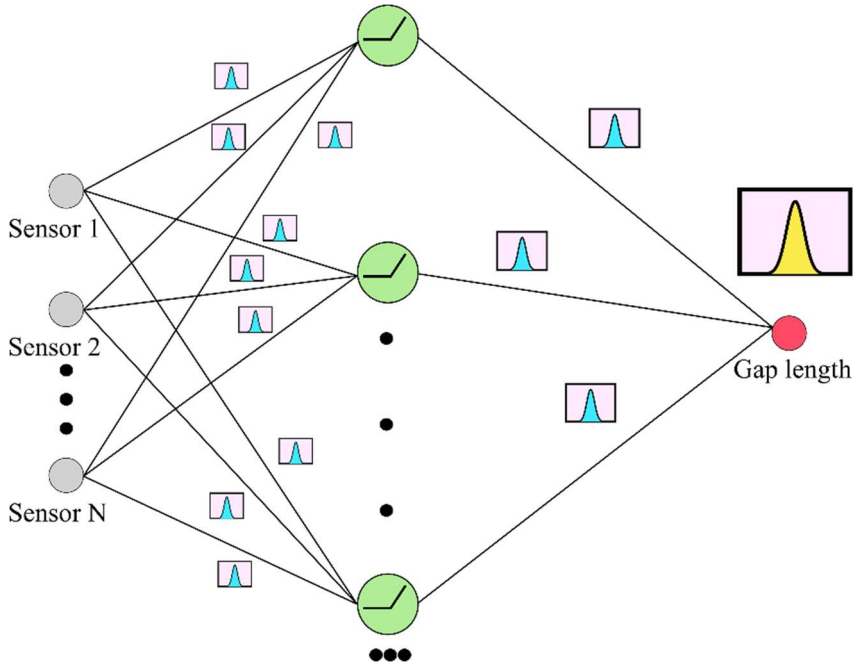

Figure 2.6: BNN model to map strain field to gap length

The hidden layers use activation functions (e.g. sigmoid) to make the BNN learn any nonlinearity between the strain values and the gap length. For the output layer, the softplus activation function was employed to impose physical constraints (e.g., the gap length cannot be negative) in the BNN. As expressed mathematically earlier, a BNN is a neural network with a prior in its weight and biases as shown in Figure 2.6.

2.4.2.1 Training Data and Testing Results

The gap length is assumed to be a random number between zero and 180 in. (Eick et al. 2018) under random loading scenarios defined by two normal distributions for upstream (h_{up}) and downstream (h_{down}) hydrostatic pressure as shown in Table 2.1. For training and testing data, 3000 data points were obtained using the ABAQUS FE model of the Greenup gate by varying the value of each random variable for training (2000 for training) and testing purposes. This data took one week using a 4-cpu desktop to be generated. Thermal effects are also considering. The temperature (T_{surf} & T_{uw}) are defined as a normal distributions with mean at a temperature, T,

which is defined as a random number based on the lowest (T_{min}) and highest temperature (T_{max}) value recorded by thermometers (underwater and surface) in an actual miter gate at different times of the year. Figure 2.7 shows how these distributions are propagated to 46 strain values, whose location are based on what is installed in the Greenup gate.

Table 2.1: Random variables used to generate training/testing data

Parameter	Distribution	Unit
Gap length	$Gap \sim Uniform\ (0,\ 180)$	Inches
h_{down}	$h_{down} \sim Normal(\mu = 168,\ \sigma = 20)$	Inches
h_{up}	$h_{up} \sim Normal(\mu = 552,\ \sigma = 10)$	Inches
T	$T \sim Uniform\ (T_{min} = 29.4, T_{max} = 47.4)$	Celsius
T_{surf}	$T_{surf} \sim Normal\ (T,\ \sigma_{surf} = 10.3)$	Celsius
T_{uw}	$T_{uw} \sim Normal(T, \sigma_{uw} = 5.37)$	Celsius

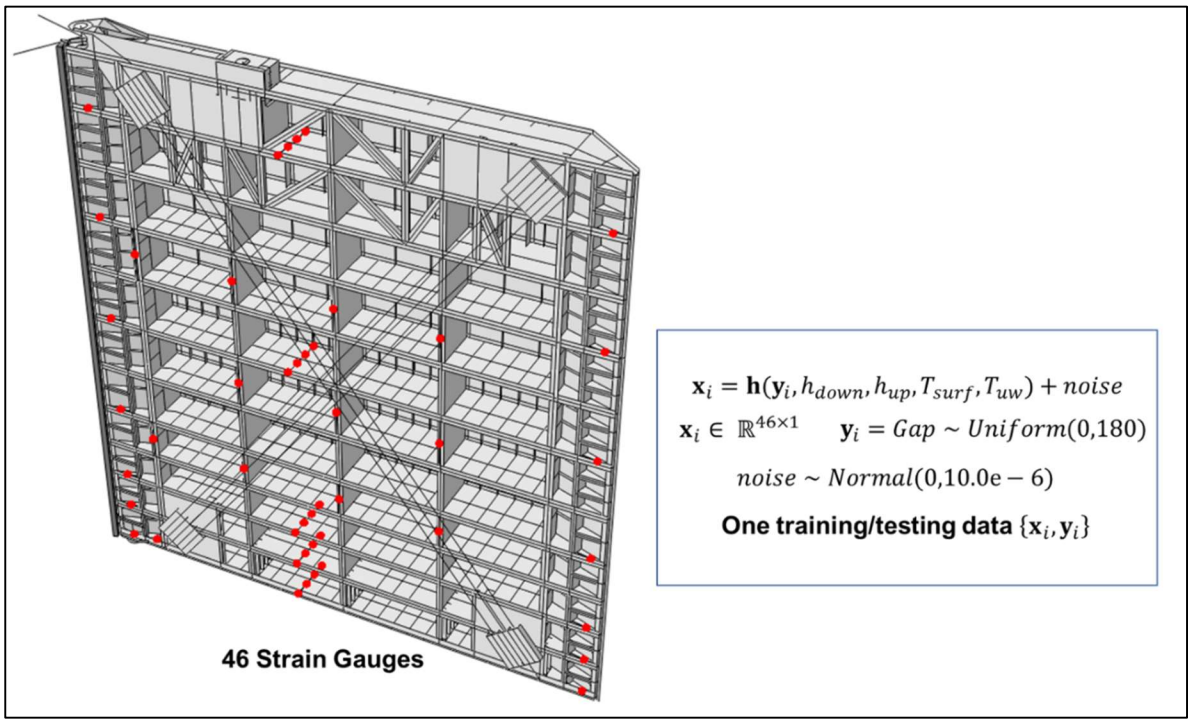

Figure 2.7: Training and testing data generation

The posterior predictive distribution is calculated using Eq. (2.6), and 2000 samples from this distribution at each testing data point are shown in Figure 2.8. It takes around 20 minutes to train this BNN model.

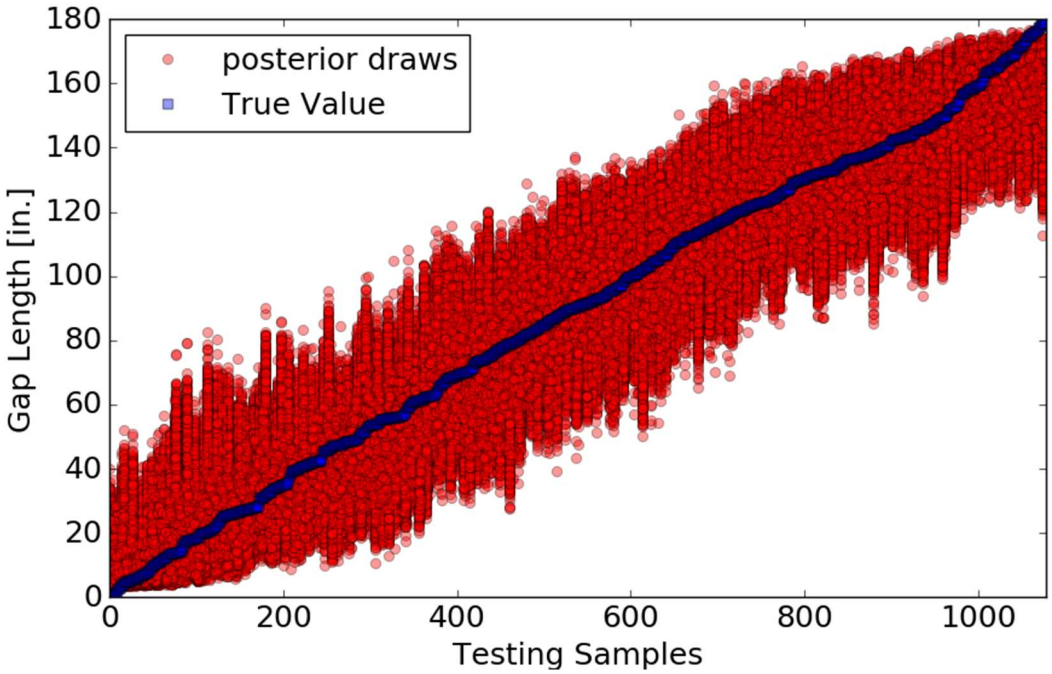

Figure 2.8: Posterior Distribution of gap length using 1000+ testing samples

The median value of the posterior distribution, as shown in Figure 2.9, may be used to calculate the mean square error (MSE) to compare the predicted gap length with the true gap length testing value as shown in Table 2.2, in order to evaluate a set of point predictions.

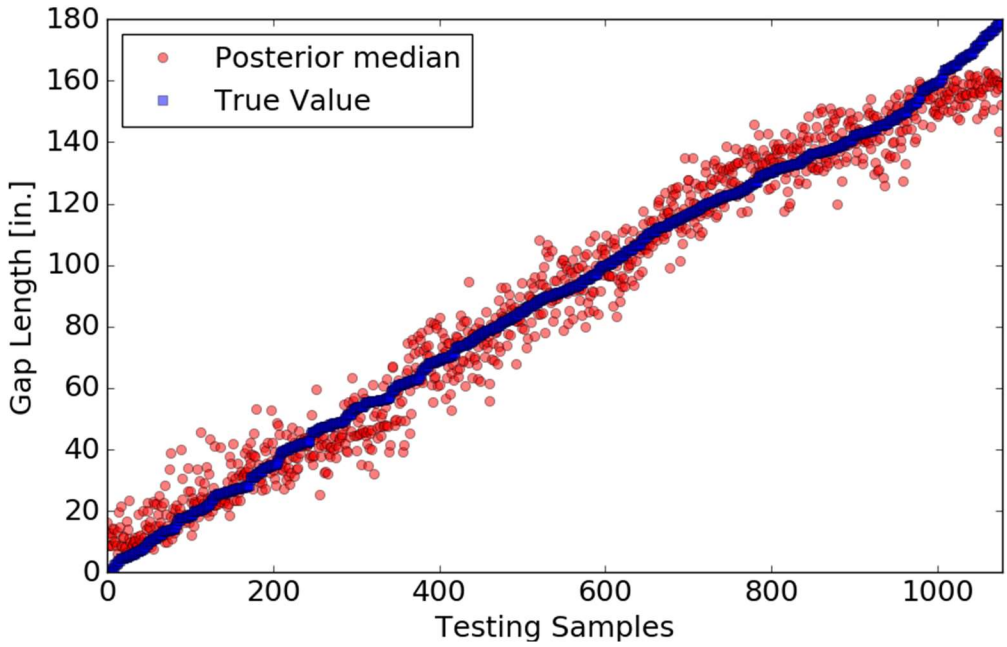

Figure 2.9: Median values of prediction of gap length

The median is a more useful metric to summarize central tendencies in cases where the distributions may potentially be highly skewed or asymmetric. Moreover, the median is more robust than the mean to outliers that can bias the central tendency.

Table 2.2: Testing accuracy

BNN Accuracy	RMSE (in.)
Median	8.34
Mean	8.39

One other advantage of using a BNN over an ANN is that the gap length using a given set of strain measurements, $\mathbf{x}_i$, may be expressed as a distribution rather than a single point estimate. Therefore, the probability of exceeding certain critical gap length may be calculated to facilitate the decision-making process for preventive maintenance actions. Figure 2.10 shows a representative prediction distribution at 4 different testing points, which seem to follow a normal distribution for each of these cases. Not that in some other applications, the posterior predictive distribution, obtained from VI, can follow multimodal distributions.

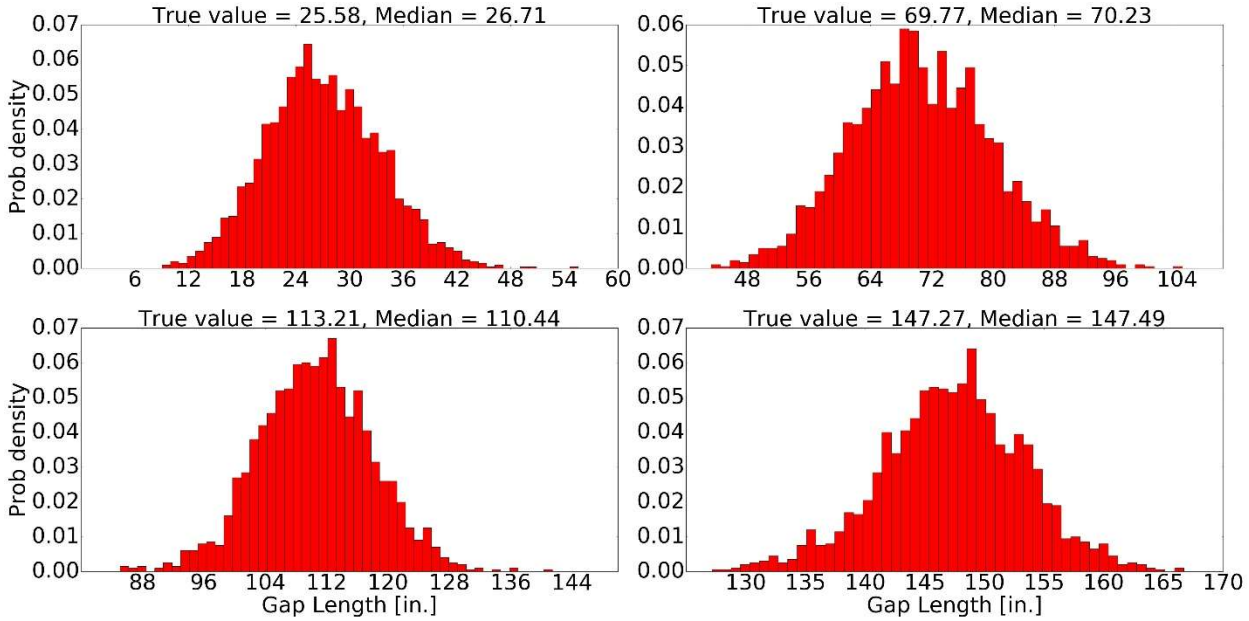

Figure 2.10: Posterior distribution of gap length using 4 different test samples

In general, a BNN surrogate, which is trained by data generated by computer simulation may not be able to capture the behavior of the real structure due to modelling error. To ensure that a trained BNN is reliable for SHM. The modelling error between the FE model and the real world should be accounted and modeled. In this chapter, modeling error was introduced to the computer simulations by varying the hydrostatic and temperature load and treating these loads as unknown quantities. Alternatively, two surrogate models can be used. One to learn the function that defines the FE simulations and one to learn the modeling error between the FE simulation and the real world. As new data comes from continuous monitoring, both surrogate models should be updated regularly. Particularly, the surrogate that fits the modelling error as modelling error extrapolation may be not be very accurate if it not updated regularly.

2.5. Value of Implementing SHM using BNN Surrogate Model

Recently, theoretical and applied approaches to quantify the value of deploying a structural health monitoring have been studied by researchers such as Konakli and Faber (Konakli and Faber 2014) and Thons (Thöns 2018). These and related studies are among the first to tie decisions that SHM informs to decision costs; this is the critical step that connects SHM to the business case for investing in and deploying an SHM system. Within the context of using the uncertainty-quantified BNN SHM "system" developed in the first part of this chapter, the BNN outputs will be matched with functions representing the consequence costs of (good and bad) decisions. This framework will be used to compare the relative merits of the BNN SHM approach to current engineering inspection data to arrive at conclusions regarding the relative "value" of such an approach.

2.5.1 Optimal Decisions using Inspection Data only

In the specific use case presented in this chapter, the USACE Asset Management team oversees the Operational Condition Assessment (OCA) process to assess structural component deficiencies by giving a category rating based on a condition and performance criteria. These ratings are performed by an inspector, who base the evaluation on engineering knowledge and information of preexisting inspections Figure 2.11 summarizes the OCA criteria currently used by USACE.

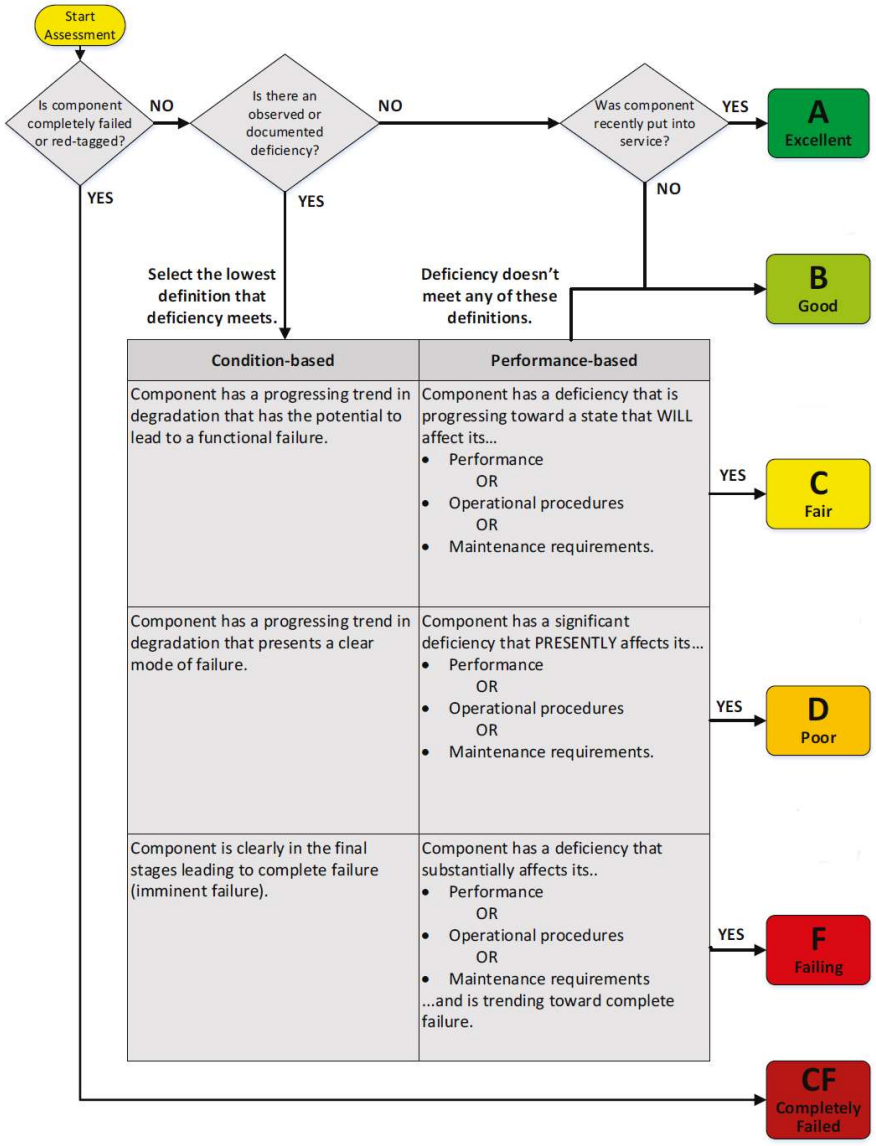

Figure 2.11: Current OCA rating criteria (Allen, Foltz, and Werth 2018)

2.5.1.1 Transition Probability Derivation

A transition matrix is defined as a square matrix with nonnegative values that represents how some process "transitions" from one state to the next. Based on an OCA database, the number of times that a component transitioned from one rating category (by engineering inspection expert judgment) to another in a given year was determined to generate a "condition" transition matrix. Thus, in this application, each value in the transition matrix represents a probability, and the sum of each row equals unity. Only the upper triangle components were considered to simulate component deterioration; the lower triangle would represent improvements or repairs, and for the purposes of this analysis, they were ignored. This "condition" transition matrix was found by normalizing the counts in each row as shown in Figure 2.12.

Transition matrices, known also as stochastic matrices, have been broadly used in different fields such as probability theory, control, economics, and meteorology (Degroot 1974; Caldarelli et al. 2012; Schoof and Pryor 2008).

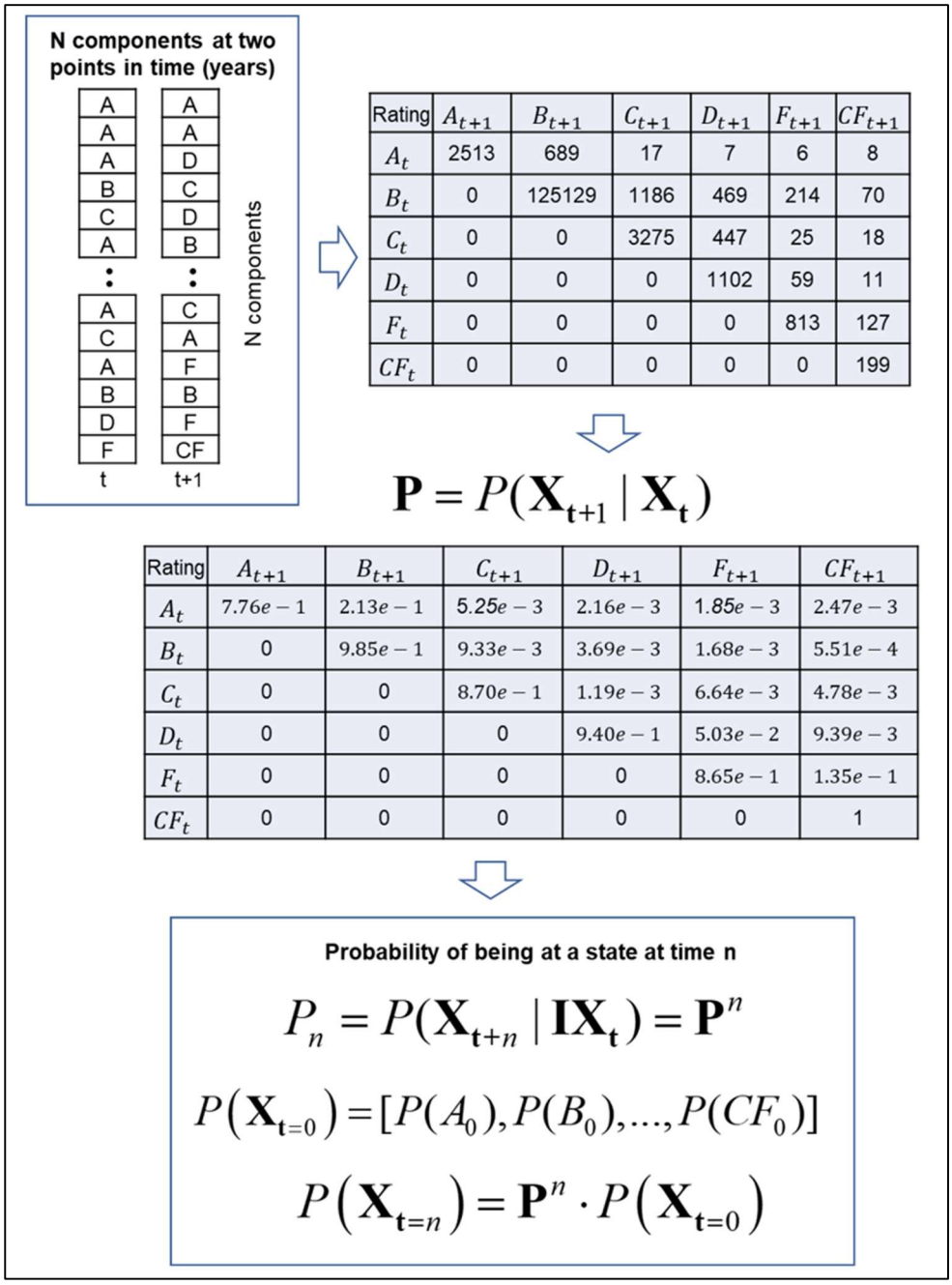

Figure 2.12: Deriving 1-step (1 year) transition matrix for quoin block components

2.5.1.2 Failure Rate of Component and Cost Function

A degradation model built from the transition matrix is used to generate a failure cumulative mass function, which can approximate the unreliability function, as described in detail

in (M. A. Vega et al. 2019). Figure 2.13 shows the unreliability function of the quoin block component with the component age in years as the random variable.

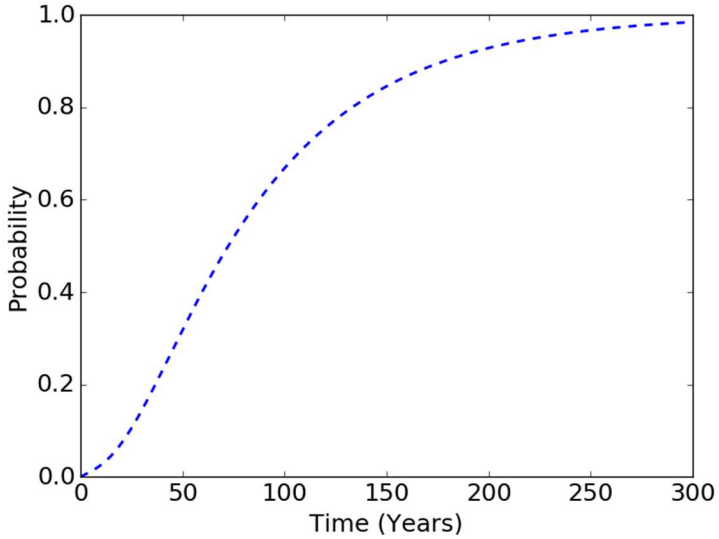

Figure 2.13: Unreliability function of quoin block component

Eq. (2.17) shows a cost function proposed by (Barlow and Hunter 1960) to find the cost per unit of time (CPUT) of performing preventive maintenance at a time t in years.

$$CPUT(t) = \frac{C_P[1-F(t)] + C_U[F(t)]}{\int_0^t [1-F(s)]\,ds}, \tag{2.17}$$

where $F(t)$ is the unreliability function, C_P is the preventive action cost, and C_U is the unplanned action cost. The unreliability function presented in Figure 2.13 was used with Eq. (2.17) to find the CPUT for different values of t as shown in Figure 2.14. This plot suggests that the optimal time to perform preventive maintenance is every 48 years when only considering the deterioration of quoin blocks and the data available from OCA inspections and the cost ratio is equal to 5. In other words, the "model" of the engineering inspection via the OCA database proposes a cost-minimized optimal inspection time of 48 years. The corresponding cost ratio (i.e. C_U/C_P) values depend on the structure and site. The values C_P and C_U can be defined as follow:

$$C_P = \begin{matrix}\text{scheduled}\\ \text{maintenance}\\ \text{costs}\end{matrix} + t_P * \begin{matrix}\text{daily economic}\\ \text{cost/loss due to}\\ \text{downtime}\end{matrix} \tag{2.18}$$

where t_P is the downtime (in days) that takes to perform regular maintenance. The maintenance cost associated is definitely lower when this is planned ahead.

$$C_U = \begin{matrix}\text{maintenance}\\ \text{cost due to}\\ \text{failure}\end{matrix} + t_U * \begin{matrix}\text{daily economic}\\ \text{cost/loss due to,}\\ \text{downtime}\end{matrix} \tag{2.19}$$

where t_U is the downtime (in days) that takes a component to be replace from the day that failed. For miter gates, the values of $t_U >> t_P$. This is essentially due to two reasons: 1) availability to start maintenance in a short period of time after failure occurrence and 2) maintenance takes longer when a component fails because it can affect other components or systems. The maintenance cost associated is definitely higher when maintenance needs to starts as soon as possible. Therefore, the unplanned cost is higher than the preventive action cost (i.e. $C_U / C_P >> 1$).

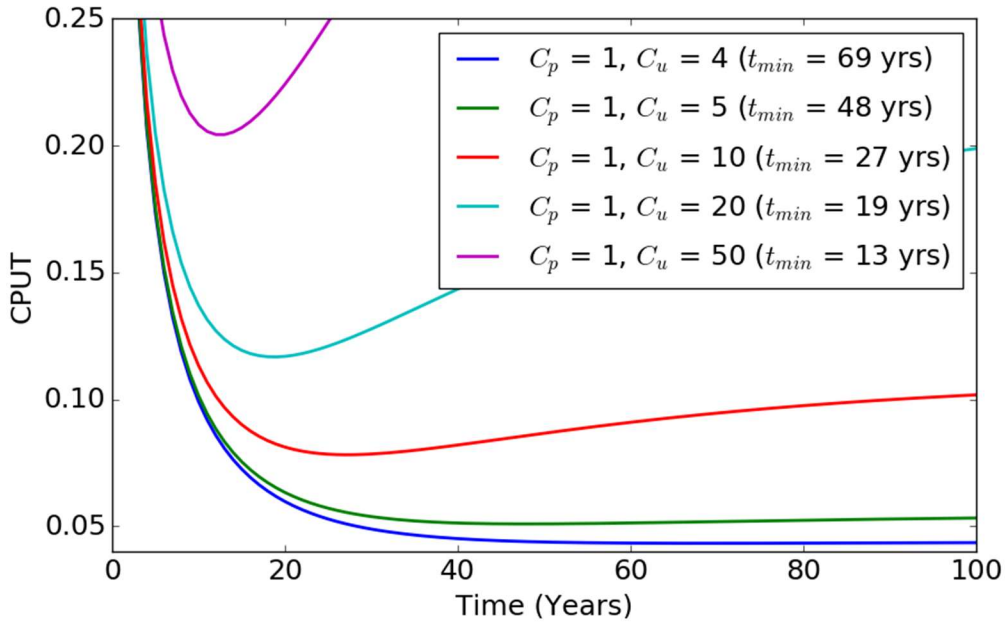

Figure 2.14: Cost per unit of time as a function of component age.

2.5.2 Optimal Decisions using BNN Surrogate Model and Value of SHM Application

Earlier, a cost function was defined, and the optimal maintenance time that corresponded to the minimum CPUT was calculated using the information provided by a model of the visual inspection process over time, presented in section 2.5.1 and reviewed in more detail in (M. A. Vega et al. 2019). Now, the BNN SHM approach will be used instead to build the unreliability function in order to compare the relative "value" of using the BNN SHM approach to the visual inspection approach for monitoring. To do that, the results shown in Figure 2.8 can be used to calculate the probability of exceedance of a certain gap length threshold as shown in Figure 2.15. This figure shows empirical cumulative mass functions for five different failure thresholds (i.e., gap lengths that correspond to criticality). Next, a mapping between the true gap length value and the component age can be used to find the corresponding unreliability functions. Eq. (2.11) can be applied to find the corresponding gap length value that minimizes the cost function as shown in Figure 2.16. Finally, the mapping from the true gap length value to the component age is used to find the optimal maintenance time as shown in Table 2.3. For these realizations, different cost ratios (i.e., values of C_P and C_U) and different failure threshold were used. It is important to note that specific results obviously depend on the choice of these values, but that the methodology shown in this section is independent of the actual values of the cost ratios and the failure threshold. After comparing different values of maintenance costs for miter gates at a specific site, the authors suggest that the corresponding cost ratio (i.e. C_U/C_P) is close to 5 based on communications with USACE personnel (Schultz 2018).

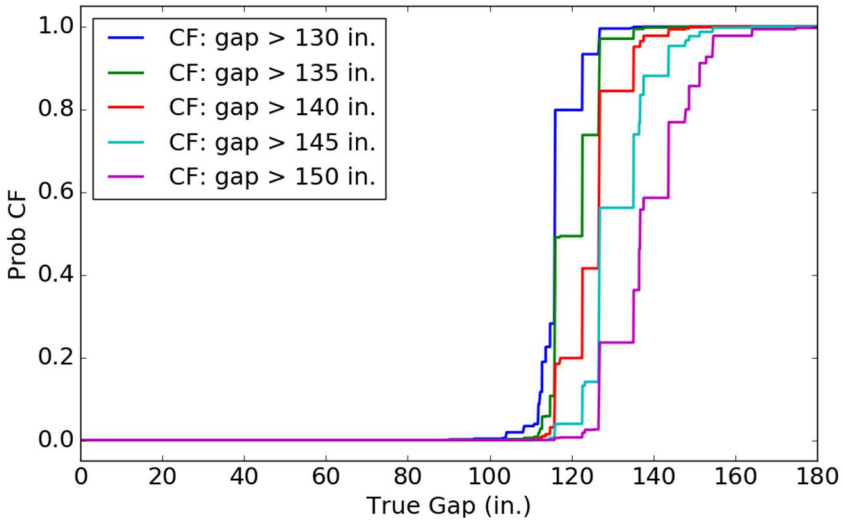

Figure 2.15: Empirical (Failure) cumulative mass function with $C_P = 1$ and $C_U = 5$

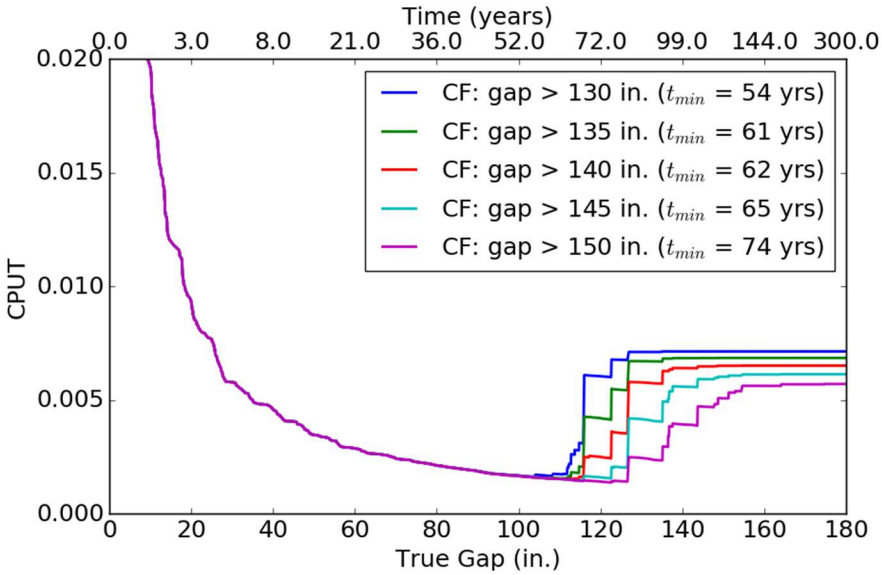

Figure 2.16: CPUT as a function of true testing gap length with $C_P = 1$ and $C_U = 5$

Table 2.3: Optimal maintenance time using BNN model with $C_P = 1$ and $C_U = 5$

Critical gap length (in.)	Optimal time (years)	Cost reduction (%)
130+	54	11.1
135+	61	21.3
140+	62	22.6
145+	65	26.2
150+	74	35.1

Different miter gate sites may have different values for the cost ratio (i.e. C_U/C_P); Figure 2.17 shows the variation in CPUT when a different value of cost ratio is used. For the realizations in this figure, the critical gap length threshold is assumed to be equal to 140 in. This figure shows less sensitivity to the cost ratio than Figure 2.14. The main reason why it is so is because there is less uncertainty when using the BNN SHM model. Of course, in an absolute judgment sense, it is important to note that the BNN model assumes that the training data generated from the FEM model is ground truth. As with any such model, its representative predictive value is only as good as its validation with regard to the real structure that it is modeling. In this case, the FEM was previously validated to the Greenup miter gate in the undamaged condition, as mentioned earlier, but the modeling of the damage itself couldn't be validated on actual data from the gate in a known damaged condition, so modeling bias error in the damage state could creep into the process. That doesn't change the demonstration of the proposed approach or its utility but rather provides caution on interpreting the specific results for this case beyond demonstration of the approach.

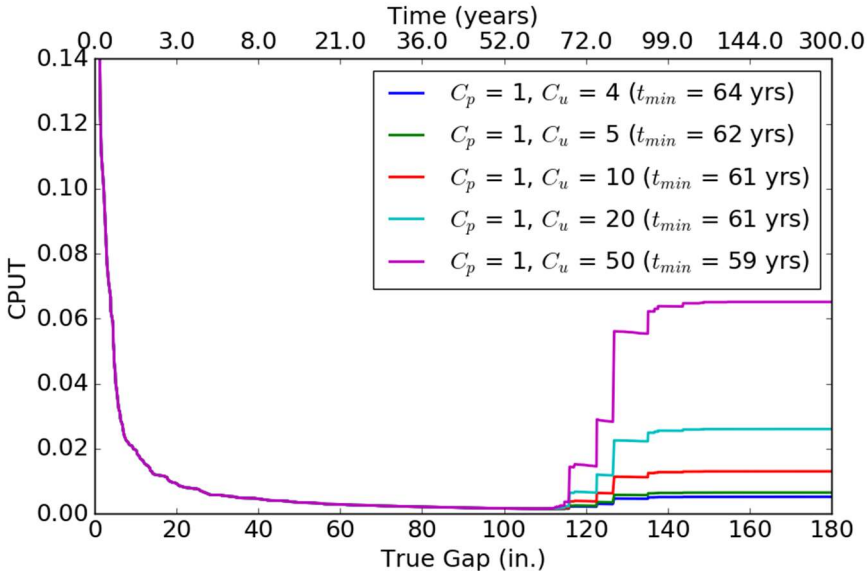

Figure 2.17: CPUT as a function of true testing gap length.

2.6. Conclusions and Discussion

The added value of using SHM in miter gates is evaluated in term of maintenance cost savings. A cost function is presented to improve prioritization of maintenance events of components of miter gates by evaluating the performance of a trained BNN model. This model is trained to assess the condition of quoin blocks in miter gates with a FE model due to such highly-limited data availability. In this work, a degradation model based on real inspection data of miter gates is used to simulate the damage evolution. A SHM workflow is set up to allows further optimization in term of cost savings within a civil structural monitoring application. As presented in this chapter, continuous monitoring via this BNN SHM "system" can lead to more economical decisions regarding maintenance policies than only using the data from visual inspection (e.g. OCA ratings). From the results shown in the previous sections, there is an 11.1% to 35.1% of maintenance cost reduction when the OCA ratings are used with a surrogate model based on a physical based model.

It is important to know that the degradation modes presented in this chapter was built from real inspection data. However, this data can still be bias to human error or insufficient information due to the difficulty to assess OCA ratings when a component is underwater, and it is not visibly available. Other degradation models can be considered when a larger historical data set is available. This chapter only focuses on the degradation of a single component. Further analysis can be carried out by considering more critical components (e.g. cracks in pintle, corrosion in the gate, etc.). Also, there are sources of uncertainty that need to be further analyzed that will lead to changes in the optimal maintenance time, such as measurement uncertainties or model uncertainties from both the BNN and FE model; the latter of these could be quantified via a sensitivity analysis of all the parameters in the FE and BNN models. Another potentially fruitful avenue for improvement is

consideration of how many strain sensors are used and where they are placed. Different such sensor designs could lead to different SHM assessment statistical performance, which in turn affects decision costs, and the sensor design itself directly influences procurement, installation, and sensor maintenance costs. Both of these could compete in a cost-minimized formulation.

2.7. Preview to Chapter 3

As mentioned in section 1.2.3, a data driven approach uses a mathematical model to learn the mapping function that transforms input variables (e.g. output response or extracted feature of the system) into the output variables (e.g. healthy and damage states of interest for the structure or SHM damage diagnosis). However, mathematical models such as BNNs still require relatively large amounts of data to provide good prediction. For civil engineering applications, many times monitoring data of the complete life of a structure is very limited. In these cases, damage diagnosis relies on using a physics-based model updating approach as described in section 1.2.2. The next chapter will show a CBM framework whose damage diagnosis would be based on the physics-based model updating approach, which it may be more suitable when such monitoring data is limited.

2.8. Remarks

Portions of this dissertation have been published or are currently being considered for publication. Chapter 2 is composed of a first authored publication:

Vega, Manuel A., and Michael D. Todd. 2020. "A Variational Bayesian Neural Network for Structural Health Monitoring and Cost-Informed Decision-Making in Miter Gates." Structural Health Monitoring, no. Special Issue. https://doi.org/10.1177/1475921720904543.

Chapter 3

OPTIMAL MAINTENANCE DECISIONS FOR DETERIORATING QUOIN BLOCKS IN MITER GATES SUBJECT TO UNCERTAINTY IN THE CONDITION RATING PROTOCOL

3.1. Abstract

Condition assessments and rating systems are frequently used by field engineers to assess inland navigation assets and components. The goal of these assessments is to initiate effective risk-informed budget plans for maintenance and repair/replace. Ideally, a degradation model of every component failure mode in the gate would facilitate maintenance decision-making. However, sometimes there is no clear physical understanding how a damage progresses in time; for example, it isn't clear how the bearing gaps change in time in the quoin blocks of a miter gate. Therefore, this is one motivation for the framework proposed in this chapter, which integrates Structural Health Monitoring with a Markov transition matrix built from historical condition assessment. To show the applicability of this framework, two examples are presented of how to find the optimal time to plan for maintenance of components in miter gates i) static maintenance planning based on operational condition assessment (OCA) ratings only and ii) dynamic maintenance planning based on integration of damage diagnostics based on monitoring data and failure prognosis based on OCA ratings. In addition, this chapter presents a new Bayesian approach to estimate the ratio of errors in the OCA ratings, which allows for improved accuracy in OCA rating-based prognosis.

3.2. Introduction

The U.S. Army Corps of Engineers (USACE) maintains and operates 236 locks at 191 sites in the United States (U.S. Army Corps of Engineers Headquarters 2018). More than half of these structural assets have surpassed their 50-year economic design life (Foltz 2017). There are several types of lock gates such as miter, sector, tainter, and vertical lift, with miter gates being the most common type used in the United States (Alexander et al. 2018). Miter gates are steel structures that allow passage of boats, and watercraft through elevation changes of the water level in canals and rivers that would otherwise be non-navigable as shown in Figure 3.1.

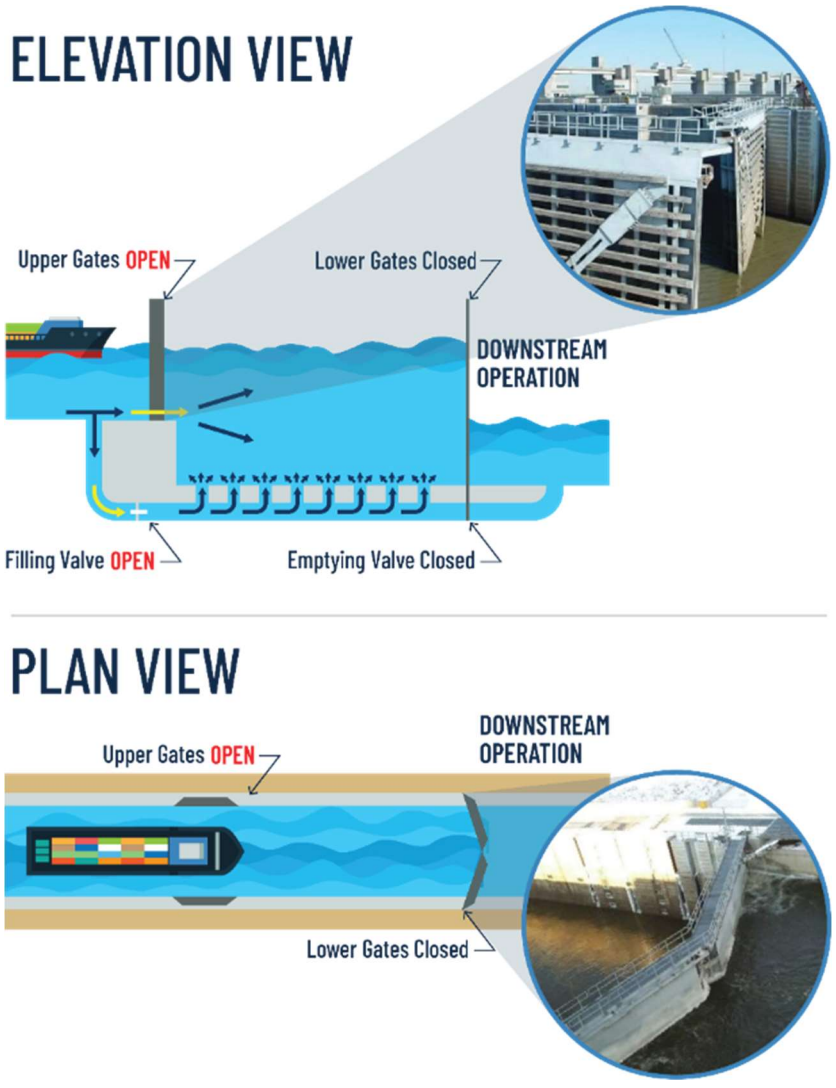

Figure 3.1: Navigation along miter gates

The USACE has developed the operational condition assessment (OCA) ratings to help prioritize repairs/replacements in their navigation assets. The OCA rating is an assessment obtained from an inspection process, which uses existing data from periodic and non-periodic inspections, including corrosion tests and dive reports. The objective of the OCA process is to obtain global consistent operational condition data to identify the current condition states of the USACE infrastructure (Przybyla 2013). Visual inspections have been used to update the reliability of miter gate components and corrosion deterioration models (Estes, Frangopol, and Foltz 2004). In the United States, horizontally-framed miter gates are laterally supported by continuous quoin blocks rather by discontinuous quoin blocks (Eick, Smith, and Fillmore 2019a). The hydrostatic load imposed upon the miter gates is transmitted through the girders to the quoin blocks and into the walls that support the gate laterally. Any fabrication defect or deterioration in the quoin blocks, especially in continuous quoin blocks, will result in changes to the lateral support force system of a miter gate, making them unknown parameters (Commander et al. 1994). The deterioration of the quoin blocks is broadly manifested as a small gap because of the loss of contact between the quoin block attached to the gate and the quoin block attached to the wall that supports the gate laterally. The formation of this gap can be detected using sensor data or from features derived from this data (Eick et al. 2018).

When measurement data from sensors is available, researchers rely on Finite Element (FE) model updating techniques to estimate the unknown parameters (e.g., gap detection in miter gates) to infer the current state of the system. For hydraulic infrastructure systems (e.g. dams, miter gates), several researchers (M. A. Vega et al. 2021; Ramancha et al. 2019; Y. Yang, Madarshahian, and Todd 2019) have updated physics-based linear and nonlinear FE models using simulated measurement data. Also, FE models have been used to study crack propagation and fatigue of

miter gates (Mahmoud, Chulahwat, and Riveros 2018). For other civil infrastructure systems, researchers have successfully performed model updating of mechanics-based linear FE models using real measurement data (Moaveni, Conte, and Hemez 2009; Jang, Li, and Spencer 2013). However, only recently, there are efforts to perform model updating of mechanics-based nonlinear FE model of full-scale civil system using real measurement data (Ramancha et al. 2020). Other efforts have performed model updating of mechanics-based nonlinear FE model using simulated measurement data (Astroza et al. 2017; Jensen et al. 2017). Furthermore, researchers have used the predictions of updated mechanics-based FE models for reliability assessments (Okasha, Frangopol, and Orcesi 2012). Recently, researchers have made use of surrogate models to serve as fast emulators of computationally expensive FE models, whose predictions are also used for reliability assessments (Bichon, McFarland, and Mahadevan 2011; Jensen et al. 2017; M. Vega, Madarshahian, and Todd 2019; Z. Wang and Shafieezadeh 2020).

For miter gates, there has been some work in detecting small gaps near the pintle area, where the gate is supported vertically (M. Vega, Madarshahian, and Todd 2019; Eick et al. 2017). Additionally, gap detection analysis has also been performed on the presence of multiple gaps in the quoin block (Hoskere et al. 2019). Another way to understand the effect of these small gaps is to infer the changes in the lateral reaction forces (Parno, O'Connor, and Smith 2018). All these approaches can provide an idea of the current operational or damage state of the gate, which can give the engineers a notion of how reliable a miter gate is at any instant in time. However, for maintenance planning purposes, knowing the reliability at *any* point in time is desired, including the future. A degradation model of the state of the structure (or a component of it) is needed to estimate the reliability in this case. Degradation models (e.g., material degradation) have been used with reliability analysis for life cycle analysis in civil infrastructure such as bridges (Strauss et al.

2009; Morcous 2006) and hydraulic steel structures (Estes, Frangopol, and Foltz 2004). Markov chain degradation models are widely used to predict future structural condition states in order to facilitate life cycle analysis (Riveros and Rosario-Pérez 2018; Bocchini, Saydam, and Frangopol 2013; Chiachío et al. 2020). A degradation model can be enhanced by information obtained from structural health monitoring (SHM) systems, which may assist in establishing more efficient maintenance, repair, and replacement priorities for navigational locks. SMART Gate (U.S. Army Corps of Engineers Headquarters 2007) was implemented for some USACE miter gates to monitor the deteriorating conditions until extensive repairs and eventual replacement could be done.

Based on (Daniel and Paulus 2019c), maintenance of hydraulic gate systems is the most vulnerable and least developed of all procedures that impact a lock gate's performance. Other more developed procedures that affect a lock gate are design, construction, operation, and management (Eick, Smith, and Fillmore 2019a). Due to the aging of navigation assets in the US and the economical strains associated with lock closures, USACE has started to build a database that includes inspections, assessments, preventative maintenance, and essential maintenance events to track and prioritize maintenance of multiple dams and hydraulic gates. Currently, USACE uses an industry maintenance management software called Maximo (Al-Fedaghi and Al-Huwais 2018), which has been customized to meet USACE requirements and is called the FEM (facilities and equipment maintenance) system. In theory, this system should enable better informed maintenance and resourcing decisions based on historical maintenance data and trend analysis (Daniel and Paulus 2019b). However, while FEM is capable of collecting various sources of maintenance-related information that can help in maintenance activities, it provides little or no programmed capability to analyze information or make probabilistic inferences (Foltz, Bislip-morales, and Hammack 2013). Furthermore, diagnosis and prognosis using data-driven models built from solely

inspection data (i.e. OCA ratings) may lead to large uncertainty in the failure prognosis as shown in previous studies (M. A. Vega, Hu, and Todd 2020) and in the case study section.

Beyond these ratings, however, structural health monitoring (SHM) systems have been developed for the miter gates to measure its distributed point strain response during operation, providing continuous data streams which may be fined for damage-related information. The SHM measurement systems are coupled with validated high-fidelity physics-based finite element (FE) models (M. A. Vega, Hu, and Todd 2020; M. A. Vega et al. 2021; Ramancha et al. 2020; Y. Yang, Madarshahian, and Todd 2019; Gomez, Spencer, Jr., and Smith 2019), allowing for inference/estimation of the damage gap using the strain measurements. This approach provides more confident estimates of the damage gap state over time. While it is true that the SHM system increases gap inference capabilities, it cannot be used directly to predict the gap degradation over time, since the physics of the gap degradation is complex and not fully understood; SHM alone is not enough to inform decisions regarding prioritizing preventive maintenance. As described above, however, the historical OCA ratings contain information that can be used to understand the gap degradation over time, even though it is highly abstracted and may be contaminated by human observation errors or bias. Synthesizing, rather than separating, OCA rating transition information and SHM system information has the potential to improve an integrated state awareness (damage state) and state prediction (future damage state).

This work proposes a new hybrid approach to overcome this challenge by integrating physics-based SHM with a statistical-based state transition matrix. According to the literature, hybrid approaches have not been studied as extensively as noted in (An, Kim, and Choi 2015) and even less for large civil infrastructure systems or miter gates. In this chapter, the focus will be on

horizontally-framed miter gates. However, the framework is applicable to other structures that have online health monitoring systems and that has condition ratings (e.g. OCA) data available.

For the USACE portfolio, this framework can be applicable to the navigation structures that are under the SMART Gate program (U.S. Army Corps of Engineers Headquarters 2007), which consists of several lock sites including Dalles Navigation Lock, Lock 27, Greenup Lock (used in this work), and Meldahl Lock on the Mississippi River (Daniel and Paulus 2019b). In this work, the component chosen to monitor is the bearing gap in the quoin blocks. It is important to optimize the maintenance of quoin block components because they directly control the stress profile in horizontally-framed miter gates, where over-stresses exceeding a certain threshold can lead to structural failure. Currently, contact blocks are effectively a continuous single piece of steel, which during maintenance requires the entire piece to be replaced even if only part is damaged (Eick, Smith, and Fillmore 2019a). However, replace cost is relatively low compared with the downtime cost during maintenance or when failure occurs. Therefore, this motivates the authors to optimize the maintenance considering not only repair/replace costs but also the impact cost when a miter gate is not operational.

The contributions of this chapter can be summarized as: (1) development of a new hybrid CBM approach that integrates high-fidelity FE model-based SHM with inspection data-based transition matrix for effective diagnosis, prognosis, and maintenance planning; (2) quantification of effects of uncertainty in OCA ratings on maintenance planning; (3) a new Bayesian scheme to update the error ratio in the OCA ratings; (4) account for the effects of human errors in the OCA rating transition information in terms of diagnosis and prognosis; (5) surrogate modeling method to overcome the computational challenge in FE model-based SHM; and (6) application of the proposed framework to a miter gate problem.

The remainder of this article is organized as follows. Sec. 3.3 gives an overview of the proposed framework for optimal maintenance decisions for deteriorating components in miter gates. Sec.3.4 explains how to approximate the unreliability function using a Markov chain approach using non-periodical inspection ratings from the quoin block in miter gates. With this unreliability function, Sec. 3.5 formulates a novel hybrid approach for condition-based maintenance where inspection ratings (e.g. OCA) are used to construct a degradation model along with a SHM system used for damage diagnostics. The proposed approach overcomes the challenges of no available degradation model and data heterogeneity (i.e. physics-based simulation data, OCA rating data, errors in the OCA rating data, and strain measurement data). Sec. 3.7 demonstrates the proposed framework applied to a real-world application problem example. Finally, Sec 3.8 proposed a degradation model, built using the OCA rating data, to improve damage prognosis accounting for human error in OCA ratings.

3.3. Overview of proposed framework

Fig. 3.2 presents an overview of the proposed framework for optimal maintenance decisions for deteriorating components in miter gates. As shown in this figure, the proposed framework consists of four main modules, namely (1) failure prognosis based on OCA ratings, (2) maintenance planning, (3) damage diagnosis using physics-based simulation, and (4) integration of failure diagnosis and prognosis to achieve on-line planning and updating. These four modules are systematically integrated together to perform two types (*static* and *dynamic*) of optimal maintenance decisions for miter gates.

The term *static* refers to the inability to update the current or future state based on the changes that a component of the system undergoes. The static maintenance planning is only based

on the field OCA ratings from a large population of miter gates. The obtained optimal maintenance decisions are therefore general to the population of miter gates of interest and are not specific for a specific gate. Thus, the obtained maintenance planning may not be truly optimal for a specific gate. For the static maintenance planning of a miter gate, there are several uncertainties to be addressed, such as how to justify a maintenance decision and how to deal with the uncertainty in the OCA rating due to both *limited data* and *incorrect rating assignments*, i.e., ratings due to protocols are sometimes given to components even when they are not inspected.

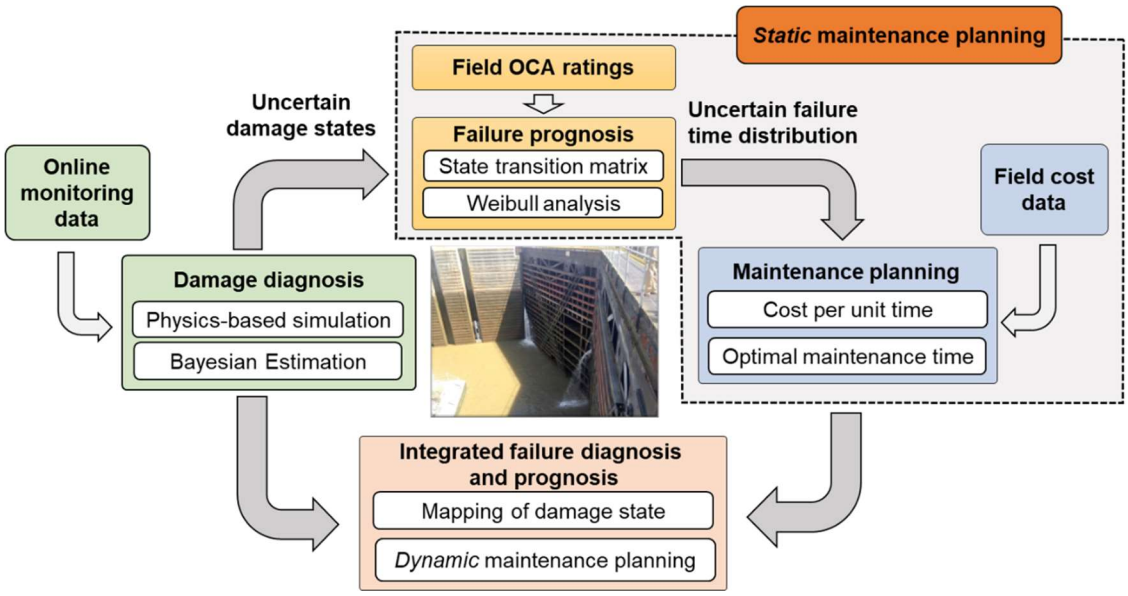

Figure 3.2: Overview of proposed framework for optimal maintenance decisions for deteriorating components in miter gates

Many miter gates are equipped with sensors which can collect strain measurement data in real time, e.g., the SMART Gate program mentioned earlier (U.S. Army Corps of Engineers Headquarters 2007). Based on the online monitoring data and the high-fidelity physics-based simulations, the damage condition is estimated using Bayesian methods. The real-time damage diagnosis provides damage information at individual gate level, which offers an opportunity to achieve optimal maintenance planning and dynamic maintenance decisions for a specific gate. The integration of failure diagnosis and prognosis (as shown in Fig. 3.2) faces several challenges. For

instance, the high-fidelity physics-based simulation model is computationally expensive, which makes Bayesian damage estimation challenging; the OCA ratings are highly abstracted and are assigned at a different time scale than the online monitoring system. The proposed framework tackles the above challenges by using the information from field OCA ratings, physics-based simulation, and online monitoring data.

Each of the following sections explains in detail one the four modules mentioned earlier. Section 3.4 and 3.5 describe the static maintenance planning based only on the field OCA ratings from a large population of miter gates. Section 3.4 describes how to build a 1-step transition matrix based on the field OCA, then a *n*-step transition matrix is used to generate an unreliability (or failure) function corresponding to quoin block components in miter gates. Section 3.5 explains the static maintenance planning using the failure function obtained in Section 3.4. Section 3.6 and 3.7 describe the formulation and application, respectively, of the dynamic maintenance planning based on the integration of prognosis models (i.e. physics-based FE model) and historical inspection data (i.e. field OCA ratings). Section 3.6 explains the damage diagnosis using physics-based model updating using two different degradation models (i.e. state equation) and formulates the integration of failure diagnosis, Bayesian updating of the error ratio of the OCA ratings based on damage diagnosis, and prognosis to achieve on-line planning and updating. Section 3.7 describes a real-world application example of the framework described in section 3.6.

3.4. Failure prognosis based on OCA ratings

3.4.1 Deriving a transition matrix from OCA ratings

The USACE Asset Management team oversees the OCA process to assess structural component deficiencies by giving a category rating based on a condition and performance criteria.

The ratings are classified as *A* (Excellent), *B* (Good), *C* (Fair), *D* (Poor), *F* (Failing) and *CF* (Completely Failed). More detailed definitions and discussion may be found in (Foltz 2017). A transition matrix **P** (see Eq. (1)) is defined as a square matrix with nonnegative values that represents how some process "transitions" from one state to the next. In this application, an inspected OCA rating at time *t*, $I_{i,t}$, (which represents the OCA rating is *i* at time *t*, with *i*=1…6, corresponding to the 6 letter ratings specified above), will transition to inspected state at time *t*+1, $I_{j,t+1}, j = 1...6$, according to

$$\mathbf{P} = P\left(I_{j,t+1} \middle| I_{i,t}\right) = \begin{bmatrix} P\left(A_{t+1} \middle| A_t\right) & \cdots & P\left(CF_{t+1} \middle| A_t\right) \\ \vdots & \ddots & \vdots \\ P\left(A_{t+1} \middle| CF_t\right) & \cdots & P\left(CF_{t+1} \middle| CF_t\right) \end{bmatrix}, \forall i,\ j = 1, \cdots, 6. \tag{3.1}$$

Based on an OCA database, the number of times that a component transitioned from one rating category to another (as determined by engineering expert elicitation) over a given inspection time step was determined to generate the rating transition matrix. Each value in the transition matrix represents a conditional probability, and the sum of each row equals unity after normalizing the counts. Only the upper triangular components were considered to simulate component deterioration; the lower triangular components would represent improvements or repairs (transitions from a worse condition to a better condition), and for the purposes of this analysis, they were ignored. Fig. 3.3 shows the overall process for generating this one-step transition matrix **P**. The foundational data used to generate the counts were obtained from the OCA ratings database for navigation locks corresponding from January 2010 to June 2018, which was provided by USACE personnel.

3.4.2 Unreliability (failure) function using transition matrix for component reliability

A failure cumulative mass function, which can approximate the probability of failure

cumulative density function, can be obtained by calculating the transition probabilities after *n* time steps. In this case, failure is defined to be achieving the rating "*CF*". The probability that a critical component goes from OCA rating *i* to OCA rating *j* after *n* inspection time steps is calculated by raising the transition matrix to the power of *n*,

$$P\left(I_{j,t+n}\middle|I_{i,t}\right)=\mathbf{P}^{n},\ \forall i=1,\cdots,6;\ j\geq i\,. \tag{3.2}$$

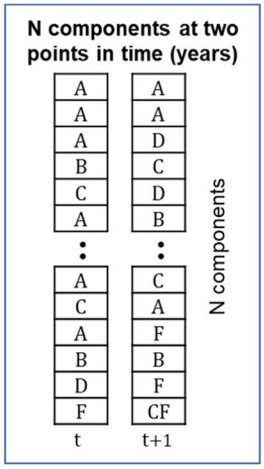

Rating	A_{t+1}	B_{t+1}	C_{t+1}	D_{t+1}	F_{t+1}	CF_{t+1}
A_t	2513	689	17	7	6	8
B_t	0	125129*($B_{inspected}/B_{total}$)	1186	469	214	70
C_t	0	0	3275	447	25	18
D_t	0	0	0	1102	59	11
F_t	0	0	0	0	813	127
CF_t	0	0	0	0	0	199

$\mathbf{P}=P\left(I_{j,t+1}\middle|I_{i,t}\right)$, *and assume* $B_{inspected}/B_{total}=1$

Rating	A_{t+1}	B_{t+1}	C_{t+1}	D_{t+1}	F_{t+1}	CF_{t+1}
A_t	$7.76e-1$	$2.13e-1$	$5.25e-3$	$2.16e-3$	$1.85e-3$	$2.47e-3$
B_t	0	$9.85e-1$	$9.33e-3$	$3.69e-3$	$1.68e-3$	$5.51e-4$
C_t	0	0	$8.70e-1$	$1.19e-3$	$6.64e-3$	$4.78e-3$
D_t	0	0	0	$9.40e-1$	$5.03e-2$	$9.39e-3$
F_t	0	0	0	0	$8.65e-1$	$1.35e-1$
CF_t	0	0	0	0	0	1

Figure 3.3: 1-step (1 year) transition matrix for quoin block components

The conditional probability *n*-step transition matrix Eq. (3.1) can then be used to transition some initial OCA rating probabilities for each rating to the state probabilities *n* time steps later, or

$$P(\mathbf{I}_n)=[P\left(I_{1,n}\right),P\left(I_{2,n}\right),P\left(I_{3,n}\right),P\left(I_{4,n}\right),P\left(I_{5,n}\right),P\left(I_{6,n}\right)]=P(\mathbf{I}_0)\cdot\mathbf{P}^{n}, \tag{3.3}$$

where $P\left(I_{i,n}\right), i=1...6,$ is the predicted OCA rating at time t_n, and $P(\mathbf{I}_0)$ is the initial inspected OCA rating probability, i.e.,

$$P(\mathbf{I}_0)\equiv\left[P\left(A_0\right),P\left(B_0\right),P\left(C_0\right),P\left(D_0\right),P\left(F_0\right),P\left(CF_0\right)\right]. \tag{3.4}$$

Fig. 3.4 shows the unreliability function, $F(t)$, of the quoin block component with the component age in years with the initial state probability specified as $P(\mathbf{I}_0) = [1, 0, ..., 0]$, i.e., the gate begins its OCA rating fully in rating "*A*". This is a reasonable assumption, but any initial OCA rating could be specified if other information is known, e.g., some initial degradation is possibly present at the initial time.

3.5. Static Optimal Maintenance Decision of Miter Gates Based on OCA Ratings

3.5.1 Maintenance decisions with uncertainty via Weibull analysis

A common statistical formula used for life cycle analysis is the Weibull distribution (Weibull 1951). The predictions about the life (i.e. reliability) of any component over time *t* in a structure can be fit to a Weibull distribution. The reliability function, $R(t)$, based on the Weibull distribution is:

$$R(t) = e^{-\left(\frac{t}{\eta}\right)^{\beta}}, \tag{3.5}$$

where $R(t)$, β, and η are the reliability, shape parameter, and characteristic life (scale parameter), respectively. The shape parameter β must be greater than 1.0 to justify preventive maintenance due to wear out failures (Jiang and Murthy 2011; Daniel and Paulus 2019b) . The characteristic life (or scale parameter) η represents the point in time when there is a 63.2% (when $t = \eta$ in Eq. (3.6)) chance of failure of the component. The next two subsections within Sec. 3.5.1 will discuss uncertainty models from the two main sources described in Sec. 3.3, namely limited data and incorrect rating assignments.

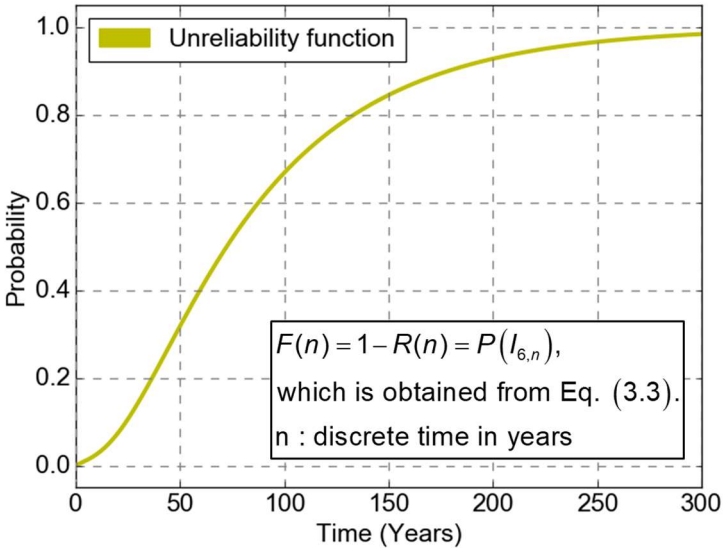

Figure 3.4: Unreliability function of quoin block component (M. A. Vega et al. 2019)

3.5.1.1 Uncertainty quantification of Weibull distribution due to limited data

The unreliability $F(t)$ based on the reliability function is given by

$$F(t)=1-R(t)=1-e^{-\left(\frac{t}{\eta}\right)^{\beta}}. \tag{3.6}$$

This unreliability function must be calibrated to the transition matrix such that the parameters β and η are chosen to match Eq. (3.6) to the unreliability (failure) function obtained from the transition matrix. To accomplish this, a Bayesian calibration method is employed to obtain not only point estimates of the parameters but also the uncertainty in their estimation; here, this problem amounts to solving for the posterior probability of the parameters

$$\underbrace{p(\beta,\eta,\sigma\,|\,y)}_{posterior} \propto \underbrace{p(y\,|\,\beta,\eta,\sigma)}_{likelihood}\,\underbrace{p(\beta,\eta,\sigma)}_{prior}, \tag{3.7}$$

where y is given by

$$y=\underbrace{1-e^{-\left(\frac{t}{\eta}\right)^{\beta}}}_{\substack{2-parameter\\ Weibull\ CDF}}+\underbrace{\varepsilon}_{error}, \tag{3.8}$$

and ε is the observation error in the state transition, assumed Gaussian-distributed with standard deviation σ, or

$$\varepsilon \sim \mathcal{N}\left(0, \sigma^2\right). \tag{3.9}$$

With this error assumption, the likelihood function $p(y \mid \beta, \eta, \sigma)$ can be expressed as

$$\begin{aligned} p(y \mid \beta, \eta, \sigma) &\equiv \mathcal{N}(1 - e^{-\left(\frac{t}{\eta}\right)^{\beta}}, \sigma^2) \\ &= \frac{1}{\sigma\sqrt{2\pi}} \exp\left\{ -\frac{1}{2}\left[\frac{y - (1 - e^{-\left(\frac{t}{\eta}\right)^{\beta}})}{\sigma} \right]^2 \right\}. \end{aligned} \tag{3.10}$$

For the prior distribution $p(\beta, \eta, \sigma)$ in Eq. (3.7), it is assumed that all the parameters are statistically independent such that $p(\beta, \eta, \sigma) = p(\beta)\, p(\eta)\, p(\sigma)$, and the individual parameter priors are assumed to be

$$\begin{aligned} p(\beta) &\sim \text{Lognormal}\left(\log(1.2), 0.2\right), \\ p(\eta) &\sim \text{Lognormal}\left(\log(50), 0.5\right), \\ p(\sigma) &\sim \left|\mathcal{N}\left(0, 0.02\right)\right|. \end{aligned} \tag{3.11}$$

Thus, there are 3 parameters to be estimated: the shape parameter β, the characteristic life η, and the standard deviation σ of the unbiased Gaussian-distributed observation error ε. Fig. 3.5 shows the prior and posterior distributions of these 3 parameters before and after performing Bayesian inference, using a Markov Chain Monte Carlo (MCMC) sampling approach to compute Eq. (7). Note that the input parameters of the prior distributions shown in Eq. (3.11) where chosen to have sufficient support, i.e., the range of possible values of a random variable is wide to account for all possibilities. Generally, the parameters of a prior distribution can be chosen from some previous knowledge based on data or previous studies.

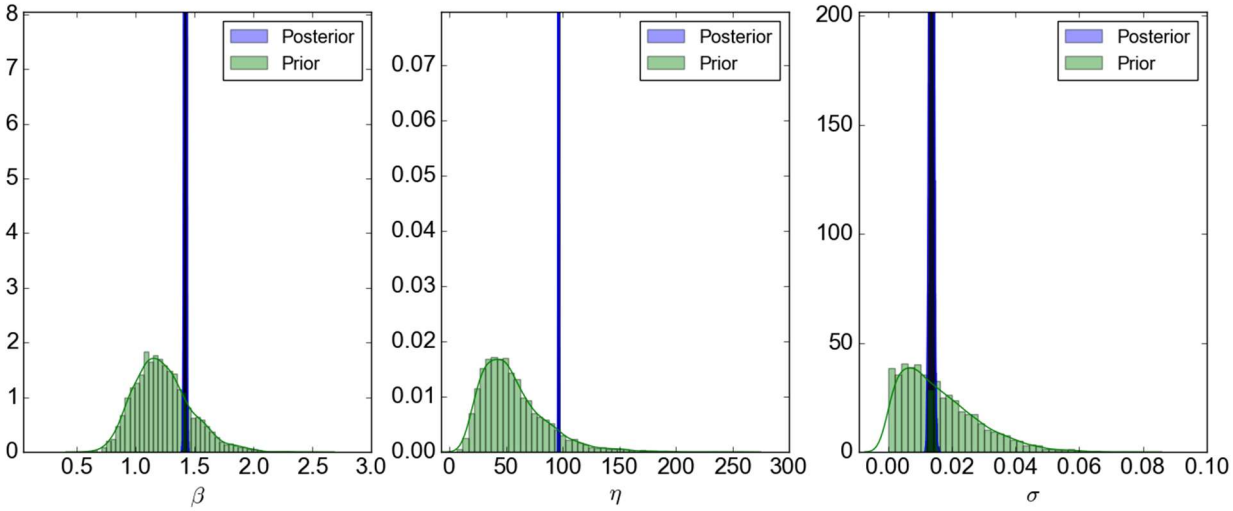

Figure 3.5: Prior and posterior distribution of Weibull parameters

The joint posterior probability obtained is shown in Figure 3.6. The mean value of the shape parameter β is equal to 1.42; since this value is greater than 1, preventive maintenance is justified. The mean value of the characteristic life η is equal to 96.2 years, implying that there is a 63.2% chance of failure of the component after 96.2 years.

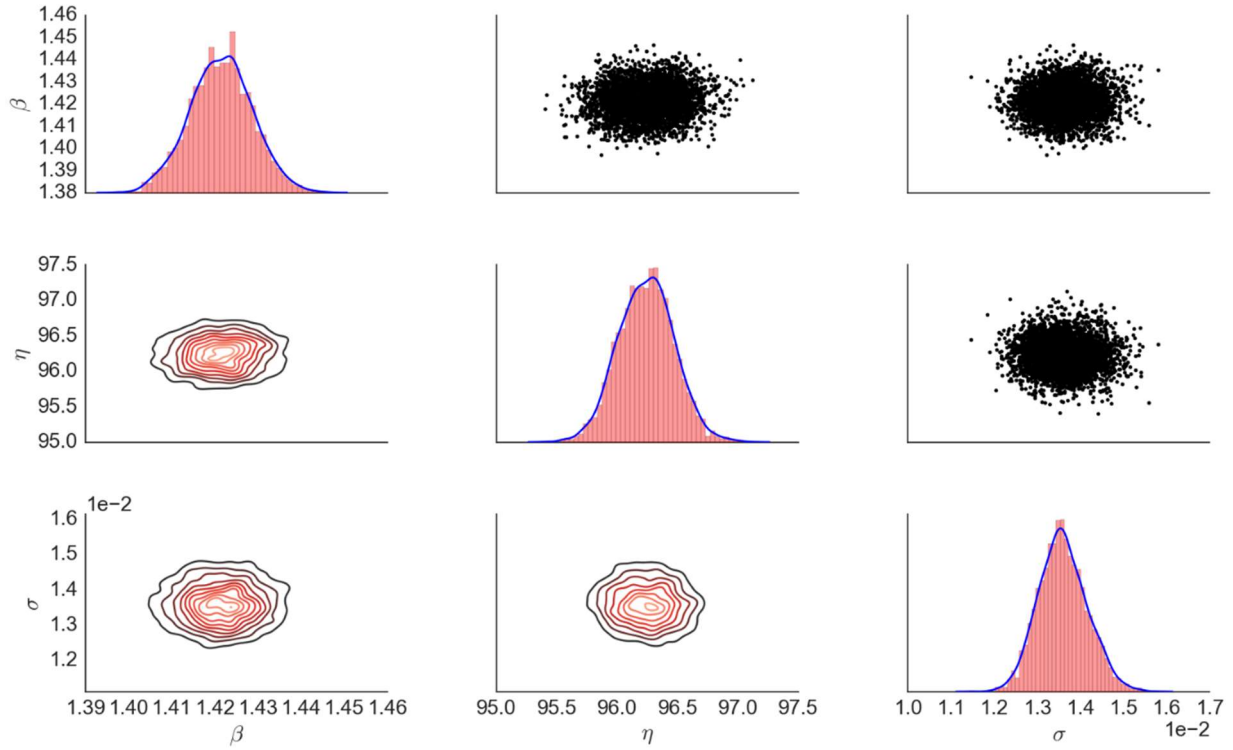

Figure 3.6: Posterior probabilities of Weibull parameters

Fig. 3.7 shows how good a Weibull distribution describes the unreliability function obtained from the 1-step transition matrix. As shown in Fig. 3.6, the standard deviation of the assumed zero mean error has its mean around 1.36%, which confirms the goodness of the parameter calibration to the transition matrix unreliability data.

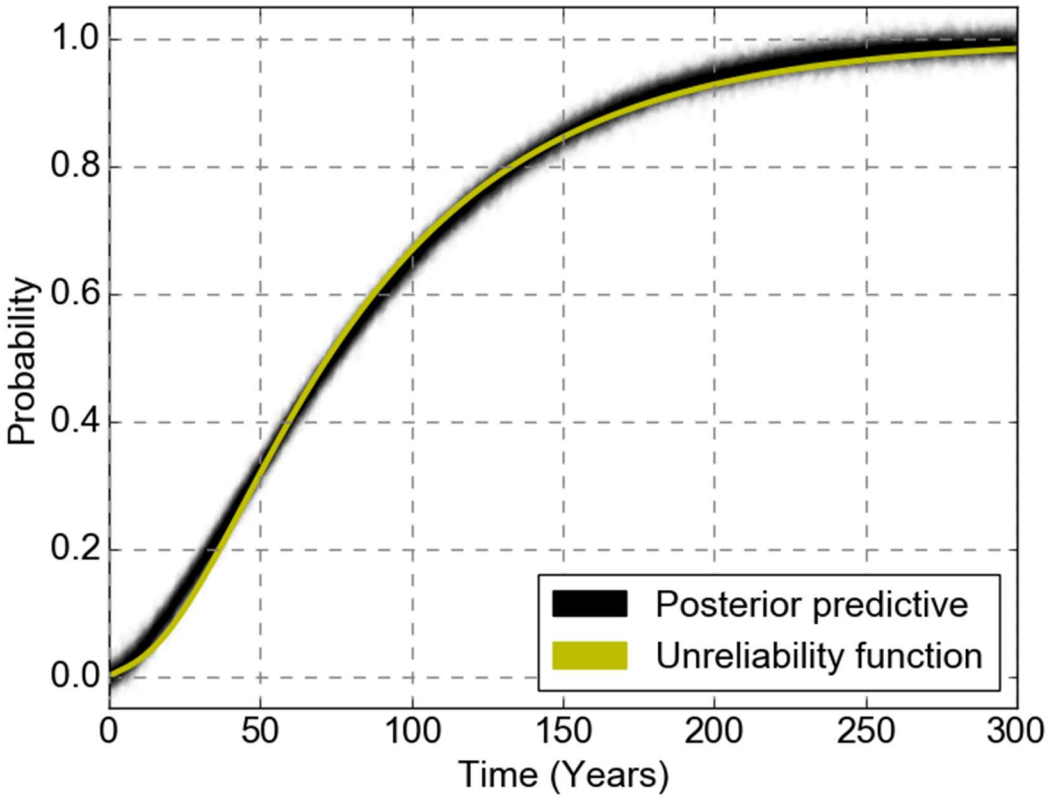

Figure 3.7: Bayesian fitting using Weibull distribution

3.5.1.2 Uncertainty of Weibull analysis due to condition rating protocol

For the locks and dams comprising the USACE infrastructure portfolio, the typical Periodic Inspection (PI) of the lock and dam varies from every year to occurring to a maximum of every 5 years (USACE 2019). However, the dewatering of a lock is much less frequent, often spanning multiple PI intervals. Therefore, unless there is evidence of degradation of a component that cannot be inspected, it is given a "*B*" rating. If a component was previously given something less than a "*B*" rating, and it is known that no work has been performed, the rating is carried over. Thus, many

of the given "*B*" ratings are not the result of an actual inspection; this is particularly true for any component that is submerged underwater. Based on direct communication with USACE personnel, this is true for all components that are "unable to be inspected at that time, which is essentially the innocent until proven guilty mindset" (A. Campbell 2019) . After analyzing the data, it was clear that the counts remaining at B after 1 year were very large (see counts of staying at B in Figure 3.3). Also, it was noted that many historical OCA ratings of quoin block components didn't transition all the way from A to CF. Sometimes, the components were replaced/repaired before passing to C, D or F (or they just simply not recorded). Therefore, after discussing with USACE engineers, the main source of uncertainty was focused upon the B ratings.

Fig. 3.8 shows how the unreliability function, *F(t)*, changes when the transition matrix changes due to the uncertainty associated in the states remaining at "*B*" as explained before.

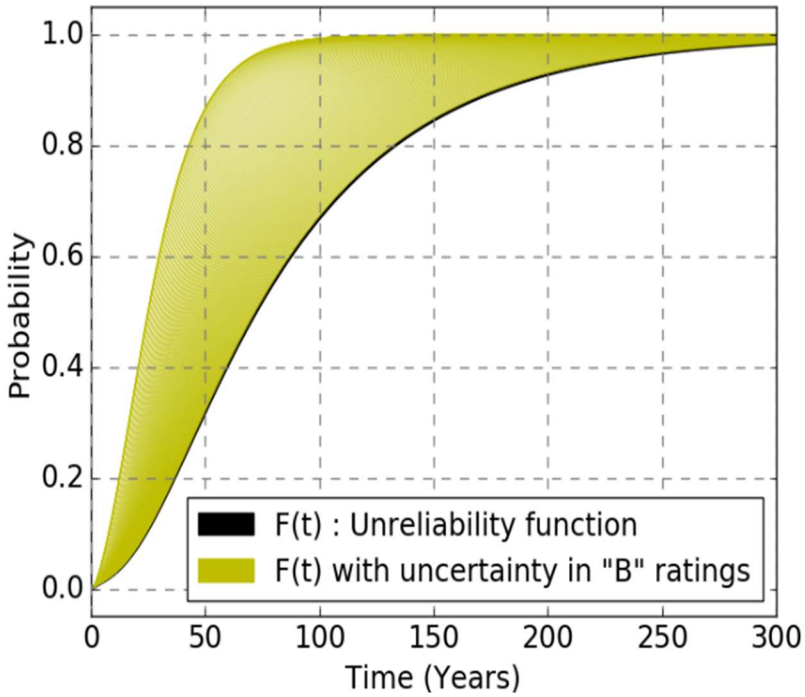

Figure 3.8: Unreliability function considering uncertainty in the condition rating protocol

The variability in the unreliability function was obtained by considering that the counts of remaining in state "*B*" that corresponded to an actual inspection was some ratio of the total counts reported (i.e., $B_{inspected}/B_{total}$ varies from 0 to 1). To understand better this variability in the unreliability function, a Bayesian fitting using a Weibull distribution (like Sec. 3.5.1.1) was performed for each sample of the unreliability function reported in this figure. Fig. 3.9 shows the variability of the shape and scale parameters due to the variation of the considered "actual" counts of staying at a "B" rating in a given year. As the $B_{inspected}/B_{total}$ ratio decreases, the characteristic life η reduces. In other words, the time when there is a 63.2% chance of failure reduces. For the shape parameter β, the values are always greater than 1 for any value of $B_{inspected}/B_{total}$, which always justifies preventive maintenance. If the value of the shape parameter is greater than 1 (i.e., the component is in the wear-out region), the variability on this parameter may not necessarily be a cause of concern (Reliasoft 2019), as much as the variability is in the scale parameter in this case.

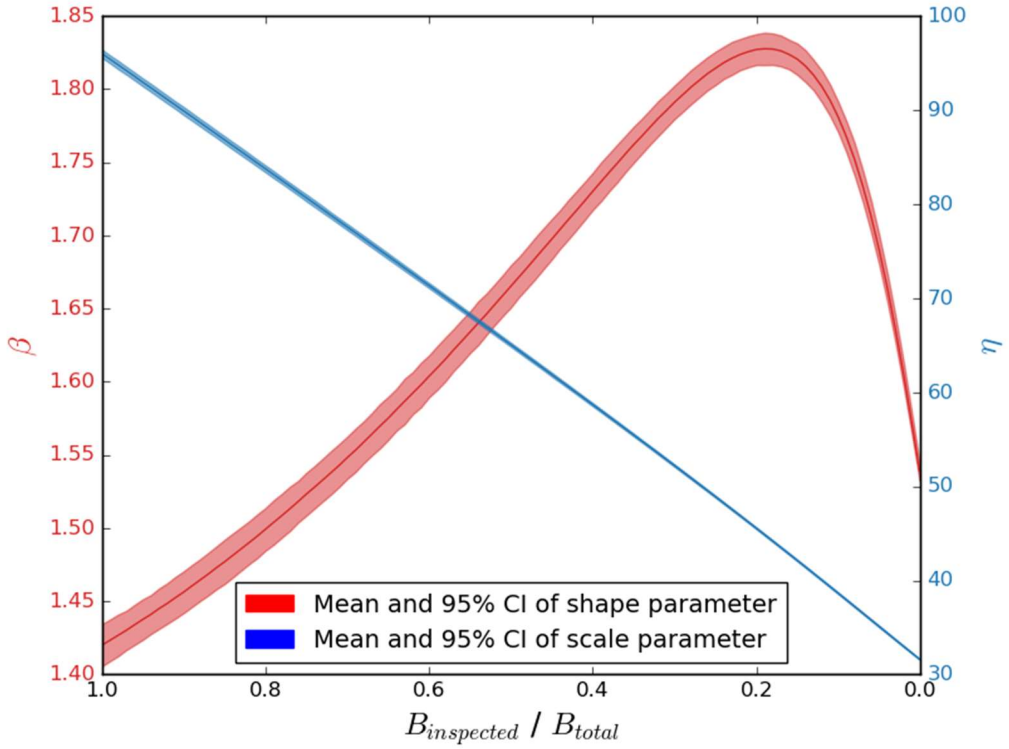

Figure 3.9: Variability of Weibull parameters

Fig. 3.10 shows the standard deviation of the assumed zero mean error. Interestingly, as the ratio $B_{\text{inspected}}/B_{\text{total}}$ decreases, the fitting with a Weibull distribution improves.

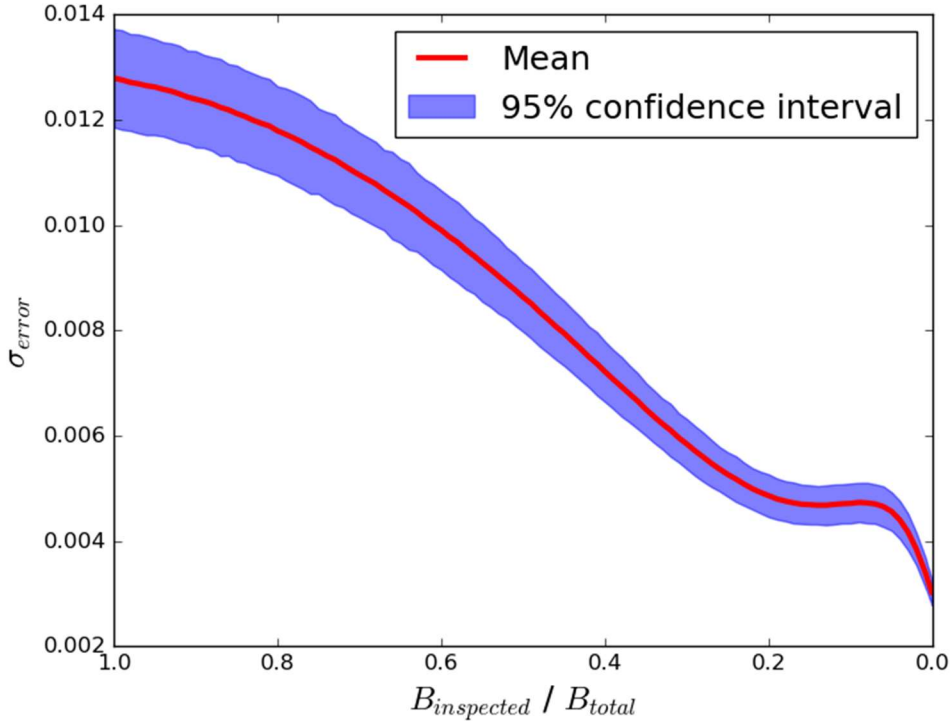

Figure 3.10: Standard deviation of the zero-mean error

3.5.2. Static optimal Maintenance Based on Failure Prognosis

Based on the unreliability function *F(t)*, the optimal maintenance time can be found by minimizing the cost function proposed by (Barlow and Hunter 1960) to find the cost per unit of time (*CPUT*) of performing preventive maintenance at time *t* (in years) as follows:

$$CPUT(t) = \frac{C_p[1-F(t)] + C_u[F(t)]}{\int_{s=0}^{s=t}[1-F(s)]ds}, \tag{3.12}$$

where C_p is the preventative action cost, and C_u is the unplanned action cost. The denominator of Eq. (3.12) represent mean time between maintenance actions. Note that Eq. (3.12) has more meaning when the cost ratios, C_u / C_p, are considerably greater than 1,

otherwise the numerator would behave as a constant function. Fig. 3.11 shows the *CPUT* computed for different cost ratios C_u / C_p, without considering the previously discussed uncertainty in the "*B*" ratings. For some miter gate, it was suggested by USACE personnel that the corresponding cost ratio is close to 5 based on cost data from lock 14 (located in the Arkansas river) (Schultz 2018), which would result in a $t_{optimal}$ of about 48 years implied by Fig. 3.11 if that were the case.

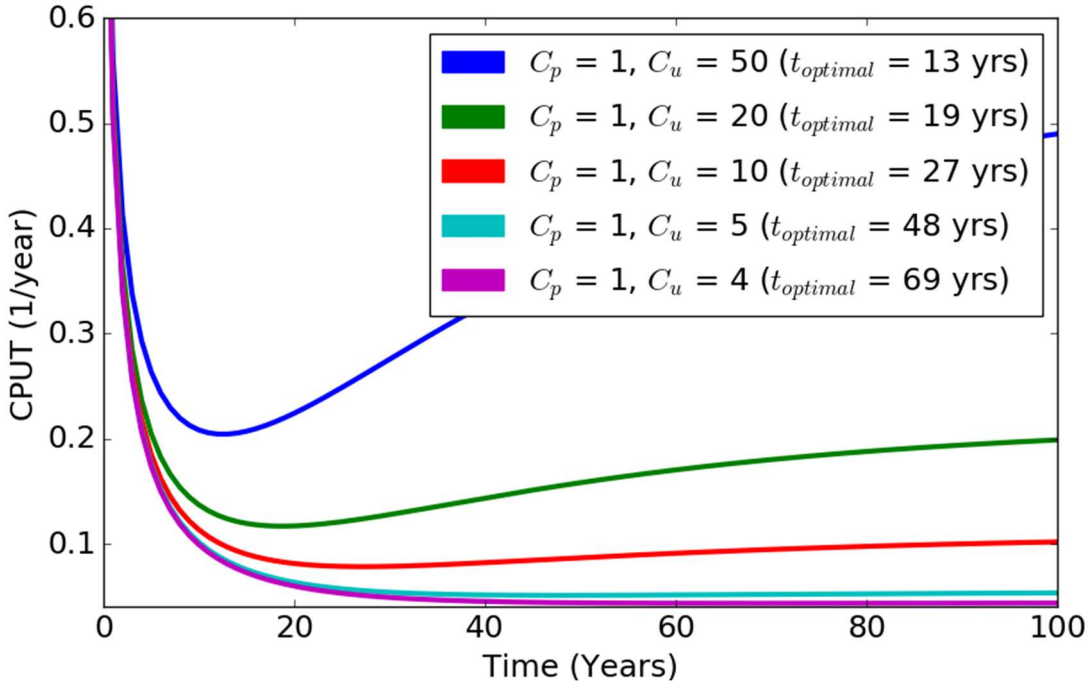

Figure 3.11: *CPUT* based on transition matrix with $B_{inspected}/B_{total} = 1$.

To understand the advantage and cost savings, the CPUT value at the optimal value is compared with the CPUT at other repair/replacement times, which can represent the average time that USACE regularly performs maintenance on quoin blocks. Fig. 3.12 shows the percentage savings using the optimal maintenance as a function of the average actual maintence time cycle. Note that if the actual maintenance time is already at its optimum, the percentage of savings is equal to 0%.

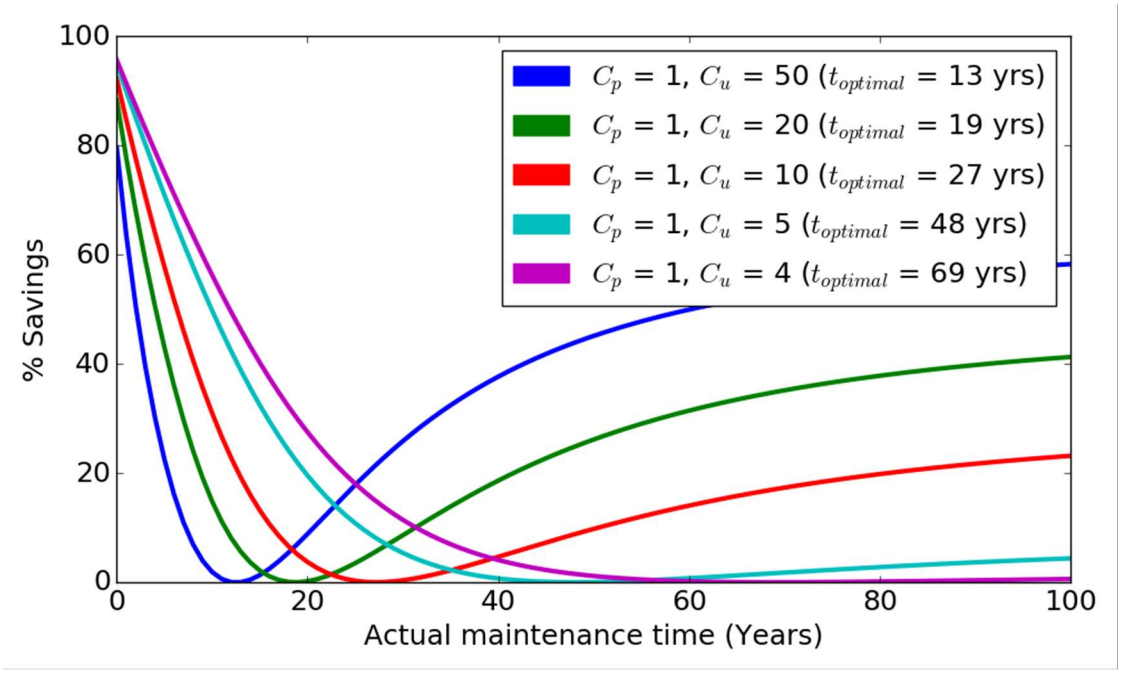

Figure 3.12: % Savings based on actual maintenance time

Fig. 3.13 shows the *CPUT* computed for different cost ratios when considering the uncertainty in the "*B*" rating in a given year. The results clearly show a lot of variability in the *CPUT*, and consequently in the optimal time to perform maintenance (i.e., the time when *CPUT* is minimized). For example, the minimum *CPUT* varies from 0.05 to 0.15 for $C_u / C_p = 5$, which is an increment of 200%. Note that the variability is larger as the cost ratio increases.

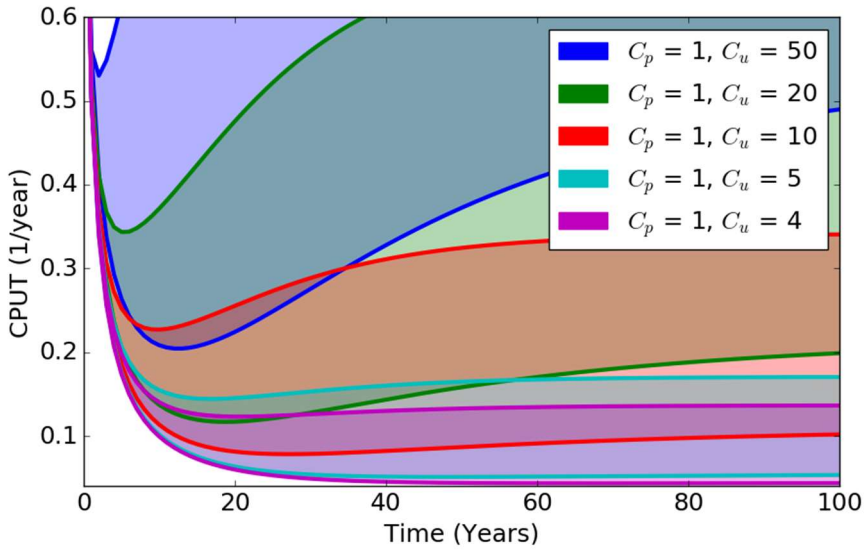

Figure 3.13: CPUT with $B_{inspected}/B_{total}$ from 0 (upper curves) to 1 (lower curves).

Fig. 3.14 shows the variability in the optimal maintenance time (between 16 and 48 years) when the cost ratio is equal to 5 (the USACE miter gate case). The variability is more pronounced when the cost ratio is small as shown in Fig. 3.15. The modal values at the ends represent the $t_{optimal}$ (at minimum CPUT) when $B_{inspected}/B_{total}$ approaches to 0 and 1 in the left and right end respectively. The reason is because as the $B_{inspected}$ (due to $B_{inspected}/B_{total} = 1$) approaches a large value, the normalized value in the transition matrix is still a large value. In other words, the transition probability, $P\left(B_{t+1}|B_t\right)$, is closer to 1 and larger relatively to the other transition probabilities from B_t (i.e. $P\left(A_{t+1}|B_t\right)$, $P\left(C_{t+1}|B_t\right)$, $P\left(D_{t+1}|B_t\right)$, $P\left(F_{t+1}|B_t\right)$ and $P\left(CF_{t+1}|B_t\right)$). Therefore, the normalized values in the transition matrix do not change as much, and consequently the $t_{optimal}$ does not change as much. Similar behavior is observed when $B_{inspected}$ (due to $B_{inspected}/B_{total} = 0$) approaches to 0. Except that, $P\left(B_{t+1}|B_t\right)$, is closer to 0 and smaller relative to the other transition probabilities.

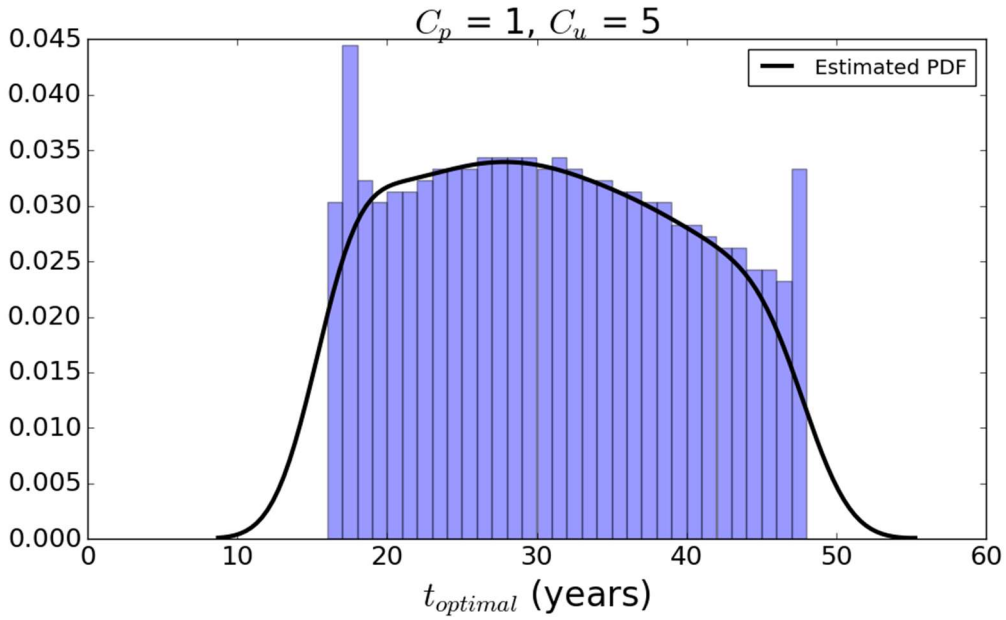

Figure 3.14: Variability in optimal maintenance time for $C_u/C_p = 5$

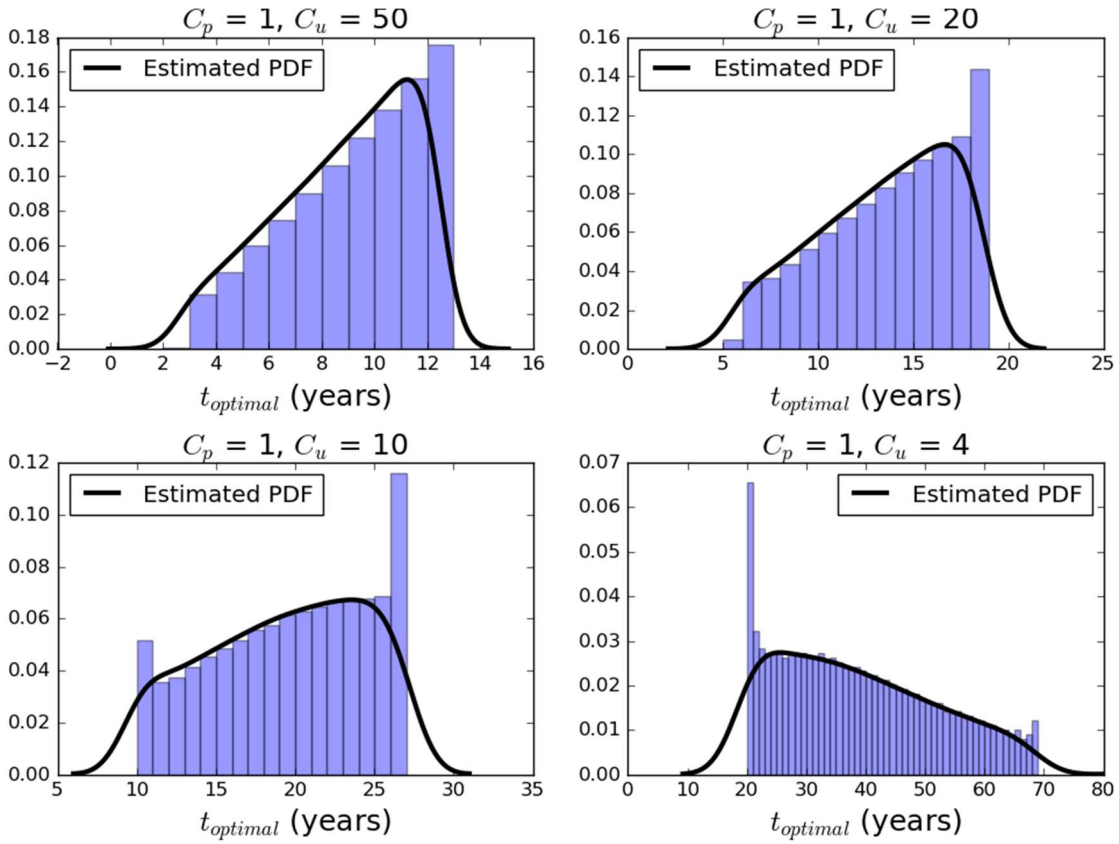

Figure 3.15: Variability in optimal maintenance time for different cost ratios

Table 3.1 summarizes the statistics of the time variability shown in Figures 3.14 and 3.15. Based on these statistics, the average optimal maintenance time considering only the reliability of quoin block in miter gates would be almost 31 years. As mentioned earlier, the cost ratio for lock 14 is close to 5, so an interpolation can be made for the optimal maintenance between 4 and 5 if needed. Also, the reason why larger cost ratio values (e.g. 10, 20 and 50) were considered is because miter gates in the Mississippi river or other rivers would have higher traffic demands than lock 14. In other words, the downtime cost for these gates will logically be increased (C_u would be larger).

Table 3.1: Optimal maintenance time (years) statistics

Cp/Cu	Mean	SD	Max	Min
50	8.82	2.59	13	2
20	13.47	3.60	19	5
10	19.27	4.99	27	10
5	30.75	9.09	48	16
4	38.52	13.48	69	20

Up to this point the maintenance planning has been depending only on the historical inspection data (i.e. field OCA ratings). However, current state (or damage) estimation can enable dynamic decision making, which may lead to reduced lifecycle cost. To achieve this, Sec. 3.6 proposes the integration of diagnostic models (i.e. physics-based FE modeling) and historical inspection data (i.e. field OCA ratings). As mentioned before, the following section formulates the integration of failure diagnosis and prognosis to achieve on-line planning and updating.

3.6. Integration of Damage Diagnosis and Failure Prognosis for Dynamic Maintenance Planning of Miter Gates

As demonstrated in Sec. 3.5, optimal maintenance highly depends on the evolution of the damage, e.g., how fast the probability of "*CF*" changes with time. Ideally, a degradation model of every damage level present in every component in the gate would facilitate the maintenance decision-making process. However, sometimes there is not a clear understanding of how the damage evolves with time. For example, such is the case with miter gates, where it is not understood how the bearing gaps change in time. This is one motivation for integrating SHM with the Markov transition matrix. Figure 3.16 shows more details of the proposed framework to integrate SHM with the Markov transition matrix. As shown in this figure, the proposed framework first estimates the damage sate (i.e. gap length) using online SHM data. The estimated gap length

is then used to update the error ratio in the "B" ratings. Based on that, the Markov transition matrix is updated, which will be used for failure prognosis and dynamical optimal maintenance planning. In what follows, each element of the proposed framework is explained in detail.

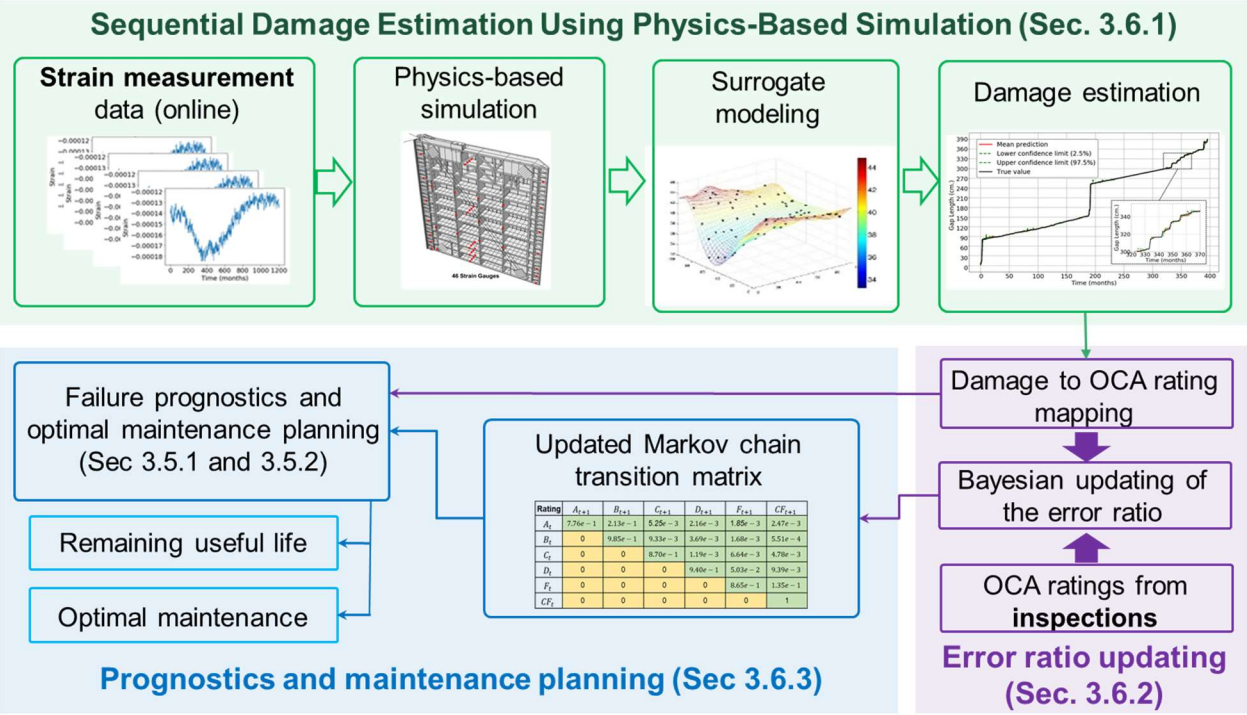

Figure 3.16: Overview of the proposed framework

3.6.1 Sequential damage estimation using physics-based simulation

Let $\mathbf{s}_i = [s_{i1}, s_{i2}, \cdots, s_{iN_S}]$ be the strain measurement data at time step t_i, where N_S is the number of strain sensors, the posterior probability density function of the gap length h_n at time step t_n conditioned on strain measurements $\mathbf{s}_{1:n} \triangleq \{\mathbf{s}_1, \mathbf{s}_2, \cdots, \mathbf{s}_n\}$ collected up to t_n is given by

$$f(h_n \mid \mathbf{s}_{1:n}) = \frac{f(\mathbf{s}_n \mid h_n) f(h_n \mid \mathbf{s}_{1:n-1})}{\int f(\mathbf{s}_n \mid h_n) f(h_n \mid \mathbf{s}_{1:n-1}) dh_n} \propto f(\mathbf{s}_n \mid h_n) f(h_n \mid \mathbf{s}_{1:n-1}), \tag{3.13}$$

where $f(h_n \mid \mathbf{s}_{1:n-1})$ is given by

$$f(h_n \mid \mathbf{s}_{1:n-1}) = \int f(h_n \mid h_{n-1}) f(h_{n-1} \mid \mathbf{s}_{1:n-1}) dh_{n-1}, \tag{3.14}$$

with $f(\mathbf{s}_n \mid h_n)$ being the likelihood function (from the measurement equation) of observing $\mathbf{s}_n$ for given h_n at time step t_n, and $f(h_n \mid h_{n-1})$ is the PDF of h_n for a given h_{n-1} obtained from the state equation which describes the damage evolution over time.

As illustrated in Fig. 3.16, the physics-based simulation model is employed as the measurement equation in this chapter. The likelihood function $f(\mathbf{s}_n \mid h_n)$, assuming that the observations $\mathbf{s}_n$ are statistically independent, is computed by

$$f(\mathbf{s}_n \mid h_n) = \prod_{j=1}^{N_S} \phi\left(\frac{s_{nj} - \mu_{sj}(h_n)}{\sigma_\varepsilon}\right), \tag{3.15}$$

where $\phi(\cdot)$ is the PDF of the standard normal distribution, σ_ε is the standard deviation of the observation noise, and $\mu_{sj}(h_n)$ is the mean strain response prediction at the location of the *j*-th sensor obtained from the physics-based simulation.

Since the physics-based computer simulation model is used to predict $\mu_{sj}(h_n), \forall j = 1, 2, \cdots, N_S$ and the likelihood function $f(\mathbf{s}_n \mid h_n)$ needs to be evaluated numerous times during the sequential damage estimation, this is computationally burdensome. To address this challenge, a surrogate model is constructed for the strain response at N_S strain locations as . $\mathbf{s} = [s^{(1)}, s^{(2)}, \cdots, s^{(N_S)}] = \hat{g}_h(\mathbf{x})$., where $s^{(j)}$, $j = 1, 2, \cdots, N_S$ is the strain response prediction at the *j*-th sensor location and $\mathbf{x} = [h, \boldsymbol{\theta}]$ including the gap length (h) and other model parameters ($\boldsymbol{\theta}$) such as hydrostatic and thermal loads applied to miter gates.

To build such a surrogate model and tackle the challenge of the high-dimensional output during surrogate modelling, *N* training points are first generated for $\mathbf{x}$ and are denoted as

$\mathbf{x}_t \triangleq \{\mathbf{x}_1, \mathbf{x}_2, \cdots, \mathbf{x}_N\}$. From physics-based simulations, a data matrix of the strain responses for N training points is obtained as below

$$\begin{aligned}\mathbf{w} &= [\mathbf{w}(\mathbf{x}_1), \mathbf{w}(\mathbf{x}_2), \ldots, \mathbf{w}(\mathbf{x}_N)]^T \\ &= \begin{bmatrix} w(1, \mathbf{x}_1) & w(1, \mathbf{x}_2) & \cdots & w(1, \mathbf{x}_N) \\ w(2, \mathbf{x}_1) & w(2, \mathbf{x}_2) & \cdots & w(2, \mathbf{x}_N) \\ \vdots & \vdots & \ddots & \vdots \\ w(N_S, \mathbf{x}_1) & w(N_S, \mathbf{x}_2) & \cdots & w(N_S, \mathbf{x}_N) \end{bmatrix}^T \in \mathbb{R}_{N \times N_S},\end{aligned} \tag{3.16}$$

where $\mathbf{w}(\mathbf{x}_i) = [w(1, \mathbf{x}_i), w(2, \mathbf{x}_i), \cdots, w(N_S, \mathbf{x}_i)]^T \in \mathbb{R}_{N_S \times 1}$ is the strain response with inputs $\mathbf{x}_i, \forall i = 1, 2, \cdots, N_S$, $w(j, \mathbf{x}_i)$ is the strain response at the *j*-th sensor location, and N_S is the number of sensors as discussed before.

The data matrix $\mathbf{w}$ shown above is then compressed using singular value decomposition (SVD) as

$$\mathbf{w} = \mathbf{V}\mathbf{M}\mathbf{U}^T, \tag{3.17}$$

where $\mathbf{V}$ is a $N \times N$ orthogonal matrix, $\mathbf{U}$ is a $N_S \times N_S$ orthogonal matrix and $\mathbf{M}$ is a $N \times N_S$ rectangular diagonal matrix with non-negative real numbers $\boldsymbol{\lambda} = [\lambda_1, \lambda_2, \ldots, \lambda_k]$ on the diagonal, in which k is minimum of N and N_S.

Defining another matrix as $\boldsymbol{\gamma} = \mathbf{V}\mathbf{M}$, the original data matrix $\mathbf{w}$ can be reconstructed

$$\mathbf{w}(\cdot, \mathbf{x}_i)^T \approx \sum_{j=1}^{r} \gamma_{ij} \mathbf{U}_j, \tag{3.18}$$

where $\boldsymbol{\gamma}_{i:} = [\gamma_{i1}, \gamma_{i2}, \cdots, \gamma_{ir}]$ is the *i*-th row of $\boldsymbol{\gamma}$, $\mathbf{w}(\cdot, \mathbf{x}_i)^T$ is the *i*-th row of $\mathbf{w}$, γ_{ij} is the element of $\boldsymbol{\gamma}$ at *i*-th row and *j*-th column, $\mathbf{U}_j$ is the *j*-th important feature vector used to approximate $\mathbf{w}$, and *r* is the number of features retained in the decomposition.

Eq. (3.18) shows that the variation in the high-dimensional response across the design domain mainly comes from the variation in $\boldsymbol{\gamma}_{i:} = [\gamma_1(\mathbf{x}_i), \gamma_2(\mathbf{x}_i), \cdots, \gamma_r(\mathbf{x}_i)]$, which denotes the value of γ for *i*-th training point. With the training points of $\boldsymbol{\gamma}_{i:} = [\gamma_1(\mathbf{x}_i), \gamma_2(\mathbf{x}_i), \cdots, \gamma_r(\mathbf{x}_i)]$ and $\mathbf{x}_i$, $i = 1, 2, \cdots, N$, a surrogate models is constructed for $\gamma_1, \gamma_2, \cdots,$ and γ_r as $\hat{\gamma}_j = \hat{g}_j(\mathbf{x}), \forall j = 1, 2, \cdots, r$ using the Kriging surrogate modelling method. In Kriging surrogate modelling, $\hat{\gamma}_j = \hat{g}_j(\mathbf{x})$ is approximated as

$$\hat{\gamma}_j = \hat{g}_j(\mathbf{x}) = \mathbf{f}(\mathbf{x})^T \boldsymbol{\alpha} + Z(\mathbf{x}), \tag{3.19}$$

where $\boldsymbol{\alpha}$ are coefficients of the trend function $\mathbf{f}(\mathbf{x})^T$, and $Z(\mathbf{x}) \sim N(0, \sigma_{GP}^2 \rho(\bullet, \bullet))$ is a stationary Gaussian process with correlation function $\rho(\bullet, \bullet)$ between the responses at any two points given by

$$\rho(\mathbf{x}, \mathbf{x}') = \exp\left\{-\sum_{l=1}^{N_V} \omega_l (x_l - x_l')^2\right\}, \tag{3.20}$$

in which N_V is the number of variables, and $\boldsymbol{\omega} = (\omega_1, \ldots, \omega_{N_V})^T$ is a vector of roughness parameters.

The hyper-parameters $\boldsymbol{\upsilon} = \left(\boldsymbol{\alpha}, \sigma_{GP}^2, \boldsymbol{\omega}\right)$ can be estimated using the maximum likelihood estimation method (used in this chapter) or the least-squares method. After the estimation of the hyper-parameters $\boldsymbol{\upsilon}$, for any given inputs $\mathbf{x}$, the GP prediction is a Gaussian random variable given by

$$\hat{\gamma}_j = \hat{g}_j(\mathbf{x}) \sim N(\mu_j(\mathbf{x}), \sigma_j^2(\mathbf{x})), \forall j = 1, 2, \cdots, r, \tag{3.21}$$

where $\mu_j(\mathbf{x})$ and $\sigma_j^2(\mathbf{x})$ are respectively the mean and variance of the prediction of γ_j at input $\mathbf{x}$. Combining Eqs. (3.18) and (3.21), the strain response in the original space (i.e. strain at N_s locations) of the kriging surrogate model can be expressed as

$$[\hat{w}(1, \mathbf{x}), \hat{w}(2, \mathbf{x}), \cdots, \hat{w}(N_s, \mathbf{x})] = \sum_{j=1}^{r} \hat{g}_j(\mathbf{x})\mathbf{U}_j. \tag{3.22}$$

For any given $\mathbf{x} = [h, \boldsymbol{\theta}]$, the prediction of the strain response in the original space is given by

$$\hat{w}(i, \mathbf{x}) \sim N(\mu_w(i, \mathbf{x}), \sigma_w^2(i, \mathbf{x})), \forall i = 1, 2, \cdots, N_S, \tag{3.23}$$

where $\mu_w(i, \mathbf{x}) = \sum_{j=1}^{r} \mu_j(\mathbf{x})U_j(i)$ and $\sigma_w(i, \mathbf{x}) = \sqrt{\sum_{i=1}^{r} \sigma_j^2(\mathbf{x})U_j^2(i)}$. The covariance of $\hat{w}(i, \mathbf{x})$ and $\hat{w}(k, \mathbf{x})$ is given by

$$\Sigma_{ik} = \sum_{j=1}^{r} \sigma_j^2(\mathbf{x})U_j(i)U_j(k), \forall i, k = 1, 2, \cdots, N_S. \tag{3.24}$$

For sensor locations $i = k$, after considering uncorrelated and unbiased observation noise, the diagonal entries of the covariance matrix become

$$\Sigma_{ii} = \sum_{j=1}^{r} \sigma_j^2(\mathbf{x})U_j^2(i) + \sigma_\varepsilon^2, \forall i = 1, 2, \cdots, N_S. \tag{3.25}$$

After substituting the original physics-based simulation with the surrogate model as discussed above, the likelihood function $f(\mathbf{s}_n \mid h_n)$ in the sequential damage estimation is computed by

$$f(\mathbf{s}_n \mid h_n) = \frac{\exp\left(-0.5(\mathbf{s}_n - \boldsymbol{\mu}_w)^T \boldsymbol{\Sigma}^{-1}(\mathbf{s}_n - \boldsymbol{\mu}_w)\right)}{\sqrt{(2\pi)^{N_S}\left|\boldsymbol{\Sigma}\right|}}, \tag{3.26}$$

where the mean and covariance terms are given by $\boldsymbol{\mu}_w = [\mu_w(1, \mathbf{x}), \mu_w(2, \mathbf{x}), \cdots, \mu_w(N_S, \mathbf{x})]$ and $\boldsymbol{\Sigma} = \{\Sigma_{ik}, \forall i, k = 1, 2, \cdots, N_S\}$, computed by plugging h_n into Eqs. (3.21) and (3.22).

From Eqs. (3.15) to (3.26), the computation of $f(\mathbf{s}_n \mid h_n)$ has been discussed in the sequential damage estimation using a physics-based simulation model. As indicated in Eqs. (3.13) and (3.14), an important step in the sequential damage estimation is the evaluation of $f(h_n \mid h_{n-1})$, which is usually based on the state equation of the damage propagation. As mentioned previously, however, the degradation mechanism of the miter gate is complicated and not fully understood; there is no appropriate physics-based degradation model available that can adequately describe the growth of the gap. The only known information is that the gap will grow over time (no self-repair/replace). In this situation, the following minimally informed state equation is employed

$$h_n = h_{n-1} + \varepsilon_h, \tag{3.27}$$

in which ε_h is a sufficiently large process noise term that imposes random gap growth over time, i.e., gap growth is a random walk. Since the gap can only grow over time, a Weibull process noise with a shape parameter of 0.5 and a scale parameter of 1.2 is used in this chapter which is able to cover a wide range (from 0 to 228 cm) of gap growth rate.

By recursively implementing Eqs. (3.13) and (3.14), the miter gate gap length is estimated based on the online strain measurement data. In this chapter, the particle filtering (PF) method (M. Orchard et al. 2008) is employed to perform the sequential damage estimation through the online strain measurement and the physics-based simulation. Let the particles from the (n-1)-th time step after performing prediction using the state equation be $\mathbf{h}_n = [h_{n1}, h_{n2}, \cdots, h_{nN_p}]$, where is the

number of particles in particle filtering, the posterior distribution at the *n*-th time step is obtained by resampling the particles according to the following weights

$$\chi_i = \frac{f(\mathbf{s}_n \mid h_{ni})}{\sum_{i=1}^{N_p} f(\mathbf{s}_n \mid h_{ni})}, \forall i = 1, 2, \cdots, N_p \tag{3.28}$$

where $f(\mathbf{s}_n \mid h_{ni})$ is obtained by plugging h_{ni} into Eq. (3.26).

As being shown in Sec. 3.7.2, the state equation given in Eq. (3.27) allows for effective damage estimation through sequential Bayesian inference. Let the distribution parameters of ε_h be λ_h and κ_h, where λ_h is the scale parameter of Weibull distribution and κ_h is the shape parameter of the distribution, if the state equation given in Eq. (3.27) is used for prognosis, the gap length h_m after m months ($m > 30$, prognosis over 30 months) can be approximated as a normal distribution as below according to the central limit theorem

$$H_m \sim N(h_n + m\mu_\varepsilon, m\sigma_\varepsilon^2), \tag{3.29}$$

where H_m stands for a random gap length, h_m is a specific realization of H_m, h_n is the current gap length, $\mu_\varepsilon = \lambda_h \Gamma(1+1/\kappa_h)$ and $\sigma_\varepsilon^2 = \lambda_h^2 \left[\Gamma(1+2/\kappa_h) - \left(\Gamma(1+1/\kappa_h) \right)^2 \right]$ are respectively the mean and variance of ε_h.

The probability that the remaining useful life (RUL), T_R, is less than a specific value q, is then given by

$$\Pr\{T_R < q\} = \Pr\{h_q > h_e\} = 1 - \Phi\left(\frac{h_e - (h_n + q\mu_\varepsilon)}{\sqrt{q}\sigma_\varepsilon} \right), \tag{3.30}$$

in which h_e is the gap failure threshold (i.e., 381 cm. this chapter).

Based on the above equation, the $(1-\alpha)$ confidence interval of the RUL conditioned on the current gap length h_n is derived as

$$\left[T_{1-\alpha/2}, T_{\alpha/2} \mid h_n\right] = \frac{2\mu_\varepsilon(h_e - h_n) + (\Phi^{-1}(\alpha/2))^2\sigma_\varepsilon^2}{2\mu_\varepsilon^2} \pm \frac{T_\varepsilon}{2\mu_\varepsilon^2}, \tag{3.31}$$

where T_ε is given by

$$T_\varepsilon = \sqrt{\left[2\mu_\varepsilon(h_e - h_n) + (\Phi^{-1}(\alpha/2))^2\sigma_\varepsilon^2\right]^2 - 4\mu_\varepsilon^2(h_e - h_n)^2}. \tag{3.32}$$

The unconditional $(1-\alpha)$ confidence interval of the RUL can then be computed by

$$T_{\alpha/2} = \int f(h_n \mid \mathbf{s}_{1:n})\left[T_{\alpha/2} \mid h_n\right] dh_n, \tag{3.33}$$

in which $f(h_n \mid \mathbf{s}_{1:n})$ is the posterior distribution of h_n obtained from the damage diagnosis.

If the state equation given in Eq. (3.27) is accurate, the above equations allow to analytically estimate the RUL. Due to the large process noise ε_h and the discrepancy between the state equation and the underlying unknown degradation model, Eq. (3.27) could lead to large error in the remaining useful life (RUL) estimation when it is applied to the failure prognosis (see the result in Sec. 3.7.3). Therefore, the state equation Eq. (3.27) cannot be used for optimal maintenance planning. Motivated to overcome this limitation, the physics-based damage estimation is integrated with the Markov transition matrix in the subsequent sections for (1) updating of the error ratios in the "B" ratings, and (2) failure prognosis of the miter gate based on SHM and transition matrix.

3.6.2 Updating of "B" ratings error ratio based on online damage estimation

As been shown in Secs. 3.5.1 and 3.5.2, the uncertainty in $B_{\text{inspected}}/B_{\text{total}}$ could significantly affect the failure prognosis results and maintenance planning. In order to reduce the uncertainty

using the damage estimation technique developed in Sec. 3.6.1, a mapping of the estimated gap length h_n on to an OCA rating is performed as follows:

$$I_n = I_{OCA}(h_n) = \begin{cases} I_{1,n}, & h_n \in [e_0, e_1) \\ I_{2,n}, & h_n \in [e_1, e_2) \\ I_{3,n}, & h_n \in [e_2, e_3) \\ I_{4,n}, & h_n \in [e_3, e_4) \\ I_{5,n}, & h_n \in [e_4, e_5) \\ I_{6,n}, & h_n \geq e_5 \end{cases}, \tag{3.34}$$

where $I_n = I_{OCA}(h_n)$ is a function that maps a gap length h_n to an OCA rating I_n at time step t_n, and $e_j, j = 0, 1, \cdots, 5$ are the gap length thresholds used to partition the gap domain into OCA ratings.

In order to use the estimated OCA ratings to update the error ratio of the "B" ratings, the variable $B_{\text{inspected}}/B_{\text{total}}$ is defined as $\gamma = B_{\text{inspected}} / B_{\text{total}}$. γ is then updated using Bayesian method based on the damage estimation as follows

$$f_{\gamma|I}(\gamma \,|\, \mathbf{I}_{1:n}) = \frac{f_{I|\gamma}(\mathbf{I}_{1:n} \,|\, \gamma) f_{\gamma}(\gamma)}{\int f_{I|\gamma}(\mathbf{I}_{1:n} \,|\, \gamma) f_{\gamma}(\gamma) d\gamma} \propto f_{I|\gamma}(\mathbf{I}_{1:n} \,|\, \gamma) f_{\gamma}(\gamma), \tag{3.35}$$

in which $\mathbf{I}_{1:n} \triangleq [I_1, I_2, \cdots, I_n]$ are the estimated OCA ratings of time steps t_1 to t_n from the SHM system by mapping the estimated gap lengths into OCA ratings using Eq. (3.34), $f_{\gamma}(\gamma)$ is the prior distribution of γ, the non-informative uniform distribution $\gamma \sim \mathrm{U}(0, 1)$ is used in this chapter (i.e. $f_{\gamma}(\gamma) = 1$), and $f_I(\mathbf{I}_{1:n} \,|\, \gamma)$ is the likelihood function of observing $\mathbf{I}_{1:n}$ for given γ.

Since the estimated $\mathbf{I}_{1:n} \triangleq [I_1, I_2, \cdots, I_n]$ are uncertain due to the uncertainty in $h_i, i = 1, 2, \cdots, n$, Eq. (3.35) is rewritten as follows by considering the uncertainty in $\mathbf{I}_{1:n}$

$$f_{\gamma|I}(\gamma \mid \mathbf{I}_{1:n}) = \sum_{\mathbf{I}_{obs}} f_{\gamma|I}(\gamma \mid \mathbf{I}_{obs}) P\{\mathbf{I}_{1:n} = \mathbf{I}_{obs}\}, \tag{3.36}$$

where $\mathbf{I}_{obs}$ is an observation realization of $\mathbf{I}_{1:n} \triangleq [I_1, I_2, \cdots, I_n]$ obtained from the physics-based damage estimation in Sec. 3.6.1, and $f_{\gamma|I}(\gamma \mid \mathbf{I}_{obs})$ is given by

$$f_{\gamma|I}(\gamma \mid \mathbf{I}_{obs}) \propto f_{I|\gamma}(\mathbf{I}_{obs} \mid \gamma) f_{\gamma}(\gamma). \tag{3.37}$$

Defining the posterior samples of gap length from Sec. 3.6.1 as h_{jk}, $\forall j = 1, 2, \cdots, n; k = 1, 2, \cdots, N_p$; (see Eq. (3.28) in Sec. 3.6.1), where N_p is the number of particles in particle filtering and h_{jk} is the *k*-th particle at time step t_j. Using the posterior samples from t_1 to t_n, Eq. (3.36) is approximated as

$$f_{\gamma|I}(\gamma \mid \mathbf{I}_{1:n}) \approx \frac{1}{N_p} \sum_{k=1}^{N_p} f_{\gamma|I}(\gamma \mid \mathbf{h}_{\bullet k}), \tag{3.38}$$

where $\mathbf{h}_{\bullet k} \triangleq [h_{1k}, h_{2k}, \cdots, h_{nk}]$ is the *k*-th realization of the gap length estimation, and $f_{\gamma|I}(\gamma \mid \mathbf{h}_{\bullet k})$ is given by

$$f_{\gamma|I}(\gamma \mid \mathbf{h}_{\bullet k}) \propto f_{I|\gamma}(\mathbf{h}_{\bullet k} \mid \gamma) f_{\gamma}(\gamma), \tag{3.39}$$

in which

$$f_{I|\gamma}(\mathbf{h}_{\bullet k} \mid \gamma) = \prod_{j=1}^{n} f_{I|\gamma}(h_{jk} \mid \gamma). \tag{3.40}$$

The $f_{I|\gamma}(h_{jk} \mid \gamma)$ is computed based on the OCA rating transition matrix as

$$f_{I|\gamma}(h_{jk} \mid \gamma) = P(I_{OCA}(h_{jk}), \gamma), \forall j = 1, 2, \cdots, n, \tag{3.41}$$

where $P(I_{OCA}(h_{jk}), \gamma)$ is an element of $\mathbf{P}_{(j)}(\gamma)$ with index of the element determined by $I_{OCA}(h_{jk})$ given in Eq. (3.34).

$\mathbf{P}_{(j)}(\gamma)$ is obtained using a transition matrix conditioned on γ (see Secs. 3.4.2 and 3.5.1.2) as follows

$$\mathbf{P}_{(j)}(\gamma)=[P(I_{1,j},\gamma),P(I_{2,j},\gamma),\cdots,P(I_{6,j},\gamma)]=P(\mathbf{I}_0)\cdot\mathbf{P}_M^j(\gamma), \tag{3.42}$$

in which $\mathbf{P}_M^j(\gamma)$ is a modified transition matrix to account for the difference in the time scales of the SHM system and the 1-year transition matrix obtained from inspection data. For instance, in this chapter the time scale of the SHM system is in months; therefore, $\mathbf{P}_M^j(\gamma)=(\mathbf{P}(\gamma))^{1/12}$ in which $\mathbf{P}(\gamma)$ is obtained by following the procedure depicted in Fig. 3.3 and setting $B_{\text{inspected}}/B_{\text{total}}=\gamma$.

Using Eqs. (3.36) through (3.42), the error ratio of the "B" ratings can be updated over time based on the SHM damage estimations. Next, it is discussed how to perform failure prognostics and maintenance planning based on the updating.

3.6.3 Failure prognosis and dynamic optimal maintenance planning

As indicated in Fig. 3.16, the above sequential damage estimation (using physics-based simulation in Sec. 3.6.1) and the updating of the error ratio (Sec. 3.6.2) are integrated with the transition matrix to overcome the challenge that there is no degradation model available for failure prognosis. To achieve this purpose, the probability mass function (PMF) of a certain OCA rating is computed based on the posterior distribution of the gap length obtained from physics-based damage estimation (Sec. 3.6.1) and the mapping from gap length to OCA rating in Eq. (3.34). Taking the OCA rating "$I_{i,n}$" (i.e. the OCA rating is *i* at time step t_n) as an example, the PMF of "$I_{i,n}$" conditioned on the strain observations $\mathbf{s}_{1:n}$ collected up to current time step t_n, is given by

$$P(I_{i,n} \mid \mathbf{s}_{1:n}) = \Pr\left\{I_n = I_{i,n} \mid \mathbf{s}_{1:n}\right\} = \begin{cases} \int_{e_{i-1}}^{e_i} f(h_n \mid \mathbf{s}_{1:n}) dh_n, \text{ if } i \le 5 \\ \int_{e_{i-1}}^{\infty} f(h_n \mid \mathbf{s}_{1:n}) dh_n, \text{ otherwise} \end{cases}, \forall i = 1, \cdots, 6, \tag{3.43}$$

in which $\Pr\{\cdot\}$ is the probability operator and $f(h_n \mid \mathbf{s}_{1:n})$ is the posterior distribution obtained from damage estimation as discussed in Sec. 3.6.1.

Since particle filtering method is employed, the PMF $P(I_{i,n} \mid \mathbf{s}_{1:n})$ is approximated as

$$P(I_{i,n} \mid \mathbf{s}_{1:n}) = \Pr\left\{I_n = I_{i,n} \mid \mathbf{s}_{1:n}\right\} \approx \frac{\sum_{k=1}^{N_p} \Lambda(h_{nk})}{N_p}, \forall i = 1, \cdots, 6, \tag{3.44}$$

where $h_{nk}, k = 1, 2, \cdots, N_p$ are the posterior samples at t_n, $\Lambda(h_{nk}) = 1$, if $I_{OCA}(h_{nk}) = I_{i,n}$ and $\Lambda(h_{nk}) = 0$, otherwise.

Based on the above equation, the PMF of all COA ratings conditioned on $\mathbf{s}_{1:n}$ can be expressed as

$$P(\mathbf{I}_n \mid \mathbf{s}_{1:n}) = [P(I_{1,n} \mid \mathbf{s}_{1:n}), P(I_{2,n} \mid \mathbf{s}_{1:n}), ..., P(I_{6,n} \mid \mathbf{s}_{1:n})]. \tag{3.45}$$

Combining Eqs. (3.45) and (3.3), the OCA rating after *m* time steps conditioned on current strain observations ($\mathbf{s}_{1:n}$) and given value of the error ratio γ is given by

$$P\left(\mathbf{I}_{n+m} \mid \mathbf{s}_{1:n}, \gamma\right) = P\left(\mathbf{I}_n \mid \mathbf{s}_{1:n}\right) \cdot \mathbf{P}^m(\gamma), \tag{3.46}$$

where $\mathbf{P}(\gamma)$ is the transition matrix given in Fig. 3.3 for given $B_{\text{inspected}} / B_{\text{total}} = \gamma$.

The cumulative density function (CDF) of the remaining useful life is then computed as

$$\begin{aligned} \Pr\{RUL \le m \mid \mathbf{s}_{1:n}\} &= \int \Pr\{RUL \le m \mid \mathbf{s}_{1:n}, \gamma\} f_{\gamma|I}(\gamma \mid \mathbf{I}_{1:n}) d\gamma, \\ &= \int F_{t|\mathbf{s}_{1:n}}(m, \gamma) f_{\gamma|I}(\gamma \mid \mathbf{I}_{1:n}) d\gamma, \\ &= \int P([I_{n+m} \mid \mathbf{s}_{1:n}] = I_{6,n+m}) f_{\gamma|I}(\gamma \mid \mathbf{I}_{1:n}) d\gamma, \end{aligned} \tag{3.47}$$

where $F_{t|\mathbf{s}_{1:n}}(m,\gamma)$ is the failure probability in the future *m* time steps conditioned on $\mathbf{s}_{1:n}$ and γ, and $f_{\gamma|I}(\gamma \mid \mathbf{I}_{1:n})$ is the posterior distribution of γ obtained in Sec. 3.6.2.

With strain observations collected through the sensors, the gap length and error ratio are updated over time through the damage estimation discussed in Sec. 3.6.1 and the error ratio updating scheme in Sec. 3.6.2. The RUL is then updated through Eqs. (3.43) and (3.47). The results of a miter gate application show that integrating physics-based damage estimation and the Markov transition matrix allows for effective RUL estimate even through there is no degradation model available.

Based on the failure prognosis, the $CPUT(t)$ in the future *m* time steps conditioned on the current strain observations and an error ratio γ is given by

$$[CPUT(m) \mid \mathbf{s}_{1:n}, \gamma] = \frac{C_P[1 - F_{t|\mathbf{s}_{1:n}}(m,\gamma)] + C_U[F_{t|\mathbf{s}_{1:n}}(m,\gamma)]}{\int_0^m [1 - F_{t|\mathbf{s}_{1:n}}(\tau,\gamma)]\,d\tau}, \tag{3.48}$$

where $F_{t|\mathbf{s}_{1:n}}(\tau,\gamma)$ is the failure probability given in Eq. (3.47), which needs to be interpolated from discrete time steps to continuous time step to evaluate the $CPUT(t)$ for any given future time.

The expected optimal maintenance plan conditioned on current observations, $\mathbf{s}_{1:n}$, is then identified as

$$[t_{opt} \mid \mathbf{s}_{1:n}] = \int \arg\min_t \{CPUT(t) \mid \mathbf{s}_{1:n}, \gamma\} f_{\gamma|I}(\gamma \mid \mathbf{I}_{1:n}) d\gamma. \tag{3.49}$$

The above equation is the result of integrating SHM with the Markov transition matrix based on field OCA ratings, which allows updating the optimal maintenance plan over time. This enables for dynamic decision making and thus leads to reduced lifecycle cost. Next, a miter gate

application is used to demonstrate the effectiveness of the proposed framework and investigate effects of the mapping function on the decision-making process.

3.7. Application to Miter Gate Failure Prognosis and Maintenance Optimization

In this section, the proposed framework is applied to an in-service USACE miter gate to demonstrate the effectiveness of the proposed prognosis and maintenance optimization.

3.7.1 Physics-based simulation model of miter gate

A FE model of the Greenup miter gate (Kentucky, USA) is used to understand the physics of a real-world miter gate. This model has been previously validated in the undamaged condition (Eick et al. 2018) with the available strain gage readings from the Greenup miter gate. Due to the SHM network already mounted in the Greenup miter gate (U.S. Army Corps of Engineers Headquarters 2007), the effect of input parameters such as the gap length (and other parameters such as the hydrostatic and thermal loads on the gates) to the strain network is analyzed using this validated FEM model.

The Greenup gate is a relatively new gate where negligible damage (gap length) was assumed for validation purposes. Most elements in the gate are 3D linear shells elements to reduce the computational cost of such a large model. A contact-type constraint is used between the quoin block attached lock wall (denoted in orange) and the gate (denoted in gray), making this a nonlinear problem. The Lagrange multiplier method was employed to impose the contact constraint. The strain gauge locations are far from the contact area, mostly due to physical constraints in the miter gate, but this far-field location also mitigates errors due to the method employed to enforce the contact constraint. The opposite side of the lock wall uses fixed boundary conditions, and symmetry boundary conditions are used at the right end (i.e., the miter) of the gate to simulate the

right leaf. Figure 3.17 shows the FE model of the Greenup gate and the modeling of bearing gap (enclosed area). The bearing gap (loss of contact) is modelled by removing the part of the quoin block attached to the lock wall (denoted in orange). Note that the size of the bearing gap in Figure 3.17 is just representative, as this will be a varying input variable to the FE model to generate "damage" data extracted from sensor locations in the gate. For more details on the quoin block mechanism, refer to Figure 8.37b in (Daniel and Paulus 2019a).

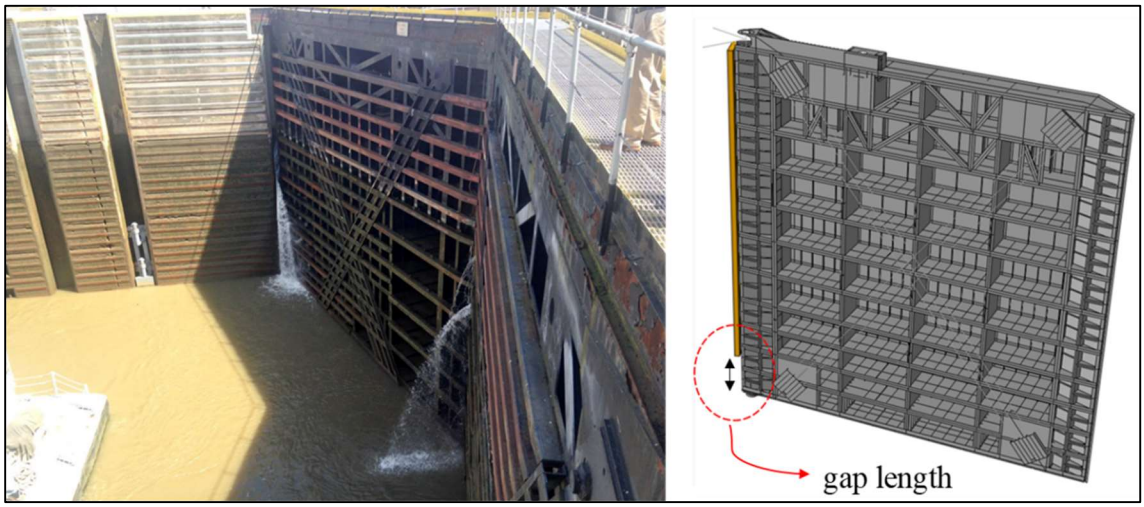

Figure 3.17: Miter Gate and physical-based FE model

In the next section, the generated data from multiple (i.e. 46 sensors) strain gauges will be used to develop diagnostics and prognostics capabilities for bearing gaps in miter gates.

3.7.2 Sequential damage detection using physics-based simulation

As discussed earlier, if continuous monitoring is introduced with the Markov transition matrix then the optimal maintenance plan over time can be updated based on the information gained by the sensor information using sequential damage estimation.

As discussed in Sec. 3.6.1, the likelihood function $f(\mathbf{s}_n \mid a_n)$ needs to be evaluated numerous times during the sequential damage estimation, which is computationally expensive especially because of the number of DOF in a FE model of a miter gate. A surrogate model is

constructed to map the relation from gap length (and other model parameters such as hydrostatic and thermal loads applied to miter gates) to the strain response at the strain gauges locations as shown in Figure 3.18. This figure shows the locations where the strain information is extracted from the physical based model to train the Kriging surrogate model. The sensor location matches with SHM strain network installed at the Greenup miter gate.

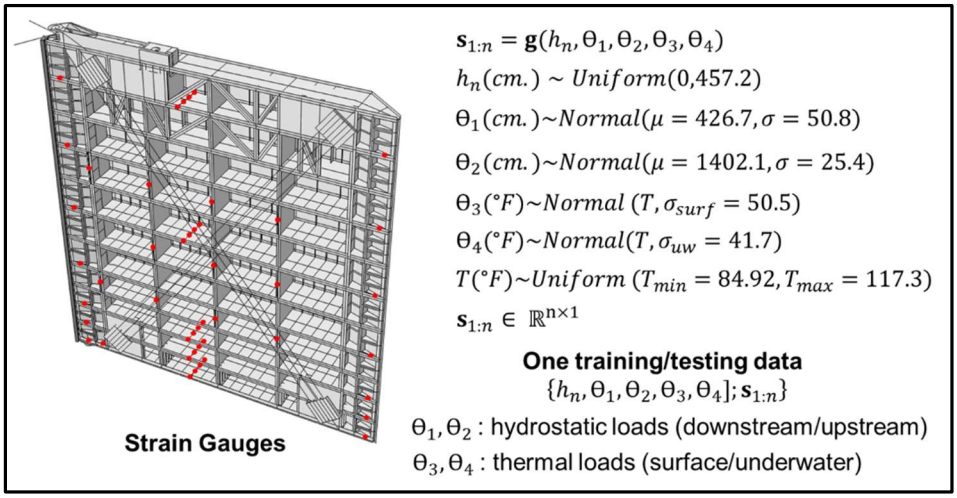

Figure 3.18: Sensor locations, and data generated to train surrogate model

Figure 3.19 shows the Kriging model testing accuracy at one strain SVD important feature (left) for different input values (i.e. gap length and other model inputs such as hydrostatic and thermal loads applied to miter gates) and the strain accuracy (in the original strain space) at different strain gauges locations for the same input value.

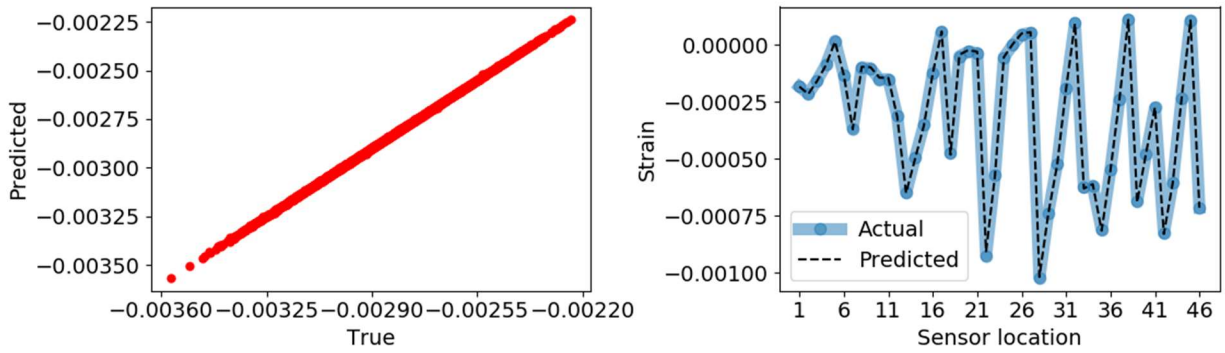

Figure 3.19: Surrogate modelling accuracy validation

Synthetic input parameters are generated using an autoregressive–moving-average (ARMA) model. These inputs are evaluated with the validated kriging model to generate strain time series measurements at every strain gauge location of the miter gate as shown in Figure 3.20.

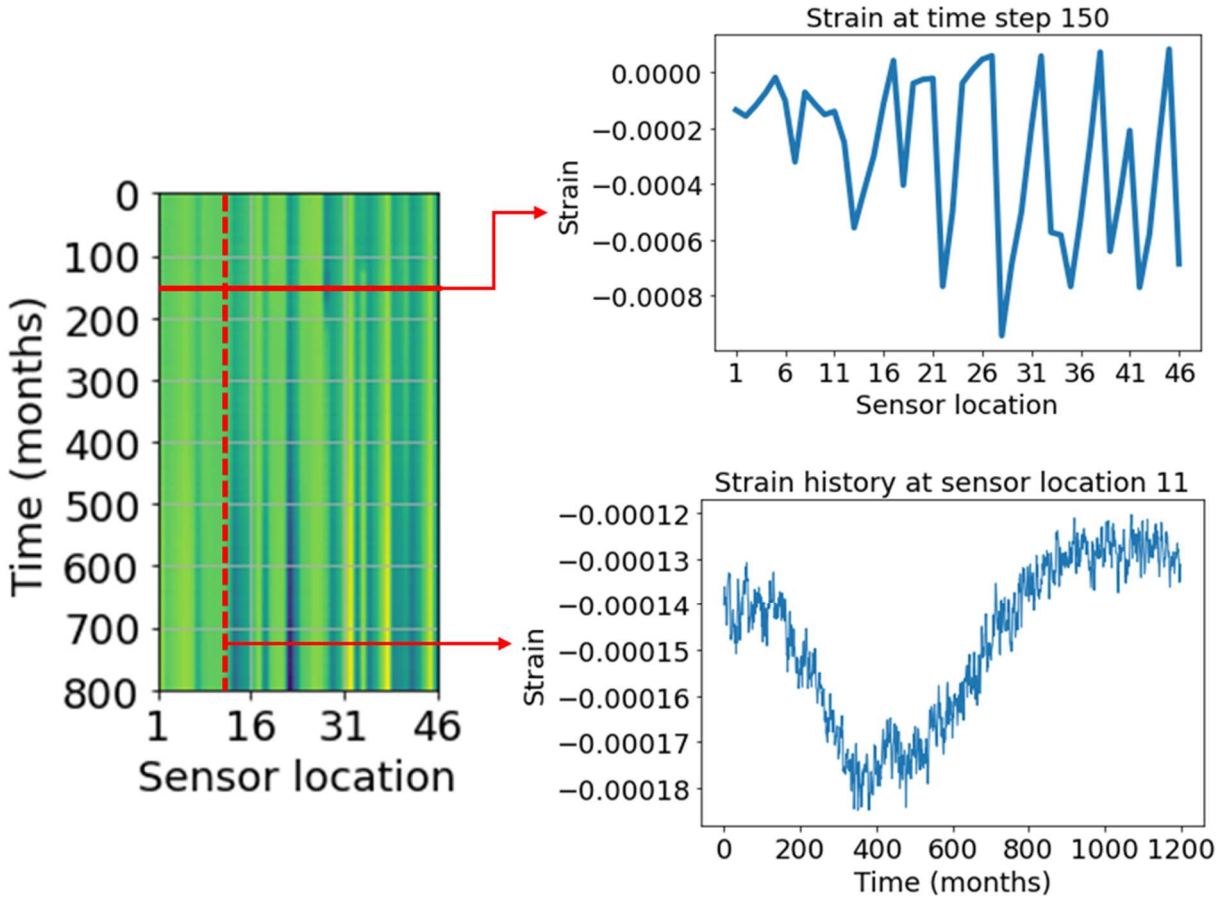

Figure 3.20: Strain observations from sensors

Following the method discussed in Sec. 3.6.1, the posterior $f(h_n \mid \mathbf{s}_{1:n})$ distribution of the gap length may be updated dynamically as strain measurements are available from the SHM network system. Figure 3.21 shows the updated predictions of the gap length against the true damage.

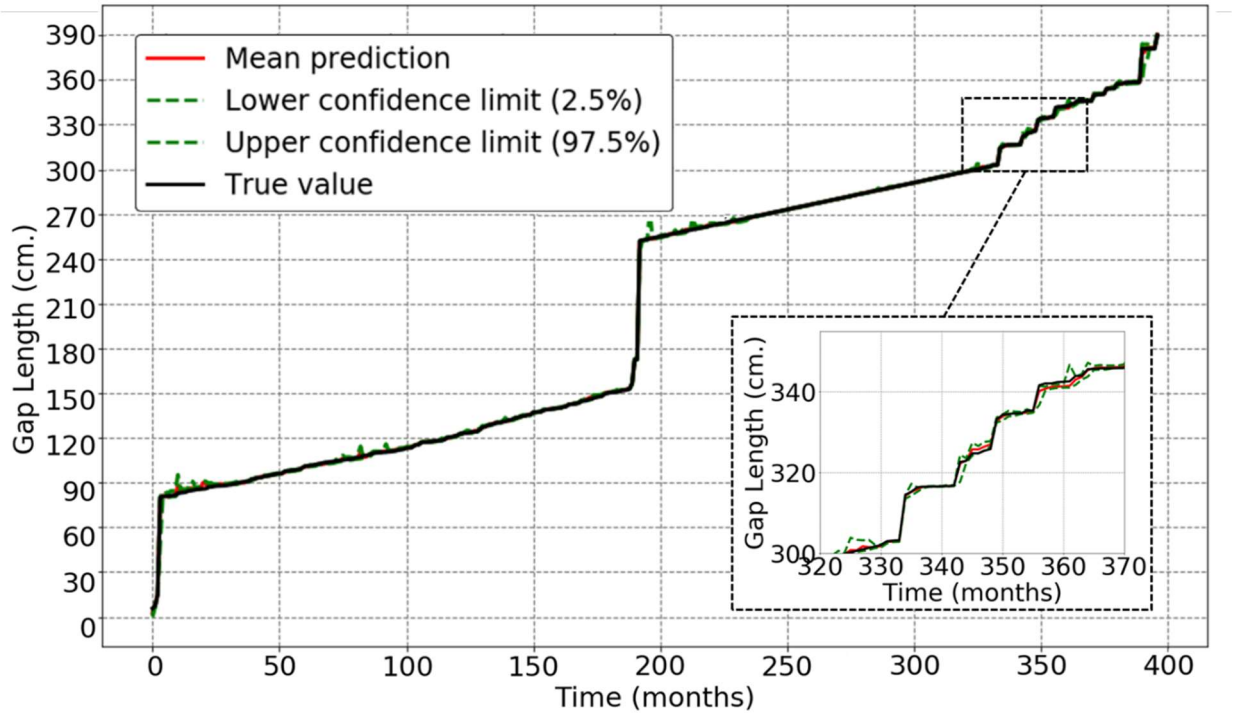

Figure 3.21: Damage detection over time using the state equation given in Eq. (3.27)

The result in Figure 3.21 shows that the proposed sequential damage estimation method is able to accurately estimate the damaged gap length based on the strain measurement data from the 46 sensors as indicated in Figure 3.18.

3.7.3 Estimation of "B" ratings error ratio based on online damage estimation

As described in Sec. 3.6.2 and indicated in Figure 3.16, the variable, $\gamma = B_{\text{inspected}} / B_{\text{total}}$, can be recursively updated using the observations obtained from the physics-based damage estimation. To achieve this, firstly, a mapping between gap length to the OCA condition rating is needing following Eq. (3.34). In this application, a uniform mapping consisting on gap length increments of 30 in. (76.2 cm.) was used as shown in Table 3.2.

Table 3.2: State mapping from discrete to continuous

OCA rating	Gap length (cm)
IA	$0 \le h_n < 76.2$
IB	$76.2 \le h_n < 152.4$
IC	$152.4 \le h_n < 228.6$
ID	$228.6 \le h_n < 304.8$
IF	$304.8 \le h_n < 381$
ICF	$h_n > 381$

Following that, the "B" rating error ratio is updated based on the damage estimation. Figure 3.22 shows the mean prediction and the 95% confidence intervals obtained for γ. As the information is acquired from the physics-based diagnosis, the variance of γ reduces significantly. Also, it is noted that as the quoin block has already surpassed the B condition, the value of γ approaches the true value (an assumed ground truth value in Sec. 3.7.2 that is used to generated the synthetic strain measurement data based on a gap growth model). This demonstrates the effectiveness of the proposed Bayesian updating scheme in estimating the "B" ratings error ratio. It worth mentioning that the error ratio updating is mainly affected by the gap length profile as given in Figure 3.21. The gap length profile is just one realization of the underlying degradation model. Since it is just one realization of many possible gap growth profiles, it leads to a small bias between the estimated error ratio and the "true" error ratio used in Sec. 3.7.2.

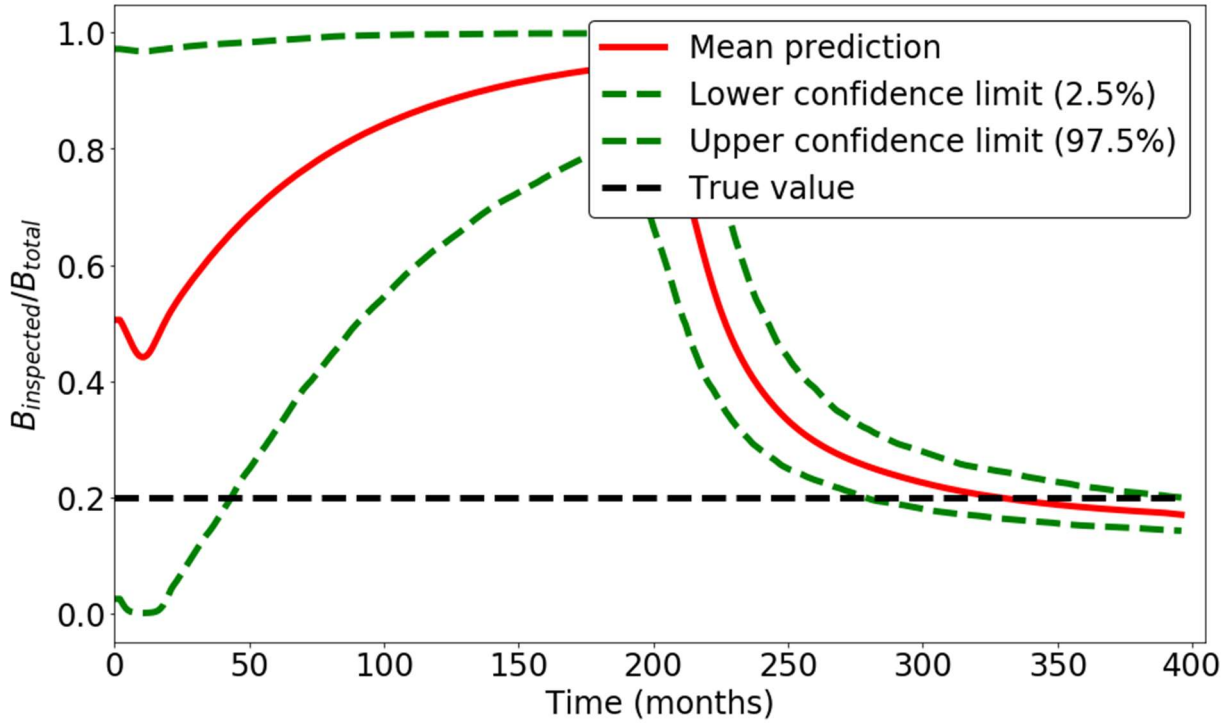

Figure 3.22: "B" ratings error ratio (γ) estimation

3.7.4 Failure prognosis and optimal maintenance planning for the miter gate

To demonstrate the improvement on the gap length prognosis, the updated over time RUL can be evaluated, and compared against its true value. Figure 3.23 shows that the RUL estimation using the state equation given in Eq. (3.27). It shows that the random-walk state equation could lead to large errors in RUL estimate even if it can effectively perform damage detection. As been discussed in Sec. 3.6.3, the information from the OCA rating can be used to improve the prognosis capabilities and overcome the limitations of the state equation in Eq. (3.27). Figure 3.24 shows that the proposed hybrid prognosis method can improve the accuracy RUL estimation while effectively performing damage detection. The jumps in Figure 3.24 are attributed to the discrete nature of the OCA ratings.

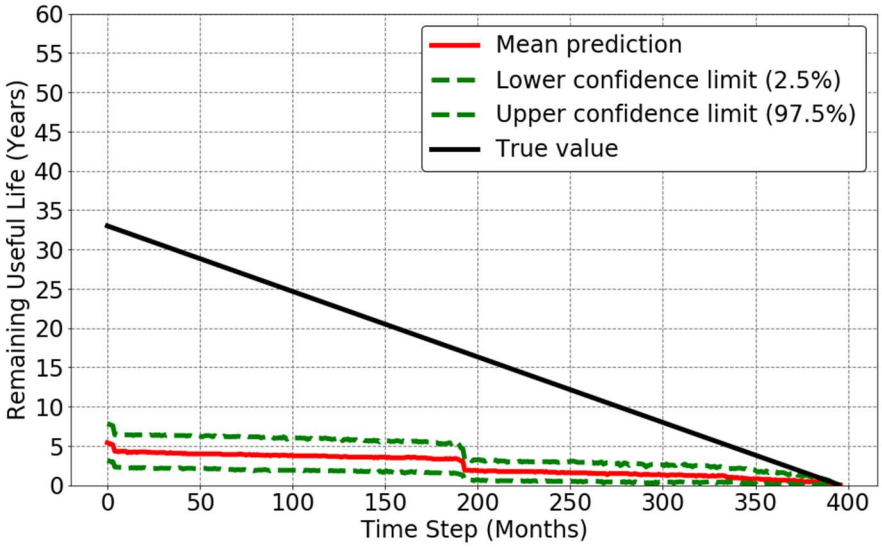

Figure 3.23: RUL estimate using the state equation given in Eq. (3.27)

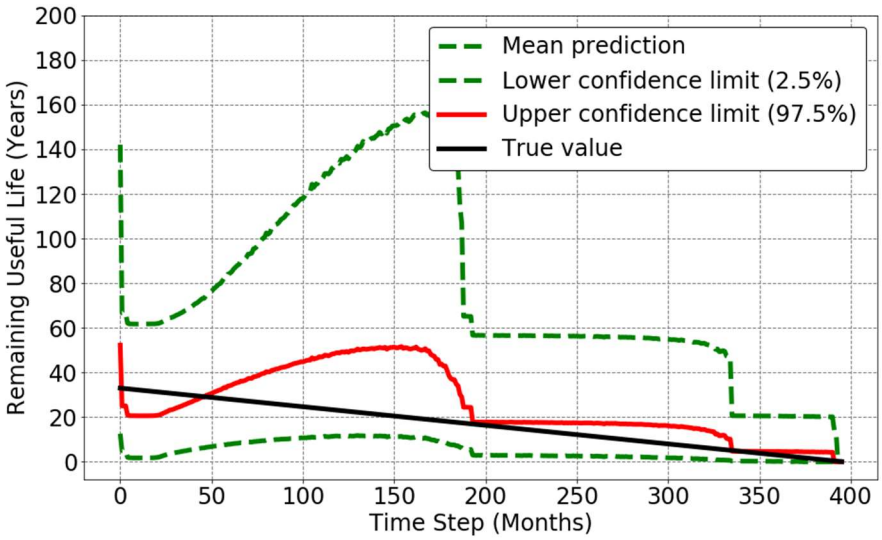

Figure 3.24: RUL estimate using the proposed method

Figure 3.25 and 3.26 show how the minimum CPUT and the optimal maintenance time are updated from the strain measurements over time. These figures were generated using a uniform mapping between the gap length to the OCA ratings as given in Table 3.2. The vertical line in these figures represent the true end of life. In other words, the true end of life is when the gap length reaches the value of 150 inch (381 cm.), which corresponds to the "CF" condition. As noted, the minimum CPUT mainly increase with time, indicating that the denominator in Eq. (3.48) is approaching to zero as the term $F_{l|\mathbf{s}_{1:n}}(\tau)$ is approaching to 1. Similarly, in contrast to the static

maintenance planning in Sec. 3.5, the optimal maintenance time (relative to the current time) can be updated dynamically as time passes based on the information collected from the SHM system.

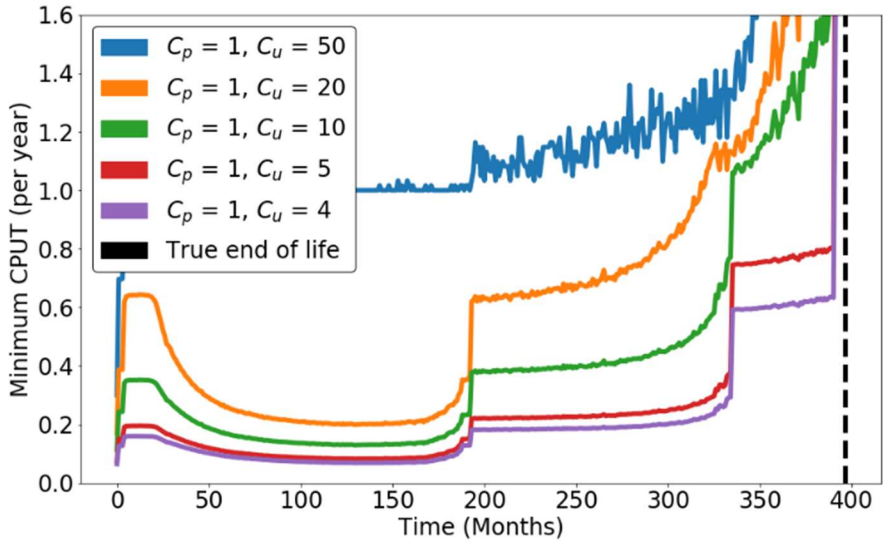

Figure 3.25: Minimum CPUT corresponding to different values of Cp and Cu

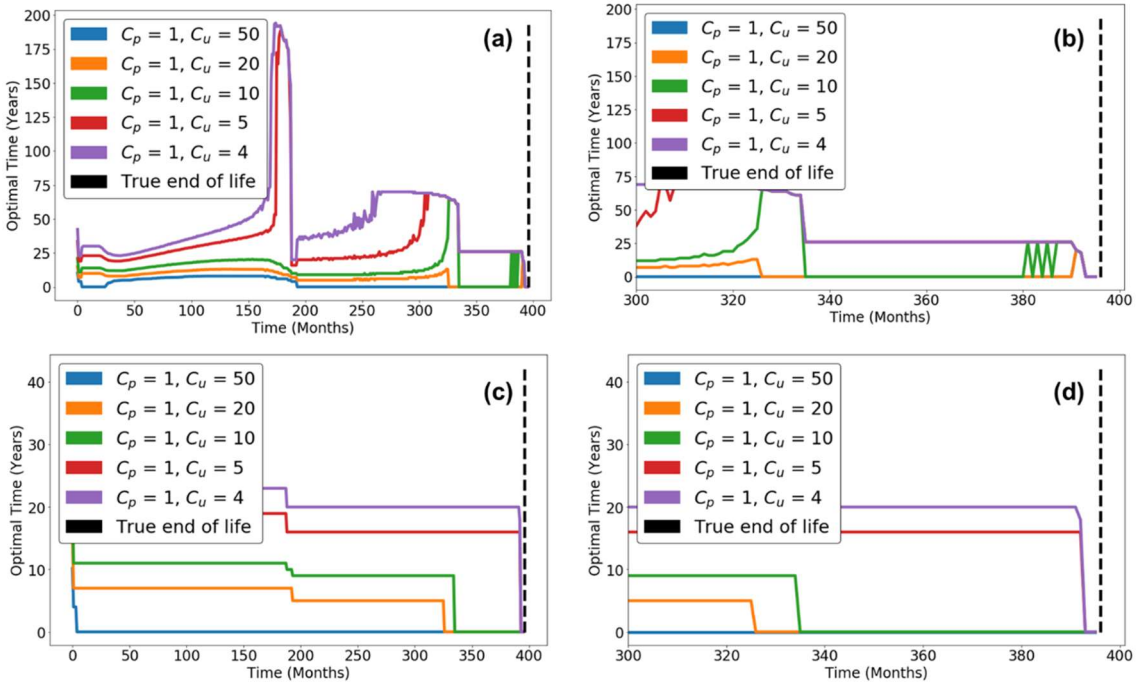

Figure 3.26: a) Optimal maintenance time corresponding to different Cp and Cu, b) optimal maintenance time approaching end of life, c) alternative optimal maintenance time corresponding to different Cp and Cu , and d) alternative optimal maintenance time approaching end of life

One of the main reasons why the optimal time (see Figure 3.26a), especially for low cost ratios, increases so dramatically at around 175 month is due to the nature of Eq. (3.48) and (3.12). In these cases, the CPUT curve obtained from Eq. (3.48) tends to be very flat. In other words, many different maintenance times may have basically the same CPUT value. For Figure 3.26c, a conservative selection for the optimal maintenance is carried out, and it is assumed that the updated optimal maintenance tends to decrease with time and holds practically the same CPUT value. Thus, with this conservative selection, the minimum CPUT corresponding to different values of Cp and Cu would show basically the same results as Figure 3.25. The next section will introduce an approach to improve the prognosis capabilities (e.g. RUL estimate) shown in Figure 3.24 by introducing a stochastic continuous degradation model, and also accounting for human error introduced in the reported OCA ratings.

3.8. Alternative Degradation Model to Improve Damage Prognosis accounting for Human Error in OCA ratings.

Let $a_t = g(t, \boldsymbol{\theta})$ be the underlying degradation model of the miter gate damage gap, where a_t is the gap length at time t and $\boldsymbol{\theta}$ is a vector of model parameters. Fig. 3.27 shows the relationship among the degradation model, OCA ratings, and the reported OCA ratings by the field engineers. As shown in Fig. 3.27, the OCA protocol maps the gap length, a_t, (i.e., the output of the unknown degradation model) into OCA ratings as if the protocol were strictly and accurately followed by the field engineers. Due to human observation error and variability, however, the OCA ratings reported by the field engineers as indicated in Fig. 3.27 may not be the same as the "true" rating that better represents the condition; this is proven true for inspectors in many application domains (L. E. Campbell et al. 2020).

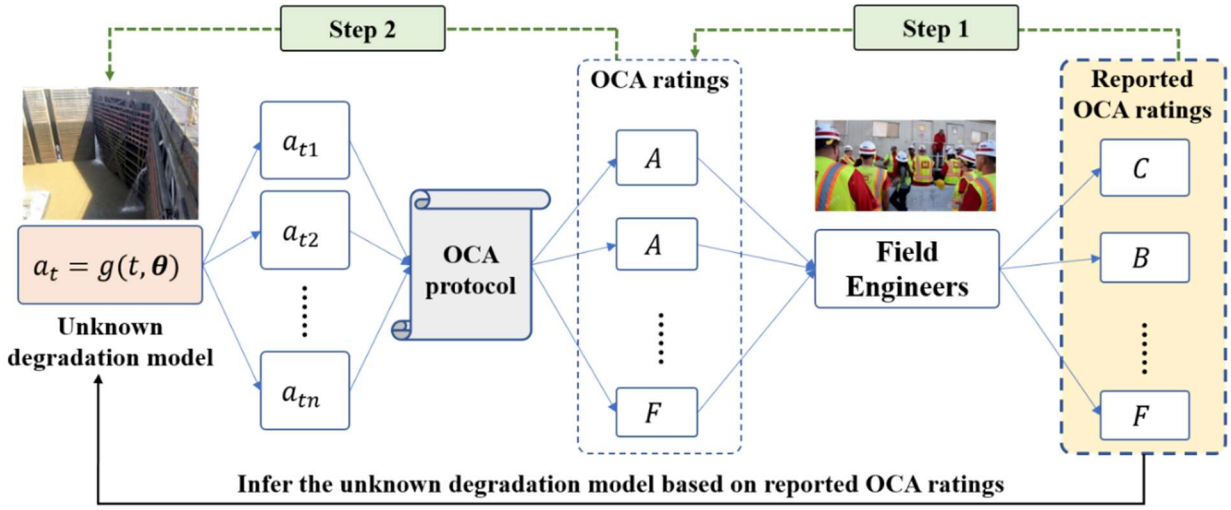

Figure 3.27: Relationship among the gap degradation, OCA ratings, and the reported OCA ratings

One of the objectives of the proposed method is to infer the unknown degradation model, $a_t = g(t, \theta)$, using *the reported OCA ratings*, which include the human variability or errors in the rating reporting process. The inferred degradation model will then be used for *integrated* damage diagnostics and prognostics of the miter gate. As shown in Fig. 3.27, the inference of the unknown degradation model in the proposed framework is accomplished through two steps:

- **Step 1**: Mapping of the reported OCA ratings to the underlying true OCA ratings for a given OCA protocol, by considering the human observation errors of field engineers in reporting.
- **Step 2**: Estimation of the degradation model parameters ($\boldsymbol{\theta}$) based on the obtained true OCA ratings (i.e. true OCA transition matrix).

In the next section, these two steps will be explained in detail.

3.8.1 Mapping of the reported OCA rating transition matrix to the true transition matrix

In order to map the reported OCA rating transition matrix to the underlying true OCA transition matrix, the underlying true OCA rating is defined at time t as I_t^{tr} and that at t+1 as

I_{t+1}^{tr}, the reported OCA rating from field engineers at time t as I_t^{obs} and that at time t+1 as I_{t+1}^{obs}. Based on these definitions, the true OCA transition matrix $\mathbf{P}_{\text{OCA}}$ (i.e. OCA "ideal" protocol is strictly followed) is denoted as

$$\mathbf{P}_{\text{OCA}} = \begin{bmatrix} P_{11}^{OCA} & P_{12}^{OCA} & \cdots & P_{16}^{OCA} \\ 0 & P_{22}^{OCA} & \cdots & P_{26}^{OCA} \\ \vdots & \vdots & \ddots & \vdots \\ 0 & 0 & \cdots & P_{66}^{OCA} \end{bmatrix}, \tag{3.50}$$

where $P_{ij}^{OCA} = \Pr\{I_{t+1}^{tr} = j \mid I_t^{tr} = i\} \triangleq P(I_{j,t+1}^{tr} \big| I_{i,t}^{tr}), \forall i = 1, 2, \cdots, 6;\ j = i, \cdots, 6$ represents the probability of transiting from OCA rating i at time t to OCA rating j at t+1.

Similarly, the reported transition matrix, built from the OCA ratings reported by field engineers, is denoted as

$$\mathbf{P}_{\text{Report}} = \begin{bmatrix} P_{11}^{R} & P_{12}^{R} & \cdots & P_{16}^{R} \\ 0 & P_{22}^{R} & \cdots & P_{26}^{R} \\ \vdots & \vdots & \ddots & \vdots \\ 0 & 0 & \cdots & P_{66}^{R} \end{bmatrix}, \tag{3.51}$$

where $P_{kq}^{R} = \Pr\{I_{t+1}^{obs} = q \mid I_t^{obs} = k\}, \forall k = 1, 2, \cdots, 6;\ q = k, \cdots, 6$ is the probability of transitioning from OCA rating k at time t to OCA rating q at t+1, based on the reported OCA ratings. In addition, from the reported OCA ratings, the state probabilities $\Pr\{I_t^{obs} = k\}, k = 1, 2, \cdots, 6$ and $\Pr\{I_{t+1}^{obs} = q\}, q = 1, 2, \cdots, 6$ may also be obtained.

The goal of Step 1 of the proposed method (see Fig. 3.27) is to map $\mathbf{P}_{\text{Report}}$ to $\mathbf{P}_{OCA}$. To achieve this goal, the human observation error matrix is defined as

$$\mathbf{P}_{\text{human}} = \begin{bmatrix} P_{11}^h & P_{12}^h & \cdots & P_{16}^h \\ P_{21}^h & P_{22}^h & \cdots & P_{26}^h \\ \vdots & \vdots & \ddots & \vdots \\ P_{61}^h & P_{62}^h & \cdots & P_{66}^h \end{bmatrix}, \tag{3.52}$$

in which $P_{ik}^h = \Pr\{I_t^{obs} = k \mid I_t^{tr} = i\}$ is the probability that the reported OCA rating is *k* given that the true OCA rating is *i*. Based on the above definitions of $\mathbf{P}_{\text{OCA}}$, $\mathbf{P}_{\text{Report}}$, and $\mathbf{P}_{\text{human}}$, the reported and true OCA ratings are connected using a Bayesian network as shown in Fig. 3.28.

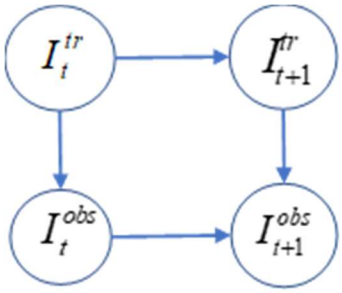

Figure 3.28: A Bayesian network connecting the observed and the true OCA ratings

From the above Bayesian network, the following conditional probability tables (CPTs) are obtained:

$$\begin{aligned} &\Pr\{I_t^{obs} = k \mid I_t^{tr} = i\} = P_{ik}^h, \forall i = 1, 2, \cdots, 6; k = 1, 2, \cdots, 6; \\ &\Pr\{I_{t+1}^{obs} = q \mid I_{t+1}^{tr} = j\} = P_{jq}^h, \forall j = 1, 2, \cdots, 6; q = 1, 2, \cdots, 6; \end{aligned} \tag{3.53}$$

and

$$\begin{aligned} &\Pr\{I_{t+1}^{obs} = q \mid (I_{t+1}^{tr} = j, I_t^{obs} = k)\} \\ &= \frac{\Pr\{I_{t+1}^{obs} = q, I_{t+1}^{tr} = j, I_t^{obs} = k\}}{\Pr\{I_{t+1}^{tr} = j, I_t^{obs} = k\}}, \\ &= \frac{\Pr\{I_t^{obs} = k \mid I_{t+1}^{obs} = q, I_{t+1}^{tr} = j\} \Pr\{I_{t+1}^{obs} = q \mid I_{t+1}^{tr} = j\} \Pr\{I_{t+1}^{tr} = j\}}{\Pr\{I_{t+1}^{tr} = j, I_t^{obs} = k\}}. \end{aligned} \tag{3.54}$$

Since the lower triangular components of $\mathbf{P}_{\text{Report}}$ are all zero, the following marginal probability is written

$$\Pr\{I_{t+1}^{tr}=j, I_t^{obs}=k\}=\sum_{w=k}^{6}\Pr\{I_{t+1}^{obs}=w, I_{t+1}^{tr}=j, I_t^{obs}=k\}. \tag{3.55}$$

With the above CPTs, the task is to obtain the true OCA transition matrix by solving $\Pr\{I_{t+1}^{tr}=j \mid I_t^{tr}=i\}, \forall i=1,2,\cdots,6; j=i,\cdots,6$ in the Bayesian network shown in Fig. 3.28. Using $\Pr\{I_{t+1}^{obs}=q\}, q=1,2,\cdots,6$, the following marginal probability is written

$$\begin{aligned}\Pr\{I_{t+1}^{obs}=q\}&=\sum_{j=1}^{6}\Pr\{I_{t+1}^{obs}=q, I_{t+1}^{tr}=j\}, \forall q=1,2,\cdots,6;\\ &=\sum_{j=1}^{6}\Pr\{I_{t+1}^{obs}=q \mid I_{t+1}^{tr}=j\}\Pr\{I_{t+1}^{tr}=j\}, \forall q=1,2,\cdots,6.\end{aligned} \tag{3.56}$$

Writing the above equation in matrix form yields

$$\begin{bmatrix}\Pr\{I_{t+1}^{obs}=1\}\\ \Pr\{I_{t+1}^{obs}=2\}\\ \vdots\\ \Pr\{I_{t+1}^{obs}=6\}\end{bmatrix}=\begin{bmatrix}P_{11}^h & P_{12}^h & \cdots & P_{16}^h\\ P_{21}^h & P_{22}^h & \cdots & P_{26}^h\\ \vdots & \vdots & \ddots & \vdots\\ P_{61}^h & P_{62}^h & \cdots & P_{66}^h\end{bmatrix}\begin{bmatrix}\Pr\{I_{t+1}^{tr}=1\}\\ \Pr\{I_{t+1}^{tr}=2\}\\ \vdots\\ \Pr\{I_{t+1}^{tr}=6\}\end{bmatrix}. \tag{3.57}$$

Based on Eq. (3.57), $\Pr\{I_{t+1}^{tr}=j\}, \forall j=1,2,\cdots,6$ can be solved using $\mathbf{P}_{\text{human}}$ and $\Pr\{I_{t+1}^{obs}=q\}, q=1,2,\cdots,6$. In this chapter, a constrained least-squares method is employed to solve Eq. (3.57) to ensure that the obtained probability estimates are in the range of [0, 1]. In order to estimate $\Pr\{I_{t+1}^{tr}=j \mid I_t^{tr}=i\}, \forall i=1,2,\cdots,6; j=i,\cdots,6$, the marginalization of $\Pr\{I_{t+1}^{obs}=q, I_t^{obs}=k\}=\Pr\{I_{t+1}^{obs}=q \mid I_t^{obs}=k\}\Pr\{I_t^{obs}=k\}$ is shown as follows

$$\begin{aligned}\Pr\{I_{t+1}^{obs}=q, I_t^{obs}=k\}&=\sum_{i=1}^{6}\sum_{j=i}^{6}\Pr\{I_{t+1}^{obs}=q, I_t^{obs}=k, I_{t+1}^{tr}=j, I_t^{tr}=i\},\\ &=\sum_{i=1}^{6}\sum_{j=i}^{6}\Pr\{(I_{t+1}^{obs}=q, I_t^{obs}=k) \mid (I_{t+1}^{tr}=j, I_t^{tr}=i)\}\Pr\{I_{t+1}^{tr}=j, I_t^{tr}=i\}.\end{aligned} \tag{3.58}$$

According to the Bayesian network given in Fig. 3.28, it follows that

$$
\begin{aligned}
&\Pr\{(I_{t+1}^{obs}=q, I_t^{obs}=k)\,|\,(I_{t+1}^{tr}=j, I_t^{tr}=i)\} \\
&= \Pr\{I_{t+1}^{obs}=q \,|\, I_{t+1}^{tr}=j, I_t^{obs}=k\}\Pr\{I_t^{obs}=k \,|\, I_t^{tr}=i\}, \\
&= \frac{\Pr\{I_{t+1}^{obs}=q, I_{t+1}^{tr}=j, I_t^{obs}=k\}}{\sum_{w=k}^{6}\Pr\{I_{t+1}^{obs}=w, I_{t+1}^{tr}=j, I_t^{obs}=k\}} P_{ik}^{h}.
\end{aligned}
\tag{3.59}
$$

Substituting Eq. (3.59) into Eq. (3.58) yields

$$
\begin{aligned}
&\Pr\{I_{t+1}^{obs}=q, I_t^{obs}=k\} \\
&= \sum_{i=1}^{6}\sum_{j=i}^{6}\left(\frac{\Pr\{I_{t+1}^{obs}=q, I_{t+1}^{tr}=j, I_t^{obs}=k\}}{\sum_{w=k}^{6}\Pr\{I_{t+1}^{obs}=w, I_{t+1}^{tr}=j, I_t^{obs}=k\}} P_{ik}^{h}\right)\Pr\{I_{t+1}^{tr}=j, I_t^{tr}=i\}.
\end{aligned}
\tag{3.60}
$$

The following is obtained from the numerator of Eq. (3.54)

$$
\begin{aligned}
&\Pr\{I_{t+1}^{obs}=q, I_{t+1}^{tr}=j, I_t^{obs}=k\} \\
&= \Pr\{I_t^{obs}=k \,|\, I_{t+1}^{obs}=q, I_{t+1}^{tr}=j\}P_{jq}^{h}\Pr\{I_{t+1}^{tr}=j\},
\end{aligned}
\tag{3.61}
$$

where $\Pr\{I_{t+1}^{tr}=j\}$ is solved in Eq. (3.57).

Combining Eqs. (3.60) and (3.61) yields

$$
\begin{aligned}
&P_{kq}^{R}\Pr\{I_t^{obs}=k\} \\
&= \sum_{i=1}^{6}\sum_{j=i}^{6}\left(\frac{\Pr\{I_t^{obs}=k \,|\, I_{t+1}^{obs}=q, I_{t+1}^{tr}=j\}P_{jq}^{h}\Pr\{I_{t+1}^{tr}=j\}}{\sum_{w=k}^{6}\Pr\{I_t^{obs}=k \,|\, I_{t+1}^{obs}=w, I_{t+1}^{tr}=j\}P_{jw}^{h}\Pr\{I_{t+1}^{tr}=j\}} P_{ik}^{h}\right)\Pr\{I_{t+1}^{tr}=j, I_t^{tr}=i\}.
\end{aligned}
\tag{3.62}
$$

In order to make $\Pr\{I_{t+1}^{tr}=j \,|\, I_t^{tr}=i\}, \forall i=1,2,\cdots,6; j=i,\cdots,6$ solvable given the current available information ($\mathbf{P}_{\text{Report}}$ and $\mathbf{P}_{\text{human}}$), it is assumed conditional independence for $\Pr\{I_t^{obs}=k \,|\, I_{t+1}^{obs}=q, I_{t+1}^{tr}=j\}=\Pr\{I_t^{obs}=k \,|\, I_{t+1}^{obs}=q\}$. This is a reasonable assumption for the Bayesian network structure given in Fig. 3.28, since the resulting joint probability mass function

$\Pr\{I_{t+1}^{obs}=q, I_{t+1}^{tr}=j, I_t^{obs}=k\}$ satisfies the constraints of all the current given information in $\mathbf{P}_{\text{Report}}$ and $\mathbf{P}_{\text{human}}$. Based on this assumption, the conditional probability and Bayes rule are exploited

$$\begin{aligned}&\Pr\{I_{t+1}^{obs}=q, I_{t+1}^{tr}=j, I_t^{obs}=k\}\\&=\Pr\{I_t^{obs}=k \mid I_{t+1}^{obs}=q\}P_{jq}^{h}\Pr\{I_{t+1}^{tr}=j\}=\frac{P_{kq}^{R}\Pr\{I_t^{obs}=k\}P_{jq}^{h}\Pr\{I_{t+1}^{tr}=j\}}{\Pr\{I_{t+1}^{obs}=q\}},\ \forall q\geq k.\end{aligned} \tag{3.63}$$

Substituting Eq. (3.63) into Eq. (3.62) as follows

$$\begin{aligned}&P_{kq}^{R}\Pr\{I_t^{obs}=k\}\\&=\sum_{i=1}^{6}\sum_{j=i}^{6}\left(\frac{\dfrac{P_{kq}^{R}\Pr\{I_t^{obs}=k\}P_{jq}^{h}\Pr\{I_{t+1}^{tr}=j\}}{\Pr\{I_{t+1}^{obs}=q\}}}{\displaystyle\sum_{w=k}^{6}\left(\frac{P_{kw}^{R}\Pr\{I_t^{obs}=k\}P_{jw}^{h}\Pr\{I_{t+1}^{tr}=j\}}{\Pr\{I_{t+1}^{obs}=w\}}\right)}P_{ik}^{h}\right)\Pr\{I_{t+1}^{tr}=j, I_t^{tr}=i\}.\end{aligned} \tag{3.64}$$

Defining $P_{ijkq}\triangleq\dfrac{\dfrac{P_{kq}^{R}\Pr\{I_t^{obs}=k\}P_{jq}^{h}\Pr\{I_{t+1}^{tr}=j\}}{\Pr\{I_{t+1}^{obs}=q\}}}{\displaystyle\sum_{w=k}^{6}\left(\frac{P_{kw}^{R}\Pr\{I_t^{obs}=k\}P_{jw}^{h}\Pr\{I_{t+1}^{tr}=j\}}{\Pr\{I_{t+1}^{obs}=w\}}\right)}P_{ik}^{h}$, it follows that

$$P_{kq}^{R}\Pr\{I_t^{obs}=k\}=\sum_{i=1}^{6}\sum_{j=i}^{6}P_{ijkq}\Pr\{I_{t+1}^{tr}=j, I_t^{tr}=i\}, \tag{3.65}$$

which again elucidated in matrix form is

$$\begin{bmatrix}P_{J,1}\\P_{J,2}\\\vdots\\P_{J,20}\\P_{J,21}\end{bmatrix}_{21\times1}=\begin{bmatrix}P_{J,1,1}^{h}&P_{J,1,2}^{h}&\cdots&P_{J,1,20}^{h}&P_{J,1,21}^{h}\\P_{J,2,1}^{h}&P_{J,2,2}^{h}&\cdots&P_{J,2,20}^{h}&P_{J,2,21}^{h}\\\vdots&\vdots&\ddots&\vdots&\vdots\\P_{J,20,1}^{h}&P_{J,20,2}^{h}&\cdots&P_{J,20,20}^{h}&P_{J,20,21}^{h}\\P_{J,21,1}^{h}&P_{J,21,2}^{h}&\cdots&P_{J,21,20}^{h}&P_{J,21,21}^{h}\end{bmatrix}_{21\times21}\begin{bmatrix}P_{J,1}^{OCA}\\P_{J,2}^{OCA}\\\vdots\\P_{J,20}^{OCA}\\P_{J,21}^{OCA}\end{bmatrix}_{21\times1}, \tag{3.66}$$

where $P_{J,x}=P_{kq}^{R}\Pr\{I_t^{obs}=k\}$, $P_{J,y}^{OCA}=\Pr\{I_{t+1}^{tr}=j, I_t^{tr}=i\}$, $P_{J,x,y}^{h}=P_{ijkq}$, in which the indices are related to each other by

$$x=\begin{cases} q, \text{if } k=1 \\ (q-k+1)+\sum_{s=1}^{k-1}(6-s+1), \text{otherwise} \end{cases}, \forall q \geq k, \tag{3.67}$$

and

$$y=\begin{cases} j, \text{if } i=1 \\ (j-i+1)+\sum_{s=1}^{i-1}(6-s+1), \text{otherwise} \end{cases}, \forall j \geq i. \tag{3.68}$$

Using Eq. (3.66), $P_{J,y}^{OCA}=\Pr\{I_{t+1}^{tr}=j, I_t^{tr}=i\}, \forall i=1,2,\cdots,6; j=i,\cdots,6$ can be solved similarly as in Eq. (3.57) using the constrained least-squares method. Using the above equations (Eq. (3.53) through (3.68)), the reported OCA rating transition matrix $\mathbf{P}_{\text{Report}}$ is mapped into the underlying true OCA rating transition matrix $\mathbf{P}_{\text{OCA}}$ considering the human observation errors $\mathbf{P}_{\text{human}}$. The next section will discuss how to estimate the degradation model parameters $\boldsymbol{\theta}$ of $a_t=g(t,\boldsymbol{\theta})$ using the transition matrix $\mathbf{P}_{\text{OCA}}$.

3.8.2 Estimation of the degradation model parameters

As noted in Step 2 in Fig. 3.27, in order to establish a connection between the degradation model $a_t=g(t,\boldsymbol{\theta})$ and the OCA transition matrix $\mathbf{P}_{\text{OCA}}$, a mapping function is defined for the OCA protocol as below

$$R=h_{OCA}(a_t,\boldsymbol{\beta})=\begin{cases} A, a\in[0,\beta_1] \\ B, a_t\in[\beta_1,\beta_2] \\ C, a_t\in[\beta_2,\beta_3] \\ D, a_t\in[\beta_3,\beta_4] \\ F, a_t\in[\beta_4,\beta_5] \\ CF, a_t\in[\beta_5,\infty) \end{cases}, \tag{3.69}$$

where R is the OCA rating, a_t is the gap length, and $\boldsymbol{\beta}=[\beta_1, \beta_2, \beta_3, \beta_4, \beta_5]$ is a vector of parameters of the mapping function related to the OCA protocol.

In the proposed method, the unknown parameters $\boldsymbol{\theta}$ are estimated for given set of parameters $\boldsymbol{\beta}$ which defines the mapping function (i.e. Eq. (3.69)). Also, given the degradation model $a_t = g(t, \boldsymbol{\theta})$, and the true OCA transition matrix, $\mathbf{P}_{\text{OCA}}$, shown in Sec.3.8.1. After that, diagnostics and prognostics are performed based on the estimated $\boldsymbol{\theta}$.

The task of estimating $\boldsymbol{\theta}$ is to solve the following optimization problem

$$\begin{aligned} &\boldsymbol{\theta}^* = \arg\min_{\boldsymbol{\theta}} \{g_{opt}(\boldsymbol{\theta}; \boldsymbol{\beta}, \mathbf{P}_{\text{OCA}})\}, \\ &s.t. \ \boldsymbol{\theta} \in \Omega, \end{aligned} \tag{3.70}$$

where $g_{opt}(\boldsymbol{\theta}; \boldsymbol{\beta}, \mathbf{R})$ is a cost function of the optimization model, and Ω is the domain of $\boldsymbol{\theta}$. In the above optimization model, the cost function $g_{opt}(\boldsymbol{\theta}; \boldsymbol{\beta}, \mathbf{R})$ is defined as

$$\begin{aligned} g_{opt}(\boldsymbol{\theta}; \boldsymbol{\beta}, \mathbf{P}_{\text{OCA}}) &= \left\| \hat{\mathbf{P}}(\boldsymbol{\theta}) - \mathbf{P}_{\text{OCA}} \right\|_2, \\ &= \sum_{i=1}^{6} \sum_{j=i}^{6} (\hat{P}(I_{j,t+1}^{s} \mid I_{i,t}^{s}; \boldsymbol{\theta}) - P(I_{j,t+1}^{tr} \mid I_{i,t}^{tr}))^2, \end{aligned} \tag{3.71}$$

in which $\hat{\mathbf{P}}(\boldsymbol{\theta}) \triangleq \{\hat{P}(I_{j,t+1}^{s} \mid I_{i,t}^{s}; \boldsymbol{\theta}), i = 1, 2, \cdots, 6; \ j = i, \cdots, 6\}$ is the simulated transition probabilities of the OCA ratings from the degradation model simulation for given $\boldsymbol{\theta}$, $\mathbf{P}_{OCA}$ is the true OCA transition matrix (i.e. Eq. (3.50)) obtained from Sec. 3.8.1 based on the reported OCA transition matrix and human observation error matrix.

It should be noted that, theoretically speaking, the optimization model Eq. (3.71) can also be formulated directly from the reported OCA transition matrix $\mathbf{P}_{\text{Report}}$ perspective by coupling the approach developed in this section with the forward uncertainty propagation of the OCA ratings based on the human error observation matrices. That kind of formulation can be considered as an

alternative approach of the proposed method and will be investigated in future work. The benefit of using $\mathbf{P}_{OCA}$ in Eq. (3.71) is two-fold: first, the identification of $\mathbf{P}_{OCA}$ in Sec. 3.8.1 allows us to perform failure prognostics with $\mathbf{P}_{OCA}$ instead of $\mathbf{P}_{Report}$ using the approach developed in Ref. (M. A. Vega, Hu, and Todd 2020) and reviewed in Sec. 3.6. Using $\mathbf{P}_{OCA}$ to replace $\mathbf{P}_{Report}$ in transition matrix-based prognostics will improve the accuracy of failure prognostics since $\mathbf{P}_{OCA}$ mitigates the effects of human observation errors. Second, the formulation given in Eq. (3.71) eliminates process of uncertainty propagation step from $\mathbf{P}_{OCA}$ to $\mathbf{P}_{Report}$ in estimating θ which reduces the complexity of the optimization process.

As shown in Eq. (3.71), the estimation of $\hat{\mathbf{P}}(\theta)$ for a given θ is the key for the optimization-based method to minimize the L2 error norm between the underlying true OCA transition matrix, $\mathbf{P}_{OCA}$, and the estimated transition matrix, $\hat{\mathbf{P}}(\theta)$ obtained from the estimated multi-stage continuous degradation model. The next section will discuss in detail on how to estimate $\hat{\mathbf{P}}(\theta)$ for given θ. After that, an explanation will be given of how to solve Eq. (3.71) based on the estimation of multi-stage continuous degradation model.

3.8.2.1 Prediction of OCA rating transition matrix $\hat{\mathbf{P}}(\theta)$ *for given* θ

As mentioned earlier, there is a need of a degradation model whose OCA transition matrix prediction, $\hat{\mathbf{P}}(\theta)$, resembles the true OCA transition matrix, $\mathbf{P}_{OCA}$. However, different criteria on selecting a degradation models are present depending on the data available and the understanding of the physics of the damage evolution.

(a) Selection of gap degradation model

i. Paris' law:

A Paris' law is a crack growth equation that gives the rate of growth of a fatigue crack. It is widely used in many engineering applications. The Paris equation is shown as follows:

$$\frac{da(t)}{dt} = C\Delta K^m, \tag{3.72}$$

where C and m are the material-related parameters and ΔK is the stress intensity function given by

$$\Delta K = 1.2F\Delta S\sqrt{\pi a_0}, \tag{3.73}$$

in which $1.2F$ is the crack shape factor, ΔS is the stress range, and a_0 is the initial crack length. Note that, the parameters in this degradation model have a physical meaning, which may be not suitable in the case of a degradation model of bearing gaps in miter gates due to the lack of physical understanding on the evolution of this type of damage. Another alternative, is to explore degradation models whose tuning parameters are very flexible and do not have a physical meaning

ii. Failure forecasting method (FFM):

The FFM is a method that has been used for capturing the characteristic form of fatigue crack growth "rate" behavior. The advantage of the FFM is that "it does not rely on assumptions of material properties, geometry, or operating conditions, but rather the observed response of the component" (Leung et al. 2019). This leads to a reduction of sources of uncertainty and may provide more confident life predictions. The rate dependant behaviour can be obtained by solving the following differential equation:

$$\frac{d^2a(t)}{dt^2} = A\left(\frac{da(t)}{dt}\right)^b, \tag{3.74}$$

in which A and b are arbitrary constants and $a(t)$ is the observable metric of damage. It is observed that b ≈ 2 for many cases including fatigue crack growth. More details can be found in (Corcoran 2017). Note that, the rate of the observable metric of damage may not be directly available from the measurements obtained specially in the case of bearing gaps in miter gates.

iii. Yang and Manning model:

A simple second order approximation for stochastic crack growth model was proposed by (J. N. Yang and Manning 1996), given by

$$\frac{da(t)}{dt} = X(t)Q(a(t))^{w}, \tag{3.75}$$

where Q and w are parameters that need to be estimated, and $X(t)$ is modelled as a stationary lognormal stochastic process with a unit mean and an auto-covariance function (J. N. Yang and Manning 1996)

$$cov(X(t_1), X(t_2)) = \sigma_x^2 \exp(-\zeta_x |t_2 - t_1|), \tag{3.76}$$

in which σ_x is the standard deviation of $X(t)$, and ζ_x controls the correlation of $X(t)$ over time. If ζ_x^{-1} approaches to zero, $X(t)$ is a stationary lognormal white noise random process and the degradation model can be considered as the most non-conservative stochastic modelling. On the other hand, If ζ_x^{-1} approaches infinity, $X(t)$ is a lognormal random variable and the model becomes to be the most conservative.

In this chapter, a model that is similar to the Yang and Manning model is selected since it does not require a good understanding of the physics and maintains some growth-law features at the same time. The model is given by

$$\frac{da(t)}{dt} = \exp(\sigma_t U(t))Q(a(t))^{w}, \tag{3.77}$$

in which $\sigma_t > 0$ is a degradation stage-dependent variable and $U(t)$ is a stationary standard Gaussian process with auto-correlation function given by

$$cov(U(t_1), U(t_2)) = \exp(-\zeta |t_2 - t_1|), \tag{3.78}$$

where ζ is a correlation related parameter similar to Eq. (3.76). In addition, it assumes that the degradation model $a_t = g(t, \boldsymbol{\theta})$ consists of N_d degradation stages (e.g. $N_d = 5$ in the studied case) and thus the multi-stage gap growth model is defined as

$$\frac{da(t)}{dt} = \exp(\sigma_i U(t)) Q_i (a(t))^{w_i}, i = 1, 2, \cdots, N_d, \tag{3.79}$$

where $a(t)$ is the gap length at time t, σ_i is a standard deviation variable of degradation stage i, and Q_i and w_i are degradation stage-dependent constants.

To account for the effect of degradation stages over time, a generalized Yang and Manning model is further defined as below

$$\frac{da(t)}{dt} = \exp(\sigma(t) U(t)) Q(t) (a(t))^{w(t)}, \tag{3.80}$$

where $\sigma(t)$, $Q(t)$, and $w(t)$ are determined through gap length $a(t)$ as follows

$$\begin{cases} \sigma(t) = \sigma_j \\ Q(t) = Q_j, \text{ where } j = h_s(a(t)), \\ w(t) = w_j \end{cases} \tag{3.81}$$

in which $j = h_s(a(t))$ is a function that maps gap length $a(t)$ into degradation stage and is given by

$$j = h_s(a(t)) = \begin{cases} 1, \text{if } a(t) \in [0, e_1], \\ 2, \text{if } a(t) \in [e_1, e_2], \\ \vdots \\ N_d, \text{if } a(t) \in [e_{N_d - 1}, \infty), \end{cases}, \tag{3.82}$$

where $e_i < e_{i+1}, \forall i = 1, 2, \cdots, N_d - 2$ are the threshold gap lengths that determine the transition of degradation stages. Note that the mapping function (i.e. $j = h_s(a(t))$) for the gap growth model is different from the mapping function (i.e. $R = h_{OCA}(a_t, \boldsymbol{\beta})$) defined by the OCA protocol. The mapping function $j = h_s(a(t))$ is governed by the underlying degradation physics while $R = h_{OCA}(a_t, \boldsymbol{\beta})$ is defined by the engineers using OCA protocols.

Moreover, in order to account for the randomness of the threshold gap lengths that govern the transition of degradation stages, $e_i, \forall i = 1, 2, \cdots, N_d - 1$ are described as Gaussian random variables as follows

$$e_i \sim N(\mu_i, \sigma_e^2), \forall i = 1, 2, \cdots, N_d - 1, \tag{3.83}$$

where $N(\mu_i, \sigma_e^2), i = 1, 2, \cdots, N_d - 1$ stands for normal distribution with mean μ_i and standard deviation σ_e.

In discrete-time space, the above degradation model given in Eqs. (3.80) through (3.83) is rewritten as

$$a(t_{k+1}) = a(t_k) + \exp(\sigma(t_{k+1})U(t_{k+1}))Q(t_{k+1})(a(t_k))^{w(t_{k+1})}, \forall k = 1, 2, \cdots, N_t, \tag{3.84}$$

$$\begin{cases} \sigma(t_{k+1}) = \sigma_j \\ Q(t_{k+1}) = Q_j, \text{ where } j = h_s(a(t_k)), \\ w(t_{k+1}) = w_j \end{cases} \tag{3.85}$$

where N_t is the number of analysis time steps in the time duration of interest.

To summarize, in the selected degradation model, the parameters $\boldsymbol{\theta}$ of the degradation model include the following parameters

$$\boldsymbol{\theta} \triangleq \left\{ \boldsymbol{\theta}_1, \boldsymbol{\theta}_2, \cdots, \boldsymbol{\theta}_{N_d}, \zeta, \mu_1, \mu_2, \cdots, \mu_{N_d - 1}, \sigma_e \right\}, \tag{3.86}$$

where $\boldsymbol{\theta}_j \triangleq \{\sigma_j, Q_j, w_j,\ j = 1, 2, \cdots, N_d\}$.

The next section will discuss the prediction of $\hat{\mathbf{P}}(\boldsymbol{\theta})$ for a given $\boldsymbol{\theta}$.

(b) *Prediction of* $\hat{\mathbf{P}}(\boldsymbol{\theta})$ *using the degradation model*

As mentioned previously, $\hat{\mathbf{P}}(\boldsymbol{\theta}) \triangleq \{\hat{P}(I^s_{j,t+1} \mid I^s_{i,t}; \boldsymbol{\theta}), i = 1, 2, \cdots, 6;\ j = i, \cdots, 6\}$, for a given $\mathbf{e} \triangleq \{e_1, e_2, \cdots, e_{N_d-1}\}$, $\hat{P}(I^s_{j,t+1} \mid I^s_{i,t}; \boldsymbol{\theta}, \mathbf{e})$ is given by

$$\hat{P}(I^s_{j,t+1} \mid I^s_{i,t}; \boldsymbol{\theta}, \mathbf{e}) = \frac{P(I^s_{j,t+1} \cap I^s_{i,t}; \boldsymbol{\theta}, \mathbf{e})}{P(I^s_{i,t}; \boldsymbol{\theta}, \mathbf{e})}, \tag{3.87}$$

where

$$P(I^s_{i,t}; \boldsymbol{\theta}, \mathbf{e}) = \begin{cases} \Pr\{0 \le a(t) < \beta_i\}, \text{ if } i = 1, \\ \Pr\{\beta_{i-1} \le a(t) < \beta_i\}, \text{ if } 1 < i < 6, \ \forall i = 1, 2, \cdots, 6 \\ \Pr\{\beta_{i-1} \le a(t) < \infty\}, \text{ if } i = 6, \end{cases} \tag{3.88}$$

$$\begin{aligned} &P(I^s_{j,t+1} \cap I^s_{i,t}; \boldsymbol{\theta}, \mathbf{e}) = \Pr\{\beta_{i-1} \le a(t) < \beta_i \cap \beta_{j-1} \le a(t+12) < \beta_j\}, \\ &\forall i = 1, 2, \cdots, 6;\ j = i, \cdots, 6, \end{aligned} \tag{3.89}$$

in which $\beta_0 = 0$, $a(t)$ and $a(t+12)$ are obtained through the degradation model given in Sec. 3.8.2.1 conditioned on given $\boldsymbol{\theta}$ and $\mathbf{e}$, and $\beta_i = \infty$ or $\beta_j = \infty$ if i=6 or j=6. The two time steps used in Eq. (3.89) are t and $t+12$ since the inspection interval is one year, and the unit of the time step of the discrete time degradation model (i.e. Eqs. (3.84) and (3.85)) is one month.

Since the inspection time t can be any time in the lifetime of the gate, Eqs. (3.87) through (3.89) are rewritten as follows

$$\begin{aligned} &\hat{P}(I^s_{j,t+1} \mid I^s_{i,t}; \boldsymbol{\theta}, \mathbf{e}) \\ &= \int_{t_l}^{t_u} \hat{P}(I^s_{j,t+1} \mid I^s_{i,t}; \boldsymbol{\theta}, \mathbf{e}, t) f(t) dt, \\ &= \int_{t_l}^{t_u} \frac{\Pr\{\beta_{i-1} \le a(t) < \beta_i \cap \beta_{j-1} \le a(t+12) < \beta_j\}}{\Pr\{\beta_{i-1} \le a(t) < \beta_i\}} \frac{1}{t_u - t_l} dt, \end{aligned} \tag{3.90}$$

where t_l and t_u are respectively the lower and upper bounds of the time duration of interest.

In general, Eqs. (3.90) is analytically intractable due to the complicated transition between stages, even though several analytical expressions have been developed for degradation model with only one stage based on assumptions and simplifications (Y. Liu et al. 2016). In this chapter, the simulation-based method is employed. For a given $\boldsymbol{\theta}$ and $\mathbf{e}$, the degradation of the gap is first simulated using the discrete-time model given in Eqs. (3.84) and (3.85). From the simulation, the samples obtained of the gap length are denoted as $\mathbf{a}_s(\boldsymbol{\theta}, \mathbf{e}) \triangleq \left\{a_{ij}, i = 1, 2, \cdots, n_{MCS}; j = 1, 2, \cdots, N_t\right\}$, where a_{ij} is the *i*-th realization of the gap growth curve at time step t_j, n_{MCS} is the number of samples at each time step and is the total number of simulation time steps. Based on the simulated samples of the gap growth, Eq. (3.90) is approximated as

$$\hat{P}(I^s_{j,t+1} \mid I^s_{i,t}; \boldsymbol{\theta}, \mathbf{e}) \approx \frac{1}{N_t - 12} \sum_{k=1}^{N_t-12} \frac{\Pr\{\beta_{i-1} \le a(t_k) < \beta_i \cap \beta_{j-1} \le a(t_k + 12) < \beta_j\}}{\Pr\{\beta_{i-1} \le a(t_k) < \beta_i\}}. \tag{3.91}$$

In the above equation, $\dfrac{\Pr\{\beta_{i-1} \le a(t_k) < \beta_i \cap \beta_{j-1} \le a(t_k + 12) < \beta_j\}}{\Pr\{\beta_{i-1} \le a(t_k) < \beta_i\}}$ is estimated using $\mathbf{a}_s$ as

$$\begin{aligned} &\frac{\Pr\{\beta_{i-1} \le a(t_k) < \beta_i \cap \beta_{j-1} \le a(t_k + 12) < \beta_j\}}{\Pr\{\beta_{i-1} \le a(t_k) < \beta_i\}} \\ &\approx \frac{1}{n_{MCS}} \frac{\sum_{q=1}^{n_{MCS}} \Lambda((\beta_{i-1} \le a_{q,k} < \beta_i) \cap (\beta_{j-1} \le a_{q,k+12} < \beta_j))}{\sum_{q=1}^{n_{MCS}} \Lambda(\beta_{i-1} \le a_{q,k} < \beta_i)}, \end{aligned} \tag{3.92}$$

where $\Lambda(E)$ is an indicator function, $\Lambda(E) = 1$ if event E is true; $\Lambda(E) = 0$ if event E is false. In the above equation, event E represents $(\beta_{i-1} \le a_{q,k} < \beta_i) \cap (\beta_{j-1} \le a_{q,k+12} < \beta_j)$ and $\beta_i \le a_{q,k} < \beta_{i+1}$.

Combining Eqs. (3.91) and (3.92), the following is obtained

$$\hat{P}(I^s_{j,t+1} \mid I^s_{i,t}; \boldsymbol{\theta}, \mathbf{e}) \approx \frac{1}{(N_t - 12) n_{MCS}} \sum_{k=1}^{N_t - 12} \frac{\sum_{q=1}^{n_{MCS}} \Lambda((\beta_{i-1} \le a_{q,k} < \beta_i) \cap (\beta_{j-1} \le a_{q,k+12} < \beta_j))}{\sum_{q=1}^{n_{MCS}} \Lambda(\beta_{i-1} \le a_{q,k} < \beta_i)}. \tag{3.93}$$

The above probability estimate is conditioned on $\boldsymbol{\theta}$ and $\mathbf{e}$. After considering the uncertainty in threshold gap lengths, $\mathbf{e} = [e_1, e_2, \cdots, e_{N_d - 1}]$, that determines the transition of degradation stages, the marginalization of $\hat{P}(I^s_{j,t+1} \mid I^s_{i,t}; \boldsymbol{\theta})$ can be written as

$$\begin{aligned} \hat{P}(I^s_{j,t+1} \mid I^s_{i,t}; \boldsymbol{\theta}) &= \int \hat{P}(I^s_{j,t+1} \mid I^s_{i,t}; \boldsymbol{\theta}, \mathbf{e}) f_{\mathbf{e}}(\mathbf{e} \mid \boldsymbol{\theta}) \mathbf{de}, \\ &= \int\int \cdots \int \hat{P}(I^s_{j,t+1} \mid I^s_{i,t}; \boldsymbol{\theta}, \mathbf{e}) \prod_{k=1}^{N_d - 1} \phi\left(\frac{e_i - \mu_i}{\sigma_e}\right) de_1 de_2 \cdots de_{N_d - 1}, \end{aligned} \tag{3.94}$$

where $f_{\mathbf{e}}(\mathbf{e} \mid \boldsymbol{\theta})$ is the joint PDF of $e_i, \text{and } e_i < e_{i+1}, \forall i = 1, 2, \cdots, N_d - 2$, and $\phi(\cdot)$ is the PDF of a standard normal distribution.

In this chapter, a sampling-based approach is employed to estimate Eq. (3.94). Using Eqs. (3.87) through (3.94), $\hat{\mathbf{P}}(\boldsymbol{\theta}) \triangleq \{\hat{P}(I^s_{j,t+1} \mid I^s_{i,t}; \boldsymbol{\theta}), i = 1, 2, \cdots, 6; j = i, \cdots, 6\}$ can be estimated for given $\boldsymbol{\theta}$. The estimated $\hat{\mathbf{P}}(\boldsymbol{\theta})$ can then be used in Eq. (3.71) to estimate the parameters $\boldsymbol{\theta}$ of the degradation model. Table 3.3 provides a pseudocode for this process.

Table 3.3: Estimation of $\hat{\mathbf{P}}(\boldsymbol{\theta})$ for given $\boldsymbol{\theta} \triangleq \{\boldsymbol{\theta}_1, \boldsymbol{\theta}_2, \cdots, \boldsymbol{\theta}_{N_d}, \zeta, \mu_1, \mu_2, \cdots, \mu_{N_d - 1}, \sigma_e\}$

Step	Description
1	**Initialization**: Generate samples of $U(t_1), \cdots, U(t_{N_t})$ for a given correlation length ζ, samples of $e_i < e_{i+1}, \forall i = 1, 2, \cdots, N_d - 2$ based on $\mu_1, \mu_2, \cdots, \mu_{N_d - 1}, \sigma_e$, and initial samples of $a(t_0)$
2	Sort the samples of $e_i < e_{i+1}, \forall i = 1, 2, \cdots, N_d - 1$
3	**For** $k = 1, 2, \cdots, N_t$:

4	Map gap length $a(t_{k-1})$ into degradation stage using Eq. (3.82)
5	Obtain samples of $a(t_k)$ using Eqs. (3.84) and (3.85)
	End
6	Obtain samples of $a(t_k)$, $k=1,2,\cdots,N_t$
7	Reshape the data and obtain samples of $a(t_k)$ and $a(t_k+12)$
8	Compute $\hat{\mathbf{P}}(\boldsymbol{\theta})$ using Eqs. (3.93) and (3.94) for a given β defined in Eq. (3.69)

The next section discusses how to estimate $\boldsymbol{\theta}$ by solving the optimization model given in Eq. (3.71).

3.8.2.2 Estimation of degradation model parameters $\boldsymbol{\theta}$

In this chapter, the Generalized Simulated Annealing (GSA) method is used to solve the optimization problem. This method is a stochastic approach for approximating the global optimum of the cost function shown in Eq. (3.71). The GSA method is mainly used when processing complicated non-linear objective functions with a large number of local minima. The Cauchy-Lorentz visiting distribution is used to generate a trial jump distance $\Delta\boldsymbol{\theta}(t)$ of the variable $\boldsymbol{\theta}(t)$,

$$\Delta\boldsymbol{\theta}(t) \propto \frac{[T_{q_v}(t)]^{-\frac{D}{3-q_v}}}{[1+(q_v-1)\frac{p^2}{[T_{q_v}(t)]^{\frac{2}{3-q_v}}}]^{\frac{1}{q_v-1}+\frac{D-1}{2}}},\ p\sim U(0,1),\ T_{q_v}(t)=T_{q_v}(1)\frac{2^{q_v-1}-1}{(1+t)^{q_v-1}-1}, \tag{3.95}$$

where D is the dimension of the variable space, $T_{q_v}(t)$ is the artificial temperature, which is a global time-varying parameter, and q_v is a time-invariant parameter that controls the rate of cooling. To avoid local minima, the trial jump uses an acceptance probability using a Metropolis algorithm. In other words, the proposed trial jump is always accepted if it is downhill and it is accepted with a probability if the jump is uphill, which allows to explore the space outside the local minima. For

more details on this method, the reader is referred to (Yang Xiang et al. 2013; Y. Xiang and Gong 2000).

After the parameters θ of the degradation model $a_t = g(t, \theta)$ are estimated, the degradation model can be used for damage diagnostics and prognostics, which is briefly discussed in the next section.

3.8.3 Diagnostics and prognostics of using the degradation model

Let $\mathbf{s}_i = [s_{i1}, s_{i2}, \cdots, s_{iN_S}]$ be the strain measurement data at time step t_i, where N_S is the number of strain sensors providing data. The posterior probability density function of the gap length $a_k \triangleq a(t_k)$ at time step t_k conditioned on strain measurements $\mathbf{s}_{1:k} \triangleq \{\mathbf{s}_1, \mathbf{s}_2, \cdots, \mathbf{s}_k\}$ collected up to t_k is then given by

$$f(a_k \mid \mathbf{s}_{1:k}) = \frac{f(\mathbf{s}_k \mid a_k) f(a_k \mid \mathbf{s}_{1:k-1})}{\int f(\mathbf{s}_k \mid a_k) f(a_k \mid \mathbf{s}_{1:k-1}) da_k} \propto f(\mathbf{s}_k \mid a_k) f(a_k \mid \mathbf{s}_{1:k-1}), \tag{3.96}$$

where $f(\mathbf{s}_k \mid a_k)$ is the likelihood function (from the measurement equation) of observing $\mathbf{s}_k$ for given a_k at time step t_k, and $f(a_k \mid \mathbf{s}_{1:k-1})$ is given by

$$f(a_k \mid \mathbf{s}_{1:k-1}) = \int f(a_k \mid a_{k-1}) f(a_{k-1} \mid \mathbf{s}_{1:k-1}) da_{k-1}, \tag{3.97}$$

where $f(a_k \mid a_{k-1})$ is the PDF of a_k for a given a_{k-1} obtained from the state equation, e.g., the degradation model $a_t = g(t, \theta)$ obtained in Sec. 3.8.2. The following state and measurement equations are thus considered,

$$\begin{aligned} &\text{State equation}: a_{k+1} = a_k + \exp(\sigma_{k+1} U_{k+1}) Q_{k+1} (a_k)^{w_{k+1}}, \\ &\text{Measurement equation}: \mathbf{s}_{k+1} = \hat{g}(a_{k+1}, \mathbf{x}_{k+1}) + \varepsilon, \end{aligned} \tag{3.98}$$

where a_{k+1}, a_k, σ_{k+1}, U_{k+1}, Q_{k+1}, and w_{k+1} are respectively $a(t_{k+1})$, $a(t_k)$, $\sigma(t_{k+1})$, $U(t_{k+1})$, $Q(t_{k+1})$, and $w(t_{k+1})$ given in Eq. (3.84), and ε is the measurement noise given by

$$\varepsilon \sim N(\mathbf{0}, \sigma_{obs}^2 \mathbf{I}), \tag{3.99}$$

in which σ_{obs} is the standard deviation of the measurement noise and $\hat{g}(a_{k+1}, \mathbf{x}_{k+1})$ is a model for the prediction of strain response for given gap state a_{k+1} and other input variables $\mathbf{x}_{k+1}$ such as water levels and temperature.

Since the original FE model $\hat{g}(a_{k+1}, \mathbf{x}_{k+1})$, is usually used to replace the original FE model. The equations above can then be solved recursively in a timely manner. A Kriging surrogate model is constructed in this paper to map the relation from gap length (and other model parameters such as hydrostatic and thermal loads applied to miter gates) to the strain response at the strain gauges locations. Based on the above degradation model, the remaining useful life of a miter gate can be estimated at every time step t_k as

$$\Pr\{T_{RUL} \le t_m \mid \mathbf{s}_{1:k}\} = \frac{1}{N_{PF}} \sum_{i=1}^{N_{PF}} \Lambda\{a(i, j+k) > a_e, \exists j = 1, 2, \cdots, m\}, \tag{3.100}$$

in which T_{RUL} stands for the remaining useful life, N_{PF} is the number of samples used in the state estimation using Eq. (3.98), a_e is the gap failure threshold, and $a(i, j+k)$ is the *i*-th realization of the gap length at the $(j+k)$-th time step. In the next section, a miter gate case study is used to demonstrate the effectiveness of the proposed framework.

3.8.4 Case Study: Miter Gate

The term, $\hat{P}\left(I_{j,t+1} \middle| I_{i,t}, \boldsymbol{\theta}\right)$, is the derived transition matrix obtained from the stochastic degradation model. To calculate this matrix, it is necessary to map the gap length value from its

continuous form to the discrete OCA ratings using β defined in Eq. (3.69). β is also needed in the evaluation of gap length using OCA ratings by the field engineers. Table 3.2 shows the mapping between gap length, $h_n = a(t)$, to its corresponding OCA rating. For the values on this table, the mapping is assumed to be known and would be treated as the inspection policy.

For the OCA ratings given in the aforementioned table, an example of the report OCA transition matrix $\mathbf{P}_{\text{Report}}$ is given as

$$\mathbf{P}_{\text{Report}} = \begin{bmatrix} 7.76e-1 & 2.13e-1 & 5.25e-3 & 2.16e-3 & 1.85e-3 & 2.47e-3 \\ 0 & 9.28e-1 & 4.40e-2 & 1.74e-2 & 7.94e-3 & 2.60e-3 \\ 0 & 0 & 8.70e-1 & 1.19e-3 & 6.64e-3 & 4.78e-3 \\ 0 & 0 & 0 & 9.40e-1 & 5.03e-2 & 9.39e-3 \\ 0 & 0 & 0 & 0 & 8.65e-1 & 1.35e-1 \\ 0 & 0 & 0 & 0 & 0 & 1 \end{bmatrix}. \quad (3.101)$$

As discussed in Sec. 3.8.1, the reported OCA transition matrix may have errors due to the human observation errors of the field engineers. Next, a demonstration is presented of how to obtain the underlying true transition matrix based on the human error matrix using the proposed method. After that, a discussion is presented on how to obtain a gap degradation model and how to use it to perform diagnostics and prognostics.

3.8.4.1 Mapping the reported OCA transition matrix to the true OCA transition matrix for different human error scenarios

As indicated by (L. E. Campbell et al. 2020), this human error/performance may be evaluated to quantify the reliability or accuracy of these inspections. For demonstration purposes, four different cases as shown in Eqs. (3.102) to (3.105) will be evaluated to see the effect of human error on the OCA transition matrix and the degradation model. Case 1 assumes that the inspection is performed without any human observation errors, in other words, $\mathbf{P}_{\text{human}}$ would be the identity

matrix. Case 2 represents the behavior of an inspector that regularly tends to assess a structural component to be in a better condition than reality. For example, as shown in Eq. (3.103), there is a 20% probability that an inspector reports a rating A to a structural component when in reality the true state of the component belongs to rating B. Contrarily, Case 3 represents an inspector that tends to be very conservative. For example, as shown in Eq. (3.104), there is a 12% probability that an inspector reports a rating F to a structural component when in reality the true state of the component belongs to rating D. Case 4 represents a case in between case 2 and case 3.

$$\mathbf{P}_{\text{human}}^{\text{case1}} = \mathbf{I}_{6x6}, \tag{3.102}$$

$$\mathbf{P}_{\text{human}}^{\text{case2}} = \begin{bmatrix} 1 & 0 & 0 & 0 & 0 & 0 \\ 0.04 & 0.96 & 0 & 0 & 0 & 0 \\ 0 & 0.40 & 0.60 & 0 & 0 & 0 \\ 0 & 0.03 & 0.17 & 0.80 & 0 & 0 \\ 0 & 0 & 0 & 0.03 & 0.97 & 0 \\ 0 & 0 & 0 & 0 & 0.03 & 0.97 \end{bmatrix}, \tag{3.103}$$

$$\mathbf{P}_{\text{human}}^{\text{case3}} = \begin{bmatrix} 0.60 & 0.40 & 0 & 0 & 0 & 0 \\ 0 & 0.90 & 0.08 & 0.02 & 0 & 0 \\ 0 & 0 & 0.90 & 0.10 & 0 & 0 \\ 0 & 0 & 0 & 0.95 & 0.05 & 0 \\ 0 & 0 & 0 & 0 & 0.98 & 0.02 \\ 0 & 0 & 0 & 0 & 0 & 1 \end{bmatrix}, \tag{3.104}$$

$$\mathbf{P}_{\text{human}}^{\text{case4}} = \begin{bmatrix} 0.9 & 0.1 & 0 & 0 & 0 & 0 \\ 0.05 & 0.9 & 0.03 & 0.02 & 0 & 0 \\ 0.04 & 0.06 & 0.8 & 0.05 & 0.035 & 0.015 \\ 0.015 & 0.035 & 0.05 & 0.8 & 0.6 & 0.04 \\ 0 & 0.015 & 0.035 & 0.05 & 0.8 & 0.1 \\ 0 & 0 & 0 & 0 & 0 & 1 \end{bmatrix}, \tag{3.105}$$

As shown in Eq. (3.58), the true OCA transition matrix ($\mathbf{P}_{OCA}$) can be obtained after knowing the reported OCA transition matrix ($\mathbf{P}_{Report}$, Eq. (3.101)) and the human observation errors ($\mathbf{P}_{human}$, Eqs. (3.102) through (3.105)). Using the different cases of human observation errors mentioned earlier, the true OCA transition matrix for each case is shown in Eqs. (3.106) to (3.109) respectively.

$$\mathbf{P}_{OCA}^{case1} = \begin{bmatrix} 7.76e-1 & 2.13e-1 & 5.25e-3 & 2.16e-3 & 1.85e-3 & 2.47e-3 \\ 0 & 9.28e-1 & 4.40e-2 & 1.74e-2 & 7.94e-3 & 2.60e-3 \\ 0 & 0 & 8.70e-1 & 1.19e-3 & 6.64e-3 & 4.78e-3 \\ 0 & 0 & 0 & 9.40e-1 & 5.03e-2 & 9.39e-3 \\ 0 & 0 & 0 & 0 & 8.65e-1 & 1.35e-1 \\ 0 & 0 & 0 & 0 & 0 & 1 \end{bmatrix}, \quad (3.106)$$

$$\mathbf{P}_{OCA}^{case2} = \begin{bmatrix} 7.02e-1 & 2.89e-1 & 7.01e-3 & 0 & 0 & 2.48e-3 \\ 0 & 9.08e-1 & 7.03e-2 & 1.06e-2 & 8.26e-3 & 2.49e-3 \\ 0 & 0 & 8.42e-1 & 1.47e-1 & 6.04e-3 & 4.73e-3 \\ 0 & 0 & 0 & 9.48e-1 & 4.55e-2 & 6.71e-3 \\ 0 & 0 & 0 & 0 & 8.60e-1 & 1.40e-1 \\ 0 & 0 & 0 & 0 & 0 & 1 \end{bmatrix}, \quad (3.107)$$

$$\mathbf{P}_{OCA}^{case3} = \begin{bmatrix} 7.89e-1 & 2.02e-1 & 3.02e-3 & 1.42e-3 & 1.87e-3 & 2.35e-3 \\ 0 & 9.50e-1 & 2.72e-2 & 1.19e-2 & 8.10e-3 & 2.48e-3 \\ 0 & 0 & 8.40e-1 & 1.48e-1 & 4.27e-3 & 7.46e-3 \\ 0 & 0 & 0 & 8.66e-1 & 1.17e-1 & 1.74e-2 \\ 0 & 0 & 0 & 0 & 8.69e-1 & 1.31e-1 \\ 0 & 0 & 0 & 0 & 0 & 1 \end{bmatrix}, \quad (3.108)$$

and

$$\mathbf{P}_{\text{OCA}}^{\text{case4}} = \begin{bmatrix} 5.63e-1 & 4.34e-1 & 3.17e-3 & 0 & 0 & 0 \\ 0 & 9.37e-1 & 4.11e-2 & 1.27e-2 & 7.80e-3 & 1.15e-3 \\ 0 & 0 & 8.93e-1 & 9.66e-2 & 8.35e-3 & 1.59e-3 \\ 0 & 0 & 0 & 9.29e-1 & 7.13e-2 & 0 \\ 0 & 0 & 0 & 0 & 9.14e-1 & 8.61e-2 \\ 0 & 0 & 0 & 0 & 0 & 1 \end{bmatrix}, \quad (3.109)$$

The human observation error has a significant effect on the true OCA transition matrix. For Case 1, the true OCA transition matrix ($\mathbf{P}_{\text{OCA}}^{\text{case1}}$, Eq. (3.106)) is equal to the reported OCA transition matrix ($\mathbf{P}_{\text{Report}}$, Eq. (3.101)) and consistent when human observation error is not present. For Case 2, the true OCA transition matrix ($\mathbf{P}_{\text{OCA}}^{\text{case2}}$, Eq. (3.107)) shows a decrease on the majority of the transition probabilities located in the diagonal when Cases 1 and 2 are compared. In other words, the degradation model should tend to deteriorate faster at the beginning. Contrarily, the true OCA transition matrix ($\mathbf{P}_{\text{OCA}}^{\text{case3}}$, Eq. (3.108)) for Case 3 shows that the majority of the transition probabilities located in the diagonal shows an increase when Cases 1 and 3 are compared. Note that not all the diagonal elements show a decrease due to the *error cancellations* in first and second assessments of the OCA ratings. But in general, the degradation model of Case 3 degrades slower than that of Case 1 (as shown in the results in Sec. 5.2). As expected, Case 4 (i.e. Eq. (3.109)) shows some of the diagonal entries increase while the other diagonals entries decrease when Cases 1 and 4 are compared. Even though effects of the human observation errors on the transition matrix is very complicated due to the "error cancellation" in the OCA ratings, the proposed approach can account for the complicated effects by mapping the reported OCA transition matrix to the true OCA transition matrix.

In the next subsection, the underlying degradation models will be identified based on the OCA transition matrices of different level of human observations errors.

3.8.4.2 Gap growth modeling based on OCA transition matrix

Figure 3.29 shows a flowchart of how to obtain the transition matrix from the stochastic degradation model, which is used to estimate the gap growth model parameters based on the OCA transition matrices obtained above.

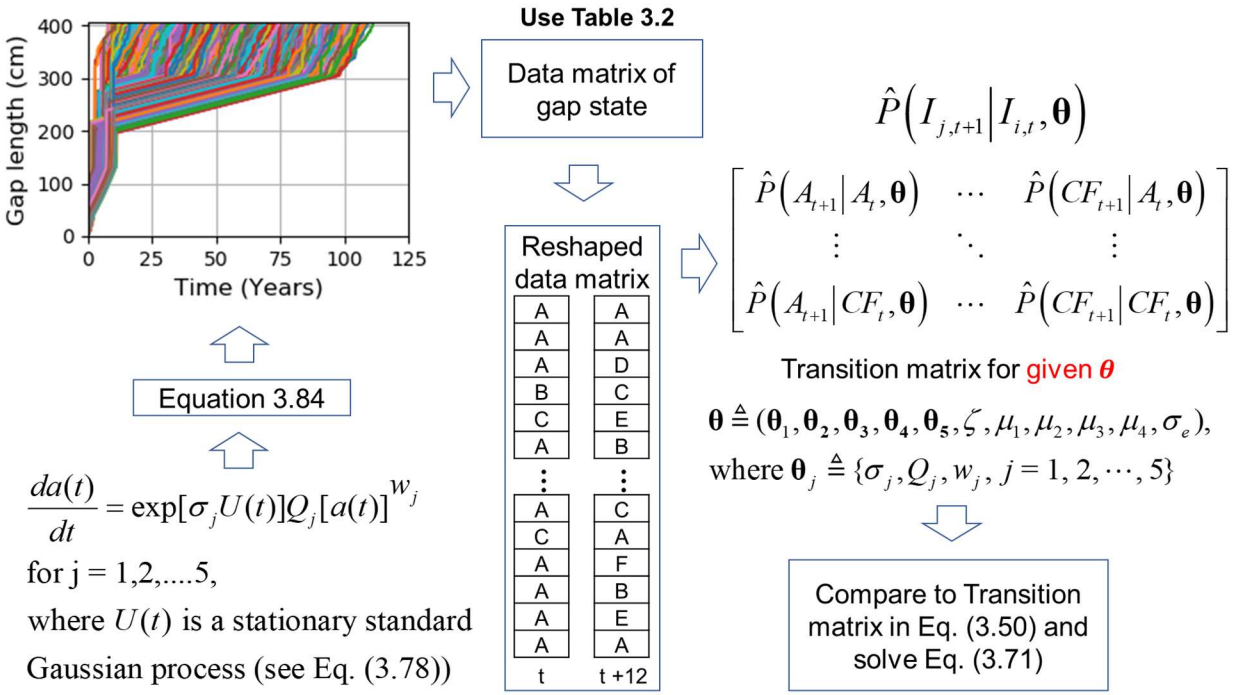

Figure 3.29: Flowchart to obtain simulated transition matrix from a gap degradation model

Figure 3.30 shows the cumulative minimum error after each iteration of the stochastic degradation model after tuning 21 parameters for four different cases (i.e. Eq. (3.102) through (3.105)). The GSA optimization algorithm successfully achieves a very small error for each case.

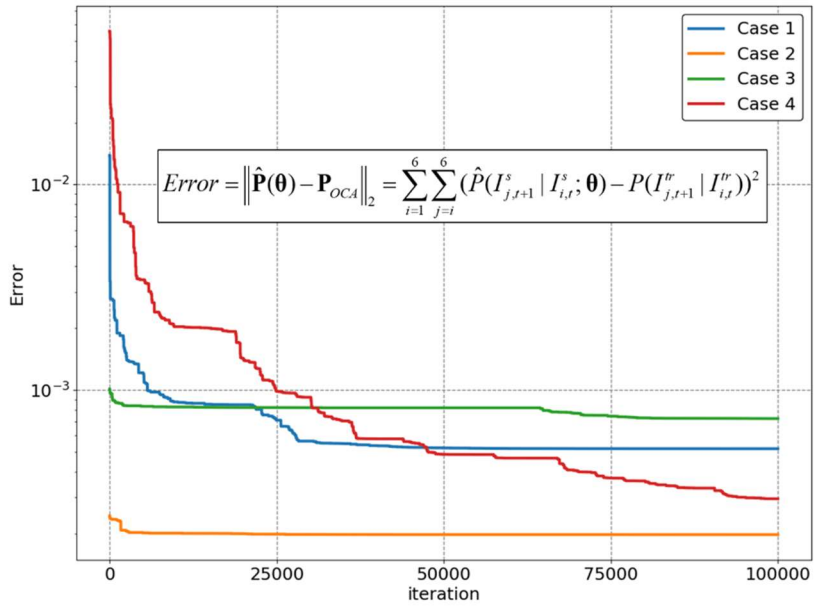

Figure 3.30: Cumulative minimum error after each iteration

Figure 3.31 presents the simulated gap growth curves corresponding to the four scenarios after identifying the optimal parameters of the gap growth model using GSA.

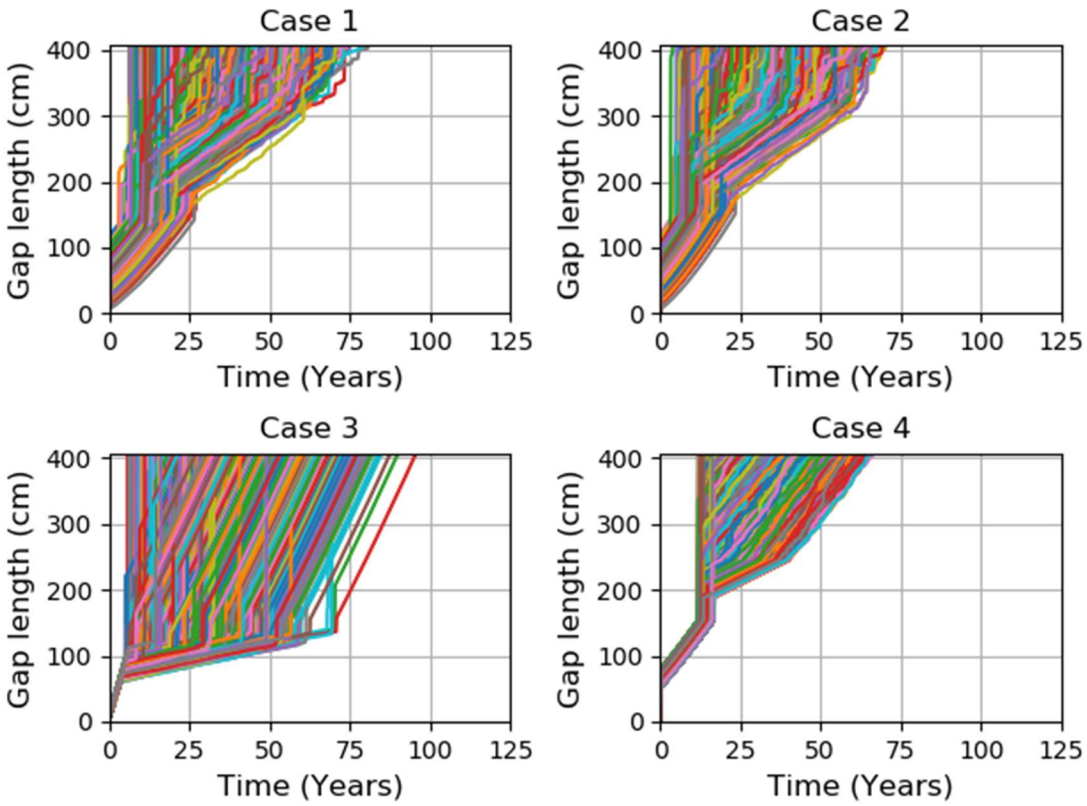

Figure 3.31: Gap growth model comparison for different human error cases

Comparing the gap growth curves of Case 2 to 4 with Case 1, similar conclusions can be obtained as that from comparing the OCA transition matrices (i.e. Eq. (3.106) to (3.109)). For Case 2, the degradation model should tend to deteriorate faster at the beginning as shown in Figure 3.31, which can also be seen in Figure 10 when comparing Case 1 and 2. Contrarily, for Case 3, the degradation model should tend to deteriorate slower as shown in Figure 3.31, when Cases 1 and 3 are compared.

Figure 3.32 shows the time distribution when the curves shown in Figure 3.31 exceed four different thresholds. As expected, the time distribution for Case 2 shifts to earlier time region (i.e. left) compared to its counterpart of Case 1. Conversely, the time distribution for Case 3 shifts towards later time region (i.e. right) if compared to Case 1. Consistently, the result for Case 4 in general shows time distributions between that of Case 2 and 3.

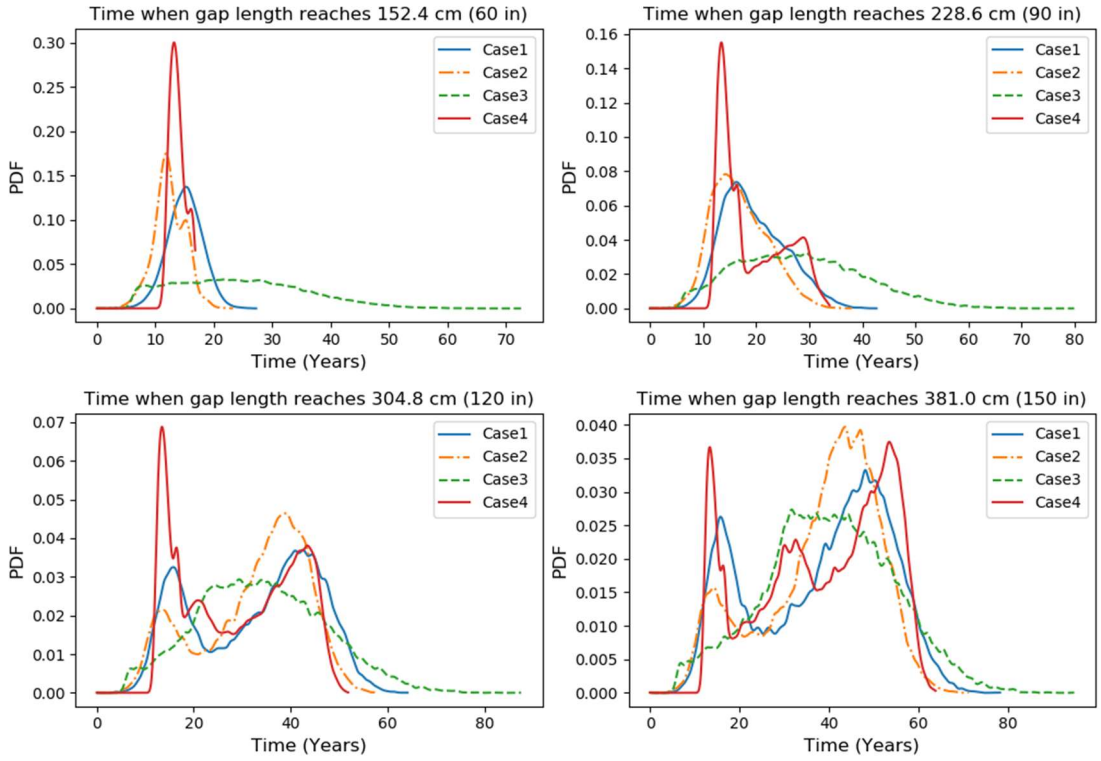

Figure 3.32:Time distribution when gap length, a, exceeds 381 cm. (CF) for different human error cases

The above results show that the proposed method is able to effectively investigate the effects of human errors on the OCA transition matrix and the gap growth of the gate over time.

3.8.4.3 Bearing gap diagnosis and prognosis using SHM and gap growth modeling

Data is extracted from the Greenup FE model (see Figure 3.18) to train a Kriging surrogate model. Two different surrogate models are built, one that would be used to generate the synthetic data (representing the true physics) and the other to be calibrated during the estimation process. Figure 3.33(a) shows the updated predictions of the gap length against the true damage using the proposed gap growth model in the estimation process.

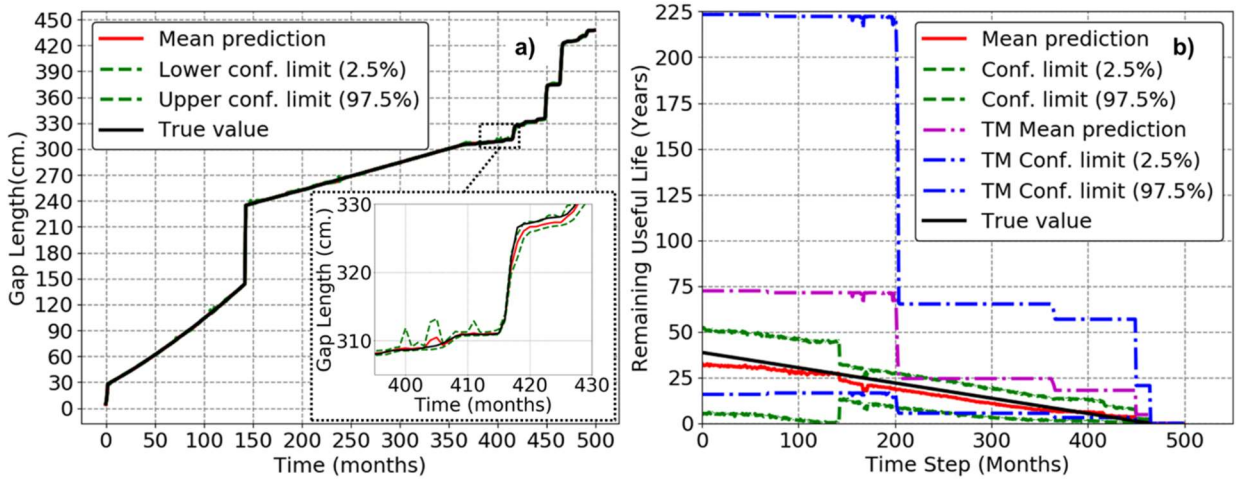

Figure 3.33: (a) Damage detection over time, and (b) RUL using the proposed method (where "TM" stands for the transition matrix-based approach as reviewed in Sec. 3.7.4)

As shown in Figure 3.33(b), the proposed method can accurately capture remaining useful life (RUL) while effectively performing damage detection (i.e. Fig. 3.33(a)). In addition, the results show that the uncertainty in the RUL estimate can be reduced significantly by mapping the OCA transition matrix into a higher-precision gap growth model, compared to that of the transition matrix-based method as reviewed in Sec. 3.6. The jumps in Figure 3.33(b) are attributed to the discrete nature of the OCA ratings, which are more pronounced in the predictions using the TM

based approach. More details of the TM approach can be found in (M. A. Vega, Hu, and Todd 2020). Results of this case study demonstrate the efficacy of the proposed method.

3.9. Conclusions

This paper presents a novel framework for failure diagnostics and prognostics for bearing damaged gaps in quoin block components of a miter gate. This framework is based on integrating abstracted inspection data and structural health monitoring data. This work is especially useful when the evolution of the damage mechanism is not well known or understood either due to the lack of enough data that relates damage to sensor information or the lack of a physics-based model that describes the evolution of the damage. It is assumed that the only available data that describes the damage evolution are based on abstracted rating assessments such as the OCA ratings. An approach is first proposed to map the reported OCA transition matrix into the underlying true OCA transition matrix. Based on that, the proposed framework successfully integrates a stochastic degradation model built from the OCA Markov transition matrix and shows how this model is suitable for integration with continuous monitoring. The damage diagnosis via physics-based FE model updating using the degradation model proposed provides satisfactory results. Also, to demonstrate the improvement on the gap length prognosis, the updated over time RUL was compared against its true value. Results of a case study show that (1) the proposed framework can effectively address the issue of human reporting errors in the OCA ratings in the prognostics of miter gate, and (2) the uncertainty in the RUL estimate can be reduced significantly using the proposed framework. Note that, this approach can be applicable to different components in miter gates, which may have different transition matrices values. However, further work needs to be done to extend this methodology from miter gate components to the miter gate system level (e.g. including all critical miter gate components); that work would need to focus on how failure mode probabilities from

multiple causes/sources are correlated and propagate towards a more global limit state failure definition. In this paper, optimization-based methods are employed to identify the underlying true OCA transition matrices as well as the gap growth model parameters. These procedures can be integrated together in a full-Bayesian framework. The development of the full-Bayesian framework and the investigation of other alternative approaches will be studied in our future work.

3.10. Preview to Chapter 4

As mentioned in section 3.9, more components in miter gates need to be considered to implement a CBM framework applicable to the system level. For these reason, other forms of damage in miter gates needs to be investigated. The next chapter presents a damage diagnosis framework considering two more forms of damage in miter gates beyond the degradation of bearing gaps.

3.11. Remarks

Portions of this dissertation have been published or are currently being considered for publication. Chapter 3 is composed by two articles that have been submitted and currently under review for publication:

Vega, Manuel A., Zhen Hu, and Michael D. Todd. 2020. "Optimal Maintenance Decisions for Deteriorating Quoin Blocks in Miter Gates Subject to Uncertainty in the Condition Rating Protocol." Reliability Engineering & System Safety 204. https://doi.org/10.1016/j.ress.2020.107147.

Vega, Manuel A., Zhen Hu, Travis B. Fillmore, Matthew D. Smith, and Michael D. Todd. 2020. "Integration of Abstracted Inspection Data and Structural Health Monitoring for Damage Prognosis of Miter Gates (under review)." Reliability Engineering & System Safety.

Chapter 4

EFFICIENT BAYESIAN INFERENCE OF MITER GATES USING HIGH-FIDELITY MODELS

4.1. Abstract

Continuous monitoring of miter gates used in navigation locks is desirable in order to prioritize maintenance and avoid unexpected failures. Substantial economic losses to the marine cargo and associated industries are caused by the closure of these inland waterway structures. Strain gauges are often installed in many of these miter gates for data collection, and various inverse finite element techniques are used to convert the strain gauges data to damage-sensitive features. Arguably, a refined finite element model of such structure can be very computationally expensive even when using linear models. An efficient way to solve an inverse problem with time-consuming model evaluations is making use of parallel model evaluations using a Sequential Monte Carlo (SMC) algorithm and parallel solution of the finite element (FE) equations using a commercial FE software. A significant advantage of SMC algorithms is that model evaluations are independent and are able to be run in parallel. In this chapter, an expensive high-fidelity model of a miter gate is used to infer damage-sensitive features given a noisy set of strain measurements.

4.2. Introduction

Navigation locks form a crucial part of inland waterways infrastructure network. Miter gates are the most common type of navigation locks in the United States (US) with other types of lock gates being sector, tainter, and vertical lift (Alexander et al. 2018). Miter gates are steel

structures that allow passage of ships, boats, and watercrafts across stretches of different water levels in canals and rivers. In the US, more than half of these structural assets have surpassed their 50-year economic design life (Foltz 2017). Damage to miter gates may lead to closure of a lock chamber. Two types of maintenance events (i.e., scheduled and unscheduled) apply to miter gates. Scheduled maintenance allows navigation users to adjust their activities to avoid unexpected delays and minimize their economic loss. However, unscheduled closures resulting from unexpected events such as undetected deterioration reaching a critical limit state or extreme events (e.g., barge impact) more substantially affect navigation users' economic bottom line and induce a higher cost of maintenance (Kress et al. 2016). Estimating the condition of a miter gate and its components can help to reduce the risk in unscheduled maintenance events and prioritizing better schedule maintenance events. The U.S. Army Corps of Engineers (USACE) have established a discrete rating system to allow inspectors to rate the components of a miter gate based on condition and performance (M. A. Vega et al. 2019), which are used by decision-makers for maintenance and operations planning. However, inspections based on this rating system can vary for different inspectors because it is based on engineer judgement. Continuous structural health monitoring (SHM) of these infrastructure assets may help to reduce the uncertainty and ensure better-informed decisions that lead to safer and more reliable operations (Eick et al. 2018).

One of the consequences of deterioration in miter gates is the formation of a bearing gap that occurs between the contact blocks that interface the lock walls and the miter gate (Eick, Smith, and Fillmore 2019b). The bearing gap governs the lateral boundary conditions on the gate, and its degradation from loading, wear, corrosion, and other sources leads to changes in the stress-strain profile of the entire miter gate (Mahmoud, Chulahwat, and Riveros 2018). Experienced inspectors and lock operators have indicated the importance of knowing the condition of contact block and

its role in identifying load transfer issues in the gate (Foltz 2017; Eick et al. 2017). Other analyses would have to be conducted to determine the critical gap parameters (size, location, etc.) that lead to some failure in the gate or in one of its components. Alternatively, the boundary conditions may also be obtained by inferring directly the forces that support the gate laterally (Parno, O'Connor, and Smith 2018). Other forms of damage in miter gates includes material losses due to corrosion (Estes, Frangopol, and Foltz 2004). There is also interest of maintaining optimal prestressing in the diagonal components of miter gates (Riveros, Ayala-Burgos, and Dixon 2017).

Many of the miter gates owned by USACE are instrumented with strain gauges for data acquisition (U.S. Army Corps of Engineers Headquarters 2007). The relationship between the formation of the bearing gap and the stress-strain profile in the entire gate can be better understood by using a finite element (FE) model. For a SHM system, the inverse relation between the input and outputs of the FE model are desired. This inverse relation can be estimated by performing Bayesian inference that uses FE model evaluations. A Bayesian approach is desirable because it is able to quantify the risk on making decisions such as corrective maintenance of components. Many powerful algorithms that perform Bayesian inference can be used to solve this problem (Y. Yang, Madarshahian, and Todd 2019). However, many of these algorithms are not feasible for real-time health monitoring.

In this chapter, a Bayesian inversion of high-fidelity FE model is accomplished by using sequential Monte Carlo (SMC), a class of batch Bayesian inference methods. SMC was selected due to its applicability in general settings (e.g.: non gaussian probability density functions) and its inherent parallelizable capabilities to perform computationally-expensive FE model evaluations (Lee et al. 2010). The chapter first explains the FE model of the testbed miter gate and then describes the different forms of damage in miter gates considered. Then, the estimation/updating

of model parameters directly related to damage is conducted using SMC. A three-stage approach to consistently and systematically handle various sources of real-world uncertainties is proposed. The formulated updating strategy is applied to the testbed structure pertaining to the first and second stage of the three-staged approach. Finally, a conclusion and further work section discusses the additional steps to be taken before deploying a SHM system in miter gates and the issues of dealing with model discrepancy (second and third stage).

4.3. Testbed Structure and Finite Element Modeling

In this research, the Greenup miter gate/lock located on the Ohio river is used as the testbed structure. A physics-based FE model of the gate was developed in ABAQUS, shown in Figure 4.1a. This FE model has been validated using the measured strain gauge readings (Eick et al. 2018). The Greenup gate is a brand-new gate therefore a negligible gap ("undamaged" condition), unaffected by corrosion, and with fully prestressed diagonals were assumed for the validation purposes. 3D linear shells elements instead of 3D solid elements were used to reduce the computational cost of such full-scale model. Figure 4.1b shows the side view of a one leaf miter gate that is subjected to upstream and downstream hydrostatic forces.

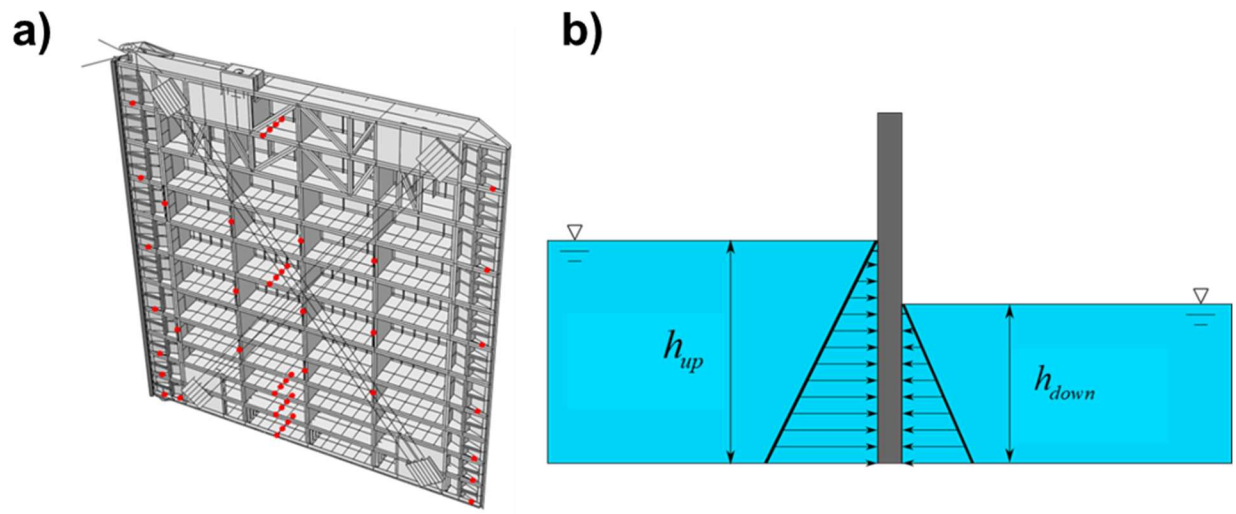

Figure 4.1: a) FE model of Greenup Gate with sensor locations and b) loading conditions

4.3.1 Modeling Options for Gap Formation

The gap formation between the contact (quoin) blocks control how the gate is supported laterally and consequently introduces a change in the stress/strain distribution of the entire gate, especially in the pintle area where the gate is supported by a pintle ball. For modeling purposes, the pintle ball is idealized as a pin support. In this chapter damage is introduced by controlling the extent of the gap. In order to model the gap itself, two different modeling approaches are presented in this work:

Option 1: A contact-type constraint is used between the contact blocks as shown in Figure 4.2a, making this a computationally expensive nonlinear problem. To impose the contact constraint, the Lagrange multiplier method was employed. The strain gauge locations are far from the contact area, mostly due to physical constraints in the miter gate, but this far-field location also mitigates errors due to the method employed to enforce the contact constraint. The opposite side of the wall quoin block uses fixed boundary conditions, and symmetry boundary conditions are used at the right end (i.e., miter) of the gate to simulate the other leaf. The variables g_l and g_w denote the gap length and depth (see Figure 4.2), respectively.

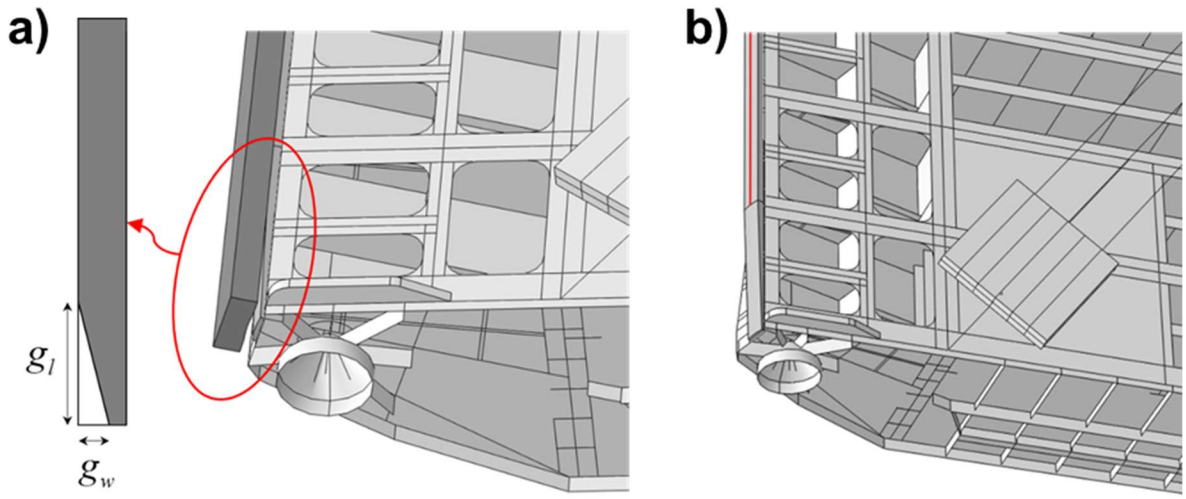

Figure 4.2: a) Option 1: Using contact between wall quoin block and gate quoin block, and b) Option 2: Pin boundary conditions along the gate quoin block (restrained in x and y directions) except at gap location

Option 2: Pin boundary conditions are used directly to support the gate quoin block instead of modeling the wall quoin block and using a contact algorithm to support the gate laterally. To model the effect of the gap formation a length (g_l) of the gate quoin block is left unrestrained as shown in Figure 4.2b. This representation may not be as accurate as Option 1, but it is a more attractive option computationally, since it is a linear FE model.

The main difference in the physics between Option 1 and 2 is that Option 1 captures the effect of partial gap closure after the gate is subjected to hydrostatic loads. However, since the portion of the gap that closes is small under most loading scenarios, Option 2 is a reasonable choice.

4.3.2 Modeling Corrosion in Miter Gates

Based on (Estes, Frangopol, and Foltz 2004; Evans et al. 2019), a miter gate can be divided into three environmental zones defined by the upstream/downstream water elevations, namely (1) the atmospheric zone, (2) the splash zone, and (3) the submerged zone, as shown in Figure 4.3(a). The atmospheric zone is the region in the gate that is generally not in contact with water even when

the water elevation changes. From the three zones, the atmospheric zone is where least damage due to corrosion occurs and where monitoring is more accessible to visually inspect by inspector or drones (Spencer, Hoskere, and Narazaki 2019). The splash zone is the region in the gate that is in contact with air and water mainly due to the water elevation changes that allows passage of marine transportation. The splash zone is where corrosion damage is the greatest, which is attributed by the rate that water changes (Melchers 2004) in the chamber that allows ships to transition to different water elevations. Lastly, the submerged zone is the region of the gate that is always underwater. Monitoring in the splash and submerged areas is not straightforward because is generally not visually available while a miter gate is in operation. Generally, dewatering a lock chamber for inspections or sending a diver is costly and make the continuous operation of a lock to stop.

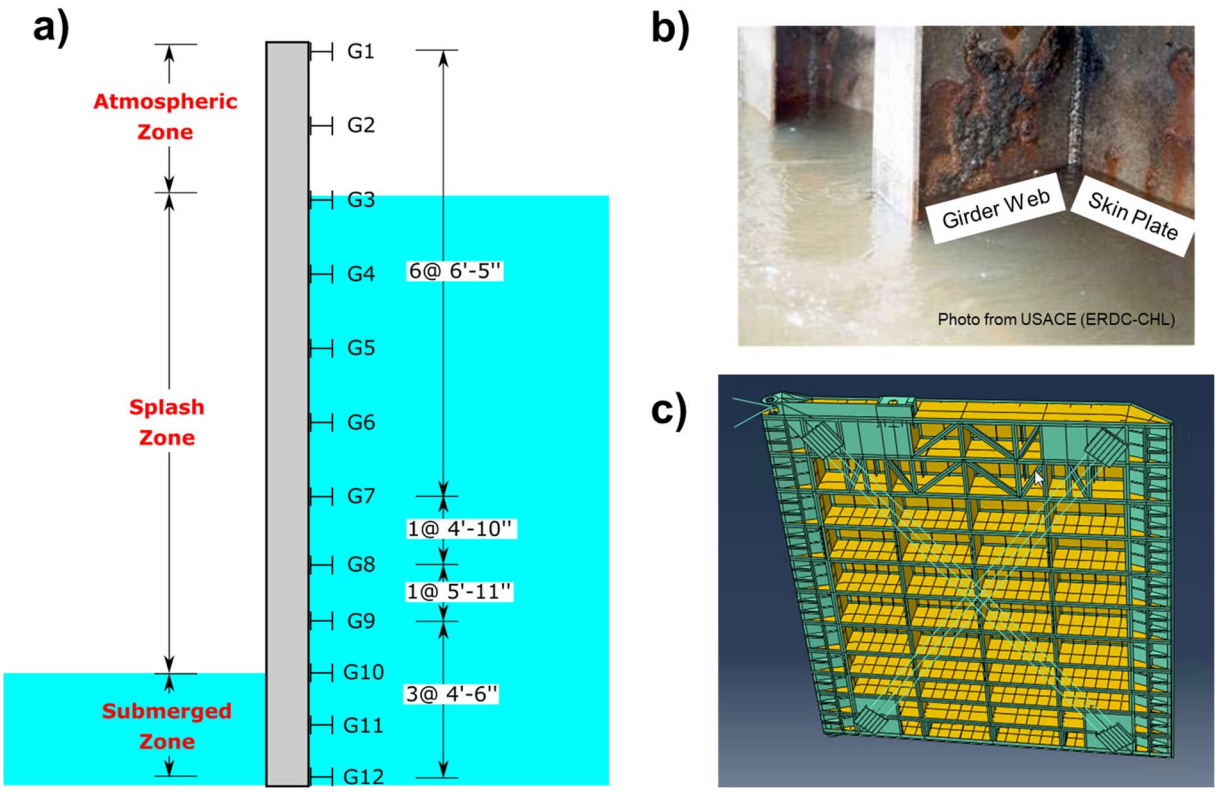

Figure 4.3: a) Environmental zones, b) Example of corrosion on steel plates in miter gates, and c) FE model highlighting plates (denoted in yellow) where thickness loss due to corrosion is modelled

Figure 4.3(b) shows an example of corrosion deterioration in the vertical girder webs and skin plates, which are components in miter gates. For modelling purposes, the corrosion is assumed to occur at every web and skin plate in the Greenup miter gate, which is observed in Figure 4.3.(c) and denoted in yellow. Corrosion can be modelled as material loss as a function of time. In the case of the of the steel plates (e.g. girder webs and skin plates) in miter gates, corrosion is modelled as thickness loss in these steel plates (Estes, Frangopol, and Foltz 2004). Now, the same thickness loss is assumed for every girder web (vertical and horizontal) and skin plate at each of the environmental zones. Furthermore, due to the fact that corrosion damage is the least and is visually accessible, the thickness loss at the atmospheric zone will be assumed as a known input parameter while solving this inverse problem.

4.3.3 Modeling Prestressing Diagonals in Miter Gates

Diagonals in each miter gate leaf, as shown in Figure 4.4, are pre-tensioned to provide two primary functions:

a) The **positive diagonal** is tensioned in order to remove the self-weight sag and deflection.

b) The **negative diagonal** is tensioned to plumb the gate leaf and to resist the hydrostatic loads as well as balance the load and deflection induced by the positive diagonal.

Based on the literature (Daniel and Paulus 2019a), prestressing the diagonals is an iterative process considering all modes of operation. Therefore, the prestressing forces at each of these diagonals (P_{pos} and P_{neg}) will be assumed different and be assumed to be initially known based on design documents. However, the loss of prestressed in the diagonals in time is unknown and it is of interest to estimate at any particular point in time.

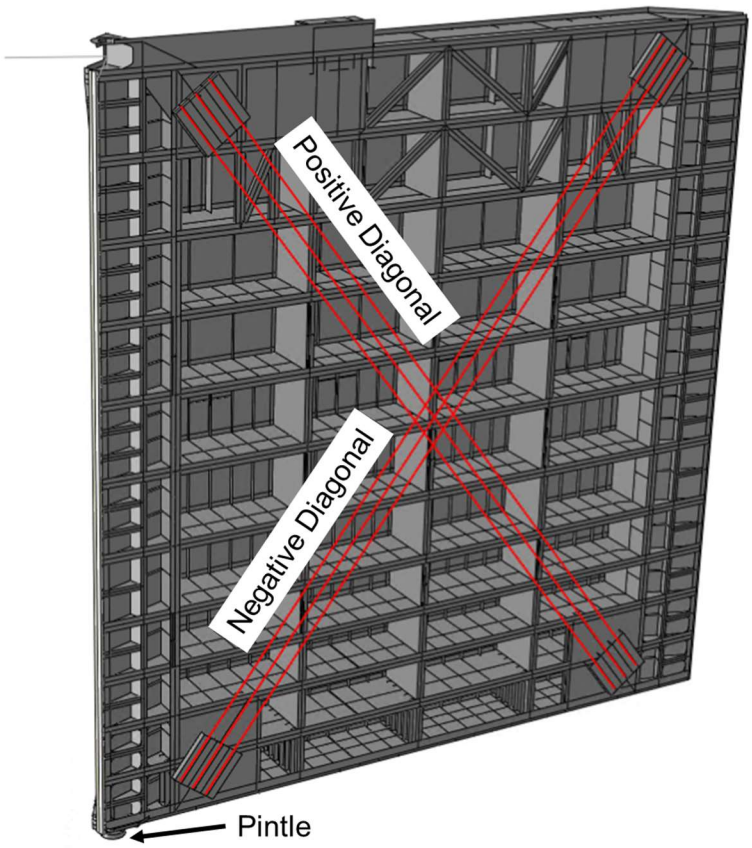

Figure 4.4: FE Model highlighting prestressed diagonals

The next section covers the process of estimating the model parameters (e.g. g_l, P_{pos}, P_{neg}, TL_{splash}, TL_{sub}) mentioned just mentioned in detailed from sections 4.3.1 to 4.3.3.

4.4. Estimating Damage Model Parameters in Miter Gates using Bayesian Inference

For given hydrostatic inputs (i.e. h_{up} and h_{down}) and model parameters of interest (e.g. g_l, P_{pos}, P_{neg}, TL_{splash}, TL_{sub}), the FE model could be evaluated as a "forward model" to yield the resulting strain field resulting in the gate; consequently, solving an inverse problem is necessary to obtain the model parameters of interest given a set of strain measurements obtained at different locations on the miter gate. There are two general ways often used to solve an inverse problem: 1)

a Bayesian approach, which computes a posterior distribution of the model parameters given prior knowledge and the data, or 2) a regularized data fitting approach, which chooses an optimal model (M. Vega, Madarshahian, and Todd 2019) by minimizing an objective function that minimize the empirical risk (i.e. training error). In SHM, estimates of gap length (or other damage parameters) are meaningful to the decision-making process of operators and stakeholders. However, a Bayesian approach is preferred because it can provide confidence regions associated with the estimates of the gap length (g_l), prestressed force in the diagonals (P_{pos} and P_{neg}), and thickness loss in the two of the three environmental zones (TL_{splash} and TL_{sub}). Confidence regions associated with the parameter estimates supports rigorous decision-making. In the Bayesian approach, the posterior distribution of the model parameters (e.g. g_l , P_{pos} , P_{neg} , TL_{splash} , TL_{sub}) can be obtained from

$$\underbrace{p\left(\boldsymbol{\theta},\sigma_{strain}\,|\,\mathbf{y}\right)}_{posterior} \propto \underbrace{p\left(\mathbf{y}\,|\,\boldsymbol{\theta},\sigma_{strain}\right)}_{likelihood}\underbrace{p\left(\boldsymbol{\theta},\sigma_{strain}\right)}_{prior}, \tag{4.1}$$

where

$$\underbrace{\mathbf{y}}_{\text{measured response}} = \underbrace{\mathbf{h}\left(\boldsymbol{\theta},\mathbf{u}\right)}_{\text{FE predicted response}} + \underbrace{\mathbf{w}}_{\substack{\text{error/}\\ \text{noise}}} \tag{4.2}$$

and where $\mathbf{y}$ represents the strain measurement at 46 gauge location, $\mathbf{u}$ represents the hydrostatic loading conditions (i.e. h_{up} and h_{down}) and known thickness loss in the atmospheric zone, and $\mathbf{w}$ is assumed to be a zero-mean uncorrelated Gaussian distribution as follows:

$$\mathbf{w} \sim \mathcal{N}\left(\underbrace{\mathbf{0}}_{46\times1}, \sigma_{strain}^2 \underbrace{\mathbf{I}}_{46\times46}\right) \tag{4.3}$$

$$\boldsymbol{\theta} = \left[\, g_l,\ P_{pos},\ P_{neg},\ TL_{splash},\ TL_{sub} \,\right]^T \in \mathbb{R}^5. \tag{4.4}$$

Computing the joint posterior distribution of the parameters is a mathematically intractable problem. In this work, the computation of the posterior is accomplished by using the SMC

algorithm to perform Bayesian inference. This algorithm was selected due to its applicability in general settings (e.g.: non gaussian prior and posterior) and its inherent parallelizable capabilities to perform computationally-expensive FE model evaluations. Note for the following sections, the parameters contained in $\boldsymbol{\theta}$ will include the standard deviation of the (noise) error σ_{strain}.

4.4.1 Batch Inference using SMC

Sequential Monte Carlo (SMC) or Transitional Markov chain Monte Carlo (TMCMC) methods are a class of simulation-based Bayesian inference techniques which sample from the complete joint posterior distribution of the unknown parameter vector $\boldsymbol{\theta}$. SMC methods do not impose any assumptions on the probability structure prior and the posterior; hence, these methods are applicable in very general settings. SMC methods are inherently parallelizable, therefore ideal for solving the inverse problem involving computationally-expensive FE model evaluations.

The idea of SMC is to avoid directly sampling the target posterior probability density function (PDF) but rather sample an easier-to-sample PDF and then weigh, resample, and perturb the samples to describe the target PDF. The achieve this, SMC constructs a series of intermediate PDFs, known as tempered posteriors, that start from prior distribution (easy to sample) and converge to the posterior distribution (hard to sample) as follows:

$$\underbrace{p(\boldsymbol{\theta}\,|\,\mathcal{D})_j}_{tempered\ posterior} \propto p(\mathcal{D}\,|\,\boldsymbol{\theta})^{\beta_j} \times \underbrace{p(\boldsymbol{\theta})}_{prior} \quad j = 0,1,...,m \quad 0 = \beta_0 < \beta_1 < ... < \beta_m = 1 \tag{4.5}$$

where β_j is the tempering parameter at stage j. When $\beta_j = 0$ at the initial stage ($j = 0$), the tempered posterior $p(\boldsymbol{\theta}|\mathcal{D})_0$ is just the prior $p(\boldsymbol{\theta})$, and when $\beta_j = 1$ at the final stage ($j = m$) the tempered posterior $p(\boldsymbol{\theta}\,|\,\mathcal{D})_m$ is the target posterior $p(\boldsymbol{\theta}\,|\,\mathcal{D})$. SMC represents the tempered posterior distribution at every stage by a set of weighted samples (also called particles). SMC

approximates j^{th} stage tempered posterior $p(\boldsymbol{\theta}|\mathcal{D})_j$ by weighing, resampling, and perturbing (using Markov chain Monte Carlo) the particles of $j-1^{th}$ stage tempered posterior $p(\boldsymbol{\theta}|\mathcal{D})_{j-1}$. The SMC algorithm for sampling the target posterior is shown in Table 4.1.

Table 4.1: SMC Algorithm

Let N be the number of particle (or weighted samples) at every stage, and ESS_j be the effective sample size at stage j

Initialize N, $j=0$, $ESS_0 = N_p$, $\beta_0 = 0$

Generate N samples $\left\{\boldsymbol{\theta}^i_{j=0};\ i=1,...,N\right\}$ from the prior distribution $p(\boldsymbol{\theta})$

while tempering parameter $\beta_j < 1$

- increase stage number $j = j+1$
- choose $\tilde{\beta}_j$ such that $ESS_j = 0.95 \times ESS_{j-1}$, $\beta_j = \min\left(\tilde{\beta}_j, 1\right)$
- <u>weighting</u>: $w^i_j = p\left(\mathcal{D} \mid \boldsymbol{\theta}^i_{j-1}\right)^{\beta_j - \beta_{j-1}}$ for $i = 1,...,N$
- <u>resampling</u>: $\tilde{\boldsymbol{\theta}}^i_j = \boldsymbol{\theta}^l_{j-1}$ with probability w^l_j for $i = 1,...,N$
- <u>perturbation</u>: start an MCMC chain at $\tilde{\boldsymbol{\theta}}^i_j$ and take N_{MCMC} steps with target distribution $p(\boldsymbol{\theta}|\mathcal{D})_j$ for each $i = 1,...,N$. Gather last sample of each MCMC chain to obtain $\left\{\boldsymbol{\theta}^i_j;\ i=1,...,N\right\}$

end

$\left\{\boldsymbol{\theta}^i_j;\ i=1,...,N\right\}$ are the samples of the target posterior $p(\boldsymbol{\theta} \mid \mathcal{D})$

Using the above algorithm, Eq. (4.1) can be solved to obtain estimates of the model parameters of interest (e.g. g_l, P_{pos}, P_{neg}, TL_{splash}, TL_{sub}) including the standard deviation of the (noise) error (σ_{strain}) as shown in Figure 4.5. The prior distributions assumed are constrained by physical knowledge of these parameters. As expected, the use of a physical based model can help to reduce the parameter estimate given by the prior distribution, which is observed by the posterior distribution of each parameter. Also, the true value lays very close to the mean of the posterior distribution. As mentioned earlier, confidence regions associated with the parameter estimates

supports rigorous decision-making. And the diagnosis of these multiple form of damage in miter gates can help with maintenance decision making.

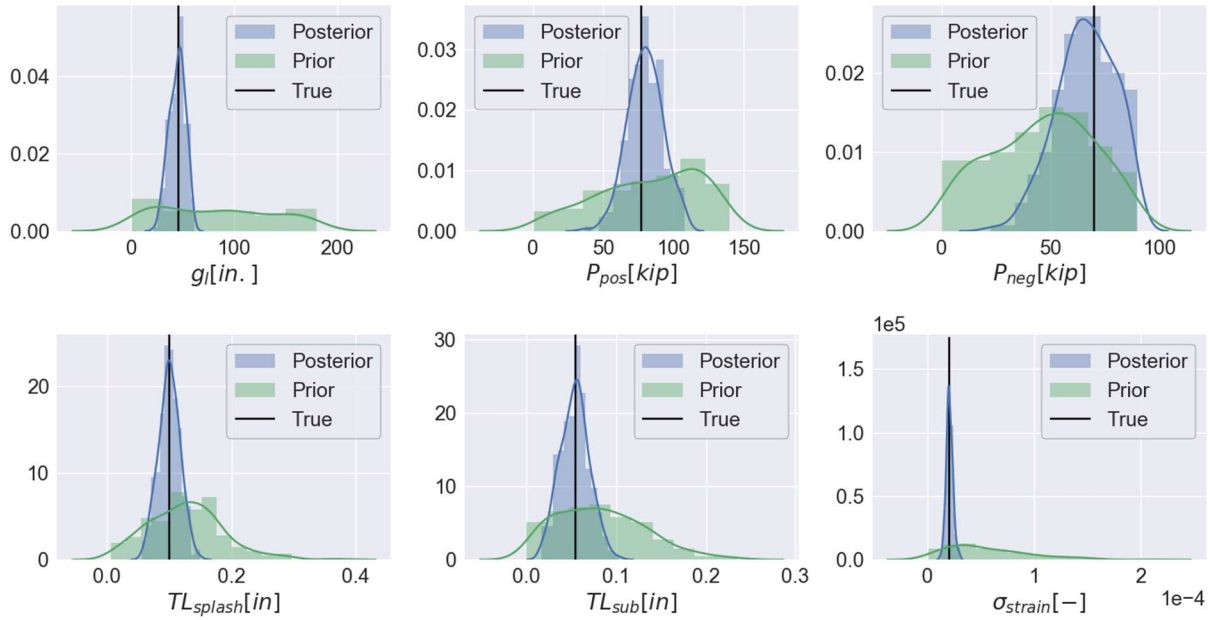

Figure 4.5: Distributions of parameters of interest

From all the model parameters estimates, probably the one with more uncertainty on the modelling would be inserting damage in the form of the bearing gap (e.g. Option 1 and 2). For the next section, model discrepancy in the form of modelling bearing gaps only would be considered.

4.5. Three-stage approach

Implementing a real SHM monitoring system will, arguably, involve several types of uncertainties that will affect the estimation process shown previously. One of the main sources of discrepancy between the estimation and the true model parameter values is due to model form uncertainty (a.k.a. model discrepancy), i.e., how the forward model (e.g. FE model) used in the inference process differs from the true physical model. A 3-staged approach (see Figure 4.3) is proposed to systematically tackle model discrepancy along with other real-world uncertainties.

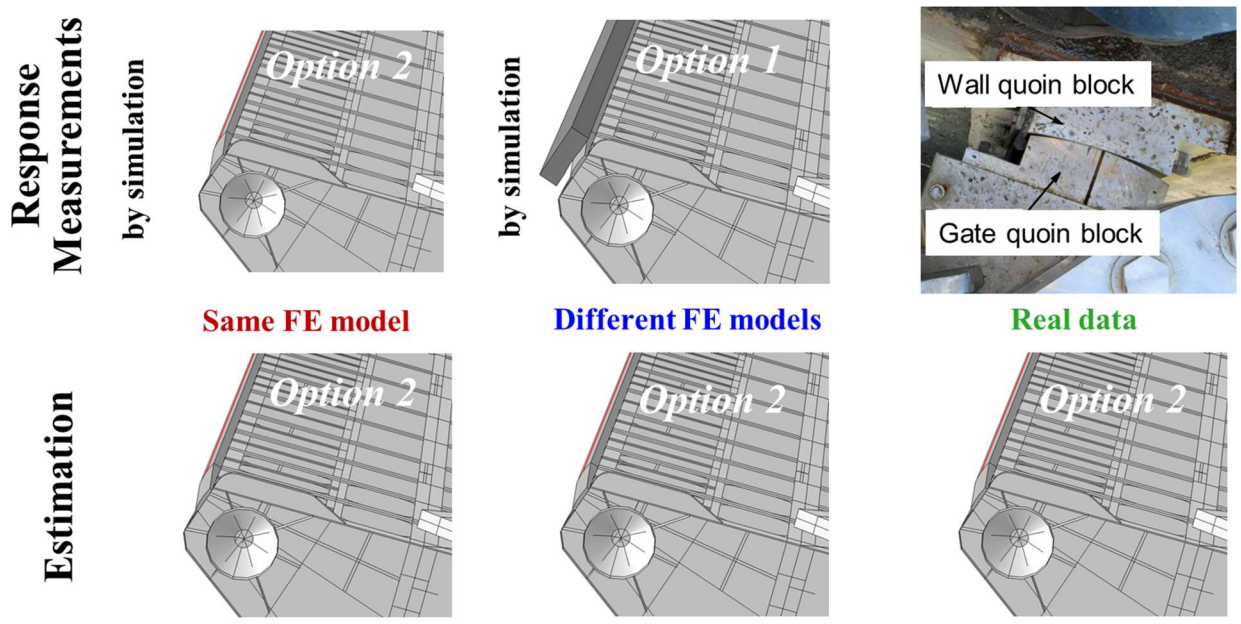

Figure 4.6: Three-staged approach to systematically and progressively approach to handle various sources of uncertainties.

4.5.1 Stage 1: same FE model

Stage 1 uses the same FE models for generating the data and for estimation purposes. Clearly, the model discrepancy is not considered in this stage. As described earlier, there are two competing gap models. Option 2 is used as the FE model in this case due to its fast model evaluations. The estimation of the gap length for a specific response measurement is shown in Figure 4.4. The parameter δ is the estimated coefficient of variation, and r is the Pearson correlation coefficient.

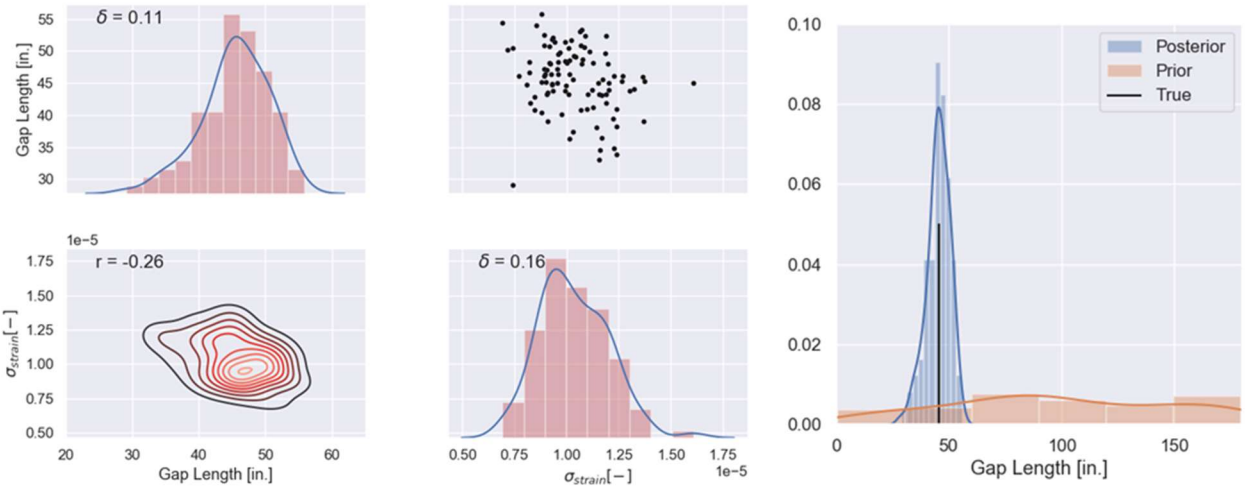

Figure 4.7: a) Joint posterior distribution using 100 particles, and b) prior and posterior distributions vs true value

As intended the posterior distribution covers the true value of the gap length and also the standard deviation of the (noise) error. The gap length prior distribution used for the inference follows a uniform distribution between 0 in and 180 in. These values are based on inputs from experienced lock operators.

4.5.2 Stage 2: different FE models

Stage 2 uses different FE models for generating the data (option 1) and for estimation purposes (option 2). Model discrepancy is considered in this case, as the way that the gap between contacts blocks is modelled is very different between options 1 and 2. The gap depth is assumed to be 0.25 in for modeling option 1, which is used to generate the measurement strain data.

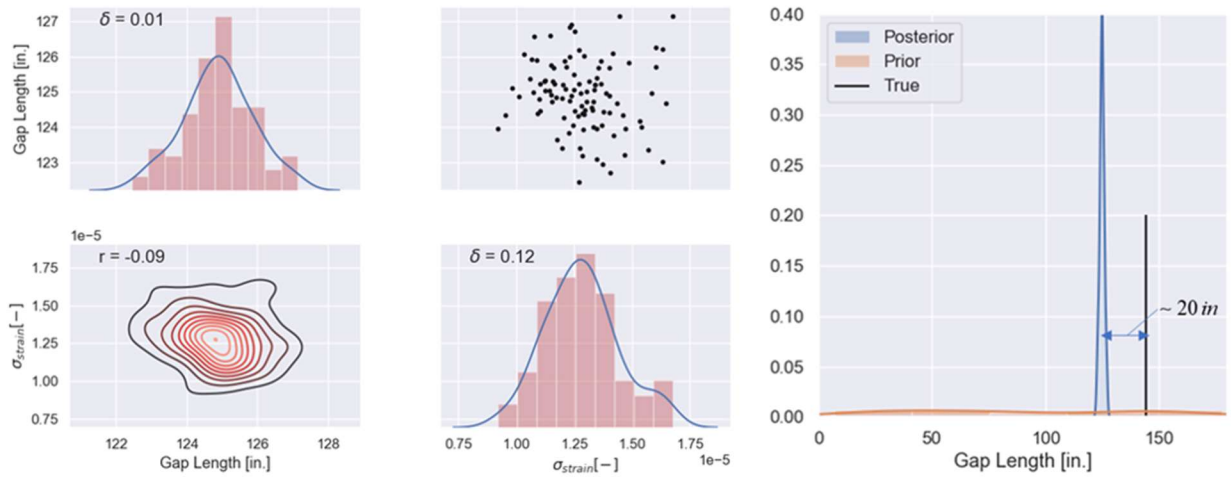

Figure 4.8: a) Joint posterior distributions using 100 particles, and b) prior and posterior distributions vs true value

The posterior distribution of the gap length is very confident at a gap length around 124 in, while the true simulated gap length is equal to 144 in. Therefore, for this case the posterior estimation is biased by ~20 in. These results are consistent with the values obtained by Brynjarsdottir and O'Hagan (Brynjarsdóttir and O'Hagan 2014) when two different models are used for simulating data and estimation purposes.

4.5.3 Stage 3: data from the actual structure in the field

Stage 3 uses "real world" data as the measurement data. For this stage, a FE model should be validated at different damage levels, which in practice it is challenging to obtain. Also, additional parameters (e.g. critical crack, corrosion, uncertainty in the material, amount of prestress in the diagonals, etc.) that are strain-sensitive should be identified to improve the predictive capabilities of this problem.

4.6. Conclusions and Further Work

Diagnosis of different form of damage in miter gates is accomplished by performing Bayesian inference using a validated high-fidelity FE model. Two different modeling techniques

are presented to simulate certain type of damage (i.e., formation of gap). This study shows that, not accounting for model discrepancy in the Bayesian inference leads to overconfident biased parameter estimates. This can seriously hamper the predictive capabilities (extrapolation) of the FE model. To improve the predictive capabilities, a bias function can be trained to learn the model discrepancy between two models as described in detail in (Kennedy and O'Hagan 2001; Brynjarsdóttir and O'Hagan 2014; Ling, Mullins, and Mahadevan 2012, 2014). This bias function should be carefully studied/interpreted when using them for interpolation or extrapolation. Physics-based models when combined with machine learning models (for modeling discrepancy) may be a better option for extrapolation, however, especially when limited damage data is available. The use of the SMC algorithm in large FE models is encouraging due to its parallelizable capabilities. Often, a (surrogate) data-driven model is created to replace an expensive FE model, but this was not needed in this work. Additional steps need to be taken before deploying a SHM system in miter gates specially when dealing with model discrepancy. Additionally, a sensitivity analysis should be studied to understand the sensitivity of the strain gages to different model parameters, as this may also lead to improved predictive capabilities.

4.7. Preview to Chapter 5

As mentioned in section 1.2.2.1, the biggest limitation of damage diagnosis using a physics-based model updating approach is that diagnosis will be affected by how well the model describes the actual, as-built structure. Undoubtably, model uncertainty needs to be accounted to improve damage diagnosis (Kennedy and O'Hagan 2001; Brynjarsdóttir and O'Hagan 2014; Ling, Mullins, and Mahadevan 2012, 2014). Alternatively, model validation can also help to reduce model uncertainty and therefore improve damage diagnosis estimates. In the next chapter, an

alternative structural testing method suitable for calibration and validation of numerical models that behaves in a highly nonlinear manner.

4.8. Remarks

Portions of this dissertation have been published or are currently being considered for publication. Chapter 4 is currently in preparation for publication as an extension of:

Vega, Manuel A., Mukesh K. Ramancha, Joel P. Conte, and Michael D. Todd. 2021. "Efficient Bayesian Inference of Miter Gates Using High-Fidelity Models." In 38th International Modal Analysis Conference. Houston, Texas: Springer.

Chapter 5

IMPLEMENTATION OF REAL-TIME HYBRID SHAKE TABLE TESTING USING THE UCSD LARGE HIGH-PERFORMANCE OUTDOOR SHAKE TABLE (LHPOST)

5.1. Abstract

Large shake tables can provide extended capabilities to conduct large- and full-scale tests examining the seismic behavior of structural systems that cannot be readily obtained from reduced scale or quasi-static testing conditions. Assessing the behavior of large or complex structural systems introduces challenges such as high cost of full-scale specimens or capacity limitations of currently available shake tables. Some of these limitations may be overcome by employing the real-time hybrid shake table test method that requires only key subassemblies to be evaluated experimentally on the shake table while the remainder of the structure is modeled numerically. As a demonstration of the applicability of this testing method using a large shake table, a series of hybrid shake table tests were conducted on the University of California, UC San Diego Large High-Performance Outdoor Shake Table (LHPOST) with capabilities to test full scale structural models. A physical specimen was coupled with a numerical model using hybrid simulation techniques and shown to reproduce reliable results with adequate mitigation of experimental errors.

5.2. Introduction

Real-time hybrid simulation (RTHS) is a cost-effective and efficient method to evaluate the response of structural systems under earthquake and other extreme loading conditions. A hybrid model consists of numerical and experimental subassemblies with the complete system response being simulated for a given natural hazard. Generally, the experimental subassembly represents parts of the domain of the structure that are difficult to model analytically. Real-time simulations make it possible to test rate-dependent devices (i.e. viscous dampers, or base isolation bearings) as part of the experimental subassembly of the hybrid model. Recent applications of real-time hybrid simulation have been extended to use shake tables to dynamically test physical subassemblies. In one of the earliest studies, Igarashi et al. (Igarashi, Iemura, and Suwa 2000) proposed a hybrid simulation technique using a shake table with an experimental specimen consisting of a mass damper supported on a roller bearings attached to four springs. The experiment interacted with a numerical SDOF system via an A/D control system. Several researchers (Ou et al. 2015; Reinhorn et al. 2003; A. Schellenberg, Shao, and Mahin 2017; R. Zhang et al. 2017) have studied this technique using different integration algorithms and compensators to control the stability of uniaxial hybrid shake tables, including applications of mid-story isolation. Nakata (Nakata and Stehman 2012) proposed a different approach, where a controlled mass, built on top of the experimental subassembly, was used to generate the restoring forces from the numerical subassembly. Schellenberg (A. Schellenberg, Shao, and Mahin 2017) applied the methodology proposed by Igarashi to conduct a hybrid test on a 6-DOF shake table at the University of California, Berkeley using a large-scale experimental subassembly. Additionally, researchers have studied RTHS using shake tables combined with dynamic actuators (X Shao,

Reinhorn, and Sivaselvan 2011). The majority of this previous work has been primarily developmental using reduced-scale shake tables and experimental subassemblies.

More recently, a moderate scale hybrid simulation was conducted by researchers at Tongji University (C. Yang et al. 2015), which consisted of real-time hybrid simulations of a girder bridge on a medium size shake table. In the test, the bridge piers were modeled numerically, while the bridge girders supported on top of four rubber bearings were installed on the shake table to represent the experimental subassembly. Consequently, the displacement response history at the top of the bridge pier (modeled numerically) served as the input signal to the shake table. While real-time hybrid shake table testing has been studied quite extensively over the last decade by various researchers (Reinhorn et al. 2003; R. Zhang et al. 2017; Nakata and Stehman 2012; A. H. Schellenberg, Becker, and Mahin 2016), most of these tests have used reduced-scale experimental subassemblies tested on small shake tables. An issue with scaling down the physical domain is that test results are less meaningful and more difficult to interpret as the size scale decreases. The work presented in this chapter describes the implementation of a framework for RTHS using one of the largest shake tables in the world. The use of the Large High-Performance Outdoor Shake Table (LHPOST) at the University of California San Diego would allow expanding potential applications of the hybrid test method with large scale experimental substructures (e.g. soil structure interaction).

The RTHS with LHPOST was implemented using two different configurations: i) hard real-time computation with the integration algorithm coded in Simulink Real-Time (SimulinkRT) (Mathworks 2015), and ii) the numerical model coded in OpenSees (OPS) (McKenna, Fenves, and Scott 2000) running on a separate non-real-time high performance computing (HPC) machine to take advantage of structural analysis software with advanced finite element modeling capabilities.

In both cases, the compensation and generation of commands to the shake table were implemented in real-time using Simulink. The hybrid models consisted of a shear building structure, where the upper story (or un-tuned mass damper) was experimentally tested on the shake table and the lower stories were modeled numerically in Simulink or OPS. The experimental setup consisted of a rigid mass supported on four triple pendulum friction bearings. Two and six degree-of-freedom buildings were examined to verify the stability of the system in the presence of high frequency modes. Multiple tests were performed by varying the structural periods of the analytical subassemblies and using different levels of intensity for the input ground motion.

5.3. Hybrid shake table formulation

The hybrid test formulation consists of decomposing the equations of motion into an analytical (numerical) and experimental (physical) domain.

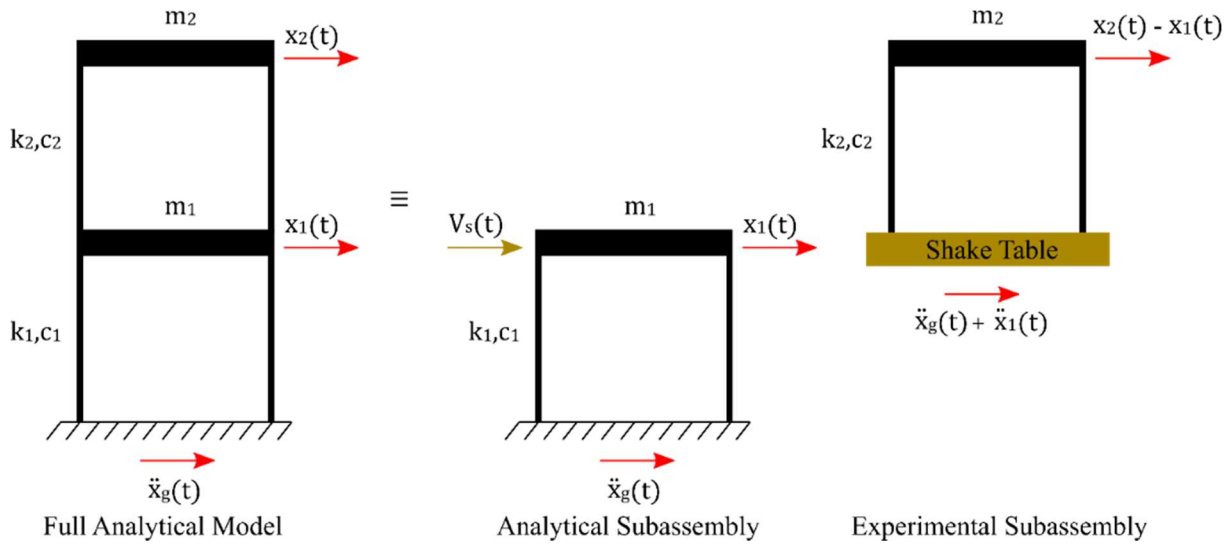

Figure 5.1: Substructuring of a 2-DOF shear frame using a shake table

The equations of motion of the two degrees of freedom (DOF) shear structure (see Figure 5.1) subjected to an input ground motion, $\ddot{x}_g$, can be written as:

$$\begin{bmatrix} m_1 & 0 \\ 0 & m_2 \end{bmatrix}\begin{Bmatrix} \ddot{x}_1 \\ \ddot{x}_2 \end{Bmatrix}+\begin{bmatrix} c_1+c_2 & -c_2 \\ -c_2 & c_2 \end{bmatrix}\begin{Bmatrix} \dot{x}_1 \\ \dot{x}_2 \end{Bmatrix}+\begin{bmatrix} k_1+k_2 & -k_2 \\ -k_2 & k_2 \end{bmatrix}\begin{Bmatrix} x_1 \\ x_2 \end{Bmatrix}=-\begin{bmatrix} m_1 & 0 \\ 0 & m_2 \end{bmatrix}\begin{Bmatrix} 1 \\ 1 \end{Bmatrix}\ddot{x}_g, \qquad (5.1)$$

where m_1, c_1 and k_1 are the mass, damping and stiffness of the first story. Similarly, m_2, c_2 and k_2 represent the structural properties for the second story. The displacements relative to the ground at each DOF are represented by x_1 and x_2. The acceleration relative to the ground at each DOF are denoted by $\ddot{x}_1$ and $\dot{x}_2$.

The decomposed equation of motion for the first story analytical subassembly can be expressed as follows:

$$m_1\ddot{x}_1 + c_1\dot{x}_1 + k_1x_1 = -m_1\ddot{x}_g + V_s, \qquad (5.2)$$

where V_s is the base shear force at the boundary of the experimental subassembly. The base shear (V_s) can be expressed as:

$$V_s = -m_2(\ddot{x}_g + \ddot{x}_2). \qquad (5.3)$$

Similarly, the decomposed equation of motion for the experimental subassembly can be expressed as:

$$m_2(\ddot{x}_2 - \ddot{x}_1) + c_2(\dot{x}_2 - \dot{x}_1) + k_2(x_2 - x_1) = -m_2(\ddot{x}_g + \ddot{x}_1). \qquad (5.4)$$

The interaction between Eq. (5.2) and Eq. (5.4) comes from solving simultaneously for the base shear force of the experimental subassembly (V_s) and the absolute acceleration at the top of the analytical subassembly ($\ddot{x}_1$). Numerical integration is used to solve Eq. (5.2) in a hybrid test. In an actual hybrid test, the base shear force (V_s) is measured from the experimental subassembly. Note that in Eq. (5.4) $\ddot{x}_2 - \ddot{x}_1$, $\dot{x}_2 - \dot{x}_1$ and $x_2 - x_1$ represent the relative acceleration, velocity and displacement at the top of the experimental subassembly relative to the shake table.

For a real-time hybrid simulation, the integration algorithm should be capable of solving the equation of motion for the analytical subassembly in a fast and accurate manner. Several researchers (Del Carpio R., Hashemi, and Mosqueda 2017; Liu et al. 2016) have extensively investigated the use of different algorithms in hybrid simulation. Most recently, the use of different explicit integration algorithms (F. Zhu et al. 2016) with improved stability have been used in hybrid simulation because of their computational efficiency.

5.4. Computational drivers

Two computational drivers were employed to solve the equations of motion of the analytical subassembly. First, the analytical subassembly was modeled entirely in a Simulink environment including the integration algorithm used to solve the equations of motion. This implementation was fully executed in hard real-time, that is, the time of execution of each task is governed by a clock and expected to complete within the allotted time step. In the second approach, the analytical subassembly was modeled using OPS in a soft real-time environment, where the computational driver is running with a nondeterministic execution time. However, in this approach, it was ensured that the computational time per step was well below the allowable time to avoid a step overrun, though this cannot be guaranteed as in the hard real-time implementation. Before the actual implementation on the LHPOST, a virtual hybrid simulation was conducted as a preliminary verification of the accuracy and performance of the hybrid model. In this case, the experimental subassembly was numerically modeled separately and coupled to the analytical substructure model. The initial verification of the hybrid model consisted of a 2-DOF system, similar to the model in Figure . The analytical sub-structure consisted of a 1-DOF shear frame coupled with an experimental super-structure represented by a rigid mass damper supported on

four isolators. For the virtual simulation, the mass of the damper and the four isolators were numerically modeled as a 1-DOF nonlinear element and analyzed in a second instance of OPS. Figure 5.2 shows one of the hybrid model configurations used in the investigation.

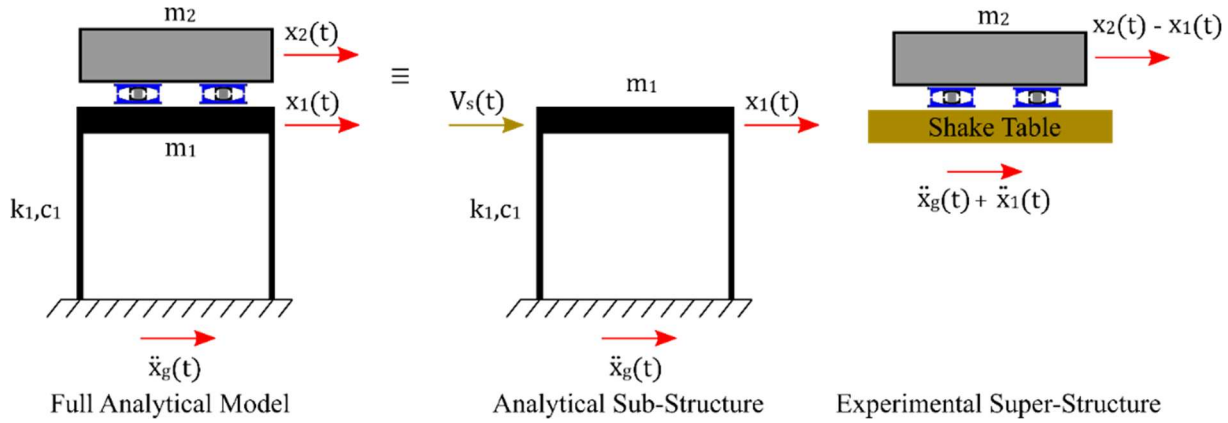

Figure 5.2: Hybrid Model configuration using 1-DOF numerical substructure

Two different integration algorithms were used for the hybrid shake table tests described in this chapter. The first algorithm is the explicit KR-α method proposed by Kolay and Ricles (Kolay et al. 2015). The second is the Generalized Alpha-OS method, which is a combination of the implicit-explicit "operator splitting" (OS) method (Hughes, Pister, and Taylor 1979) and the implicit generalized-α method (Chung and Hulbert 1993). Details on the derivation of the KR-α and Generalized Alpha-OS methods as implemented can be found in (Kolay and Ricles 2014) and (A. H. Schellenberg, Mahin, and Fenves 2009) respectively. The sampling rate of the shake table control system used in these experiments was 2048 Hz. Therefore, an integration time step or substep of 1/2048 seconds was selected to ensure real-time execution with an update rate identical to the controller and to provide for stability and accuracy of the integration algorithms.

5.4.1 Hard real-time implementation

A real-time digital signal processor (Simulink Real-Time) was used to run compiled real-time code from the Simulink model on a dedicated target computer hardware connected via a

shared memory network (*SCRAMNet+*) to the shake table controller. Figure 5.3 shows a schematic of the coupling between the analytical and experimental subassemblies.

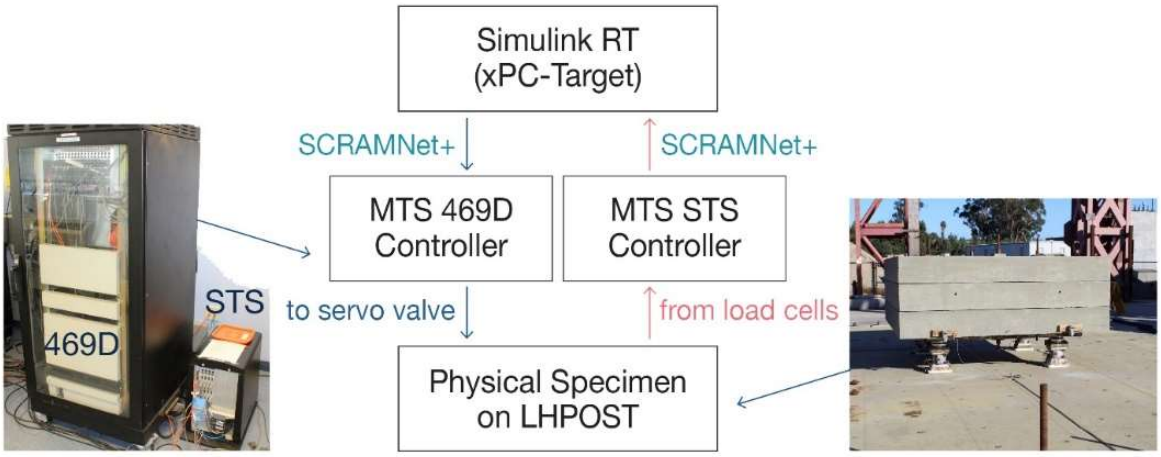

Figure 5.3: Block diagram of RTHS implementation using Simulink RT

SCRAMNet+ is a shared-memory product for high-speed transfer of data between the target computer (Simulink RT) and the control system (MTS 469D and MTS STS). The *MTS 469D Controller* is a digital control system for the shake table whose software includes control and compensation algorithms to command each actuator of the shake table to track a desired command. *The MTS STS Controller* is a digital control system for external actuators that can be added for other testing configurations. Here, it was used to acquire data from external load cells that were installed beneath the four isolators and that were used as feedback for the numerical model built in Simulink RT.

Figure 5.4 shows a schematic of the hard real-time implementation of hybrid simulation in Simulink. This figure includes the blocks that send and receive inputs from the control system (i.e. LHP). Also, a block that contains the Adaptive Time Series (ATS) compensator (Chae, Kazemibidokhti, and Ricles 2013) to reduce system delays is employed. The measured shear force was filtered (using a 7-step moving average), and this delay was also accounted for in the ATS compensator.

The numerical subassembly block contains the implementation of the KR-α integration algorithm. Code verification was performed by comparing results of other integration algorithms with smaller time steps. Numerical simulations were performed to ensure that this implementation was stable in the presence of system delay and noise. Numerical damping was not needed to achieve stability in the pretest simulations and in the actual hybrid tests performed. Additionally, blocks that included moving average filters to store the data for post-processing were used along with blocks that limit the displacement sent to the shake table to prevent instability during testing. The Simulink model includes additional blocks (e.g. 'force_fbk%' and '1-force_fbk%') that are used during development to gradually increase the measured force feedback from a numerical representation of the experimental substructure to the actual experimental substructure. In this manner, the risk of unstable or undesired responses are reduced.

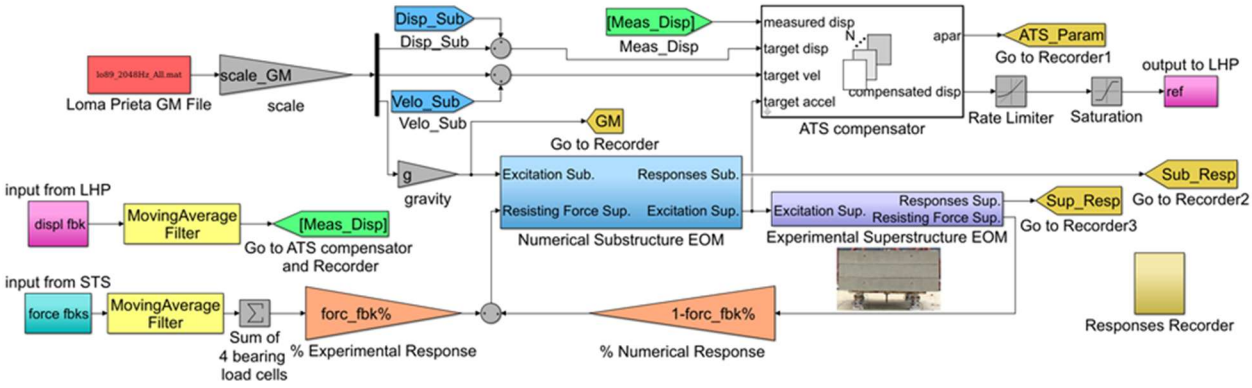

Figure 5.4: Hard real-time implementation built in Simulink RT

5.4.2 Soft real-time implementation

The implementation of the soft real-time hybrid simulations using OPS involves an additional computer known as the host computer, a middleware software OpenFresco (A. H. Schellenberg, Mahin, and Fenves 2013), and a predictor-corrector algorithm running on the hard

real-time target computer. Figure 5.5 illustrates the hardware layout deployed to use OPS for hybrid shake table testing.

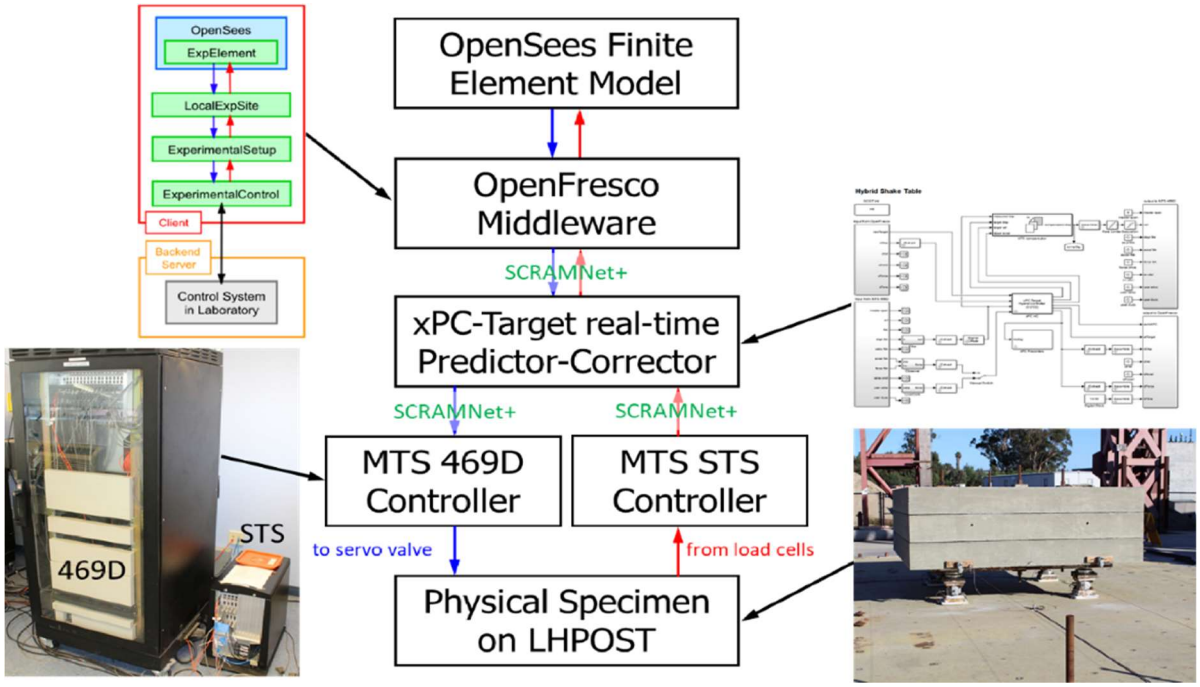

Figure 5.5: Block diagram of RTHS implementation using OpenSees-OpenFresco

OpenFresco (OPF) is a middleware that facilitates the communication between the OPS finite element (FE) model and the control system and data acquisition systems in the laboratory. It also includes several libraries that can be added to OPS to represent the experimental portion as experimental elements in this FE software. The *Predictor-Corrector* algorithm provides the synchronization of the soft real-time FE execution with the hard real-time control system sampling rate. The predictor-corrector algorithm runs on the Target PC digital signal processor.

5.5. Experimental setup

The experimental super-structure consisted of a 249.1 kN concrete weight supported on four triple friction pendulum (TFP) isolators as shown in Figure 5.6. Note that this payload is small relative to the 20 MN payload capacity of the shake table. In this configuration, external load cells

were installed beneath the bearings to measure the shear force experienced by the isolation system. This shear force is recorded by a data acquisition system (STS) and used as feedback to the numerical subassembly as shown in Equation 5.2. Solving this equation will give the table displacement at the next time step. Also, displacement transducers were installed to track the position of the isolators and the super-structure mass.

Figure 5.6: Experimental subassembly on shake table

A schematic of the triple pendulum friction bearing used in the experiments is shown in Figure 5.7 with the dimensions given in Table 5.. The friction coefficients were calibrated after performing tests and fitted to numerical models. The surface number in Table 5.1 is the same as the subscript shown for R in Figure 5.7.

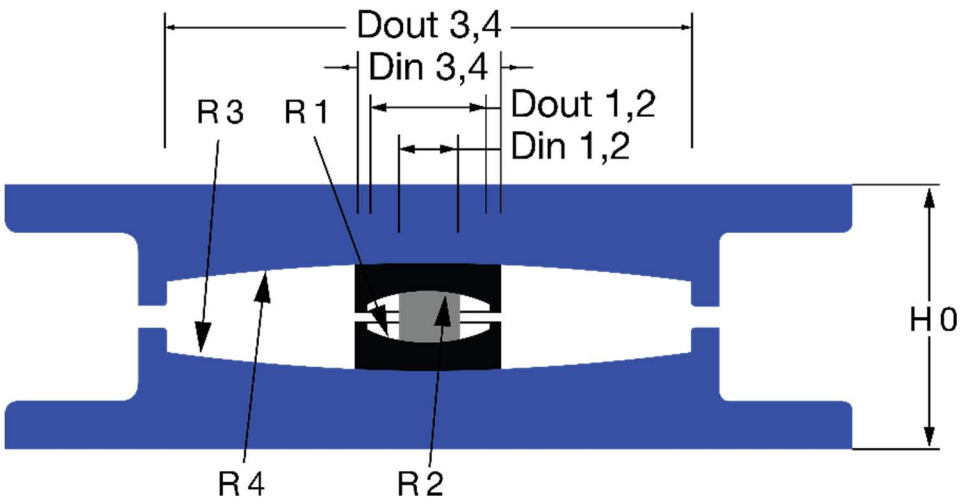

Figure 5.7: Triple pendulum friction bearing cross section

Table 5.1: Triple pendulum friction bearing properties

Parameter	Surfaces 1, 2	Surfaces 3, 4
R	76 mm	473 mm
D_{in}	44 mm	76 mm
D_{out}	66 mm	229 mm
μ	0.07 (0.055)	0.125 (0.13)

5.5.1 Acceleration vs displacement control

The LHPOST control system can be configured for displacement control, acceleration control and the three-variable control (TVC: displacement, velocity, and acceleration). The acceleration input generated by the hybrid simulation algorithm tended to be noisy, which was problematic for the shake table. Therefore, a displacement control approach was used to minimize the effect of the noise since the displacement command provided a smoother signal to the table. Note that the three-variable control capability of the MTS 469D system was not used for this implementation since the acceleration command generated from displacement derivatives was also contaminated with noise.

5.5.2 Test protocol

Table 5.2 shows the hybrid tests performed on LHPOST. In cases 1 to 6, the 2-DOF hybrid model (Figure 5.2) was tested by varying the fundamental period of vibration in the numerical subassembly and by varying the intensity of the ground motion. It is important to note that, for validation purposes, both hard and soft real-time approaches were implemented in these 6 cases.

In cases 7 and 8, the 1-DOF numerical sub-structure was replaced by a 5-DOF shear building. The numerical response was simulated in OPS, and the test was performed with the soft real-time approach.

Table 5.2: Cases used in LHPOST

Case #	Tnum	Scale $\ddot{x}_g$	DOFs	SimulinkRT	OPS-OPF
1	1 s.	100%	1	X	X
2	1 s.	200%	1	X	X
3	0.5 s.	100%	1	X	X
4	0.5 s.	200%	1	X	X
5	0.25 s.	100%	1	X	X
6	0.25 s	150%	1	X	X
7	1 s.	100%	5	-	X
8	1 s.	150%	5	-	X

The test protocol is intended to evaluate test-to-test variability in the results and demonstrate the benefits of hybrid simulation in studying multiple model cases with the same experimental subassembly.

5.5.3 System delay compensation

The system response delay of the actuators in the shake table introduces an effect equivalent to negative damping (Mosqueda, Yang, and Stojadinovic 2008), meaning that more energy is added to the structural system. To control the effect of negative damping due to an average system delay of 34 milliseconds, an adaptive time series compensator was implemented in this setup. The ATS compensator continuously updates the coefficients of the system transfer function during a RTHS to try to reduce the system delay and amplitude changes that are caused

by the dynamics of the shake table control combined with the experimental subassembly. The compensated displacement (u^c) used in the ATS compensator is based on a second-order compensator expressed as follows:

$$u^c = a_0 x^t + a_1 \dot{x}^t + a_2 \ddot{x}^t, \tag{5.5}$$

where x^t, $\dot{x}^t$ and $\ddot{x}^t$ are the target displacement, velocity and acceleration respectively. The coefficients a_0, a_1 and a_2 are constantly updated using the measured table displacement. Table 5.3 shows the parameter values (initial, lower and upper limits) and the maximum rate of change used to achieve stable compensation. The values of each of these coefficients were monitored to avoid clipping by its maximum values. For implementation details, see Figure 5.3 in (Chae, Kazemibidokhti, and Ricles 2013). Additionally, the Simulink model used and data generated from the experiments is available in DesignSafe (Rathje et al. 2017) as published data (M. Vega et al. 2018a, 2018b, 2018c).

Table 5.3: Limit values for the coefficients of the ATS compensator.

Coefficient	Initial Value	Range (minimum, maximum)	Maximum rate of change, $\frac{\triangle a_j}{\triangle t}$
a0	1	(0.90, 1.10)	0.2/s
a1	0.020 s	(0.0, 0.04) s	0.005 s/s
a2	0.0002 s2	(0, 0.0008) s2	0.0001 s2/s

Figure 5.8 shows the displacement history at the shake table level for case 3 (see Table 5.2). In this case, there was 35.2 milliseconds of system delay, shown as the time shift between the compensated displacement sent to the MTS 469D (LHP) and the measured table displacement. The line labeled as 'Compensated Disp. to LHP' represents the displacement predicted by the ATS compensator and sent to the MTS 469D controller.

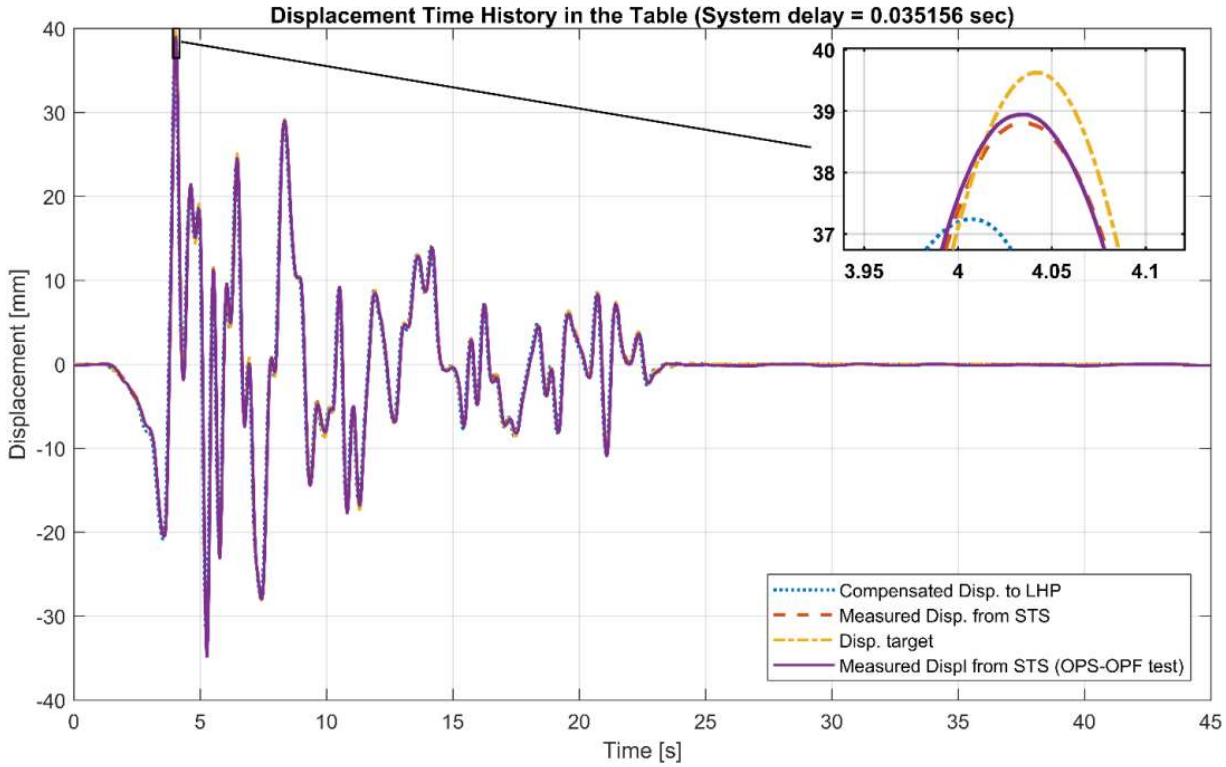

Figure 5.8: Displacement history at table level (case 3)

The line labeled as 'Disp. target' represents the target displacement that the compensator is expected to achieve. The line labeled as 'Measured Disp. from STS' represents the measured displacements of the shake table platen. These signals were obtained using Simulink as the computational driver. These results show that the ATS compensator under-predicts the target displacements. Overall, the performance of the ATS compensator is favorable for this hybrid setup. The line labeled as 'Measured Disp. from STS (OPS-OPF test)' represents the measured displacement, after repeating the same test, but this time using OPS as the computational driver. Considering test to test variability expected in hybrid shake table simulations, it can be concluded that the solution obtained by OPS-OPF is nearly identical to the solution obtained by Simulink.

Table 5.4 shows the average system delay in the response of the shake table (between dotted and dash-dot lines) for the first 6 cases. The actual delay after compensation is also included. Additionally, the normalized root mean square of the error (NRMSE), defined as the difference

between the measured displacement (labeled as 'Measured Disp. from STS') and the target displacement (labeled as 'Disp. target'), is included.

$$\text{NRMSE} = \sqrt{\frac{\sum_{k=1}^{n}(x_k^t - x_k^m)^2}{\sum_{k=1}^{n}(x_k^t)^2}}, \tag{5.6}$$

where x_k^t and x_k^m are the target and measured displacement respectively at the k time step.

Table 5.4: System delay and error at the table level

Case #	Avg. System delay (ms.)	Avg. delay after ATS comp (ms.)	NRMSE (%)
1	33.2	0.98	2.49
2	29.8	0.49	1.27
3	35.2	0.49	3.14
4	33.2	0.49	1.84
5	38.1	0.49	3.39
6	37.1	0.00	2.55

As shown in the table above, the average system delay varies from case to case. Therefore, an adaptive time series compensator is desired. And based on the RMSE results, the performance of the compensator is satisfactory. An interesting trend is that for the larger amplitude tests, cases 2, 4 and 6, the average system delay and NRMSE decrease.

5.6. Analysis of results

Multiple sub-structures and software configurations were used to examine and compare the performance of the real-time hybrid shake table tests. A comparison and analysis of the results is provided here.

5.6.1 Comparison of SimulinkRT and OpenSees

Figure 5.9 shows a comparison of the measured and numerically predicted hysteresis loops of the isolation system for the first 6 cases shown in Table 5.2. These simulations included variations in the amplitude of the ground motion and the numerical sub-structure period. The full

numerical simulation (labeled as Full OS) consists of the same hybrid simulation software utilizing a numerical model of the experimental setup for feedback of restoring forces. This numerical model of the TFP is based on a OPS element, which is explained in detail in (Dao et al. 2013). The peak drift magnitudes compare well for both experimental cases but show significant deviations with the predicted numerical model. Figure 5.10 and Figure 5.11 more clearly show the hysteresis comparison for cases 3 and 5, respectively, which have the smallest and largest difference in drift. Given that the measured experimental errors are small, it is concluded that the main source of this difference is due to the idealizations in the numerical model of the super-structure.

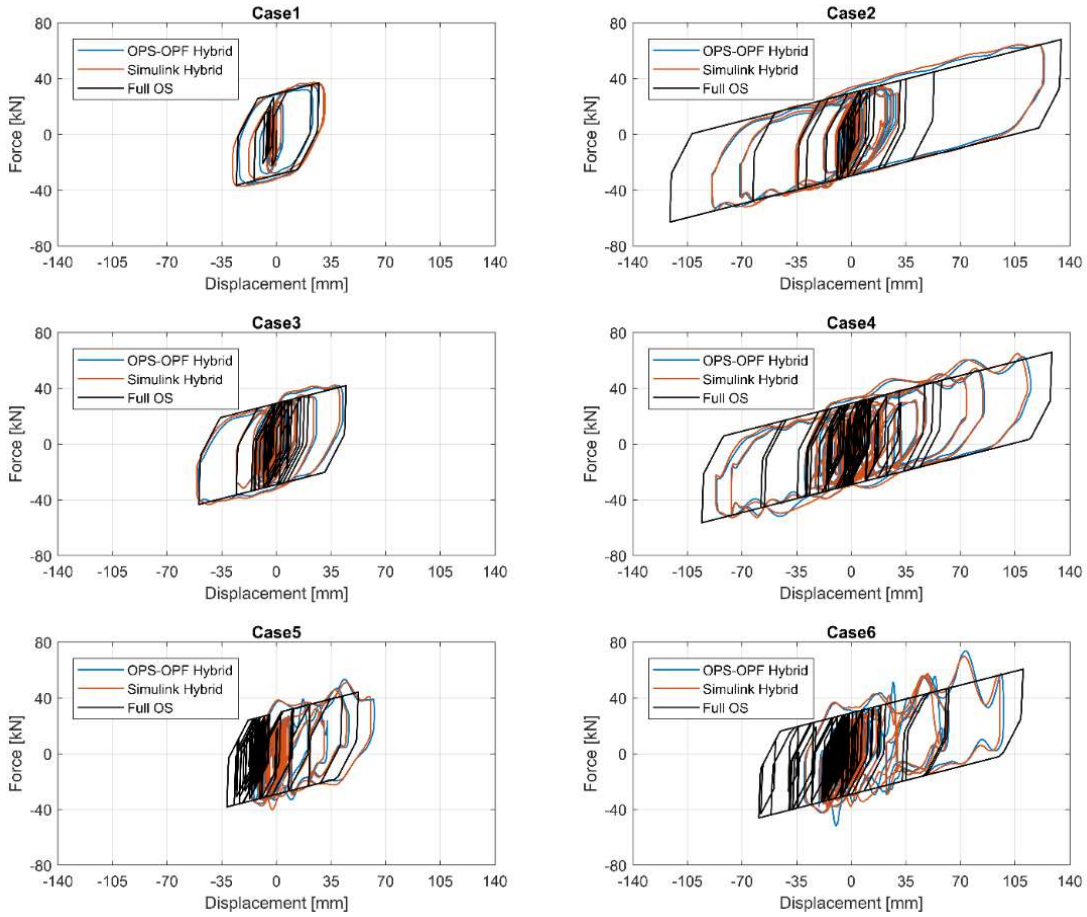

Figure 5.9: TPF bearing hysteresis loops for Full OS Model vs Hybrid Models (cases 1-6)

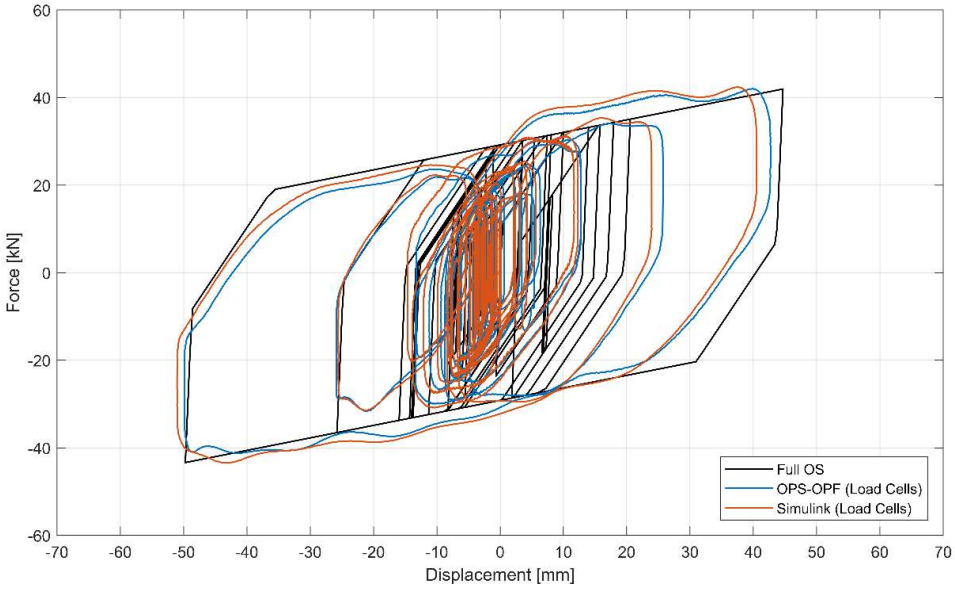

Figure 5.10: TPF bearing hysteresis loops for Full OS Model vs Hybrid Models (case 3)

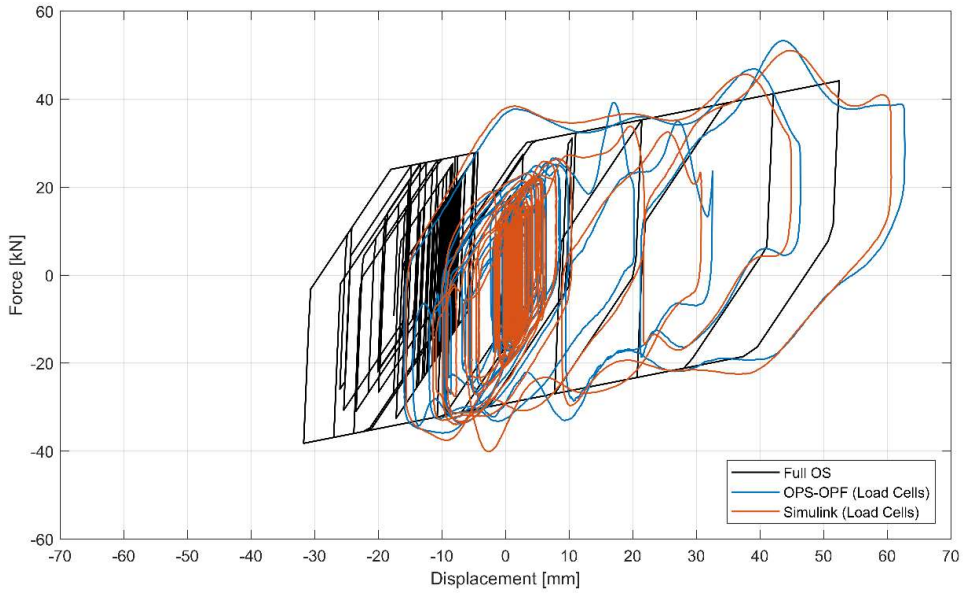

Figure 5.11: TPF bearing hysteresis loops for Full OS Model vs Hybrid Models (case 5)

Figure 5.12 shows the relative displacement error magnitude for case 3 and 5. The calculated relative displacement error consists of the difference between the relative displacement obtained from the full numerical model and the OPS-OPF hybrid implementation. These figures show clearly how the error oscillates due to loading and unloading behavior. The relative displacement error does not accumulate as much for case 3 as for case 5. This observation is likely

because the cumulative error is reduced when the errors change signs for certain cases more than for others. This behavior can be attributed to the sensitivity of non-smooth hysteretic models on residual drifts as explained in (Ruiz-García and Miranda 2006).

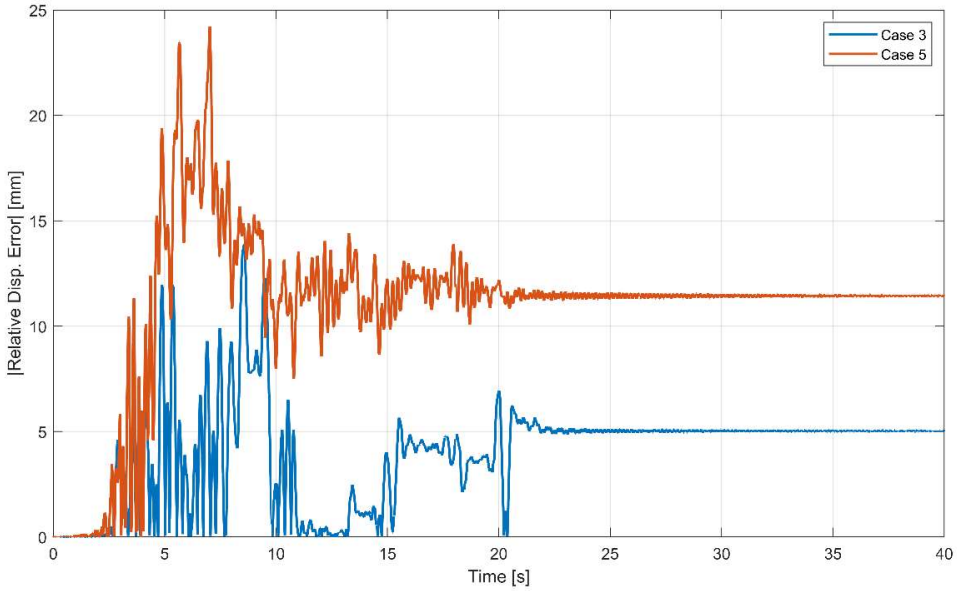

Figure 5.12: Relative displacement error magnitude

It is also important to mention that the numerical TPF element used for the full numerical model had some limitations. For example, the axial force is assumed to be constant even though in a dynamic test the actual axial force varies with time due to overturning forces. In addition, the change of stiffness transition between regimes is not smooth in the numerical model.

5.6.2 MDOF case

A more challenging hybrid model is implemented by increasing the number of degrees of freedom in the numerical sub-structure from 1 to 5 for cases 7 and 8. These tests can further evaluate the performance of the shake table in the presence of higher modes in the numerical model that can be more sensitive to experimental errors. Table 5.2 shows the test protocol for this MDOF hybrid model. The five frequencies of the 5-DOF numerical subassembly are calculated as 1 Hz., 2.90 Hz, 4.52 Hz, 5.70 Hz. and 6.31 Hz.

Figure 5.13 and Figure 5.14 show the TPF isolator hysteresis loops of the full numerical simulation and an OPS-OPF hybrid implementation for cases 7 and 8, respectively.

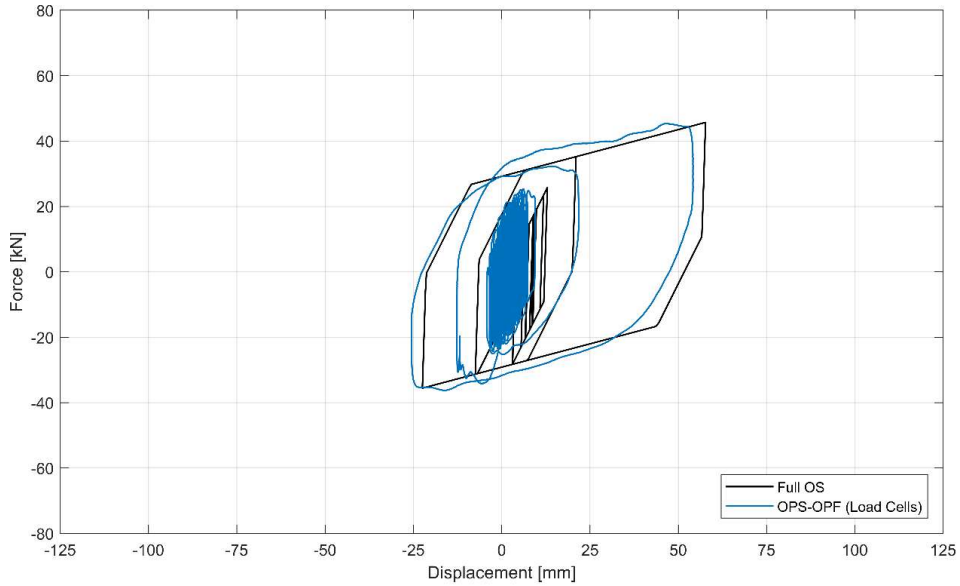

Figure 5.13: TPF bearing hysteresis for Full OS Model vs Hybrid Model (case 7)

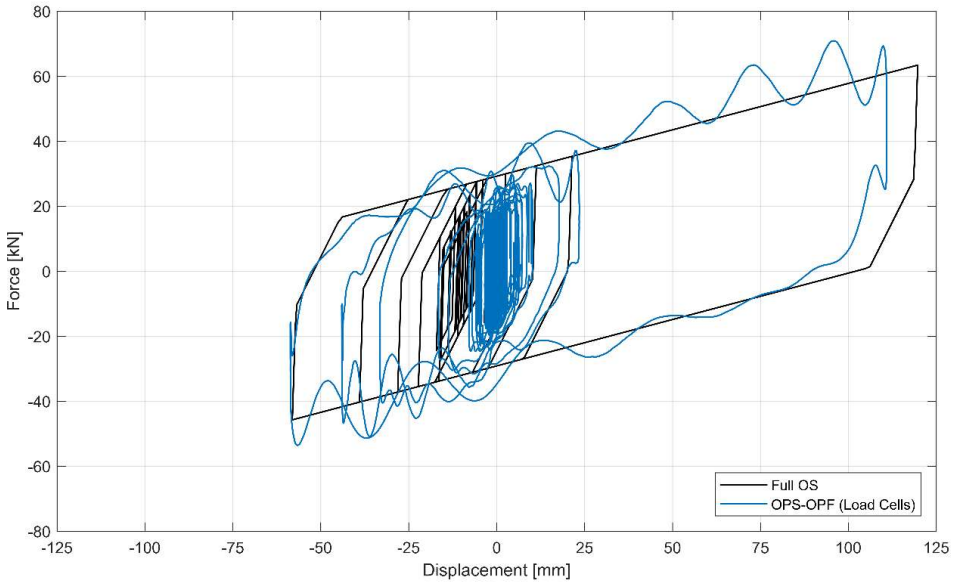

Figure 5.14: TPF bearing hysteresis for Full OS Model vs Hybrid Model (case 8)

Similar to the SDOF cases, there are slight differences in residual displacements, but overall, the numerical simulation agrees reasonably well with the hybrid experiment. This comparison further verifies that the LHPOST can be effectively used for hybrid simulations and

that the compensation and control algorithms implemented, adequately minimize errors in the experiments.

While it was also evident in the previous comparison of SDOF models, Figure 5.14 shows higher frequency oscillations in the hysteresis loop corresponding to the higher amplitude motion. This is investigated further given that the structural model of case 7 and 8 is the same. Therefore, a time frequency analysis of this data is conducted. Figure 5.15 and Figure 5.16 (left side) show the Short-Time Fourier Transform (STFT) of the shear force history experienced by the isolation system for case 7 and 8, respectively. The STFT plot shows clearly the fundamental structural period of the entire model (around 1 Hz), and other frequencies (around 7 and 17 Hz) that correspond to higher modes in the structural model. Figure 5.14 shows how these high frequencies affect the response of the isolation system. The STFT for case 7 shows an amplification of the frequency around 12 Hz. The six frequencies of the entire model are calculated as 0.90 Hz., 2.69 Hz, 4.36 Hz, 5.73 Hz., 6.64 Hz and 12.7 Hz. The 12.7 Hz frequency is estimated to be the highest 6^{th} mode frequency of the combined hybrid model when considering the measured stiffness of the bearing from experimental data in the first regime of the friction pendulum (corresponding to the unloading stiffness).

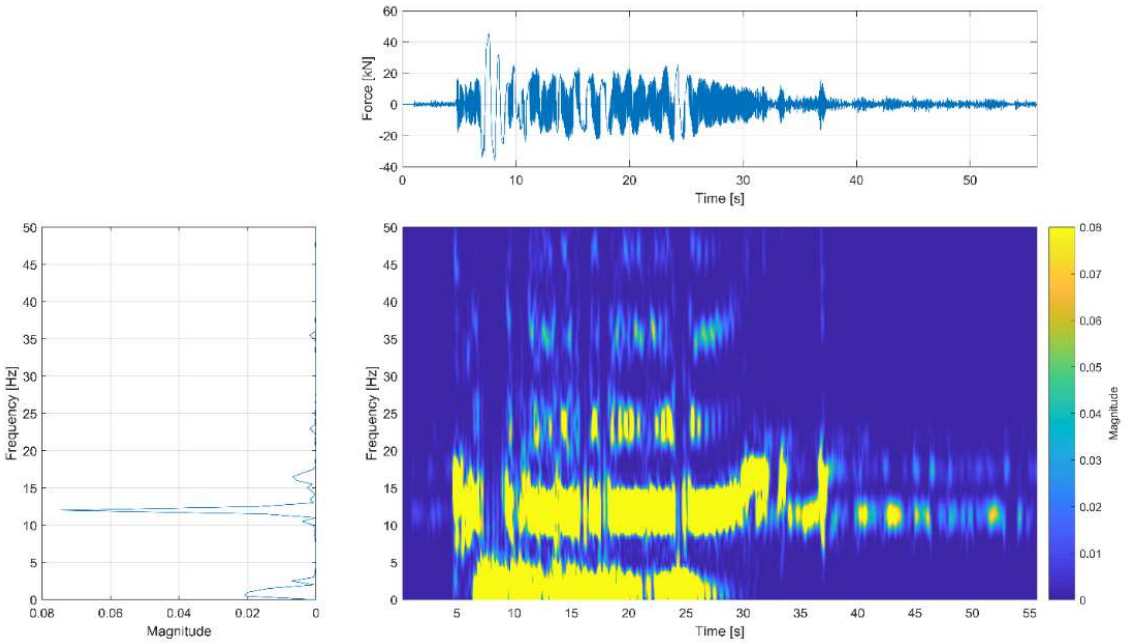

Figure 5.15: Time-frequency analysis of isolator shear forces (case 7)

One significant difference in the STFT plots is that in Figure 5.15 the high frequencies between 7-17 Hz. vanish between 7 and 10 s. This range of time corresponds to the large displacement cycles of the isolation system. Therefore, this could explain why the hysteresis in Figure 5.13 does not have the higher frequency oscillations. And, it clearly shows some high frequency content after 40 seconds, which explains the amplification of the frequency around 12 Hz in the STFT plot. Figure 5.16 shows that the high frequencies remain in case 8 even during the 7 to 10 second window with the large displacement cycles. This explains why the hysteresis loop in Figure 5.14 exhibits oscillations during large displacement cycles. Almost no high frequency content after 40 second is exhibited in this case.

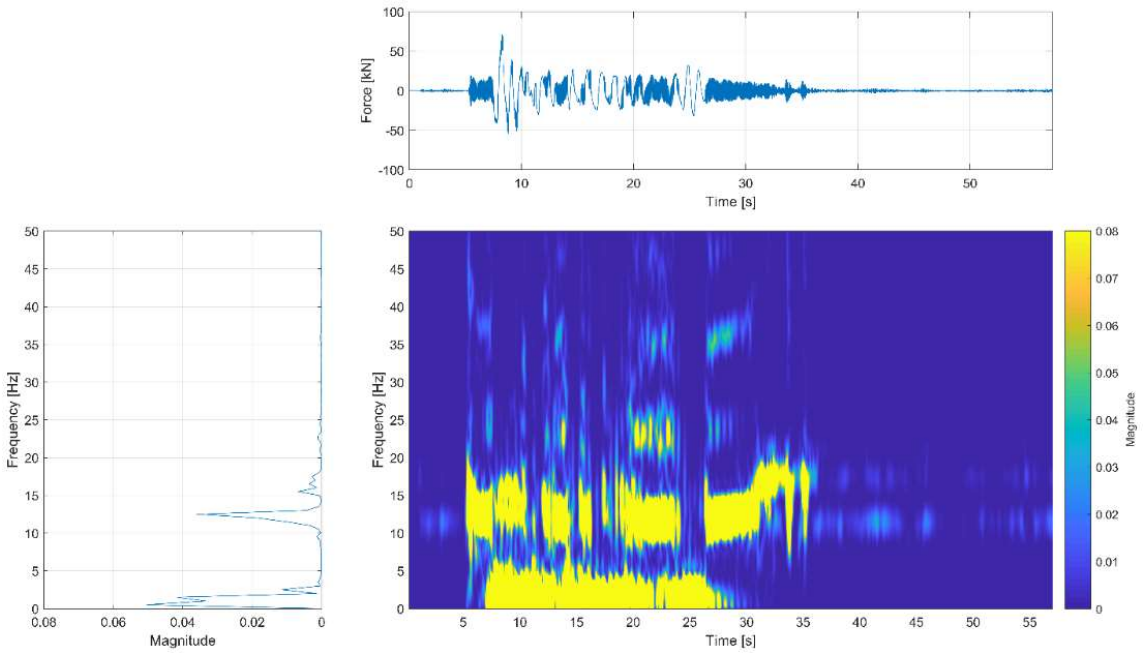

Figure 5.16: Time-frequency analysis of isolator shear forces (case 8)

To further examine the source of the high frequencies present in case 8 between the 7 to 10 second window, the contribution of the ATS compensator and interaction between the shake table and the experimental subassembly is examined. Figure 5.17 shows the time-frequency analysis of the isolator shear forces for case 6, which is also a case that has a lager amplitude ground motion and that exhibits non-smooth hysteresis. Additionally, Figure 5.18 shows the frequency content of the compensated displacement, measured displacement and target displacement. From this figure, it is noted that the compensated and measured displacements experience higher magnitudes at the higher frequency levels. Further, the high frequencies amplified in cases 6 and 8 when comparing the target and compensated displacements indicate that the ATS compensator could be adding higher frequency content to the signals.

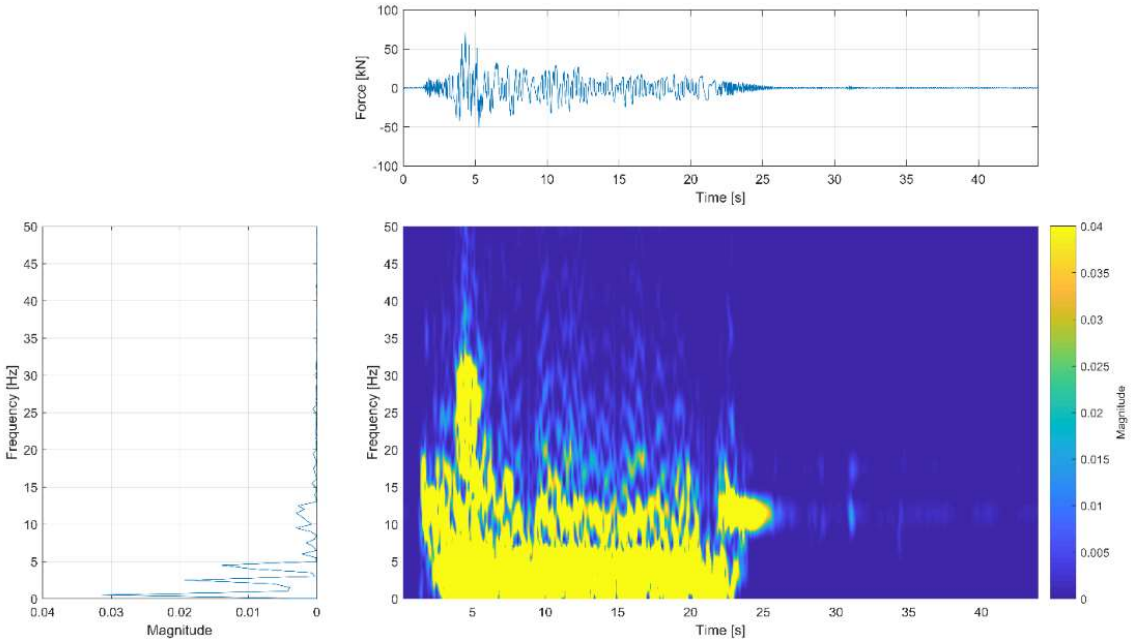

Figure 5.17: Time-frequency analysis of isolator shear forces (case 6)

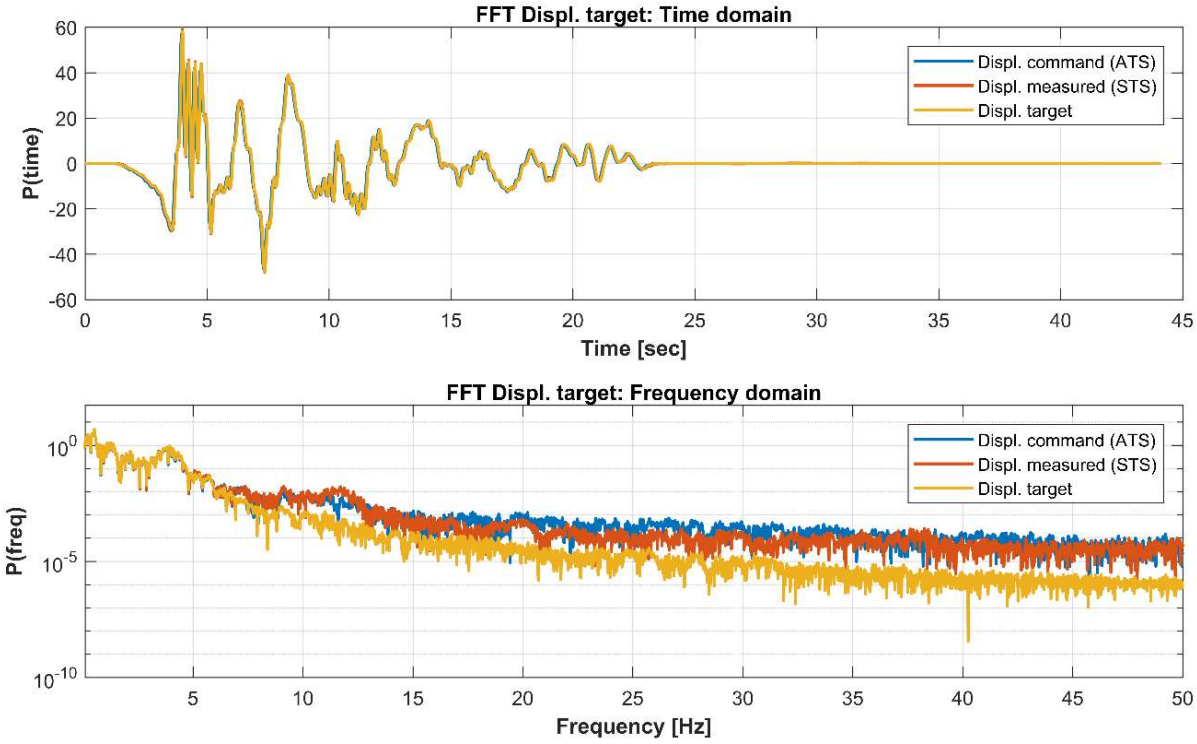

Figure 5.18: Frequency content of displacement at table level (case 6)

5.6.3 Midlevel isolation as an un-tuned mass damper

Midlevel isolation has recently been implemented as a means to retrofit buildings. The 185 Berry Street Building in San Francisco is a good example of such practice (Dutta et al. 2009). The response of the sub-structure improved after adding additional stories on top of a midlevel isolation layer. Similar behavior is found in the numerical sub-structure of this MDOF model that was examined. Figure 5.19 shows the effect of adding an isolated mass above the numerical sub-structure on the peak inter-story drift (PIDR) at each story. The added isolated mass behaves as an un-tuned mass damper (TMD) for the entire structure.

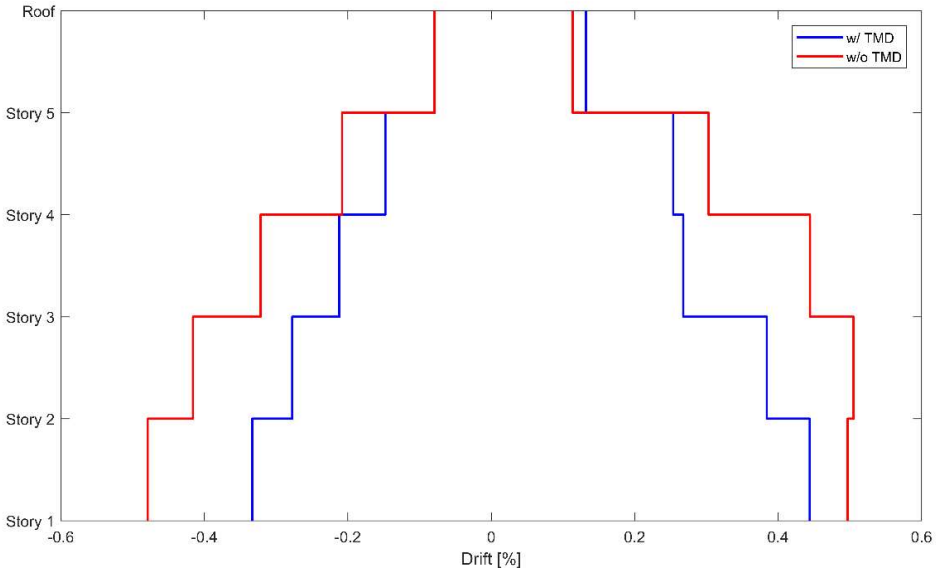

Figure 5.19: Peak inter-story drifts comparison (case 7)

The roof PIDR is reduced by an average of 30% when the isolated mass is added. If the hybrid result is used, a greater reduction would be obtained because the full numerical model tends to overestimate the drift responses. Interestingly, this approach presented here can be used to economically test competing mass damper devices.

5.7. Lessons learned/future work

With the first application of hybrid simulation on a large-scale shake table, there are several challenges encountered that are worth noting. In terms of shake table control, the LHPOST is typically commanded with a target acceleration record, and operates in a three-variable control mode (displacement, velocity and acceleration). Due to high levels of noise in the generated acceleration command from a hybrid simulation, it is recommended that displacement only control is used. Limited feedforward control was used to minimize the delay in the shake table. For this particular setup, SCRAMNet shared memory networks provide fast communication between the controllers and the Target PC. However, in this case one of the cards was found to be faulty (SCRAMNet) and resulted in synchronization problems of the shake table control command. The command error was amplified in taking the derivative of the signal and in some instances resulted in unstable behavior of the shake table.

For the application shown, the feedback from the experiment consisted of the specimen base shear measured directly with load cells below the isolators. For larger specimens, shear load cells may not be available and would require the use of load cells on the shake table actuators. These load cells include inertia and friction effects of the platen. To recover the specimen base shear, a force correction model should be implemented to remove these additional forces (Alireza Sarebanha et al. 2019).

To extend this hybrid technique to larger and more complex structures, further work on the hybrid simulation framework must be performed to combine more complex subassemblies. Larger nonlinear numerical models, with larger computational requirements may necessitate the use of reduce order models that can run in real time (A. Sarebanha et al. 2018) or use data driven models

(Cesmelioglu, Song, and Drignei 2017). Further, the LHOPOST is currently undergoing an upgrade to 6-DOF and will require the extension of this method to multi-DOF.

There are many uncertainties involved in a hybrid test, such as the interaction between the numerical integrators, compensators, shake table control system, and nonlinear response of the experiment. These components are not fully understood in practice and thus a gradual step-by step implementation of a hybrid simulation is recommended. Additionally, constraints were imposed on variable parameters such as a rate limiter and bounding value (see Figure 5.4) especially for adaptive control and compensation algorithms.

5.8. Conclusions

Hybrid simulation provides a cost-efficient framework for testing of structural systems at large or full scale. It was verified that RTHS can be conducted using LHPOST with a soft real-time implementation allowing advanced modeling capabilities or in hard real-time for simpler configurations. This framework can allow parametric studies using the same experimental subassembly while varying the analytical subassembly structural properties. The equipment used here had large delays and the use of the ATS compensator was able to effectively mitigate control errors. However, the compensation signal can add higher frequencies into the control signal of the shake table that manifested itself as high frequency oscillations observed in the hysteresis response of the specimen.

The tests demonstrate new capabilities that can expand the complexity of large-scale geotechnical and structural systems tested on LHPOST. The demonstrated capabilities will enable researchers to investigate different configurations and take advantage of the large capacity of LHPOST including the available soil boxes to include geotechnical elements.

5.9. Remarks

Portions of this dissertation have been published or are currently being considered for publication. Chapter 5 is composed of a first authored publication:

Vega, Manuel A., Andreas H. Schellenberg, Humberto Caudana, and Gilberto Mosqueda. 2020. "Implementation of Real-Time Hybrid Shake Table Testing Using the UCSD Large High-Performance Outdoor Shake Table." International Journal of Lifecycle Performance Engineering Volume 4 (Special Issue on Hybrid Simulation for Multi-Hazard Engineering): 80–102. https://doi.org/10.1504/IJLCPE.2020.108939.

Chapter 6

CONCLUSIONS AND FUTURE RESEARCH

Maintenance planning has been studied for several decades. Two maintenance approaches—time-based maintenance (TBM) and condition-based maintenance (CBM)—have been reviewed and studied. An emphasis has been made on the implementation of a CBM framework applicable to miter gates structures. The different pieces needed for this CBM framework have been addressed which includes diagnosis, prognosis, and maintenance decisions.

As discussed in Chapter 2, 3 and 4, diagnosis heavily depends on the availability of sufficient monitoring data through the life cycle of the structure of interest. On the other hand, when historical monitoring data is limited, diagnosis has to rely heavily on physics-based models. In this scenario, accurate diagnosis will depend on how well the physics-based model represent the true behavior of the structure. In this dissertation, it is assumed that the physics-based model does well-represent the true physics. However, further studies need to be made to account for model discrepancy and its impact to diagnosis, prognosis, and maintenance decisions. Physics-informed surrogate models have been used to tackle the challenge of evaluating computational expensive FE models. Model discrepancy correction and model validation should be explored before deploying this framework to a real structure. Model validation can be achieved through structural testing such as hybrid simulation. Real time hybrid simulation however has been limited by the run time of the numerical portion of the model. Chapter 5 uses a somewhat simple model to allow real time simulation. However, further studies using surrogate models should be carried out to allow more complex structures in the numerical portion of the hybrid model.

As discussed in Chapter 3, prognosis heavily depends on the availability of degradation data through the life cycle of the structure or on the availability of physics-based degradation models (e.g. Paris law). Human error on inspection data heavily influences prognosis and therefore directly impacts maintenance planning. Further studies need to be made account for degradation models built from many sources of inspection data (e.g. OCA rating, inspection data from Maximo, etc.).

Finally, as discussed in Chapter 2 and 3, the proposed CBM approach allowed to obtain the optimal maintenance plan (based on cost minimization) over time based on the information gained by the sensor information using a physics-informed surrogate model. This approach can be applicable to different nonrepairable components in miter gates, which may have different transition matrices values. However, further work needs to be done to extend this methodology to other components in miter gates and then from miter gate components to whole miter gate system level (e.g. including all critical miter gate components). Additionally, further work needs be done to the optimization target criterion to accommodate multi-objective system performance criteria (e.g. cost, availability, reliability, etc.). In this work the damage threshold used for RUL computation is assumed to be known, but further studies should determine impact of different damage thresholds. Many times, variability in damage thresholds depends on the judgement of engineers, inspectors, and decision-making personnel.

REFERENCES

Abadi, Martín, Paul Barham, Jianmin Chen, Zhifeng Chen, Andy Davis, Jeffrey Dean, Matthieu Devin, Sanjay Ghemawat, Geoffrey Irving, Michael Isard, Manjunath Kudlur, Josh Levenberg, Rajat Monga, Sherry Moore, Derek G. Murray, Benoit Steiner, Paul Tucker, Vijay Vasudevan, Pete Warden, Martin Wicke, Yuan Yu, Xiaoqiang Zheng. 2016. "TensorFlow: A System for Large-Scale Machine Learning," May. http://arxiv.org/abs/1605.08695.

Abaza, Khaled A. 2017. "Empirical Approach for Estimating the Pavement Transition Probabilities Used in Non-Homogenous Markov Chains." *International Journal of Pavement Engineering* 18 (2): 128–37. https://doi.org/10.1080/10298436.2015.1039006.

Adeli, H., and C. Yeh. 1989. "Perceptron Learning in Engineering Design." *Computer-Aided Civil and Infrastructure Engineering* 4 (4): 247–56. https://doi.org/10.1111/j.1467-8667.1989.tb00026.x.

Adeli, Hojjat. 2001. "Neural Networks in Civil Engineering: 1989–2000." *Computer-Aided Civil and Infrastructure Engineering* 16 (2): 126–42. https://doi.org/10.1111/0885-9507.00219.

Ahmad, Rosmaini, and Shahrul Kamaruddin. 2012. "An Overview of Time-Based and Condition-Based Maintenance in Industrial Application." *Computers & Industrial Engineering* 63 (1): 135–49. https://doi.org/10.1016/j.cie.2012.02.002.

Al-Fedaghi, Sabah, and Nourah Al-Huwais. 2018. "Toward Modeling Information in Asset Management: Case Study Using Maximo." In *2018 4th International Conference on Information Management (ICIM)*, 117–24. IEEE. https://doi.org/10.1109/INFOMAN.2018.8392821.

Alaswad, Suzan, and Yisha Xiang. 2017. "A Review on Condition-Based Maintenance Optimization Models for Stochastically Deteriorating System." *Reliability Engineering & System Safety* 157 (January): 54–63. https://doi.org/10.1016/j.ress.2016.08.009.

Alexander, Quincy, Anton Netchaev, Matthew Smith, Clayton Thurmer, and Jordan D. Klein. 2018. "Telemetry Techniques for Continuous Monitoring of Partially Submerged Large Civil Infrastructure." In *Sensors and Smart Structures Technologies for Civil, Mechanical, and Aerospace Systems 2018*, edited by Hoon Sohn, 1059823:76. SPIE. https://doi.org/10.1117/12.2298413.

Allen, James P., Stuart D. Foltz, and Matthew H. Werth. 2018. "Sustainment Management System Dams Inspection Module: Department of Defense Dams Inventory and Inspection Template." https://erdc-library.erdc.dren.mil/xmlui/handle/11681/27351.

An, Dawn, Joo-Ho Choi, and Nam H. Kim. 2012. "Identification of Correlated Damage Parameters under Noise and Bias Using Bayesian Inference." *Structural Health Monitoring: An International Journal* 11 (3): 293–303. https://doi.org/10.1177/1475921711424520.

An, Dawn, Joo-Ho Choi, Tony L. Schmitz, and Nam H. Kim. 2011. "In Situ Monitoring and

Prediction of Progressive Joint Wear Using Bayesian Statistics." *Wear* 270 (11–12): 828–38. https://doi.org/10.1016/j.wear.2011.02.010.

An, Dawn, Nam H. Kim, and Joo-Ho Choi. 2015. "Practical Options for Selecting Data-Driven or Physics-Based Prognostics Algorithms with Reviews." *Reliability Engineering & System Safety* 133 (January): 223–36. https://doi.org/10.1016/j.ress.2014.09.014.

Arangio, Stefania, and Franco Bontempi. 2015. "Structural Health Monitoring of a Cable-Stayed Bridge with Bayesian Neural Networks." *Structure and Infrastructure Engineering* 11 (4): 575–87. https://doi.org/10.1080/15732479.2014.951867.

Arzaghi, Ehsan, Mohammad Mahdi Abaei, Rouzbeh Abbassi, Vikram Garaniya, Christopher Chin, and Faisal Khan. 2017. "Risk-Based Maintenance Planning of Subsea Pipelines through Fatigue Crack Growth Monitoring." *Engineering Failure Analysis* 79 (May): 928–39. https://doi.org/10.1016/j.engfailanal.2017.06.003.

Astroza, Rodrigo, Hamed Ebrahimian, Yong Li, and Joel P. Conte. 2017. "Bayesian Nonlinear Structural FE Model and Seismic Input Identification for Damage Assessment of Civil Structures." *Mechanical Systems and Signal Processing* 93 (September): 661–87. https://doi.org/10.1016/j.ymssp.2017.01.040.

Barlow, Richard, and Larry Hunter. 1960. "Optimum Preventive Maintenance Policies." *Operations Research* 8 (1): 90–100. https://doi.org/10.1287/opre.8.1.90.

Bichon, Barron J., John M. McFarland, and Sankaran Mahadevan. 2011. "Efficient Surrogate Models for Reliability Analysis of Systems with Multiple Failure Modes." *Reliability Engineering & System Safety* 96 (10): 1386–95. https://doi.org/10.1016/j.ress.2011.05.008.

Blei, David M., Alp Kucukelbir, and Jon D. McAuliffe. 2017. "Variational Inference: A Review for Statisticians." *Journal of the American Statistical Association* 112 (518): 859–77. https://doi.org/10.1080/01621459.2017.1285773.

Bocchini, Paolo, Duygu Saydam, and Dan M. Frangopol. 2013. "Efficient, Accurate, and Simple Markov Chain Model for the Life-Cycle Analysis of Bridge Groups." *Structural Safety* 40 (January): 51–64. https://doi.org/10.1016/j.strusafe.2012.09.004.

Brynjarsdóttir, Jenný, and Anthony O'Hagan. 2014. "Learning about Physical Parameters: The Importance of Model Discrepancy." *Inverse Problems* 30 (11): 114007. https://doi.org/10.1088/0266-5611/30/11/114007.

Caldarelli, Guido, Matthieu Cristelli, Andrea Gabrielli, Luciano Pietronero, Antonio Scala, and Andrea Tacchella. 2012. "A Network Analysis of Countries' Export Flows: Firm Grounds for the Building Blocks of the Economy." Edited by Alessandro Flammini. *PLoS ONE* 7 (10): e47278. https://doi.org/10.1371/journal.pone.0047278.

Campbell, Alexander. 2019. "Personal Communication, Feb. 25, 2019."

Campbell, Leslie E., Robert J. Connor, Julie M. Whitehead, and Glenn A. Washer. 2020.

"Benchmark for Evaluating Performance in Visual Inspection of Fatigue Cracking in Steel Bridges." *Journal of Bridge Engineering* 25 (1): 04019128. https://doi.org/10.1061/(ASCE)BE.1943-5592.0001507.

Castro, I.T., and Attahiru Sule Alfa. 2004. "Lifetime Replacement Policy in Discrete Time for a Single Unit System." *Reliability Engineering & System Safety* 84 (2): 103–11. https://doi.org/10.1016/j.ress.2003.11.005.

Cesmelioglu, A., M. Song, and D. Drignei. 2017. "Physics-Based Kriging Surrogates for a Class of Finite Element Codes." *SIAM/ASA Journal on Uncertainty Quantification* 5 (1): 870–89. https://doi.org/10.1137/16M1092489.

Chae, Yunbyeong, Karim Kazemibidokhti, and James M. Ricles. 2013. "Adaptive Time Series Compensator for Delay Compensation of Servo-Hydraulic Actuator Systems for Real-Time Hybrid Simulation." *Earthquake Engineering & Structural Dynamics* 42 (11): 1697–1715. https://doi.org/10.1002/eqe.2294.

Chiachío, Juan, María L. Jalón, Manuel Chiachío, and Athanasios Kolios. 2020. "A Markov Chains Prognostics Framework for Complex Degradation Processes." *Reliability Engineering & System Safety* 195 (January 2019): 106621. https://doi.org/10.1016/j.ress.2019.106621.

Childress, Suzanne, and Pablo Durango-Cohen. 2005. "On Parallel Machine Replacement Problems with General Replacement Cost Functions and Stochastic Deterioration." *Naval Research Logistics* 52 (5): 409–19. https://doi.org/10.1002/nav.20088.

Chua, C.G., and Anthony T.C. Goh. 2005. "Estimating Wall Deflections in Deep Excavations Using Bayesian Neural Networks." *Tunnelling and Underground Space Technology* 20 (4): 400–409. https://doi.org/10.1016/j.tust.2005.02.001.

Chung, Jintai, and G M Hulbert. 1993. "A Time Integration Algorithm for Structural Dynamics With Improved Numerical Dissipation: The Generalized-α Method." *Journal of Applied Mechanics* 60 (2): 371. https://doi.org/10.1115/1.2900803.

Commander, Brett C., Jeff X. Schulz, George G. Goble, and Camneron P. Chasten. 1994. "Detection of Structural Damage on Miter Gates."

Corcoran, Joseph. 2017. "Rate-Based Structural Health Monitoring Using Permanently Installed Sensors." *Proceedings of the Royal Society A: Mathematical, Physical and Engineering Sciences* 473 (2205): 20170270. https://doi.org/10.1098/rspa.2017.0270.

Csáji, B. 2001. "Approximation with Artificial Neural Networks." Eötvös Loránd University, Hungary. https://doi.org/10.1.1.101.2647.

Daigle, Matthew, and Kai Goebel. 2011. "Multiple Damage Progression Paths in Model-Based Prognostics." In *2011 Aerospace Conference*, 1–10. IEEE. https://doi.org/10.1109/AERO.2011.5747574.

Daniel, Ryszard, and Tim Paulus. 2019a. “Detailed Gate Design☆.” In *Lock Gates and Other Closures in Hydraulic Projects*, 531–620. Elsevier. https://doi.org/10.1016/B978-0-12-809264-4.00008-2.

———. 2019b. “Hydraulic Gates in View of Asset Management.” In *Lock Gates and Other Closures in Hydraulic Projects*, 945–60. Elsevier. https://doi.org/10.1016/B978-0-12-809264-4.00017-3.

———. 2019c. “Maintenance Issues.” In *Lock Gates and Other Closures in Hydraulic Projects*, 883–916. Elsevier. https://doi.org/10.1016/B978-0-12-809264-4.00015-X.

Dao, Nhan D, Keri L Ryan, Eiji Sato, and Tomohiro Sasaki. 2013. “Predicting the Displacement of Triple Pendulum™ Bearings in a Full-Scale Shaking Experiment Using a Three-Dimensional Element.” *Earthquake Engineering & Structural Dynamics* 42 (11): 1677–95. https://doi.org/10.1002/eqe.2293.

Das, A.N., and Damodar Acharya. 2004. “Age Replacement of Components During IFR Delay Time.” *IEEE Transactions on Reliability* 53 (3): 306–12. https://doi.org/10.1109/TR.2004.833422.

Degroot, Morris H. 1974. “Reaching a Consensus.” *Journal of the American Statistical Association* 69 (345): 118–21. https://doi.org/10.1080/01621459.1974.10480137.

Del-Carpio R., Maikol, M Javad Hashemi, and Gilberto Mosqueda. 2017. “Evaluation of Integration Methods for Hybrid Simulation of Complex Structural Systems through Collapse.” *Earthquake Engineering and Engineering Vibration* 16 (4): 745–59. https://doi.org/10.1007/s11803-017-0411-z.

Dutta, Anindya, J. F Sumnicht, R. L Mayes, R. O Hamburger, and A Citipitioglu. 2009. “An Innovative Application of Base Isolation Technology.” In *Improving the Seismic Performance of Existing Buildings and Other Structures*, 841–54. Reston, VA: American Society of Civil Engineers. https://doi.org/10.1061/41084(364)77.

Eick, Brian A., Matthew D. Smith, and Travis B. Fillmore. 2019a. “Feasibility of Retrofitting Existing Miter-Type Lock Gates with Discontinuous Contact Blocks.” *Journal of Structural Integrity and Maintenance* 4 (4): 179–94. https://doi.org/10.1080/24705314.2019.1657617.

Eick, Brian A., Billie F. Treece, Zachary R., Spencer Jr., Matthew D. Smith, Steven C. Sweeney, Quincy G. Alexander, and Stuart D. Foltz. 2017. “Miter Gate Gap Detection Using Principal Component Analysis.”

Eick, Brian A., Zachary R. Treece, Billie F. Spencer, Matthew D. Smith, Steven C. Sweeney, Quincy G. Alexander, and Stuart D. Foltz. 2018. “Automated Damage Detection in Miter Gates of Navigation Locks.” *Structural Control and Health Monitoring* 25 (1): 1–18. https://doi.org/10.1002/stc.2053.

Eick, Brian A, Matthew D Smith, and Travis B Fillmore. 2019b. “Feasibility of Discontinuous Quoin Blocks for USACE Miter Gates.”

Elkordy, M. F., K. C. Chang, and G. C. Lee. 1994. "A Structural Damage Neural Network Monitoring System." *Computer-Aided Civil and Infrastructure Engineering* 9 (2): 83–96. https://doi.org/10.1111/j.1467-8667.1994.tb00364.x.

Estes, Allen C., Dan M. Frangopol, and Stuart D. Foltz. 2004. "Updating Reliability of Steel Miter Gates on Locks and Dams Using Visual Inspection Results." *Engineering Structures* 26 (3): 319–33. https://doi.org/10.1016/j.engstruct.2003.10.007.

Evans, James A, James R Tallent, Richard D Brown, Anton Netchaev, and Clayton R Thurmer. 2019. "Determining Miter Gate Plate Corrosion and Thickness of Anti-Corrosion Coatings ; and Development of a Mobile Sensor Inspection Platform Information Technology Laboratory." Vicksburg, MS.

Farrar, Charles R., and Keith Worden. 2012. *Structural Health Monitoring*. *Structural Health Monitoring: A Machine Learning Perspective*. Chichester, UK: John Wiley & Sons, Ltd. https://doi.org/10.1002/9781118443118.

Feng, Maria Q., and Eun Y. Bahng. 1999. "Damage Assessment of Jacketed RC Columns Using Vibration Tests." *Journal of Structural Engineering* 125 (3): 265–71. https://doi.org/10.1061/(ASCE)0733-9445(1999)125:3(265).

Flam-shepherd, Daniel, James Requeima, and David Duvenaud. 2017. "Mapping Gaussian Process Priors to Bayesian Neural Networks." In *31st Conference on Neural Information Processing Systems (NeurIPS 2017)*, 1–8. Long Beach, CA, USA: Curran Associates Inc. http://bayesiandeeplearning.org/2017/papers/65.pdf.

Foltz, Stuart D. 2017. "Investigation of Mechanical Breakdowns Leading to Lock Closures." Champaign, IL.

Foltz, Stuart D, Carlos B Bislip-morales, and E Allen Hammack. 2013. "Asset Management and Facility Equipment Maintenance Nexus : Maintenance Effectiveness Engineer Research and Development Center."

Galar, D., U. Kumar, J. Lee, and W. Zhao. 2012. "Remaining Useful Life Estimation Using Time Trajectory Tracking and Support Vector Machines." *Journal of Physics: Conference Series* 364 (1): 012063. https://doi.org/10.1088/1742-6596/364/1/012063.

Geman, Stuart, and Donald Geman. 1984. "Stochastic Relaxation, Gibbs Distributions, and the Bayesian Restoration of Images." *IEEE Transactions on Pattern Analysis and Machine Intelligence* PAMI-6 (6): 721–41. https://doi.org/10.1109/TPAMI.1984.4767596.

Gomez, Fernando, Billie F. Spencer, Jr., and Matthew D. Smith. 2019. "Bayesian Modeling Updating of Miter Gates with Uncertain Boundary Conditions." In *Structural Health Monitoring 2019*. Lancaster, PA: DEStech Publications, Inc. https://doi.org/10.12783/shm2019/32129.

Gong, Changqing, and Dan M. Frangopol. 2020. "Condition-Based Multiobjective Maintenance Decision Making for Highway Bridges Considering Risk Perceptions." *Journal of Structural*

Engineering 146 (5): 04020051. https://doi.org/10.1061/(ASCE)ST.1943-541X.0002570.

Graybeal, Benjamin A., Brent M. Phares, Dennis D. Rolander, Mark Moore, and Glenn Washer. 2002. "Visual Inspection of Highway Bridges." *Journal of Nondestructive Evaluation* 21 (3): 67–83. https://doi.org/10.1023/A:1022508121821.

Guedes Soares, C., Y. Garbatov, and A. Zayed. 2011. "Effect of Environmental Factors on Steel Plate Corrosion under Marine Immersion Conditions." *Corrosion Engineering, Science and Technology* 46 (4): 524–41. https://doi.org/10.1179/147842209X12559428167841.

Hajela, P., and L. Berke. 1991. "Neurobiological Computational Models in Structural Analysis and Design." *Computers & Structures* 41 (4): 657–67. https://doi.org/10.1016/0045-7949(91)90178-O.

Hashemi, M. Javad, Armin Masroor, and Gilberto Mosqueda. 2014. "Implementation of Online Model Updating in Hybrid Simulation." *Earthquake Engineering & Structural Dynamics* 43 (3): 395–412. https://doi.org/10.1002/eqe.2350.

Hoskere, Vedhus, Brian Eick, Billie F Spencer, Matthew D. Smith, and Stuart D. Foltz. 2019. "Deep Bayesian Neural Networks for Damage Quantification in Miter Gates of Navigation Locks." *Structural Health Monitoring*, November, 147592171988208. https://doi.org/10.1177/1475921719882086.

Hughes, Thomas J.R., Karl S. Pister, and Robert L. Taylor. 1979. "Implicit-Explicit Finite Elements in Nonlinear Transient Analysis." *Computer Methods in Applied Mechanics and Engineering* 17–18 (PART 1): 159–82. https://doi.org/10.1016/0045-7825(79)90086-0.

Igarashi, Akira, Hirokazu Iemura, and Takanori Suwa. 2000. "Development of Substructured Shaking Table Test Method." In *12th World Conference on Earth- Quake Engineering*. Auckland, New Zealand.

Jang, Shinae, Jian Li, and Billie F. Spencer. 2013. "Corrosion Estimation of a Historic Truss Bridge Using Model Updating." *Journal of Bridge Engineering* 18 (7): 678–89. https://doi.org/10.1061/(ASCE)BE.1943-5592.0000403.

Jensen, H.A., C. Esse, V. Araya, and C. Papadimitriou. 2017. "Implementation of an Adaptive Meta-Model for Bayesian Finite Element Model Updating in Time Domain." *Reliability Engineering & System Safety* 160 (July 2016): 174–90. https://doi.org/10.1016/j.ress.2016.12.005.

Jiang, R., and D.N.P. Murthy. 2011. "A Study of Weibull Shape Parameter: Properties and Significance." *Reliability Engineering & System Safety* 96 (12): 1619–26. https://doi.org/10.1016/j.ress.2011.09.003.

Kennedy, Marc C., and Anthony O'Hagan. 2001. "Bayesian Calibration of Computer Models." *Journal of the Royal Statistical Society: Series B (Statistical Methodology)* 63 (3): 425–64. https://doi.org/10.1111/1467-9868.00294.

Kim, Sang-Hyo, Chongyul Yoon, and Byoung-Jin Kim. 2000. "Structural Monitoring System Based on Sensitivity Analysis and a Neural Network." *Computer-Aided Civil and Infrastructure Engineering* 15 (4): 189–95. https://doi.org/10.1111/0885-9507.00194.

Kolay, Chinmoy, and James M. Ricles. 2014. "Development of a Family of Unconditionally Stable Explicit Direct Integration Algorithms with Controllable Numerical Energy Dissipation." *Earthquake Engineering & Structural Dynamics* 43 (9): 1361–80. https://doi.org/10.1002/eqe.2401.

Kolay, Chinmoy, James M. Ricles, Thomas M. Marullo, Akbar Mahvashmohammadi, and Richard Sause. 2015. "Implementation and Application of the Unconditionally Stable Explicit Parametrically Dissipative KR- α Method for Real-Time Hybrid Simulation." *Earthquake Engineering & Structural Dynamics* 44 (5): 735–55. https://doi.org/10.1002/eqe.2484.

Konakli, Katerina, and Michael H Faber. 2014. "Value of Information Analysis in Structural Safety." In *Vulnerability, Uncertainty, and Risk*, 1605–14. Reston, VA: American Society of Civil Engineers. https://doi.org/10.1061/9780784413609.161.

Kress, Marin M, Kenneth N Mitchell, Patricia K Dijoseph, J Scott Rainey, Matthew Chambers, Jonathan Hsieh, and W Jeff Lillycrop. 2016. "ERDC / CHL TR-16-8 Marine Transportation System Performance Measures Research Coastal and Hydraulics Laboratory." Vicksburg, MS.

Lam, Heung-Fai, Ka-Veng Yuen, and James L. Beck. 2006. "Structural Health Monitoring via Measured Ritz Vectors Utilizing Artificial Neural Networks." *Computer-Aided Civil and Infrastructure Engineering* 21 (4): 232–41. https://doi.org/10.1111/j.1467-8667.2006.00431.x.

Lee, Anthony, Christopher Yau, Michael B. Giles, Arnaud Doucet, and Christopher C. Holmes. 2010. "On the Utility of Graphics Cards to Perform Massively Parallel Simulation of Advanced Monte Carlo Methods." *Journal of Computational and Graphical Statistics* 19 (4): 769–89. https://doi.org/10.1198/jcgs.2010.10039.

Leung, Michael Siu Hey, Joseph Corcoran, Peter Cawley, and Michael D. Todd. 2019. "Evaluating the Use of Rate-Based Monitoring for Improved Fatigue Remnant Life Predictions." *International Journal of Fatigue* 120 (July 2018): 162–74. https://doi.org/10.1016/j.ijfatigue.2018.11.012.

Li, Chenzhao, Sankaran Mahadevan, You Ling, Sergio Choze, and Liping Wang. 2017. "Dynamic Bayesian Network for Aircraft Wing Health Monitoring Digital Twin." *AIAA Journal* 55 (3): 930–41. https://doi.org/10.2514/1.J055201.

Liao, Linxia, and Felix Kottig. 2014. "Review of Hybrid Prognostics Approaches for Remaining Useful Life Prediction of Engineered Systems, and an Application to Battery Life Prediction." *IEEE Transactions on Reliability* 63 (1): 191–207. https://doi.org/10.1109/TR.2014.2299152.

Ling, You, Joshua Mullins, and Sankaran Mahadevan. 2012. "Calibration of Multi-Physics

Computational Models Using Bayesian Networks." *ArXiv Preprint ArXiv:1206.5015*, June, 1–38. http://arxiv.org/abs/1206.5015.

———. 2014. "Selection of Model Discrepancy Priors in Bayesian Calibration." *Journal of Computational Physics* 276 (November): 665–80. https://doi.org/10.1016/j.jcp.2014.08.005.

Liu, Haitao, Yew-Soon Ong, Xiaobo Shen, and Jianfei Cai. 2018. "When Gaussian Process Meets Big Data: A Review of Scalable GPs," July, 1–20. http://arxiv.org/abs/1807.01065.

Liu, Yanhui, Kevin Goorts, Ali Ashasi-Sorkhabi, Oya Mercan, and Sriram Narasimhan. 2016. "A State Space-Based Explicit Integration Method for Real-Time Hybrid Simulation." *Structural Control and Health Monitoring* 23 (4): 641–58. https://doi.org/10.1002/stc.1798.

Lu, Susan, Yu-Chen Tu, and Huitian Lu. 2007. "Predictive Condition-Based Maintenance for Continuously Deteriorating Systems." *Quality and Reliability Engineering International* 23 (1): 71–81. https://doi.org/10.1002/qre.823.

Mahmoud, Hussam, Akshat Chulahwat, and Guillermo Riveros. 2018. "Fatigue and Fracture Life-Cycle Cost Assessment of a Miter Gate with Multiple Cracks." *Engineering Failure Analysis* 83 (September 2017): 57–74. https://doi.org/10.1016/j.engfailanal.2017.09.008.

Masri, S. F., M. Nakamura, A. G. Chassiakos, and T. K. Caughey. 1996. "Neural Network Approach to Detection of Changes in Structural Parameters." *Journal of Engineering Mechanics* 122 (4): 350–60. https://doi.org/10.1061/(ASCE)0733-9399(1996)122:4(350).

Mathworks. 2015. "MATLAB, Simulink, Stateflow, SimulinkRT."

McKenna, Frank, Gregory L. Fenves, and Micheal H. Scott. 2000. "Open System for Earthquake Engineering Simulation." Pacific Earthquake Engineering Research Center. http://opensees.berkeley.edu/.

Melchers, R. E. 2004. "Mathematical Modeling of the Effect of Water Velocity on the Marine Immersion Corrosion of Mild Steel Coupons." *CORROSION* 60 (5): 471–78. https://doi.org/10.5006/1.3299243.

Mikami, Ichizou, Shigenori Tanaka, and Tatsuya Hiwatashi. 1998. "Neural Network System for Reasoning Residual Axial Forces of High-Strength Bolts in Steel Bridges." *Computer-Aided Civil and Infrastructure Engineering* 13 (4): 237–46. https://doi.org/10.1111/0885-9507.00102.

Mitchell, John S. 2007. "From Vibration Measurements to Condition Based Maintenance Seventy Years of Continuous Progress." *Sound and Vibration* 41 (1): 62–78.

Moaveni, Babak, Joel P. Conte, and François M. Hemez. 2009. "Uncertainty and Sensitivity Analysis of Damage Identification Results Obtained Using Finite Element Model Updating." *Computer-Aided Civil and Infrastructure Engineering* 24 (5): 320–34. https://doi.org/10.1111/j.1467-8667.2008.00589.x.

Mohanty, Subhasish, Santanu Das, Aditi Chattopadhyay, and Pedro Peralta. 2009. "Gaussian Process Time Series Model for Life Prognosis of Metallic Structures." *Journal of Intelligent Material Systems and Structures* 20 (8): 887–96. https://doi.org/10.1177/1045389X08099602.

Mohseni, Hessam, Sujeeva Setunge, Guomin Zhang, and Ron Wakefield. 2017. "Markov Process for Deterioration Modeling and Asset Management of Community Buildings." *Journal of Construction Engineering and Management* 143 (6): 04017003. https://doi.org/10.1061/(ASCE)CO.1943-7862.0001272.

Morcous, G. 2006. "Performance Prediction of Bridge Deck Systems Using Markov Chains." *Journal of Performance of Constructed Facilities* 20 (2): 146–55. https://doi.org/10.1061/(ASCE)0887-3828(2006)20:2(146).

Morzfeld, Matthias, Xin T. Tong, and Youssef M. Marzouk. 2017. "Localization for MCMC: Sampling High-Dimensional Posterior Distributions with Local Structure." *Journal of Computational Physics* 380 (i): 1–28. https://doi.org/10.1016/j.jcp.2018.12.008.

Mosqueda, Gilberto, T. Y. Yang, and B Stojadinovic. 2008. "Assessment of Experimental Errors in Hybrid Simulation of Seismic Structural Response." In *Hybrid Simulation: Theory, Implementation and Applications*, edited by Victor E. Saouma and Mettupalayam V. Sivaselvan, 35–45. Boulder, CO: Taylor & Francis.

Nakagawa, Toshio, and Kazumi Yasui. 2005. "Note on Optimal Redundant Policies for Reliability Models." *Journal of Quality in Maintenance Engineering* 11 (1): 82–96. https://doi.org/10.1108/13552510510589398.

Nakata, Narutoshi, and Matthew Stehman. 2012. "Substructure Shake Table Test Method Using a Controlled Mass: Formulation and Numerical Simulation." *Earthquake Engineering & Structural Dynamics* 41 (14): 1977–88. https://doi.org/10.1002/eqe.2169.

Neal, Radford M. 1996. *Bayesian Learning for Neural Networks*. Vol. 118. Lecture Notes in Statistics. New York, NY: Springer New York. https://doi.org/10.1007/978-1-4612-0745-0.

Okasha, Nader M., Dan M. Frangopol, and André D. Orcesi. 2012. "Automated Finite Element Updating Using Strain Data for the Lifetime Reliability Assessment of Bridges." *Reliability Engineering & System Safety* 99 (March): 139–50. https://doi.org/10.1016/j.ress.2011.11.007.

Orchard, Marcos E., and George J. Vachtsevanos. 2007. "A Particle Filtering Approach for On-Line Failure Prognosis in a Planetary Carrier Plate." *International Journal of Fuzzy Logic and Intelligent Systems* 7 (4): 221–27. https://doi.org/10.5391/IJFIS.2007.7.4.221.

Orchard, Marcos, Gregory Kacprzynski, Kai Goebel, Bhaskar Saha, and George Vachtsevanos. 2008. "Advances in Uncertainty Representation and Management for Particle Filtering Applied to Prognostics." In *2008 International Conference on Prognostics and Health Management*, 1–6. IEEE. https://doi.org/10.1109/PHM.2008.4711433.

Ostwald, Dirk. 2019. “Variational Inference.” In *Probabilistic Models for Functional Neuroimaging*, 163–71. Berlin, Germany: Dirk Ostwald CC. https://ssl2.cms.fu-berlin.de/ewi-psy/einrichtungen/arbeitsbereiche/computational_cogni_neurosc/PMFN/15-Variational-inference.pdf.

Ou, Ge, Ali Irmak Ozdagli, Shirley J Dyke, and Bin Wu. 2015. “Robust Integrated Actuator Control: Experimental Verification and Real-Time Hybrid-Simulation Implementation.” *Earthquake Engineering & Structural Dynamics* 44 (3): 441–60. https://doi.org/10.1002/eqe.2479.

Parno, Matthew, Devin O’Connor, and Matthew Smith. 2018. “High Dimensional Inference for the Structural Health Monitoring of Lock Gates,” December, 1–29. http://arxiv.org/abs/1812.05529.

Petcherdchoo, Aruz, Luis A. Neves, and Dan M. Frangopol. 2008. “Optimizing Lifetime Condition and Reliability of Deteriorating Structures with Emphasis on Bridges.” *Journal of Structural Engineering* 134 (4): 544–52. https://doi.org/10.1061/(ASCE)0733-9445(2008)134:4(544).

Przybyla, John. 2013. “Best Practices in Asset Management.” *USACE Institute for Water Resources*. Alexandria, Virginia. https://www.iwr.usace.army.mil/Portals/70/docs/iwrreports/2013-R-08_Best_Practices_in_Asset_Management.pdf.

Ramancha, Mukesh Kumar, Rodrigo Astroza, Joel P. Conte, Jose I. Restrepo, and Michael D. Todd. 2020. “Bayesian Nonlinear Finite Element Model Updating of a Full-Scale Bridge-Column Using Sequential Monte Carlo.” In *38th International Modal Analysis Conference*. Houston, Texas: Springer.

Ramancha, Mukesh Kumar, Ramin Madarshahian, Rodrigo Astroza, and Joel P. Conte. 2019. “Non-Unique Estimates in Material Parameter Identification of Nonlinear FE Models Governed by Multiaxial Material Models Using Unscented Kalman Filtering.” In , 257–65. Orlando, Florida: Springer. https://doi.org/10.1007/978-3-030-12075-7_29.

Rathje, Ellen M., Clint Dawson, Jamie E. Padgett, Jean-Paul Pinelli, Dan Stanzione, Ashley Adair, Pedro Arduino, Scott J. Brandenberg, Tim Cockerill, Charlie Dey, Maria Esteva, Fred L. Haan Jr., Matthew Hanlon, Ahsan Kareem, Laura Lowes, Stephen Mock, and Gilberto Mosqueda. 2017. “DesignSafe: New Cyberinfrastructure for Natural Hazards Engineering.” *Natural Hazards Review* 18 (3): 06017001. https://doi.org/10.1061/(ASCE)NH.1527-6996.0000246.

Reinhorn, A. M., M. Bruneau, S. Y. Chu, Xiaoyun Shao, and M. C. Pitman. 2003. “Large Scale Real Time Dynamic Hybrid Testing Technique – Shake Tables Substructure Testing.” In *ASCE Proceedings of the Structures Congress and Exposition*, 67–72. https://doi.org/10.1.1.115/eqe.5862.

Reliasoft. 2019. “A High Value of Beta Is Not Necessarily Cause for Concern.” 2019. https://www.reliasoft.com/resources/resource-center/a-high-value-of-beta-is-not-necessarily-cause-for-concern.

Riveros, Guillermo A., Jorge L. Ayala-Burgos, and Deanna Dixon. 2017. "Numerical Investigation of Diagonals in Miter Gates: Looking for the Optimum Prestressing." *Journal of Performance of Constructed Facilities* 31 (1): 04016073. https://doi.org/10.1061/(ASCE)CF.1943-5509.0000896.

Riveros, Guillermo A., and Manuel E. Rosario-Pérez. 2018. "Deriving the Transition Probability Matrix Using Computational Mechanics." *Engineering Computations* 35 (2): 692–709. https://doi.org/10.1108/EC-02-2017-0051.

Rocchetta, Roberto, Matteo Broggi, Quentin Huchet, and Edoardo Patelli. 2018. "On-Line Bayesian Model Updating for Structural Health Monitoring." *Mechanical Systems and Signal Processing* 103 (March): 174–95. https://doi.org/10.1016/j.ymssp.2017.10.015.

Ruder, Sebastian. 2016. "An Overview of Gradient Descent Optimization Algorithms," September, 1–14. http://arxiv.org/abs/1609.04747.

Ruiz-García, Jorge, and Eduardo Miranda. 2006. "Evaluation of Residual Drift Demands in Regular Multi-Storey Frames for Performance-Based Seismic Assessment." *Earthquake Engineering & Structural Dynamics* 35 (13): 1609–29. https://doi.org/10.1002/eqe.593.

Sarebanha, A., G. Mosqueda, M.K. Kim, and J.H. Kim. 2018. "Seismic Response of Base Isolated Nuclear Power Plants Considering Impact to Moat Walls." *Nuclear Engineering and Design* 328 (January): 58–72. https://doi.org/10.1016/j.nucengdes.2017.12.021.

Sarebanha, Alireza, Reas H. Schellenberg, Matthew J. Schoettler, Gilberto Mosqueda, and Stephen A. Mahin. 2019. "Real-Time Hybrid Simulation of Seismically Isolated Structures with Full-Scale Bearings and Large Computational Models." *Computer Modeling in Engineering & Sciences* 120 (3): 693–717. https://doi.org/10.32604/cmes.2019.04846.

Saydam, Duygu, and Dan M. Frangopol. 2015. "Risk-Based Maintenance Optimization of Deteriorating Bridges." *Journal of Structural Engineering* 141 (4): 04014120. https://doi.org/10.1061/(ASCE)ST.1943-541X.0001038.

Schellenberg, A, B Shao, and S Mahin. 2017. "Developemnt of a Large-Scale 6Dof Hybrid Shake Table and Application To Testing Response Modification Devices for Tall Buildings." In *Proceedings of the 16th World Conference on Earthquake Engineering (16WCEE)*. Santiago, Chile.

Schellenberg, Andreas H, Tracy C Becker, and Stephen A Mahin. 2016. "Hybrid Shake Table Testing Method: Theory, Implementation and Application to Midlevel Isolation." *Structural Control and Health Monitoring* 24 (5): e1915. https://doi.org/10.1002/stc.1915.

Schellenberg, Andreas H, Stephen A Mahin, and Gregory L Fenves. 2009. "Advanced Implementation of Hybrid Simulation." http://peer.berkeley.edu/publications/peer_reports.html.

———. 2013. "Open-Source Framework for Experimental Setup and Control." http://openfresco.berkeley.edu.

Schoof, J. T., and S. C. Pryor. 2008. “On the Proper Order of Markov Chain Model for Daily Precipitation Occurrence in the Contiguous United States.” *Journal of Applied Meteorology and Climatology* 47 (9): 2477–86. https://doi.org/10.1175/2008JAMC1840.1.

Schultz, Martin T. 2018. “Personal Communication, Sept. 18, 2018.”

Shao, X, A M Reinhorn, and M V Sivaselvan. 2011. “Real-Time Hybrid Simulation Using Shake Tables and Dynamic Actuators.” *Journal of Structural Engineering* 137 (7): 748–60. https://doi.org/10.1061/(ASCE)ST.1943-541X.0000314.

Shao, Xiaoyun, Adam Mueller, and Bilal Ahmed Mohammed. 2016. “Real-Time Hybrid Simulation with Online Model Updating: Methodology and Implementation.” *Journal of Engineering Mechanics* 142 (2): 04015074. https://doi.org/10.1061/(ASCE)EM.1943-7889.0000987.

Shi, Jiaxin, Mohammad Emtiyaz Khan, and Jun Zhu. 2019. “Scalable Training of Inference Networks for Gaussian-Process Models.” In . http://arxiv.org/abs/1905.10969.

Shu, Jiangpeng, Ziye Zhang, Ignacio Gonzalez, and Raid Karoumi. 2013. “The Application of a Damage Detection Method Using Artificial Neural Network and Train-Induced Vibrations on a Simplified Railway Bridge Model.” *Engineering Structures* 52 (July): 408–21. https://doi.org/10.1016/j.engstruct.2013.02.031.

Spencer, Billie F., Vedhus Hoskere, and Yasutaka Narazaki. 2019. “Advances in Computer Vision-Based Civil Infrastructure Inspection and Monitoring.” *Engineering* 5 (2): 199–222. https://doi.org/10.1016/j.eng.2018.11.030.

Stoffel, Marcus, Franz Bamer, and Bernd Markert. 2018. “Artificial Neural Networks and Intelligent Finite Elements in Non-Linear Structural Mechanics.” *Thin-Walled Structures* 131 (July): 102–6. https://doi.org/10.1016/j.tws.2018.06.035.

Strauss, A., S. Hoffmann, R. Wendner, and K. Bergmeister. 2009. “Structural Assessment and Reliability Analysis for Existing Engineering Structures, Applications for Real Structures.” *Structure and Infrastructure Engineering* 5 (4): 277–86. https://doi.org/10.1080/15732470601185638.

Sun, Shengyang, Guodong Zhang, Jiaxin Shi, and Roger Grosse. 2019. “Functional Variational Bayesian Neural Networks,” March, 1–22. http://arxiv.org/abs/1903.05779.

Tan, Z.X., D.P. Thambiratnam, T.H.T. Chan, and H. Abdul Razak. 2017. “Detecting Damage in Steel Beams Using Modal Strain Energy Based Damage Index and Artificial Neural Network.” *Engineering Failure Analysis* 79 (May): 253–62. https://doi.org/10.1016/j.engfailanal.2017.04.035.

Theocaris, P.S., and P.D. Panagiotopoulos. 1993. “Neural Networks for Computing in Fracture Mechanics. Methods and Prospects of Applications.” *Computer Methods in Applied Mechanics and Engineering* 106 (1–2): 213–28. https://doi.org/10.1016/0045-7825(93)90191-Y.

Thöns, Sebastian. 2018. “On the Value of Monitoring Information for the Structural Integrity and Risk Management.” *Computer-Aided Civil and Infrastructure Engineering* 33 (1): 79–94. https://doi.org/10.1111/mice.12332.

Tian, Zhigang, Tongdan Jin, Bairong Wu, and Fangfang Ding. 2011. “Condition Based Maintenance Optimization for Wind Power Generation Systems under Continuous Monitoring.” *Renewable Energy* 36 (5): 1502–9. https://doi.org/10.1016/j.renene.2010.10.028.

Tian, Zhigang, and Haitao Liao. 2011. “Condition Based Maintenance Optimization for Multi-Component Systems Using Proportional Hazards Model.” *Reliability Engineering & System Safety* 96 (5): 581–89. https://doi.org/10.1016/j.ress.2010.12.023.

Todd, Michael D., and Erick B. Flynn. 2011. “A Bayesian Experimental Design Approach for Structural Health Monitoring.” In *14th International Symposium on Dynamic Problems of Mechanics (DINAME 2011)*. Sao Sebastio, Brazil.

Tran, Dustin, Matthew D. Hoffman, Rif A. Saurous, Eugene Brevdo, Kevin Murphy, and David M. Blei. 2017. “Deep Probabilistic Programming,” January, 1–18. http://arxiv.org/abs/1701.03757.

U.S. Army Corps of Engineers Headquarters. 2007. “SMART GATE.” 2007. https://www.erdc.usace.army.mil/Media/Fact-Sheets/Fact-Sheet-Article-View/Article/476668/smart-gate/.

———. 2018. “Navigation.” 2018. http://www.usace.army.mil/Missions/CivilWorks/Navigation.aspx.

USACE. 2019. “Policy for Operational Condition Assessments of USACE Assets.” 2019. https://www.publications.usace.army.mil/Portals/76/Users/182/86/2486/EC-11-2-218.pdf?ver=2019-09-04-162858-440.

Vega, Manuel A., Zhen Hu, and Michael D. Todd. 2020. “Optimal Maintenance Decisions for Deteriorating Quoin Blocks in Miter Gates Subject to Uncertainty in the Condition Rating Protocol.” *Reliability Engineering & System Safety* 204. https://doi.org/10.1016/j.ress.2020.107147.

Vega, Manuel A., Ramin Madarshahian, Travis B. Fillmore, and Michael D. Todd. 2019. “Optimal Maintenance Decision for Deteriorating Components in Miter Gates Using Markov Chain Prediction Model.” In *Structural Health Monitoring 2019: Enabling Intelligent Life-Cycle Health Management for Industry Internet of Things (IIOT)*, 1471–78. Lancaster, PA: DEStech Publications, Inc. https://doi.org/10.12783/shm2019/32269.

Vega, Manuel A., Mukesh K. Ramancha, Joel P. Conte, and Michael D. Todd. 2021. “Efficient Bayesian Inference of Miter Gates Using High-Fidelity Models.” In *38th International Modal Analysis Conference*. Houston, Texas: Springer.

Vega, Manuel, Ramin Madarshahian, and Michael D. Todd. 2019. “A Neural Network Surrogate

Model for Structural Health Monitoring of Miter Gates in Navigation Locks." In *37th International Modal Analysis Conference*, 93–98. Orlando, Florida. https://doi.org/10.1007/978-3-030-12075-7_9.

Vega, Manuel, Andreas Schellenberg, Humberto Caudana, and Gilberto Mosqueda. 2018a. "Five Story Building with Tunned Mass Damper." DesignSafe-CI. 2018. https://doi.org/doi.org/10.17603/DS2C687.

———. 2018b. "One Story Building with Tuned Mass Damper - OpenSees." DesignSafe-CI. 2018. https://doi.org/doi.org/10.17603/DS2GX1B.

———. 2018c. "One Story Building with Tuned Mass Damper - SimulinkRT." DesignSafe-CI. 2018. https://doi.org/doi.org/10.17603/DS27D69.

Wang, Changxi, and Elsayed A. Elsayed. 2020. "Stochastic Modeling of Corrosion Growth." *Reliability Engineering & System Safety* 204 (June): 107120. https://doi.org/10.1016/j.ress.2020.107120.

Wang, Niannian, Qingan Zhao, Shengyuan Li, Xuefeng Zhao, and Peng Zhao. 2018. "Damage Classification for Masonry Historic Structures Using Convolutional Neural Networks Based on Still Images." *Computer-Aided Civil and Infrastructure Engineering* 33 (12): 1073–89. https://doi.org/10.1111/mice.12411.

Wang, Zeyu, and Abdollah Shafieezadeh. 2020. "Real-Time High-Fidelity Reliability Updating with Equality Information Using Adaptive Kriging." *Reliability Engineering & System Safety* 195 (March 2018): 106735. https://doi.org/10.1016/j.ress.2019.106735.

Waszczyszyn, Zenon, and Leonard Ziemiański. 2005. "Neural Networks in the Identification Analysis of Structural Mechanics Problems." In *Parameter Identification of Materials and Structures*, 469:265–340. Vienna: Springer Vienna. https://doi.org/10.1007/3-211-38134-1_7.

Weibull, Waloddi. 1951. "A Statistical Distribution Function of Wide Applicability." *Journal of Applied Mechanics* 103: 293–97.

Wu, X., J. Ghaboussi, and J.H. Garrett. 1992. "Use of Neural Networks in Detection of Structural Damage." *Computers & Structures* 42 (4): 649–59. https://doi.org/10.1016/0045-7949(92)90132-J.

Xiang, Y., and X. G. Gong. 2000. "Efficiency of Generalized Simulated Annealing." *Physical Review E* 62 (3): 4473–76. https://doi.org/10.1103/PhysRevE.62.4473.

Xiang, Yang, Sylvain Gubian, Brian Suomela, and Julia Hoeng. 2013. "Generalized Simulated Annealing for Global Optimization: The GenSA Package." *The R Journal* 5 (1): 13. https://doi.org/10.32614/RJ-2013-002.

Xu, Hongpo, and JagMohan Humar. 2006. "Damage Detection in a Girder Bridge by Artificial Neural Network Technique." *Computer-Aided Civil and Infrastructure Engineering* 21 (6):

450–64. https://doi.org/10.1111/j.1467-8667.2006.00449.x.

Xu, Jiuping, and Lei Xu. 2011. “Health Management Based on Fusion Prognostics for Avionics Systems.” *Journal of Systems Engineering and Electronics* 22 (3): 428–36. https://doi.org/10.3969/j.issn.1004-4132.2011.03.010.

Yam, R. C. M., P.W. Tse, L. Li, and P. Tu. 2001. “Intelligent Predictive Decision Support System for Condition-Based Maintenance.” *The International Journal of Advanced Manufacturing Technology* 17 (5): 383–91. https://doi.org/10.1007/s001700170173.

Yang, Cheng-yu, Gao-jie Dong, Xiao-song Ren, Shawn You, and Andreas Schellenberg. 2015. “Real-Time Hybrid Testing on a Girder Bridge Model by Using Shaking- Table and Actuator.” In *6th International Conference on Advances in Experimental Structural Engineering*. http://sstl.cee.illinois.edu/papers/aeseancrisst15/180_Yang_Real-Time.pdf.

Yang, J.N., and S.D. Manning. 1996. “A Simple Second Order Approximation for Stochastic Crack Growth Analysis.” *Engineering Fracture Mechanics* 53 (5): 677–86. https://doi.org/10.1016/0013-7944(95)00130-1.

Yang, Yichao, Ramin Madarshahian, and Michael D. Todd. 2019. “Bayesian Damage Identification Using Strain Data from Lock Gates.” In , 47–54. Springer,. https://doi.org/10.1007/978-3-030-12115-0_7.

Ye, Zhi-Sheng, and Min Xie. 2015. “Stochastic Modelling and Analysis of Degradation for Highly Reliable Products.” *Applied Stochastic Models in Business and Industry* 31 (1): 16–32. https://doi.org/10.1002/asmb.2063.

Yin, Tao, and Hong-ping Zhu. 2018. “Probabilistic Damage Detection of a Steel Truss Bridge Model by Optimally Designed Bayesian Neural Network.” *Sensors* 18 (10): 3371. https://doi.org/10.3390/s18103371.

Zhang, Ruiyang, Brian M. Phillips, Shun Taniguchi, Masahiro Ikenaga, and Kohju Ikago. 2017. “Shake Table Real-Time Hybrid Simulation Techniques for the Performance Evaluation of Buildings with Inter-Story Isolation.” *Structural Control and Health Monitoring* 24 (10): e1971. https://doi.org/10.1002/stc.1971.

Zhang, Yi, Chul-Woo Kim, and Kong Fah Tee. 2017. “Maintenance Management of Offshore Structures Using Markov Process Model with Random Transition Probabilities.” *Structure and Infrastructure Engineering* 13 (8): 1068–80. https://doi.org/10.1080/15732479.2016.1236393.

Zhu, Fei, Jin-Ting Wang, Feng Jin, and Yao Gui. 2016. “Comparison of Explicit Integration Algorithms for Real-Time Hybrid Simulation.” *Bulletin of Earthquake Engineering* 14 (1): 89–114. https://doi.org/10.1007/s10518-015-9816-0.

Zhu, Y., E.A. Elsayed, H. Liao, and L.Y. Chan. 2010. “Availability Optimization of Systems Subject to Competing Risk.” *European Journal of Operational Research* 202 (3): 781–88. https://doi.org/10.1016/j.ejor.2009.06.008.

Zio, Enrico, and Francesco Di Maio. 2010. “A Data-Driven Fuzzy Approach for Predicting the Remaining Useful Life in Dynamic Failure Scenarios of a Nuclear System.” *Reliability Engineering & System Safety* 95 (1): 49–57. https://doi.org/10.1016/j.ress.2009.08.001.